Synthesis and Kinetic Study of CeO_2 and SiO_2 Supported CuO Catalysts for CO Oxidation

by

Shaikh Tofazzel Hossain

Submitted in Partial Fulfillment of the Requirements

for the Degree of

Doctor of Philosophy

in the

Materials Science and Engineering Program

YOUNGSTOWN STATE UNIVERSITY

May, 2018

Synthesis and Kinetic Study of CeO_2 and SiO_2 Supported CuO Catalysts for CO Oxidation

Shaikh Tofazzel Hossain

I hereby release this dissertation to the public. I understand that this dissertation will be made available from the OhioLINK ETD Center and the Maag Library Circulation Desk for public access. I also authorize the University or other individuals to make copies of this thesis as needed for scholarly research.

Signature:

Shaikh Tofazzel Hossain, Student Date

Approvals:

Dr. Ruigang Wang, Thesis Advisor Date

Dr. Timothy Wagner, Co-Advisor Date

Dr. Clovis Linkous, Committee Member Date

Dr. Sherri Lovelace-Cameron, Committee Member Date

Dr. Snjezana Balaz, Committee Member Date

Dr. Salvatore A. Sanders, Dean of Graduate Studies Date

ABSTRACT

Shape- and size-controlled CeO_2 and SiO_2 have been used in many catalysis applications. This research focused on the low-temperature CO oxidation for the automotive exhaust system. After starting a car, it needs to increase the temperature of catalytic converter to achieve full CO conversion. Toxic gas from the car pollutes the environment till the car reaches the required temperature. Thus, the preparation of efficient catalyst is much needed to lower the CO conversion temperature. This work especially focused on the correlation of the effect of catalyst supports' kind and morphology with their catalytic activity. Copper nitrate and copper carbonate precursors for wet impregnation method and copper nitrate for thermal decomposition method have been used to impregnate CuO onto hydrothermally prepared CeO_2 nanorods. Several characterization techniques, such as X-ray diffraction (XRD), Raman spectroscopy, transmission electron microscopy (TEM) and hydrogen temperature programmed reduction (H_2-TPR) have confirmed the presence of three different copper species (α, β, and γ) interacting with CeO_2 nanorods while forming oxygen vacancies in CeO_2 lattice by compensating the charges between copper and cerium.

Cu-O-Ce solid solutions and CuO impregnated on CeO_2 nanorods catalysts (CuO/CeO_2) with various compositions have been prepared using thermal decomposition and hydrothermal methods, to understand the distribution effect of copper species on low temperature CO oxidation. A series of temperature programmed reduction-temperature programmed oxidation (TPR-TPO) thermal cycling studies have been conducted to

understand the interactions between three assigned copper species (α, β, and γ) with CeO_2 support and the corresponding catalytic performance of the catalysts.

The effect of support reducibility and reduction treatment has been studied in SiO_2 nanospheres and CeO_2 nanorods supported CuO_x ($0 \leq x \leq 1$) catalysts on CO oxidation. CuO nanoparticles have been impregnated on SiO_2 nanospheres and CeO_2 nanorods using thermal decomposition method and then the samples have been oxidized in air at different temperatures (400-600 ^oC). The sample oxidized at 400 ^oC has also been further reduced under hydrogen atmosphere to compare the effect of thermal treatment (oxidation vs. reduction treatments) on the catalytic activity. In comparison to SiO_2 nanospheres supported CuO_x catalysts, both CuO/CeO_2 and reduced CuO_x/CeO_2 catalysts exhibited superior catalytic performance in terms of CO conversion and low-temperature hydrogen consumption. The enhanced activity of CeO_2 nanorods supported CuO_x catalysts has been correlated strongly to the surface defects on CeO_2 nanorods and interfacial structures.

In addition, in a novel design of co-supported scaffold structure catalyst, CeO_2 nanorods and SiO_2 nanospheres have been mixed in various ratios and 10 wt% CuO nanoparticles have been impregnated onto CeO_2-SiO_2 composite support using thermal decomposition method. Agglomeration of CeO_2 nanorods have been stopped by introducing SiO_2 nanospheres in the catalyst system, and this design can increase the chance to expose more CeO_2 surface to CuO nanoparticles in order to form higher amount of surface defects (incorporation of Cu ions and oxygen vacancies) and lead to higher synergistic interaction between CuO and CeO_2. H_2 TPR and CO oxidation

experiments suggested an enhanced low-temperature catalytic performance for 1:1 ratio mixture of CeO_2 and SiO_2 due to a strong interfacial interaction among SiO_2-CeO_2-CuO.

For kinetic study, 5%CO-95%He and O_2 gases have been used to reduce and oxidize CuO/CeO_2 catalyst respectively at a constant temperature of 400 ^oC (isothermal process). Mathematical formulas for power law, diffusion, nucleation and contraction models have been used to compare with the experimental data collected during the reduction and oxidation process of the catalyst to determine the best fitted reaction mechanism.

Acknowledgement

I would like to express gratitude to several people who contributed in many ways to my Ph.D. experience at YSU and Youngstown. First, I am wholeheartedly thankful to my advisor Dr. Ruigang Wang for his invaluable suggestions and help at each point of my research. I also want to express my gratitude to Dr. Timothy Wagner, Dr. Clovis Linkous, Dr. Snjezana Balaz, and Dr. Sherri Lovelace-Cameron for their critical comments on my research and dissertation.

Moreover, I would like to thank two special friends, Elizabeth Zell and Matt Caputo for supporting me in my academic work and in life in Youngstown. Also, I appreciate the work and effort of two undergraduate students, Yazeed Almesned and Elizaveta Azeeva who helped me in the synthesis and characterization of several samples for my research. Furthermore, I would love to express my gratitude to one of my best friends, Anastasiya Gulak who always supported and helped me to make important decisions of my life for last few years, and she relentlessly supported me morally to handle the stress of doctoral degree. I would also like to thank ABM Mustafizur Rahman and his wife Shanzida Alam for making Youngstown like a home for me, and thus, I have never felt being away from Bangladesh due to their hospitality and adoration for me.

Additionally, I would like to acknowledge Lisa Devore (Secretary of Chemistry Department), Dr. Dingqiang Li (Former manager of YSU electron microscopy facility), Tim Styranec (Chemical management), and Ray Hoff (Instrumentation specialist). As well, I want to thank all of the professors of YSU Materials Science & Engineering Program. YSU Center of Excellence for Advanced Materials Analysis is gratefully

acknowledged. I would also like to thank STEM College and Graduate Studies of YSU for giving me the opportunity to achieve my dream of getting a Ph.D. degree. Also, I like to acknowledge Dr. Balaz and her research group for collecting XPS data for me.

Lastly, I should not forget to acknowledge the contribution of my parents (Shaikh Anwar Hossain and Taslima Hossain), uncle (Md. Wahiduzzaman), sister (Shaikh Amima Hossain), and brother (Shaikh Shihab Hossain) who single-mindedly supported me all the way through my doctoral degree and life in Youngstown. I would have not been in this position without their sincere effort and faith in me. Finally, I would love to express my gratitude to Almighty Allah for His blessings on me.

Table of Contents

List of Figures

List of Tables

Chapter 1: Introduction

1.1. Background

A catalyst is affixed on a support material to maximize the surface area, as the activity of catalyst-support occurs at the surface atoms. Oxide support metal catalysts have several applications, such as catalytic converter, water gas shift reaction, SO_2 reduction, steam reforming of methanol/ethanol, oxidation of ammonia, solid oxide fuel cells etc.

The conversion of carbon monoxide (CO) to carbon dioxide (CO_2) has made an influence on the modern world. The invention of the internal combustion engine reintroduced scientific interest in CO oxidation catalysis. Car companies required a way to convert the toxic gases into non-toxic and nonthreatening gaseous products. These activities eventually led to the improvement of the current three-way catalytic converters. A catalytic converter is a device that controls the emission of toxic gas by converting toxic gases to less toxic pollutants via catalyzing a redox reaction. Eugene Houdry invented the catalytic converter, and was awarded a US Patent in 1952. Catalytic converters with two-way catalysts were first introduced in automobile industries to use in the exhaust system. Two-way catalysts are used to oxidize unburnt hydrocarbons and CO gas efficiently. Three-way catalysts which could reduce nitrogen oxides as well were introduced in 1981. In a catalytic converter, three reactions occur as shown below:

Oxidation:

$$C_xH_{2x+2} + [(3x+1)/2]\ O_2 = xCO_2 + (x+1)\ H_2O \quad (1)$$

$$2CO + O_2 = 2CO_2 \quad (2)$$

Reduction:

$2NO_x = xO_2 + N_2$ (3)

The above reactions usually occur at the interface of a catalyst-support, as shown in Fig. 1.1. Noble metals, such as Pt, Rh and Pd have been used as the catalyst on various metal oxide supports, such as Al_2O_3, SiO_2, ZrO_2 and CeO_2. In Fig. 1.2, it can be seen that the catalyst can interact with the support in three ways. The catalyst can highly interact with the support, as shown in Fig. 1.2a. Small and bulk size catalysts can loosely interact with the support, as shown in Fig. 1.2b and Fig. 1.2c, respectively.

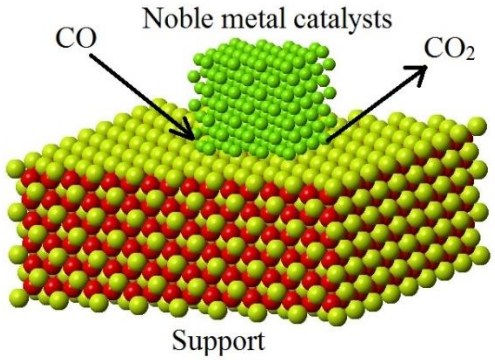

Figure 1.1. Simulated heterogeneous catalyst-support.

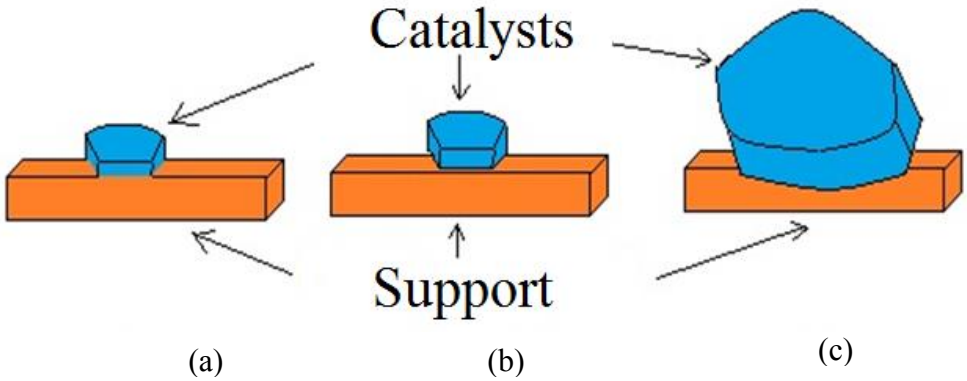

Figure 1.2. Various ways of interaction of the catalyst with the support.

1.2. Problem statement

The activity of a heterogeneous catalyst usually occurs at the surface [1]. Thus, a catalyst support is used to increase the surface area in order to enhance the catalytic activity. Metal oxide supports, such as Al_2O_3 and SiO_2, have been used as inactive support in commercial catalytic converters. The reaction rate and mechanism highly depend on the reducibility of the catalyst supports. Oxygen in an inactive support does not play any role in catalyzing the reaction rate. Therefore, non-reducible Al_2O_3 shows lower catalytic activity than the reducible and active CeO_2 supports [2]. Commercially prepared CeO_2 has octahedral shape. Although CeO_2 is an active support the oxygen storage and release capacity is very low in octahedral CeO_2 due to the presence of eight highly stable (111) planes. Researchers have been focusing on the shape-controlled catalyst support to improve the catalytic activity. In the latest advances, researchers have established several synthesis processes to control the shape and size of cerium oxide nanostructures. Controlled shape and size of ceria support can affect the catalytic activity [3]. Base metals/promoters are used to catalyze the reaction rate. Noble metals have been used as a promoter in the catalysis applications [4-6]. Various metals, such as Pt, Au, Pd, Ir, and Rh have been supported on several metal oxides for redox applications [6,7]. A mixture of Pt, Pd and Rh have been used in the catalytic converter, where Pd helps in oxidation, Rh helps in reduction, and Pt works as both [7]. The reactions (1-3) shown earlier usually occur in the range of 400-650 ^{o}C with the presence of noble metal catalysts. When a car is started, it needs time to increase the temperature of the catalytic converter. In the meantime, catalysts cannot convert toxic gases into non-toxic products. Thus, it affects the environment. Lowering the reaction temperature with 100%

conversion of toxic gases is still challenging. The high cost, the future availability, and the complicated preparation methods of noble metals forced researchers to think of different catalysts with similar performance. CuO has attracted attention as one of the most active and cheapest catalysts. CuO nanoparticles have been impregnated on controlled-shape CeO_2 using several methods. However, researchers have not yet investigated how to control the shape of CuO in order to use as a promoter in catalysis applications. Controlled shape and size of both catalysts and supports with the large surface area may enhance synergistic interaction at the interface, leading to higher catalytic activity. Limited investigation has been conducted on the interfacial structure to understand the mechanism of the catalytic reactions. Researchers like Burch et al. [8] and Rodriguez et al. [9] raised a question regarding whether the catalyst is activated or the support is activated or a new site formed at the interface is activated during the redox reaction. The contribution of oxygen vacancies and surface defects in the reaction is still unclear. An in-depth study of the mechanism of this catalytic reaction is challenging.

1.3. Literature review

1.3.1. Heterogeneous catalysis

Catalysts are used to speed up a reaction by arranging a reaction path with lower activation energy, but catalysts stay unchanged at the end of the reaction. There are two types of catalysts: homogeneous and heterogeneous. Homogeneous catalysts are in the same phase as the reactants and the products. Heterogeneous catalysts are the materials that are in a different phase than the reactants and the products. In this work, heterogeneous catalysts are prepared to use in catalytic converters.

Adsorption is the most important step in heterogeneous catalysis. Molecules in gas phase or in solution bind to atoms on a solid surface. The catalytic reactions occur at the surface of either the catalyst or the support. There are three mechanisms to explain the surface reaction. In the Langmuir-Hinshelwood mechanism shown in Fig. 1.3a, the two molecules A and B both are adsorbed on the surface of the catalysts. A and B meet at the surface and make A-B bonds which desorb away from the surface. In the Rideal-Eley mechanism (Fig. 1.3b), molecule A is adsorbed on the surface and molecule B meets A on the surface. Molecule B never gets adsorbed on the surface. After the reaction between A and B, they bond and desorb away from the surface. The precursor mechanism shown in Fig. 1.3c explains that one of the molecules (A) is adsorbed on the surface and the other (B) collides with the surface. Molecule B forms a mobile precursor state by colliding with the surface. Then B molecule collides with A on the surface and they react. Finally, new molecules (A-B) desorb away [10].

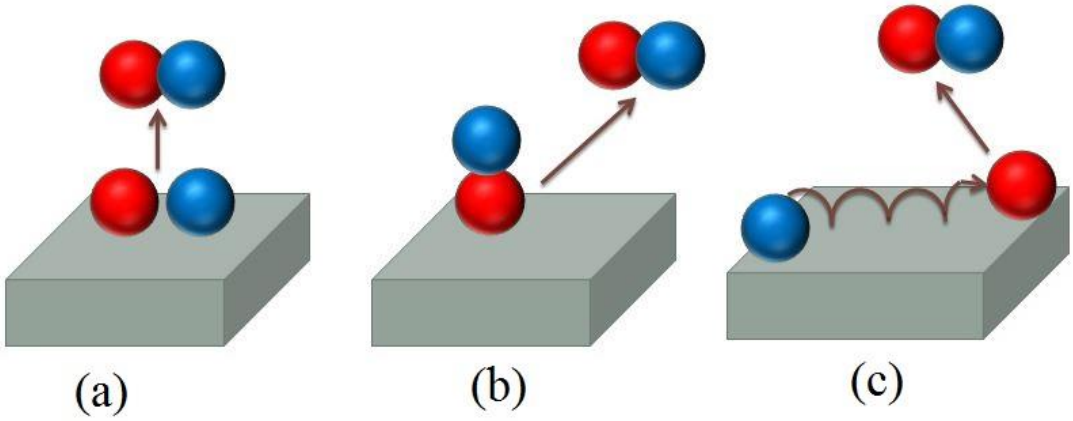

Figure 1.3. The Mechanisms of heterogeneous catalysts' surface reactions: (a) Langmuir-Hinshelwood, (b) Rideal-Eley, and (c) Precursor mechanism.

Catalytic activity can be measured using different techniques, which depend on the following applications: catalytic converters [11], water gas shift [12], organic synthesis

reactions [13] and other industrial applications. In this work, our focus is to prepare catalysts for the application of catalytic converters, where reactions (1), (2), and (3) occur as shown previously. Researchers have been trying to increase the catalytic activity by designing various catalyst-support systems. Table 1.1 shows various catalysts synthesized to increase the catalytic efficiency toward the oxidation of H_2 and CO. Usually, noble metals, such as Pt, Rh, Pd, and Au have been used as catalysts on supported metal oxides, such as Al_2O_3, ZrO_2, TiO_2, SiO_2, and CeO_2. Metal oxide supports can be two different types: reducible and non-reducible. Reducible metal oxide supports are those which can participate in the reaction by providing its oxygen. Transition metal oxides have received attention as substitutes for noble metal catalysts. Researchers have been trying to achieve similar performance by using various transition metal oxides, such as NiO, CuO, MnO, Mn_2O_7, FeO, and Fe_2O_3.

Table 1.1. Catalytic activity of various catalyst-support

Catalyst	**Support**	**Catalytic activity**	**Ref.**
Pt	Al_2O_3	H_2 consumption at 325 ^oC.	14
Pt	CeO_2	H_2 consumption in the range of 180-320 ^oC.	15
Pd	ZrO_2	100% CO conversion at ~175 ^oC	16
Pd	CeO_2-TiO_2	100% CO conversion at 60 ^oC.	17
Au	$Ce_{0.75}Zr_{0.25}O_2$	100% CO conversion at 65 ^oC.	18

NiO	γ-Al_2O_3	The highest amount of H_2 consumption at 430 ^oC for 20% Ni addition.	19
NiO	CeO_2	100% CO conversion at 210 ^oC and two peaks for H_2 consumption at 263 ^oC and 320 ^oC.	20
CuO	ZrO_2	H_2 consumption at 190, 210 and 270 ^oC for 2% Cu addition.	21
CuO	TiO_2	100% CO conversion at 110 ^oC and 140 ^oC for 8% Cu addition calcined at 400 and 500 ^oC, respectively.	22
Fe	TiO_2	H_2 consumption in the range of 200-350 ^oC and 530-850 ^oC.	23
CuO	SiO_2	H_2 consumption at 346 ^oC.	24
CuO	CeO_2	H_2 consumption at 200 ^oC.	25

The effect of support on catalytic activity has been documented. Researchers have been using various metal oxide supports for different catalysis applications. Supports are being used to stabilize catalyst nanoparticles along with an optimal catalytic performance. Strong metal-support interactions and/or electronic metal-support interactions are considered to be the reason of enhancing the catalytic activity due to charge transfers between metal and support, as well as the opportunity in creating highly reactive reaction sites at the interface of metal and support. As shown in Fig. 1.4, Green et al. [26] reported that CO molecules were delivered to the active sites (Au-TiO_2

interface) through diffusion on the TiO_2 surface. The O-O bond from molecular oxygen was dissociated near the active sites and reacted with CO to produce CO_2. Kim et al. [27] used density functional theory (DFT) to study the activity of CeO_2 support toward the CO oxidation reaction on Au as seen in Fig. 1.5. For the Au-CeO_2 catalyst, they reported that CO oxidation occurs by lattice oxygen of CeO_2, adsorbed oxygen at Au-Ce^{3+} interface, and coadsorbed CO and O_2 on Au nanoparticles. In this research, we have focused on reducible CeO_2 and non-reducible SiO_2 supported CuO catalysts.

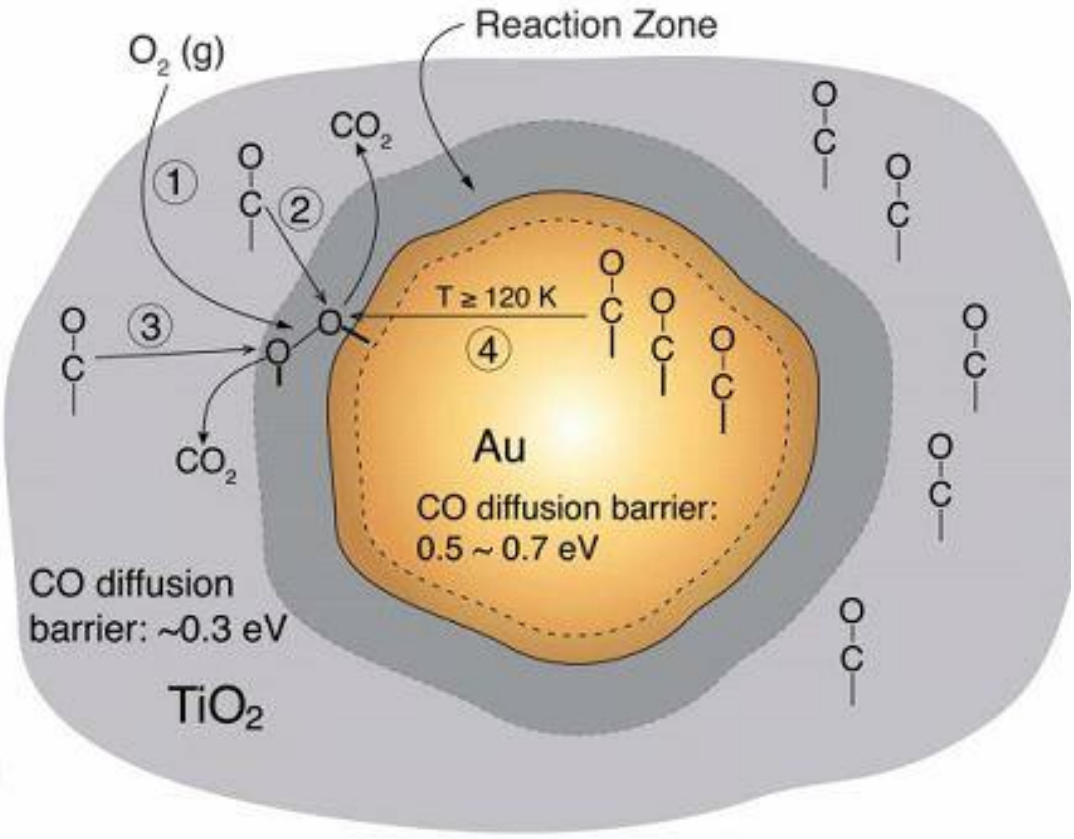

Figure 1.4. CO oxidation reaction over Au-TiO_2 catalysts. Reprinted with permission from Science [26].

Figure 1.5. CO oxidation reaction over Au-CeO_2 catalysts. Reprinted with permission from Kim et al. [27]. Copyright (2012) American Chemical Society.

1.3.2. Cerium oxide

Cerium is a well-known, rare-earth metal, situated in the lanthanide group with an atomic number of 58. Cerium has two valence states: III and IV. Cerium (III) oxide (Ce_2O_3) is not stable and can be easily oxidized to form cerium (IV) oxide (CeO_2). CeO_2 is also known as ceria. It has a fluorite structure with a face-centered cubic unit cell (shown in Fig. 1.6) whose lattice constant is 5.411 Å [28].

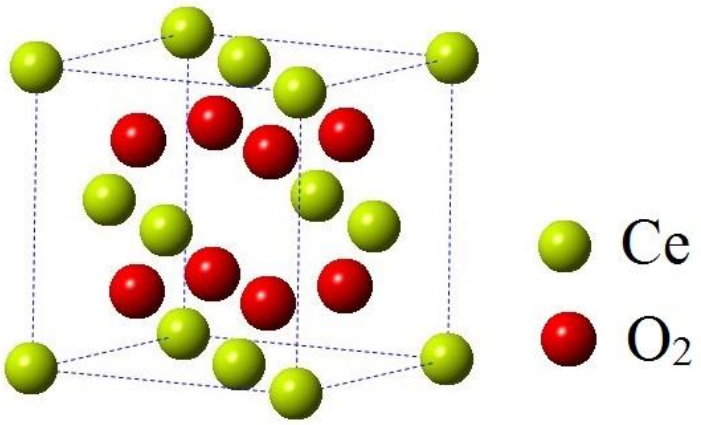

Figure 1.6. Atomic structure of CeO_2 unit cell.

Surface properties, which play an important role in catalysis, can be influenced by the morphology. CeO_2 with cubic fluorite structure shows mainly three low index planes, such as (100), (110) and (111). The stability of these planes are as follows: (111) > (110) > (100) [29,30]. Various shapes of CeO_2 play a key role in lowering the reduction temperature due to different exposed surface planes. Several nanostructures, such as rods, cubes, octahedron, polyhedron, and tube have been studied in recent years. Ceria octahedron usually exposes the most stable (111) planes on the surface [30,31]. According to many researchers, two planes, (110) and (100), are seen in ceria rods. However, in the previous research of our group, it was shown that (111) plane could also be found in rods [11]. Ceria cubes predominantly expose six of (100) planes [31]. Fig. 1.7 shows typical TEM images of nanorods, nanocubes, and nano-octahedral along with the corresponding simulated schematic.

Cerium oxide (CeO_2) is known as a three-way catalyst support because of its unique properties. It has the ability to take in and release oxygen under oxygen-rich and oxygen-lean conditions, respectively [11]. Cerium can change its valence states from Ce^{3+} to Ce^{4+} or from Ce^{4+} to Ce^{3+}, depending on oxygen-rich and -lean conditions. Fluorite structure CeO_2 can have three different types of defects, such as Frenkel (cation) defects, anti-Frenkel (anion) defects and Schottky defects [32]. However, due to the difference in energies among the aforementioned defects, anti-Frenkel or Frenkel-type oxygen defects, which have the lowest energies, are more likely to be present in ceria. These defects play a significant role during reduction. Due to the low defects concentration, the formation of oxygen pair vacancies does not change the stoichiometry of CeO_2. Nevertheless, during reduction, ceria can increase the defect concentration by removing oxygen ions. High

vacancy defect concentration can affect the stoichiometry, which changes from CeO_2 to CeO_{2-x} ($0 < x \leq 0.5$). After removing oxygen, the CeO_2 lattice compensates the negative charge by changing the charge of two cerium atoms from +4 to +3 [32]. Due to the oxygen vacancy defects and the interchange of valence states, Ce^{4+} and Ce^{3+}, CeO_2 has a unique ability to act as an oxygen reservoir under oxygen-rich conditions and to release oxygen under oxygen-lean conditions, as shown in Fig. 1.8.

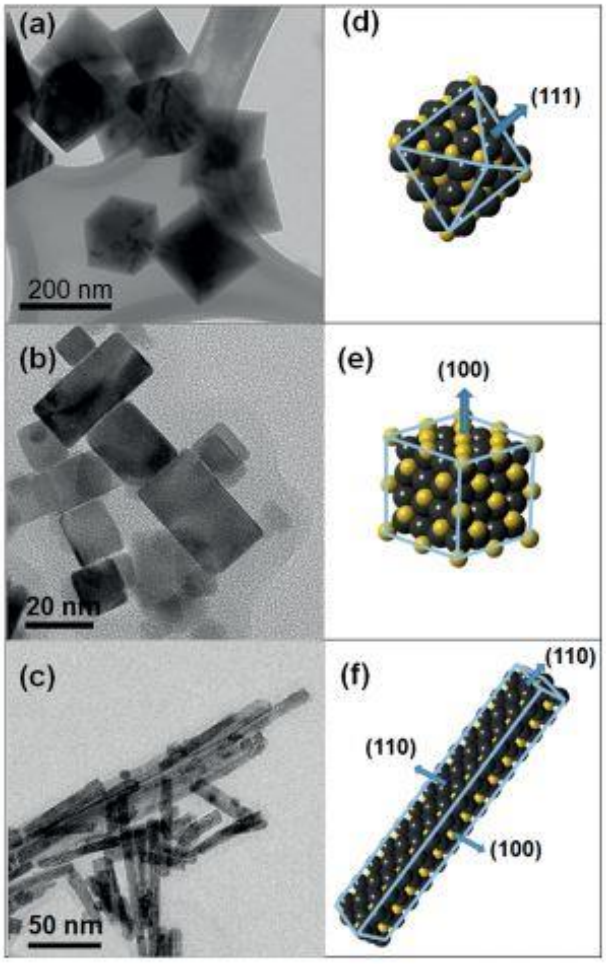

Figure 1.7. Typical TEM images of CeO_2 nano-octahedra (a), nanocubes (b), and nanorods (c). Structural simulated model of a CeO_2 nano-octahedra (d), nanocubes (e), and nanorods (f). Reprinted with permission from Wiley [31].

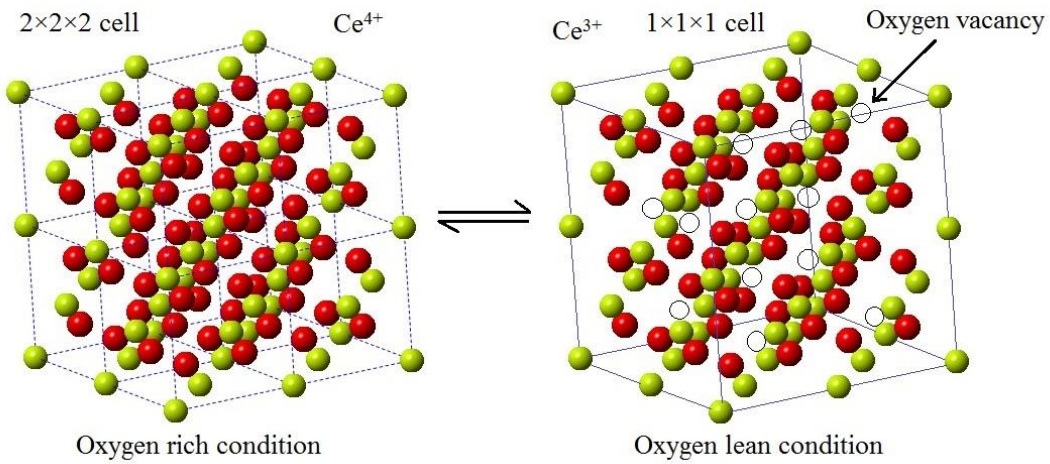

Figure 1.8. Structural change of CeO_2 during redox reactions.

1.3.3. Silicon oxide

Silicon is a semiconductor with atomic number 14. It is one of the most common elements in the earth's crust and can be found in many forms. Silicon is often bonded with oxygen and forms silicon oxide (SiO_2). Silicon oxide is also known as silica. As silicon is tetravalent element, each silicon atom is surrounded by four oxygens to form silica with largely interconnected network. Silica can have both crystalline and amorphous structures. Silica has a wide range of applications, such as producing glass, construction industries, optical fibers, heterogeneous catalysts support, sensor, drug delivery and biomedical applications [33,34]. Various size and shape of silica has been synthesized for last few decades. Researchers have made possible to control the size, shape, porosity and crystallinity of silica nanoparticle depending on its applications. Furthermore, various surface modifications of silica nanoparticles allow modulating precise surface chemistry. Researchers have also showed various synthesis methods to

prepare silica rods, tubes, fibers, spheres and wires. The following table shows different synthesis methods of silica nanoparticles:

Table 1.2. Methods to synthesize shape-controlled silica

Synthesis method	**Shape**	**Size**	**Ref.**
Stöber method	Nanospheres	0.25 – 2.0 μm in diameter	35
Surfactant templated	Nanorods	~100 nm in length	36
Co-condensation	Nanorods	Average 10 nm in diameter	37
Excimer laser ablation method	Nanowires	~10 nm in diameter	38
Hydrolysis	Nanotubes	~5 nm in diameter	39

For this work, amorphous silica nanospheres have been synthesized using modified Stöber method and this is commonly used process to synthesize silica nanosphere. Silica nanoshperes can be modified using different solvent as shown in Fig. 1.9 [40]. It can be seen that tetraethoxysilane (TEOS), mixed with alcohol, ammonia and water, is used to synthesize solid silica nanospheres. By adding CTAB or polymer, mesoporous silica nanosphres can be prepared. Polyelectrolyte is used to synthesize hollow structures. Fig. 1.10 shows scanning electron microscope (SEM) images of silica nanoshperes of different size synthesized using Stober method. By changing the ratios of TEOS and methanol, size of silica nanospheres can be varied. Particle size of silica decreases from 1500 nm to 10 nm with increasing MeOH/TEOS ratios from 1125 to 6000.

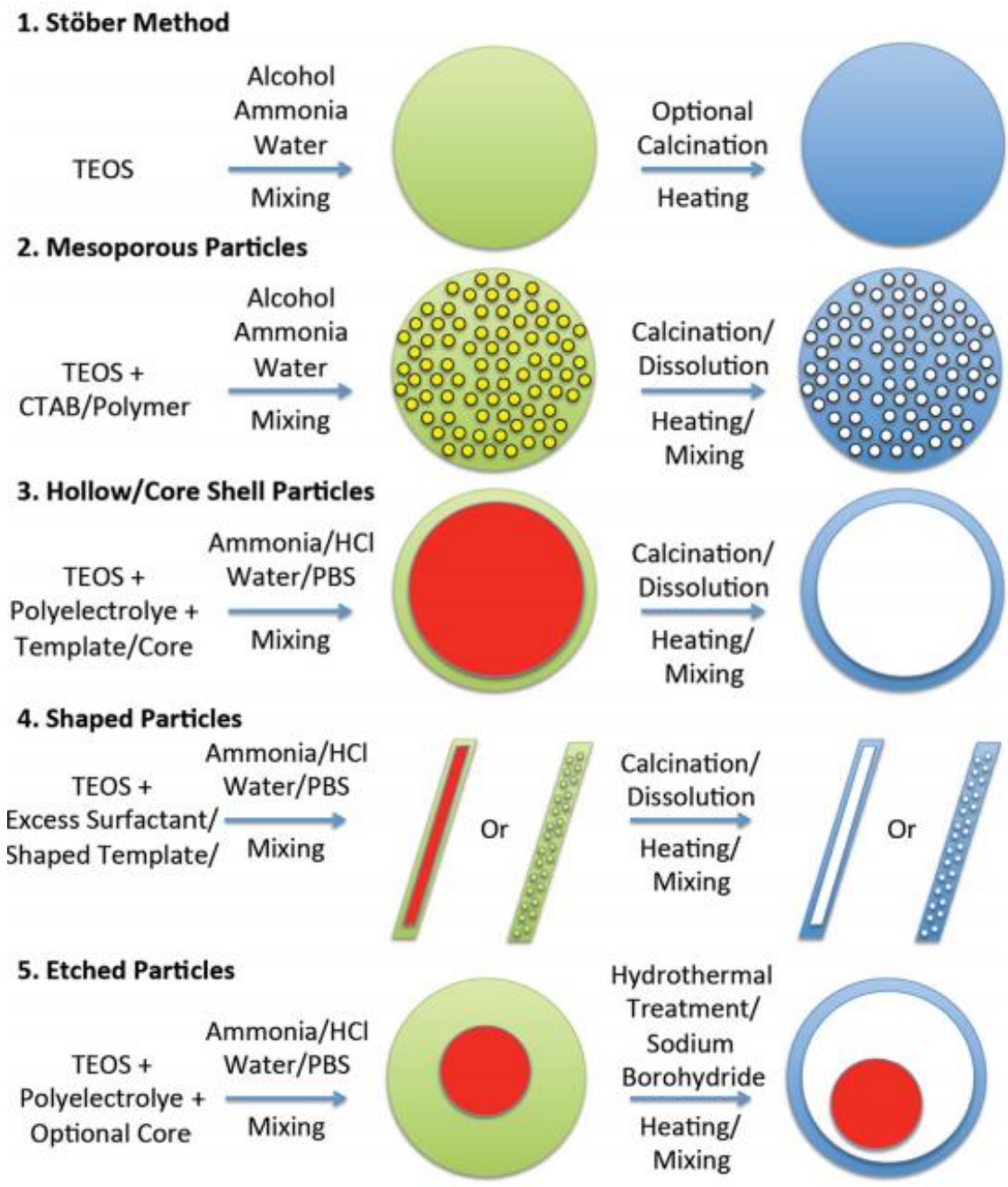

Figure 1.9. Various methods to synthesized different types of silica nanoscpheres. Reprinted with permission from Elsevier [40].

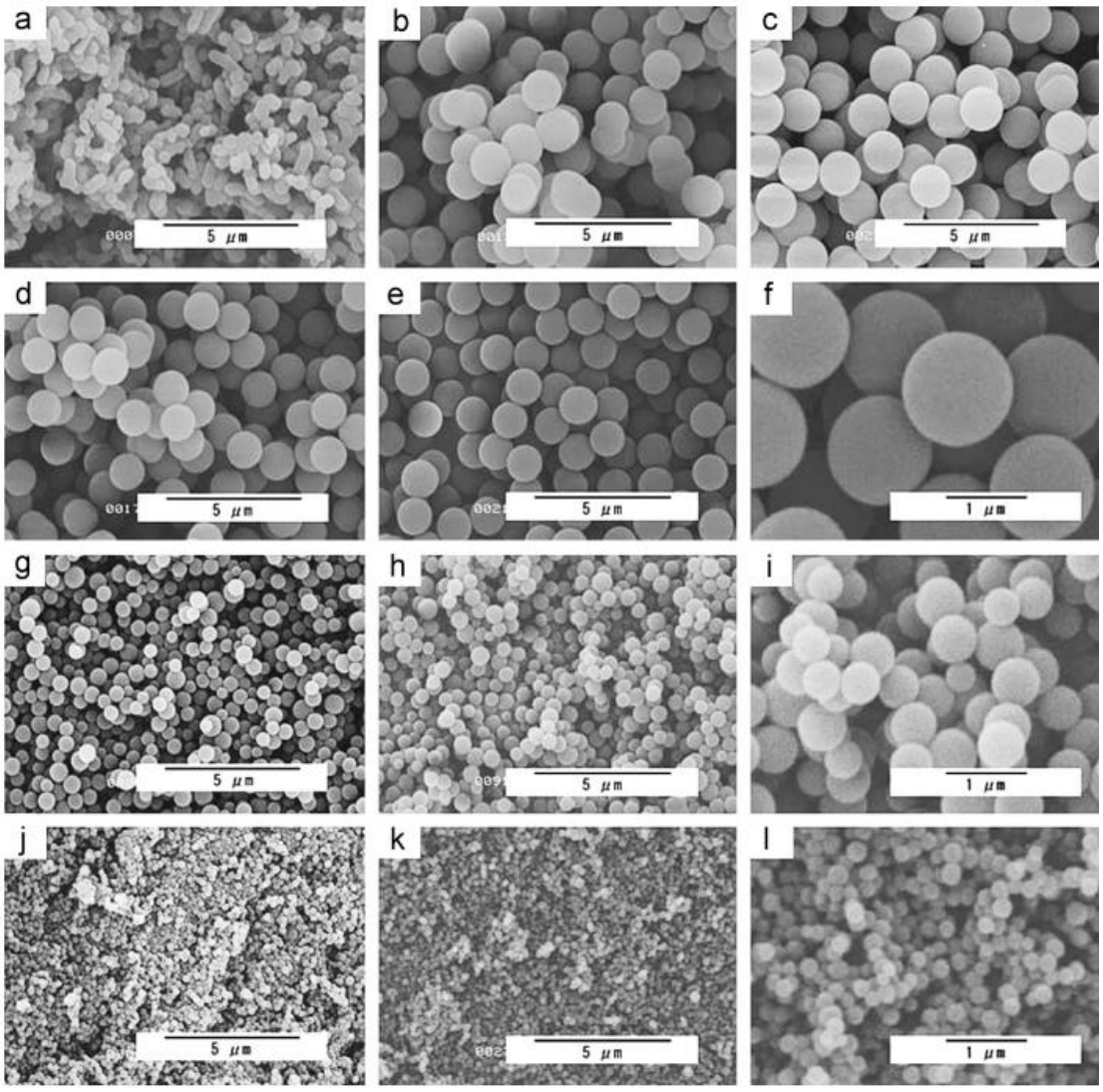

Figure 1.10. SEM images of silica nanospheres synthesized using Stober method with variable MeOH/TEOS ratios before and after calcination. Reprinted with permission from Elsevier [40].

1.3.4. Copper oxide

Copper is a transition metal with the atomic number 29. It has high thermal and electrical conductivity. Copper can be found in two valence states (I and II) in biomolecular compounds. Thus, two different oxides of copper are copper (I) oxide

(Cu_2O) and copper (II) oxide (CuO). Cu_2O is red color solid and crystallizes in cubic structure (shown in Fig. 1.11) with the lattice constant of 4.2696 Å [41]. CuO, which is a black solid, has monoclinic structure. CuO belongs to C2/c space group where a = 4.6837 Å, b = 3.4226 Å, c = 5.1288 Å and $\beta = 99.54^o$ [42].

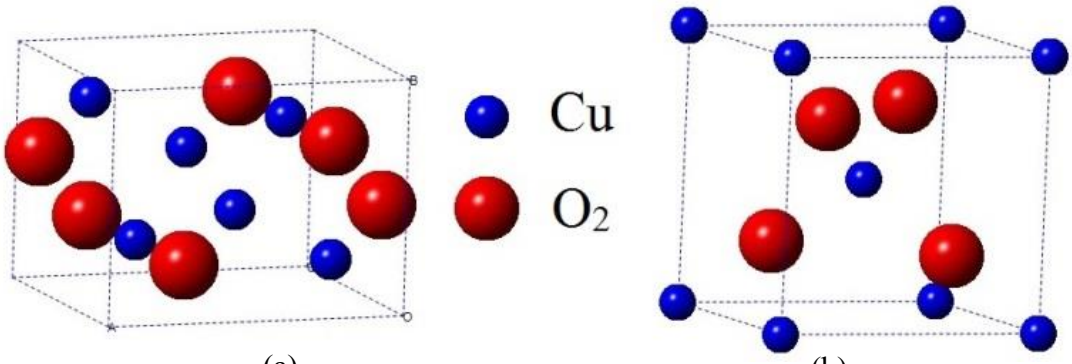

Figure 1.11. Simulated atomic structure of (a) CuO and (b) Cu_2O unit cells.

While researchers have focused on controlling the shape and size of CeO_2 support to elevate the catalytic activity, similarly the shape and size of CuO_x ($0 \leq x \leq 1$) can have an effect on the catalytic activity. Shape-controlled CuO_x has been used for different applications. Thus, a literature review has been done on the synthesis methods to control the shape and size of CuO_x. Various Cu phases of different shapes and sizes along with their synthesis methods are shown in Table 1.3.

Table 1.3. Synthesis methods of controlled shape and size of copper oxides

Cu phase	**Shape**	**Size**	**Synthesis method**	**Remarks**	**Ref**
CuO	Nanorods,	5-10 nm	Wet chemical	Increasing NaOH	43

	nanoribbons	breadth	aging method	molarity can change the shape from nanorods to nanoplatelets.	
CuO	Nanosphere	200-500 nm diameter	Hydrothermal	Poly-crystal nanospheres consist of many small nanoneedles.	44
Cu_2O	Nanocubes	500-700 nm edge lengths	Hydrothermal	A mixture of ethanol and water as the solvent can make the surfaces smooth.	45
CuO	Nanosphere	200 nm diameter	Hydrothermal		46
CuO	Nanorods	10-20 nm breadth and several hundred nm long	Hydrothermal		47
CuO, Cu_2O	Nanorods	1-3 nm diameter and 7-10 nm long	Solid-liquid phase arc discharge		48
CuO	Nanorods	12-17 nm	Solvothermal	The final product was	49

		diameter and 80-150 nm long		annealed at 350 ^{o}C.	
CuO	Nanorods, nanospheres	20-30 nm diameter and 150-180 nm long, 10-15 nm dia	Wet chemical	The addition of 0.2 M acetic acid produced nanospheres.	50
Cu_2O	Hexahedron octahedron decahedron	1.2-3.8 μm	Wet chemical	The addition of glucose both changed the shape and increased the particle size.	51

Controlling size and shape of CuO_x can be vital in the application of catalysis. Researchers have synthesized several different shapes, such as nanowires [52,53], rods [54], octahedron [55], platelets [56], spheres [57] and tubes [58] of CuO and Cu_2O. Derrick et al. [59] showed that CuO nanorods expose (100) and (111) faces, and nanocubes expose (100) faces. In decahedron nanoparticles, (111) faces grow faster than (100), which lead to nanorod-shaped particles. Nanocubes come from cuboctahedron nanoparticles, where (111) faces grow faster than (100). They also suggested that increasing the temperature during the hydrothermal process can increase the particle size. At 190 ^{o}C, nanorods are 700 nm in length and 100 nm in breadth. Cao et al. [48] used cetyltrimethylammonium bromide (CTAB) as a surfactant to synthesize nanorods and

nanotubes. Cu, Cu_2O and CuO nanorods expose (111) faces with d-spacing of 2.09, 2.47 and 2.53 Å, respectively. Chang et al. [43] showed (110) planes of CuO nanorods as their growth direction. Zhao et al. [45] synthesized Cu_2O nanocubes with (100) exposed planes.

1.3.5. Supported CuO catalysts

Among all of the transition metal oxides, CuO has gotten more attention because it shows similar performances as noble metal catalysts as shown in Table 1.1. Researchers have tried various ways to impregnate CuO on active support CeO_2. Table 1.4 shows the catalytic activity of CuO/CeO_2 catalysts where CeO_2 has different morphologies. It can be seen in the Table 1.4 that CeO_2 nanorods with CuO shows better catalytic activity. However, the method of impregnation of CuO on CeO_2 has also an effect on the catalytic reaction. Liu et al. [60] improved catalytic activity of CuO/CeO_2 nanorods using wet impregnation method where $Cu(NO_3)_2$ solution was mixed with as-prepared CeO_2 nanorods and the solution was stirred for 3 hrs.

Table 1.4. The catalytic activity of CuO/CeO_2 catalysts

CeO_2 morphology	**Impregnation method**	**Catalytic activity**	**Ref.**
Octahedral	Deposition-precipitation	H_2 consumption at 187 and 226 ^oC	61
Octahedral	Surfactant-templated	H_2 consumption at 200 and 228 ^oC	62

Octahedral	Urea nitrates combustion	H_2 consumption at 170 and 220 ^oC	63
Nanorods	Precipitation method	H_2 consumption at 196 and 226 ^oC	64
Nanorods	Wet impregnation method	H_2 consumption at 157 and 179 ^oC	60

High-resolution transmission electron microscopy (HRTEM) can be cooperative to investigate the catalyst-support interface and the crystal defects. Lattice parameter and d-spacing can also be calculated from HRTEM images. Zabilskiy et al. [65] showed TEM and HRTEM images of CuO-CeO_2 catalysts with different morphologies shown in Fig. 1.12 (left). Shape-controlled CeO_2 exposes various lattice planes. CeO_2 nanocubes show the interplanar spacing of 0.27 nm which corresponds to (100) planes. CeO_2 nanorods expose both (100) and (110) planes with d-spacing of 0.27 and 0.19 nm, respectively. Polyhedral CeO_2 shows only (111) plane with d-spacing of 0.31 nm. Scanning TEM (STEM) and energy dispersive X-ray spectroscopy (EDX) were also conducted by Zabilskiy et al. [65] Fig. 1.12 (right) shows STEM images with EDX mapping of CuO-CeO_2 catalysts. The homogeneous Cu distribution on CeO_2 rods and polyhedral can be observed in EDX mapping. Liu et al. [60] found that CeO_2 exposed similar (100) and (110) for nanorods and (111) plane for nanopolyhedra shown in Fig. 1.13. Yao et al. [66] prepared CeO_2 nanorods of ~11 nm diameter shown in Fig. 1.14 (left). In the same figure, the spotlike contrast variation observed in HRSTEM image corresponds to the voids.

Chen et al. [67] investigated STEM-EDX mapping on CuO/CeO_2 nanorods in order to find the uniform distribution of Cu on CeO_2 shown in Fig. 1.14 (right).

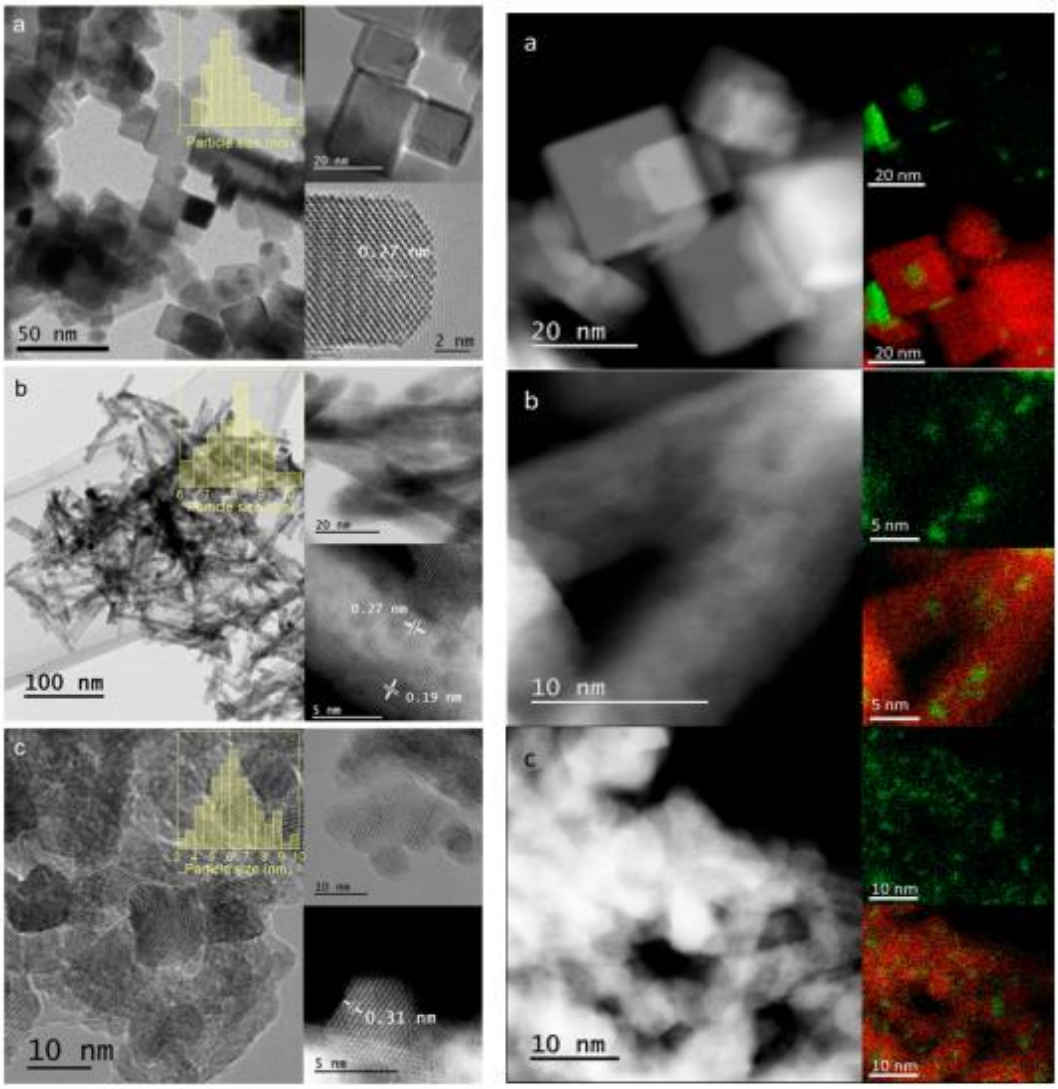

Figure 1.12. TEM and HRTEM images (left), and STEM images with EDX mapping (right) of CuO-CeO_2 catalysts with various morphologies. Reprinted with permission from Zabilsky et al. [65]. Copyright (2015) American Chemical Society.

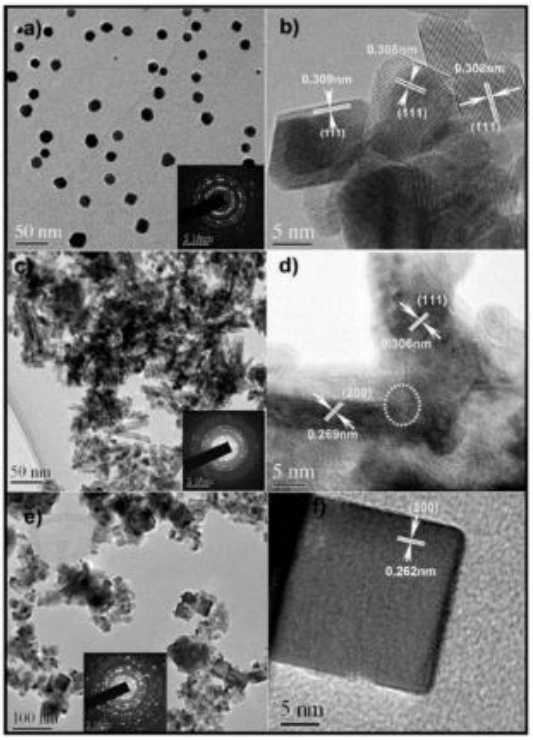

Figure 1.13. TEM and HRTEM images of CuO/CeO_2 nanopolyhedra, nanorods and nanocubes. Reprinted with permission from Wiley [60].

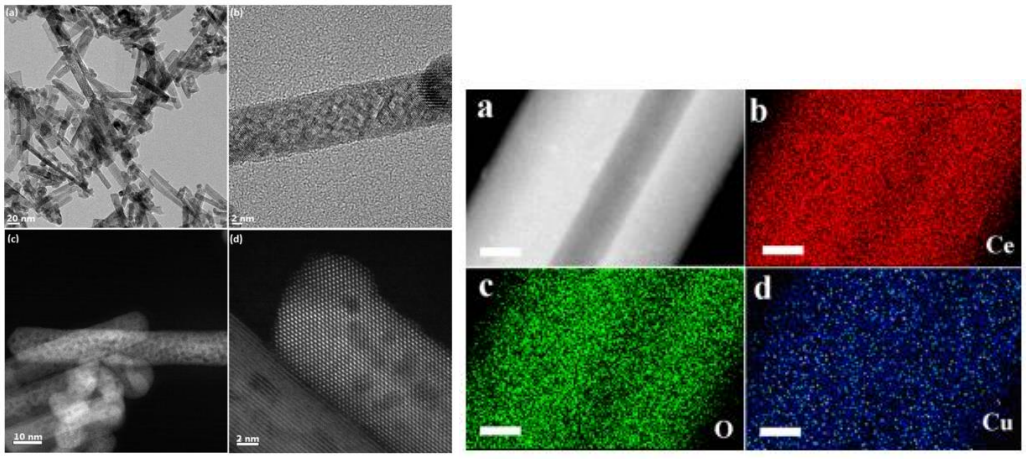

Figure 1.14. TEM, HRTEM, STEM and HRSTEM images of CuO/CeO_2 nanorods (left) and STEM-EDX mapping of CuO/CeO_2 nanorods (right). Reprinted with permission from Yao et al. [66] and Chen et al. [67]. Copyright (2014 and 2015) American Chemical Society.

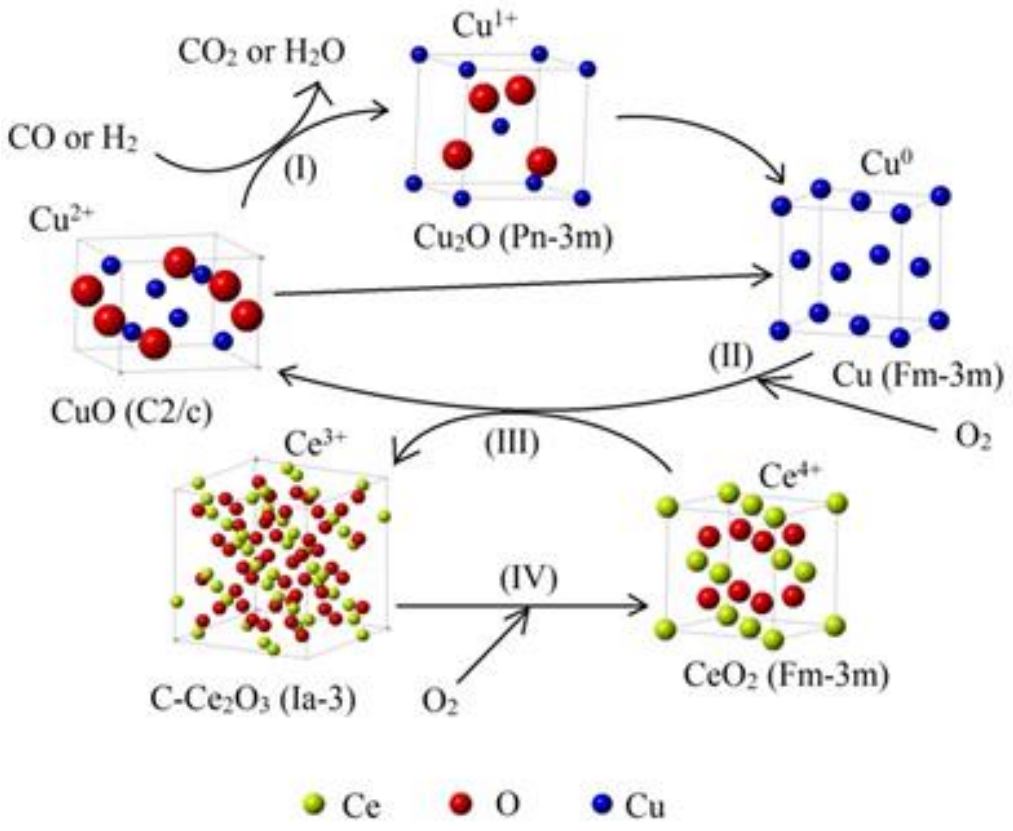

Figure 1.15. Schematic illustration of proposed mechanism for H_2 and CO oxidation reaction over CuO/CeO_2 catalysts.

Catalytic activity can be improved by the synergistic interaction between the base material and the support. [11] The base material can be highly interacted or loosely interacted with the support. The investigation of these interactions is very important to understand the mechanism of CO oxidation. Researchers, like Stephanopoulos [68], Sedmak [69], and Arias [70] proposed a mechanism for the catalytic CO oxidation of CuO/CeO_2 catalysts, using which they described that the catalytic process can be accomplished in several steps as shown in Fig. 1.15. Step I includes the reaction of bulk CuO with CO to reduce to Cu^{1+} and a further reduction to Cu^0. In step II, O_2 reacts with reduced Cu. In step III and IV, the role of CeO_2 support for well-dispersed CuO can be

seen. CeO_2 supplies oxygen to the reduced Cu species at the interface to re-oxidize these Cu species, and Ce^{4+} reduces to Ce^{3+} by itself. Oxygen vacancies are formed at the CuO/CeO_2 interface, which can be filled by adsorbed oxygen. Redox potentials of CuO are decreased due to the electron charge transfer among Cu, O, Ce and oxygen vacancies (or other defect areas), which aid the diffusion of oxygen from bulk to surface in CeO_2. This diffusion, ultimately, increases the redox action of Ce^{4+}/Ce^{3+} couples. An in-depth study of the proper mechanism is still unclear. Kinetic study and HRTEM of the interface of the catalysts can be useful to build a proper mechanism, including the effect of the shape controlled CuO_x.

Researchers have also impregnated CuO on SiO_2 nanoparticles due to its intrinsic structural characteristics. Niu et al. [71] synthesized solid SiO_2, and hollow SiO_2 nanospheres supported CuO catalysts. Hollow SiO_2 nanospheres were prepared using silica encapsulation via using Cu@C composite sphere hard template. The average diameter of hollow SiO_2 was 240 nm with 30 nm thin shell layer. CuO on hollow SiO_2 and solid SiO_2 nanospheres both showed two reduction peaks at 254 and 266 ^oC, and 243 and 278 ^oC, respectively. These two samples converted 100% CO into CO_2 at 210 and 420 ^oC, respectively. Niu et al. [71] suggested that CuO on hollow SiO_2 can have more highly dispersed CuO nanoclusters which led to its higher catalytic activity compared to catalytic activity of CuO on solid SiO_2 nanospheres. Fig. 1.16 shows hollow SiO_2 nanosphere supported CuO catalyst where SiO_2 spheres were ~250 nm in diameter. In EDX mapping, it can be seen that Cu was distributed homogeneously on SiO_2. Song et al. [72] also synthesized hollow SiO_2 sphere supported CuO catalyst using carbonaceous microspheres as template. They proposed that hollow texture with porosity increased gas

diffusion into the interior of sphere and this circumstance made possible for gas to access to exterior and interior of sphere as well as active sites of CuO. SiO_2 spheres were about 1 µm in diameter with 100 nm thick wall as shown in Fig. 1.17. They mentioned that the wall was made of plentiful small SiO_2 particles (average diameter of 80 nm) linking with each other. Astudillo et al. [73] and Luo et al. [74] showed the influence of CeO_2 on CuO/SiO_2 catalyst. Astudillo et al. [73] synthesized SiO_2 supported $CuO\text{-}CeO_2$ catalysts where the loading amount of Cu and Ce was varied from 1 to 9 with a constant total (Cu+Ce) 10% loading amount on SiO_2 particles. They showed that as the Ce loading amount was increased, the reduction peak in H_2-TPR started shifting from ~300 ^oC to 180 and 220 ^oC. From the catalytic activity of $CuO\text{-}CeO_2/SiO_2$ catalysts, they concluded that optimum ratio of Cu/Ce was 0.43 (3Cu-7Ce) which showed the maximum reducibility to both oxides' interface. Luo et al. [74] suggested that 8% Ce loading on CuO/SiO_2 showed the best catalytic activity when SiO_2 had large porosity.

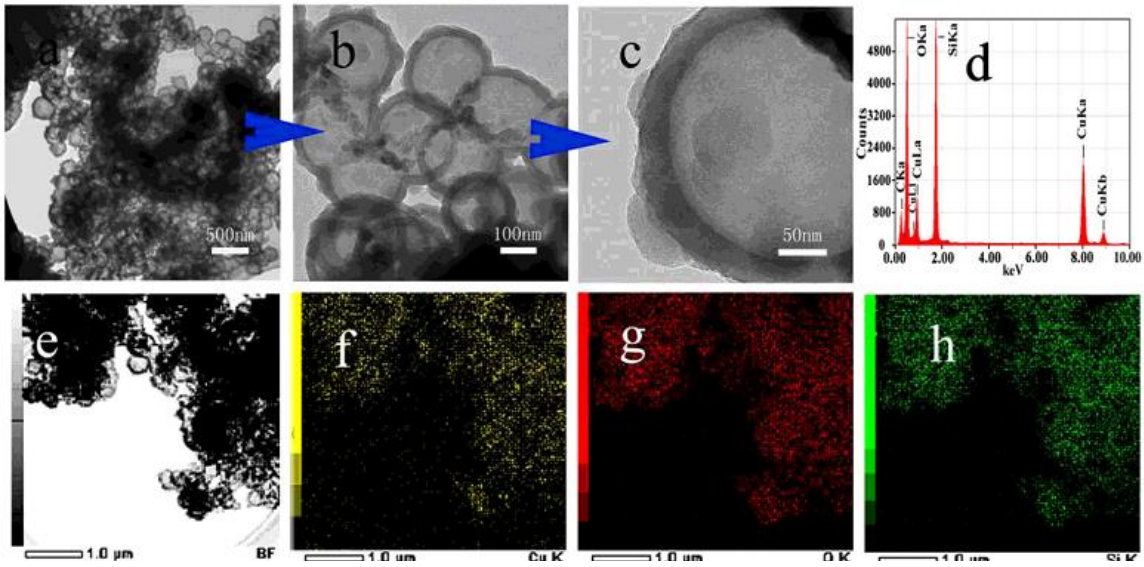

Figure 1.16. TEM images of CuO on hollowSiO_2 (a-c) and EDX mapping of CuO on hollowSiO_2 (d-h). Reprinted with permission from Nature [71].

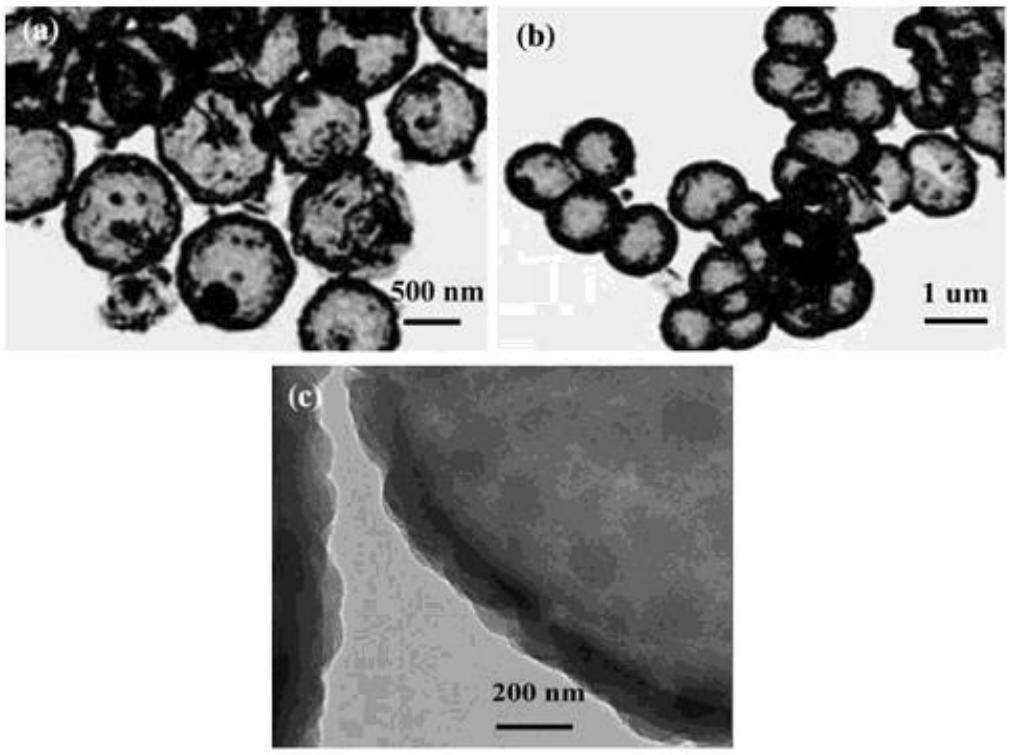

Figure 1.17. TEM images of CuO on hollow SiO_2 spheres. Reprinted with permission from Springer [72].

1.3.6. Reaction rate and mechanism for CO oxidation

Catalyst can change the reaction rate by providing a new reaction path with lower activation energy (E_A) of the reaction without being expended. Prior to the conversion of reactants into products, the free energy (G) of the system has to overcome E_A for the application, as shown in Fig. 1.18. Thus, a lower E_A is desired for most of the applications, and hence a faster catalytic rate is needed. For heterogeneous catalyst, each elementary step of reaction shows a local maximum which directs the speed of the step and this is called reaction determining step (rds).

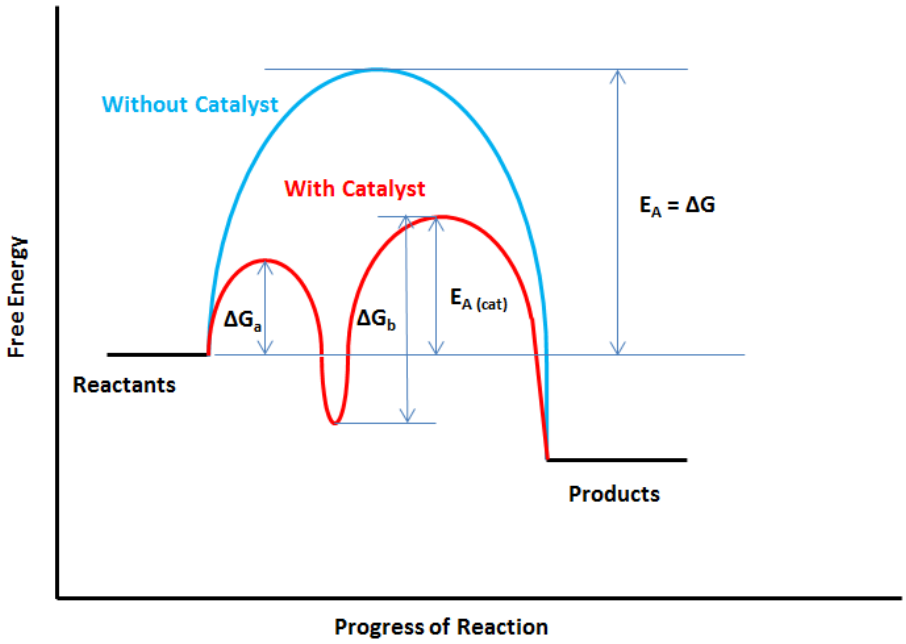

Figure 1.18. Reaction coordinate diagram of an arbitrary reaction with and without the catalyst.

The most popular, LFS model for the kinetic study of the catalysts toward CO oxidation has been proposed by Liu and Flytzani-Stephanopoulos [75]. They have assumed that oxygen and CO, provided by the adsorbed amount onto metal oxide support and noble metal surface, react at the interface of noble metal and metal oxide support particle, respectively (Fig. 1.19d-f). No oxygen from the lattice is involved in this reaction. They have developed an equation of the rate of reaction as shown below. In this equation, k_{CO} and K_{CO} are the surface reaction rate constant and CO adsorption equilibrium constant, respectively. Po_2 and P_{CO} are the partial pressure of oxygen and CO, respectively and n is a value, which is close to zero.

$$R_{CO} = \frac{k_{CO}K_{CO}P_{O_2}^{n}}{1 + K_{CO}P_{CO}} \qquad \text{(Eq. 1.1)}$$

$$k_{CO} = A\exp\left(\frac{-E_a}{RT}\right) \qquad \text{(Eq. 1.2)}$$

$$K_{CO} = K \exp(\frac{Q}{RT}) \quad \text{(Eq. 1.3)}$$

In modified Langmuir-Hinshelwood (LH) model [76], they have suggested adsorption of oxygen molecules as the rate determining step for noble metal supported on non-active supports and developed the rate of reaction as shown below.

$$R_{CO} = \frac{K_{O_2} P_{O_2}}{1 + K_{CO} P_{CO}} \quad \text{(Eq. 1.4)}$$

Table 1.5. Kinetic models of heterogeneous catalysts for CO oxidation

Model	Description of mechanism	Reaction rate	Ref
LH	(i) CO + #NM = CO#NM (ii) O_2 + 2@MOS = 2O@MOS (iii) O@MOS + #NM = O#NM + @MOS (RDS) (iv) CO#NM + O#MOS = CO_2 + 2#NM	$R_{CO} = \frac{k_{O_2}}{1 + K_{CO} P_{CO}}$	76
LFS	(i) CO + #NM = CO#NM (ii) O_2 + 2@MOS = 2O@MOS (iii) CO#NM + O@MOS = CO_2 + #NM + @MOS (RDS) • Reaction occurs at the boundary. • No lattice oxygen is involved in the reaction.	$R_{CO} = \frac{k_{CO} K_{CO} P_{O_2}^n}{1 + K_{CO} P_{CO}}$	75

MVK	(i) CO + oxidized catalyst = CO_2 + reduced catalyst (ii) Reduced catalyst + O_2 = oxidized catalyst (RDS)	$R_{CO} = \frac{k_{CO}k_{O_2}P_{CO}P_{O_2}^{n}}{0.5k_{CO}P_{CO} + K_{CO}P_{C}}$	77

#NM = Noble metal site @MOS = Metal oxide support site
RDS = Reaction determining step

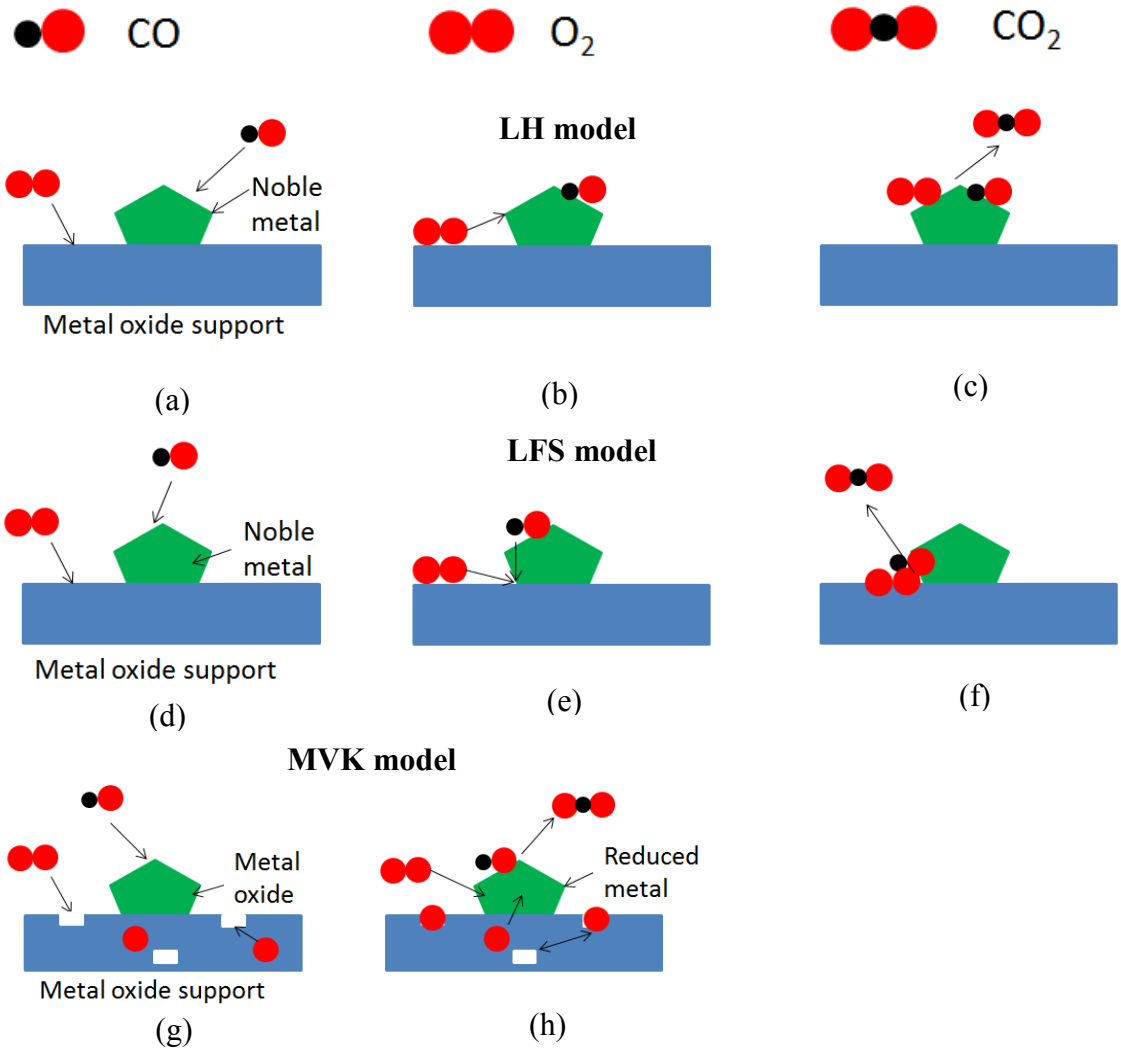

Figure 1.19. Mechanism for CO oxidation over metal oxide supported catalysts. LH model (a-c), LFS model (d-f), and MVK model (g-h).

In LH model (Fig. 1.19a-c), CO and O_2 molecules are adsorbed at the surface of CuO and CeO_2 similar to LFS model. Adsorbed oxygen moves to CuO surface from ceria surface and this part is assumed as the rate determining step. Reaction occurs at the metal surface and then CO_2 is desorbed away. For Mars-Van Krevelen (MVK) model (Fig. 1.19g-h), CO reacts with lattice oxygen at the surface of CuO and reduces CuO to metallic Cu. The reduced Cu gets oxidized by adsorbing oxygen molecules through the transfer of mobile oxygen from ceria lattice. Ceria can have oxygen vacancy due to transferring oxygen to metallic Cu. Thus, ceria adsorbs oxygen to fill the vacancy.

1.4. References

1. Prasad, R.; Rattan, G. Preparation methods and applications of CuO-CeO_2 catalysts: A short review. *B. Chem. Reaction Eng. Catal*. **2010**, 5, 7-30.

2. Ivanova, A. S.; Slavinskaya, E. M.; Gulyaev, R. V.; Zaikovskii, V. I.; Stonkus, O. A.; Danilova, I. G.; Plyasova, L. M.; Polukhina, I. A.; Boronin, A. I. Metal-support interactions in Pt/Al_2O_3 and Pd/Al_2O_3 catalysts for CO oxidation. *Appl. Catal. B-Environ*. **2010**, 97, 57-71.

3. Qia, Z.; Wu, Z.; Dai, S. Shape-controlled ceria-based nanostructures for catalysis applications. *ChemSusChem* **2013**, 6, 1821-1833.

4. Holmgren, A.; Andersson, B.; Duprez, D. Interaction of CO with Pt/ceria catalysts. *Appl. Catal. B-Environ*. **1999**, 22, 215-230.

5. Vindigni, F.; Manzoli, M.; Tabakova, T.; Idakiev, V.; Boccuzzi, F.; Chiorino, A. Effect of ceria structural properties on the catalytic activity of Au-CeO_2 catalysts for WGS reaction. *Phys. Chem. Chem. Phys.* **2013**, 15, 13400-13408.

6. Cordatos, H.; Bunluesin, T.; Stubenrauch, J.; Vohs, J. M.; Gorte, R. J. Effect of ceria structure on oxygen migration for Rh/ceria catalysts. *J. Phys. Chem*. **1996**, 100, 785-789.

7. Bardi, U.; Caporali, S. Precious metals in automotive technology: An unsolvable depletion problem? *Minerals* **2014**, 4, 388-398.

8. Burch, R. Gold catalysts for pure hydrogen production in the water-gas-shift reaction: activity, structure and reaction mechanism. *Phys. Chem. Chem. Phys*. **2006**, 8, 5483-5500.

9. Rodriguez, J. A.; Liu, G.; Jirsak, T.; Hrbek, J.; Chang, Z.; Dvorak, J.; Maiti, A. Activation of gold on titania: adsorption and reaction of SO_2 on Au/TiO_2(110). *J. Am. Chem. Soc*. **2002**, 124, 5242-5250.

10. Masel, R. I. "Principles of Adsorption and Reaction on Solid Surfaces", Wiley Series in Chemical Engineering, Wiley-Interscience, New York, USA, **1996**, ISBN 978-0-471-30392-3.

11. Mock, S. A.; Sharp, S. E.; Stoner, T. R.; Radetic, M. J.; Zell, E. T.; Wang, R. CeO_2 nanorods supported transition metal oxide catalysts for CO oxidation. *J. Colloid Interf. Sci*. **2016**, 466, 261-267.

12. Yao, S. Y.; Xu, W. Q.; Johnston-Peck, A. C.; Zhao, F. Z.; Liu, Z. Y.; Luo, S.; Senanayake, S. D.; Martinez-Arias, A.; Liu, W. J.; Rodriguez, J. A. Morphological effects of the nanostructured ceria support on the activity and stability of CuO/CeO_2 catalysts for the water gas shift reaction. *Phys. Chem. Chem. Phys*. **2014**, 16, 17183-17195.

13. Zhuan, H. D.; Bai, S. F.; Liu, X. M.; Yan, Z. F. Structure and performance of Cu/ZrO_2 catalyst for the synthesis of methanol from CO_2 hydrogenation. *J. Fuel Chem. Technol*. **2010**, 38, 462-467.

14. Santos, A. C. S. F.; Damyanova, S.; Teixeira, G. N. R.; Mattos, L. V.; Noronha, F. B.; Passos, F. B.; Bueno, J. M. C. The effect of ceria content on the performance of $Pt/CeO_2/Al_2O_3$ catalysts in the partial oxidation of methane. *Appl. Catal. A-Gen*. **2005**, 290, 123-132.

15. Damyanova, S.; Bueno, J. M. C. Effect of CeO_2 loading on the surface and catalytic behaviors of CeO_2-Al_2O_3 supported Pt catalysts. *Appl. Catal. A-Gen*. **2003**, 253, 135-150.

16. Vedyagin, A. A.; Volodin, A.M.; Kenzhin, R. M.; Chesnokov, V. V.; Mishakov, I. V. CO oxidation over Pd/ZrO_2 catalysts: Role of support's donor sites. *Molecules* **2016**, 21, 1289 (1-15).

17. Zhu, H.; Qin, Z.; Shan, W.; Shen, W.; Wang, J. CO oxidation at low temperature over Pd supported on CeO_2-TiO_2 composite oxide. *Catal. Today* **2007**, 126, 382-386.

18. Gomez, D.; Garcia, M. A.; Rynkowski, J. M. CO oxidation over Au/CeO_2-ZrO_2 catalysts: The effect of the support composition of the Au-support interaction. *Kinetics Catal*. **2010**, 51, 823-827.

19. Zangouei, M.; Moghaddam, A. Z.; Arasteh, M. The influence of nickel loading on reducibility of NiO/Al_2O_3 catalysts synthesized by sol-gel method. *Chem. Eng. Res. Bulletin* **2010**, 14, 97-102.

20. Wang, Y.; Zhu, A.; Zhang, Y.; Au, C. T.; Yang, X.; Shi, C. Catalytic reduction of NO by CO over NiO/CeO_2 catalyst in stoichiometric NO/CO and NO/CO/O_2 reaction. *Appl. Catal. B-Environ.* **2008**, 81, 141-149.

21. Aguila,G.; Gracia, F.; Araya, P. CuO and CeO_2 catalysts supported on Al_2O_3, ZrO_2 and SiO_2 in the oxidation of CO at low temperature. *Appl. Catal. A-Gen*. **2008**, 343, 16-24.

22. Huang, J.; Wang, S.; Zhao, Y.; Wang, X.; Wang, S.; Wu, S.; Zhang, S.; Huang, W. Synthesis and characterization of CuO/TiO_2 catalysts for low-temperature CO oxidation. *Catal. Commun*. **2006**, 7, 1029-1034.

23. Einaga, H.; Urahama, N. CO oxidation over TiO_2 supported Pt-Fe catalysts prepared by coimpregnation method. *Catal. Lett*. **2014**, 144, 1653-1660.

24. Mo, L.; Kawi, S. An in situ self-assembled core-shell precursor route to prepare ultrasmall copper nanoparticles on silica catalysts. *J. Mater. Chem. A* **2014**, 2, 7837-7844.

25. Yang, W.; Li, D.; Xu, D.; Wang, X. Effect of CeO_2 preparation method and Cu loading on CuO/CeO_2 catalysts for methane combustion. *J. Nat. Gas. Chem*. **2009**, 18, 458-466.

26. Green, I. X.; Tang, W.; Neurock, M.; Yates Jr., J. T. Spectroscopic observation of dual catalytic sites during oxidation of CO on a Au/TiO_2 catalyst. *Science*, **2011**, 333, 736-739.

27. Kim, H. Y.; Lee, H. M.; Henkelman, G. CO oxidation mechanism on CeO_2-supported Au nanoparticles. *J. Am. Chem. Soc*., **2012**, 134, 1560-1570.

28. Gangopadhyay, S.; Frolov, D. D.; Masunov, A. E.; Seal. S. Structure and properties of cerium oxides in bulk and nanoparticulate forms. *J. Alloy Compd*. **2014**, 584, 199-208.

29. Na, T.; Jingyue, L.; Wnjie, S. Tuning the shape of ceria nanomaterials for catalytic applications. *Chinese J. Catal*. **2013**, 34, 838-850.

30. Sayle, D. C.; Maicaneanu, S. A.; Watson, G. W. Atomistic models for CeO_2 (111), (110) and (100) nanoparticles supported on yttrium-stabilized zirconia. *J. Am. Chem. Soc*. **2002**, 124, 11429-11439.

31. Zhao, E. W.; Zheng, H.; Zhou, R.; Hagelin-Weaver, H. E.; Bowers, C. R. Shaped ceria nanocrystals catalyze efficient and selective para-hydrogen-enhanced polarization. *Angew. Chem. Int. Ed.* **2015**, 54, 14270-14275.

32. Zhou, Y. Nanostructured cerium oxide based catalysts: Synthesis, physical properties and catalytic performance. *Diss*. University of Nebraska-Lincoln, **2015**.

33. Filippov, V. I.; Terentjev, A. A.; Yakimov, S. S. MOS structure (Pd-SiO_2-Si) based gas sensor with an external catalyst element. *Sensor Actuat. B: Chem.* **1997**, 41, 153-158.

34. Li, L.; Gu, Z.; Gu, W.; Liu, J.; Xu, Z. P. Efficient drug delivery using SiO_2 –layered double hydroxide nanocomposites. *J. Colloid Interf. Sci*. **2016**, 470, 47-55.

35. Stober, W.; Fink, A. Controlled growth of monodisperse silica spheres in the micron size range. *J. Colloid Interf. Sci*. **1968**, 26, 62-69.

36. Tsai, C. P.; Hung, Y.; Chou, Y. H.; Huang, D. M.; Hsiao, J. K.; Chen, Y. C.; Mou, C. Y. High-contrast paramagnetic fluorescent mesophorous silica nanorods as a multifunctional cell-imaging probe. *Small* **2008**, 4 (2), 186-191.

37. Giri, S.; Trewyn, B. G.; Stellmaker, M. P.; Lin, V. Stimuli-responsive controlled-release delivery system based on mesoporous silica nanorods capped with magnetic nanoparticles. *Angew. Chem. Int. Ed*. **2005**, 44, 5038-5044.

38. Yu, D. P.; Hang, Q. L.; Ding, Y.; Zhang, H. Z.; Bai, Z. G.; Wang, J. J.; Zou, Y. H.; Qian, W.; Xiong, G. C.; Feng, S. Q. Amorphous silica nanowires: Intensive blue light emitters. *Appl. Phys. Lett*. **1998**, 73, 3076-3078.

39. Harada, M.; Adachi, M. Surfactant mediated fabrication of silica nanotubes. *Adv. Mater*. **2000**, 12 (11), 839-841.

40. Liberman, A.; Mendez, N.; Trogler, W. C.; Kummel, A. C. Synthesis and surface functionalization of silica nanoparticles for nanomedicine. *Surf. Sci. Rep*. **2014**, 69, 132-158.

41. Ruiz, E.; Alvarez, S. Electronic structure and properties of Cu_2O. *Phys. Rev. B* **1997**, 56, 7189-7196.

42. Yao, W. T.; Yu, S. H.; Zhou, Y.; Jiang, J.; Wu, W. S.; Zhang, L.; Jiang, J. Formation of uniform CuO nanorods by spontaneous aggregation: Selective synthesis of CuO, Cu_2O and Cu nanoparticles by a solid-liquid phase arc discharge process. *J. Phys. Chem. B* **2005**, 109, 14011-14016.

43. Chang, Y.; Zeng, H. C. Controlled synthesis and self-assembly of single-crystalline CuO nanorods and nanoribbons. *Cryst. Growth Des*. **2004**, 4, 397-402.

44. Reitz, E.; Jia, W.; Gentile, M.; Wang, Y.; Lei, Y. CuO nanospheres based nonenzymatic glucose sensor. *Electroanal*. **2008**, 20, 2482-2486.

45. Zhao, H. Y.; Wang, Y. F.; Zeng, J. H. Hydrothermal synthesis of uniform cuprous oxide microcrystals with controlled morphology. *Cryst. Growth Des*. **2008**, 8, 3731-3734.

46. Khan, R.; Vaseem, M.; Jang, L. W.; Yun, J. H.; Hahn, Y. B.; Lee, I. H. Low temperature preparation of CuO nanospheres and urchin-shaped structures via hydrothermal route. *J. Alloy Compd*. **2014**, 609, 211-214.

47. Gao, X. P.; Bao, J. L.; Pan, G. L.; Zhu, H. Y.; Huang, P. X.; Wu, F.; Song, D. Y. Preparation and electrochemical performance of polycrystalline and single crystalline CuO nanorods as anode materials for Li ion battery. *J. Phys. Chem. B* **2004**, 108, 5547-5551.

48. Cao, M.; Hu, C.; Wang, Y.; Guo, Y.; Guo, C.; Wang, E. A controllable synthetic route to Cu, Cu_2O and CuO nanotubes and nanorods. *Chem. Commun*. **2003**, 1884-1885.

49. Gopalakrishnan, M.; Jeevaraj, A. K. S. Template-free solvothermal synthesis of copper oxide nanorods. *Mat. Sci. Semicon. Proc*. **2014**, 26, 512-515.

50. Konar, S.; Kalita, H.; Puvvada, N.; Tantubay, S.; Mahto, M. K.; Biswas, S.; Pathak, A. Shape dependent catalytic activity of CuO nanostructures. *J. Catal*. **2016**, 336, 11-22.

51. Yin, M.; Liu, S. Synthesis of CuO microstructures with controlled shape and size and their exposed facets induced enhanced ethanol sensing performance. *Sensor Actuat. B-Chem*. **2016**, 227, 328-335.

52. Jiang, X.; Herricks, T.; Xia, Y. CuO nanowires can be synthesized by heating copper substrates in air. *Nano Lett*. **2002**, 2, 1333-1338.

53. Zhang, X.; Wang, G.; Liu, X.; Wu, J.; Li, M.; Gu, J.; Liu, H.; Fang, B. Different CuO nanostructures: Synthesis, characterization and applications for glucose sensors. *J. Phys. Chem. C* **2008**, 112, 16845-16849.

54. Jia, W.; Liu, Y.; Hu, P.; Yu, R.; Wang, Y.; Ma, L.; Wang, D.; Li, Y. Ultrathin CuO nanorods: controllable synthesis and superior catalytic properties in styrene epoxidation. *Chem. Commun*. **2015**, 51, 8817-8820.

55. Feng, L.; Xuan, Z.; Bai, Y.; Zhao, H.; Li, L.; Chen, Y.; yang, X.; Su, C.; Guo, J.; Chen. X. Preparation of octahedral CuO micro/nanocrystals and electrochemical performance as anode for lithium-ion battery. *J. Alloy Compd*. **2014**, 600, 162-167.

56. Zou, G.; Li, H.; Zhang, D.; Xiong, K.; Dong, C.; Qian. Y. Well-aligned arrays of CuO nanoplatelets. *J. Phys. Chem. B* **2006**, 110, 1632-1637.

57. Jian, G.; Liu, L.; Zachariah, M. R. Facile aerosol route to hollow CuO spheres and its superior performance as an oxidizer in nanoenergetic gas generators. *Adv. Funct. Mater*. **2013**, 23, 1341-1346.

58. Park, S.; Kim, S.; Park, S.; Lee, C. Facile synthesis of CuO nanotubes and their formation mechanism. *Mater. Lett*. **2015**, 138, 110-112.

59. Mott, D.; Galkowski, J.; Wang, L.; Luo, J.; Zhong, C. J. Synthesis of size controlled and shaped copper nanoparticles. *Langmuir* **2007**, 23, 5740-5745.

60. Liu, L.; Yao, Z.; Deng, Y.; Gao, F.; Liu, B.; Dong, L. Morphology and crystal-plane effects of nanoscale ceria on the activity of CuO/CeO_2 for NO reduction by CO. *ChemCatChem* **2011**, 3, 978-989.

61. Tang, X.; Zhang, B.; Li, Y.; Xu, Y.; Xin, Q.; Shen, W. Carbon monoxide oxidation over CuO/CeO_2 catalysts. *Catal. Today* **2004**, 93-95, 191-198.

62. Luo, M. F.; Ma, J. M.; Lu, J. Q.; Song, Y. P.; Wang, Y. J. High-surface area CuO-CeO2 catalysts prepared by a surfactant-templated method for low temperature CO oxidation. *J. Catal*. **2007**, 246, 52-59.

63. Avgouropoulos, G.; Ioannides, T.; Matralis, H. Influence of the preparation method on the performance of CuO-CeO_2 catalysts for the selective oxidation of CO. *Appl. Catal. B: Environ*. **2005**, 56, 87-93.

64. Zhao, K.; Xu, R.; Sun, X.; Chen, H.; Tian, Q.; Shen, D.; Li, Y. Favorable synergistic effects between CuO and the reactive planes of ceria nanorods. *Catal. Lett*. **2005**, 101, 169-173.

65. Zabilskiy, M.; Djinović, P.; Tchernychova, E.; Tkachenko, O. P.; Kustov, L. M.; Pintar, A. Nanoshaped CuO/CeO_2 materials: Effect of the exposed ceria surfaces on catalytic activity in N_2O decomposition reaction. *ACS Catal*. **2015**, 5, 5357−5365.

66. Yao. S.; Mudiyanselage, K.; Xu, W.; Johnston-Peck, A. C.; Hanson, J. C.; Wu, T.; Stacchiola, D.; Rodriguez, J. A.; Zhao, H.; Beyer, K. A.; Chapman, K. W.; Chupas, P. J.; Martinez-Arias, A.; Si, R.; Bolin, T. B.; Liu, W.; Senanayake, S. D. Unraveling the dynamic nature of a CuO/CeO_2 catalyst for CO oxidation in Operando: A combined study of XANES (Fluorescence) and DRIFTS. *ACS Catal*. **2014**, 4, 1650-1661.

67. Chen, G.; Xu, Q.; Yang, Y.; Li, C.; Huang, T.; Sun, G.; Zhang, S.; Ma, D.; Li, X. Facile and mild strategy to construct mesoporous CeO_2-CuO nanorods with enhanced catalytic activity toward CO oxidation. *ACS Appl. Mater. Interfaces* **2015**, 7, 23538-23544.

68. Liu, W.; Flytzani-Stephanopoulos, M. Total oxidation of carbon monoxide and methane over transition metal fluorite oxide composite catalysts: Catalyst composition and activity. *J. Catal.* **1995**, 153, 304−316.

69. Sedmak, G.; Hocevar, S.; Levec, J. Kinetics of selective CO oxidation in excess of H_2 over the nanostructured $Cu_{0.1}Ce_{0.9}O_{2-y}$ catalyst. *J. Catal*. **2003**, 213, 135-150.

70. Martinez-Arias, A.; Fernandez-Garcia, M.; Soria, J.; Conesa, J. C. Spectroscopic study of a Cu/CeO_2 catalyst subjected to redox treatments in carbon monoxide and oxygen. *J. Catal*. **1999**, 182, 367−377.

71. Niu, X.; Zhao, T.; Yuan, F.; Zhu, Y. Preparation of hollow $CuO@SiO_2$ spheres and its catalytic performances for the NO+CO and CO oxidation. *Sci. Rep*. **2015**, 5, 9153 (1-8).

72. Song, C.; Wang, C.; Zhu, H.; Wu, X.; Dong, L.; Chen, Y. Preparation, characterization and catalytic activity for CO oxidation of SiO_2 hollow spheres supporting CuO catalysts. *Catal. Lett*. **2008**, 120, 215-220.

73. Astudillo, J.; Aguila, G.; Diaz, F.; Guerrero, S.; Araya, P. Study of $CuO\text{-}CeO_2$ catalysts supported on SiO_2 on the low temperature oxidation of CO. *Appl. Catal. A: Gen*. **2010**, 381, 169-176.

74. Luo, J.; Chu, W.; Xu, H.; Jiang, C.; Zhang, T. Low-temperature CO oxidation over $CuO\text{-}CeO_2/SiO_2$ catalysts: Effect of CeO_2 content and carrier porosity. *J. Nat. Gas Chem*. **2010**, 19, 355-361.

75. Liu, W.; Flytzani-Stephanopoulos, M. Total oxidation of carbon monoxide and methane over transition metal fluorite oxide composite catalysts: Catalyst composition and activity. *J. Catal.* **1995**, 153, 304−316.

76. Djega-Mariadassou, G.; Boudart, M. Classical kinetics of catalytic reactions. *J. Catal*. **2003**, 216. 89-97.

77. Sedmak, G.; Hocevar, S.; Levec, J. Kinetics of selective CO oxidation in excess of H_2 over the nanostructured Cu0.1Ce0.9O2−y catalyst. *J. Catal*. **2003**, 213, 135-150.

Chapter 2: Experimental

2.1. Synthesis methods

2.1.1. Hydrothermal method

Hydrothermal synthesis method includes a technique where substances in aqueous form react under low temperature and high vapor pressure in a steel-closed vessel called autoclave (Fig. 2.1). This is one of the best synthesis methods to control the size and shape of the particles. Various parameters, such as reaction temperature, duration, and solvents, can modify the size and shape by changing the growth direction and mechanism. A temperature gradient created by heating the autoclave is maintained between the two opposite ends. Dissolved nutrient in the hotter zone at the bottom of the autoclave is transported to colder zone at the upper part of the autoclave. The solution at the upper part becomes supersaturated and then crystallization starts. The low reaction temperature is a great advantage to saving energies and to avoiding problems occurred by high temperature. This method is used to synthesize various morphologies of CeO_2.

2.1.2. Wet impregnation method

This is the most common method to prepare CuO_x-CeO_2 catalysts. In this method, the copper salt solution has been used as a precursor in order to make contact with the support. The precursor dissolves in the solution with same volume as the pore volume of the support. Due to the capillary action, the solution is attracted to the pores. The amount of solution in excess of pore volume of the support starts diffusing in. During the process, heat can be given into the system to create a better contact between copper oxide and the

support. Stirring of the solutions is crucial to having a homogeneous distribution of copper oxide on the support. The schematic representation of this process is shown in Fig. 2.2.

Figure 2.1. Autoclave in the furnace.

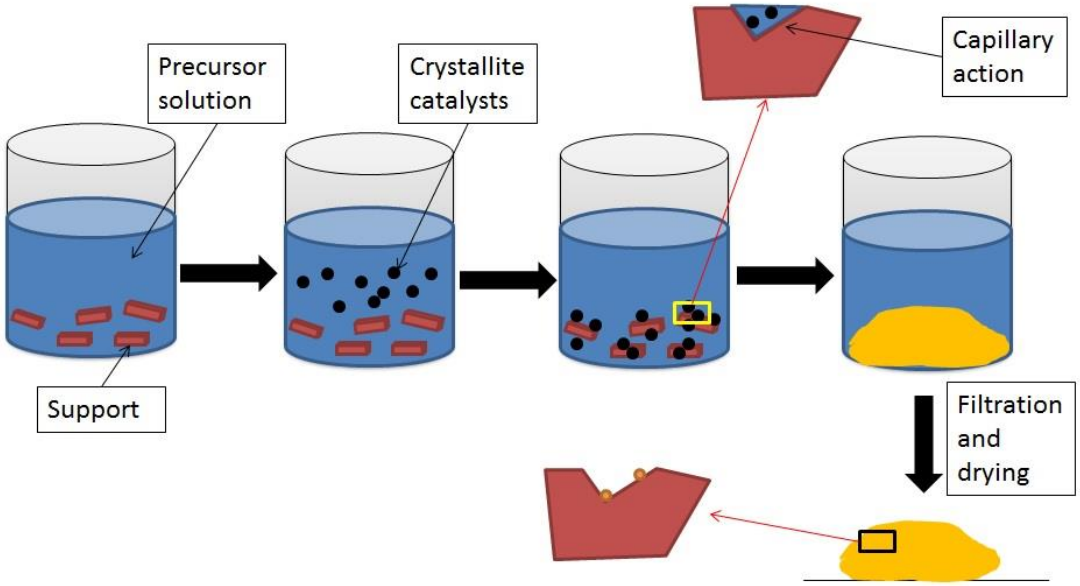

Figure 2.2. Schematic representation of wet impregnation method.

2.2. Instrumentation

In this work, various instruments, such as X-ray diffraction, Raman spectroscopy, transmission electron microscopy, X-ray photoelectron spectroscopy, and BET surface area have been used to characterize the materials, and the catalytic activity of the materials has been tested using chemisorption instruments. Kinetic study has been conducted using thermogravimetric analyzer. To evaluate the results, it is imperative to understand how these instruments work.

2.2.1. X-ray diffraction (XRD)

XRD, which is one of the common, non-destructive characterization techniques, has been used for phase identifications and crystal structures of the materials. However, this technique can be used only for crystalline materials. X-rays are generated in a cathode ray tube where a filament is heated to produce electrons and these electrons are accelerated by applying voltage. Accelerated electrons bombard the target materials to produce characteristics X-rays. Copper is used as the target materials with CuK_{α} = 1.5418 Å radiation. These X-rays incident on the sample leading to produce a constructive interference which satisfies Bragg's law ($n\lambda = 2d \sin\theta$), as shown in Fig. 2.3a. A peak in intensity occurs at the constructive interference. Detectors identify the diffracted X-rays in a range of 2θ angles to reach all possible diffraction directions of the lattice (Fig. 2.3b). Diffraction peaks are converted to d-spacing to identify the phases. Each phase has a unique set of d-spacing. For our sample, we have used Rigaku Miniflex II XRD from 5 to 90^{o} of 2θ with a scan rate of 0.5^{o} per min. XRD pattern has been utilized to calculate the particle size using the following equation.

$$particle\ size = \frac{0.94\,\lambda}{\beta_{1/2}\,Cos\theta} \qquad \text{(Eq. 2.1)}$$

Here, λ is wavelength (1.541); θ is diffraction angle; $\beta_{1/2}$ is full-width-half-maximum (FWHM) of the particular peak.

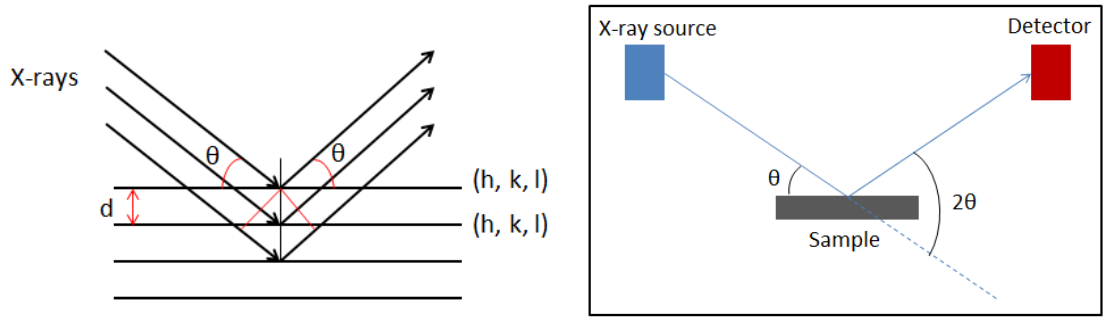

(a) (b)

Figure 2.3. (a) Bragg's law, (b) X-ray diffraction setup.

2.2.2. Raman spectroscopy

Raman spectroscopy is a commonly-used, non-destructive characterization technique. The spectrometer works based on the molecular vibrations, rotational and other low-frequency modes of the materials. A laser beam illuminates the materials and excites the molecules from ground state to virtual energy state for a short period of time. As shown in Fig. 2.4a, excited molecules come back to the different ground energy states instead of returning to the original energy state and this incident is called inelastic scattering. If excited molecules come back to higher energy state than the original state (resulting low energy), then this process is called Stokes; and if excited molecules come back to lower energy state than the original state (resulting higher energy), then this process is called Anti-stokes or Raman scattering. The differences between the state energies lead to a

shift of the emitted photon's frequency for the total energy to remain stable. After interaction of photons with the sample, the lenses collect the electromagnetic radiation and send through the monochromator. Later the notch filters or edge filters filter out the elastic scattering and send the rest of the energy to the CCD detectors. In this project, we have worked with Horiba iHR 320 Raman spectrometer (Fig. 2.4b) using a green laser beam with 532 nm of wavelength. Silicon single crystal wafer has been used to calibrate with a reference peak at 520 cm^{-1}.

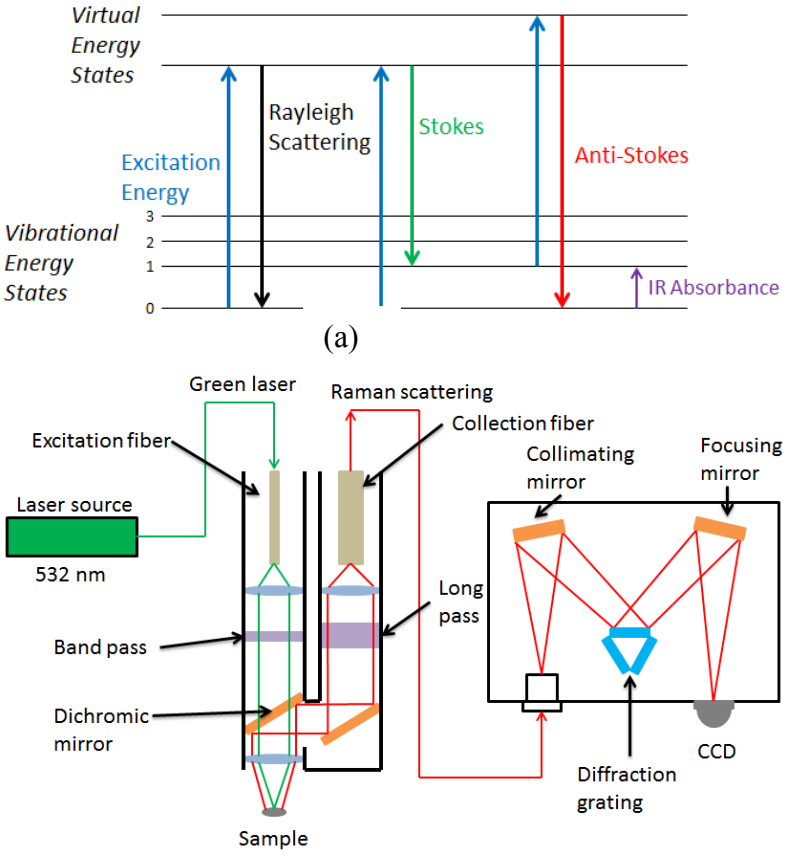

Figure 2.4. (a) Elastic and inelastic scattering, (b) Raman spectroscopy setup.

2.2.3. Transmission electron microscopy (TEM)

TEM has been frequently used to achieve an atomic resolution of the materials. When compared to light microscopy, in TEM, electrons are used instead of light. However, TEM works on the same principle of light microscope. With the help of high voltage (around 200 KV), electron gun produces electrons which travel through several electromagnetic lenses and are focused into a very thin beam. The electrons travel through the thin materials (around 100 nm) and the unscattered electrons produce an image on the fluorescent screen at the bottom. A CCD camera can be used to collect the image in the computer. In our facility, we have access to JEOL 2100 model of TEM along with energy dispersive spectroscopy (EDS) in our facility. This TEM can be used to magnify up to 1.5 million times and has a point resolution of 0.19 nm and informational resolution of 0.14 nm. For this research, 400 mesh copper grid (from Ted Pella) has been used to prepare TEM sample. At first, catalysts have been mixed in ethanol, and then these have been sonicated for 1 min. Samples have been taken from the solution by a small pipette, and one or two drops of sample have been poured on the copper grid.

EDS is usually attached to TEM to conduct the elemental analysis of the materials. Every element has a unique atomic structure which leads to different energies of X-ray emission. Electrons or photons with high energy hit the electron shells of the specimen and knock out an electron from the inner shell by exciting the electron creating a hole. An electron from higher-energy shell fills the hole leading to an emission of X-ray with the energy equaling to the energy difference between two shells. The X-ray is recognized by the detector and the crystal inside the detector turns the signal into a voltage signal. The

electrical signals are measured by the pulse processor and then, are passed to the analyzer.

2.2.4. X-ray photoelectron spectroscopy (XPS)

XPS is a surface analysis technique which provides information about elemental, chemical state, and electronic properties of the surface of materials. Photoemission process has been used in this technique to collect information of the materials. Electrons from the core level adsorb x-ray energy (hυ) when x-rays incident on the surface. After overcoming the binding energy (E_B), electrons are emitted out with a certain kinetic energy (E_k). Einstein equation can be used to describe this process.

$$E_k = h\upsilon - E_B - \Psi \qquad \text{(Eq. 2.2)}$$

In this equation, hυ is the energy of x-ray, E_k is the kinetic energy of emitted electrons, E_B is the binding energy of core level electrons, and Ψ is the work function of the instrument. For our sample, Al K_α x-ray source has been used and it has energy of 1486.6 eV. Kinetic energy can be measured by an analyzer. Thus, binding energy can easily be calculated using equation 2.2. We have used XPS PHI 5100 instrument which is from RBD Instruments and is housed in an Ultra High Vacuum (UHV) chamber with the base pressure of $5x10^{-10}$ Torr. It is equipped with a dual anode X-ray source (hν (Al Kα) =1486.6 eV and hν (Mg Kα) =1253.6 eV, ΔE = 0.9 eV) and a hemispherical analyzer. The system is also equipped with an Ar^+ ion gun which enables depth profiling. In addition, it can be operated at room temperature as well as liquid nitrogen temperature, 80 K. The instrument has been calibrated using Au 4f peaks. All of the XPS data have been collected by Dr. Balaz's research group.

2.2.5. BET surface area

Surface area is an important physical property which affects the usefulness of solid phase. Same material with the different surface area can affect its performance characteristics. Gas adsorption technique has been frequently used to determine the surface area. In this method, gas molecules come in contact with solid surfaces under a variety of conditions in order to evaluate sample volume. Brunauer-Emmett-Teller (BET) theory is a commonly-used technique to determine the surface area of powder and porous materials. Solid surfaces are exposed to nitrogen gas which is engaged as the probe molecules at liquid nitrogen conditions. The weight of the sample, the cross-sectional area of nitrogen gas (in this case, 16.2 $Å^2$/molecule) and the measured monolayer capacity evaluate the surface area of the sample. The equation to measure BET surface area is given below.

$$\frac{1}{V\left(\frac{P_o}{P}-1\right)} = \frac{C-1}{V_m}\left(\frac{P_o}{P}\right) + \frac{1}{V_m C} \qquad \text{(Eq. 2.3)}$$

Here, P is equilibrium pressure for a specific surface coverage, P_o is the standard vapor pressure of the liquid adsorbate at the adsorption temperature, V is the volumetric uptake of gas at pressure P and C is a constant. For our project, we have used Micromeritics AutoChem™ II 2920 to measure the surface area of the sample. The sample is placed in a U-tube, and nitrogen gas is flown through it. The temperature of the sample is decreased to ~77 K. Nitrogen gas molecules get trapped at the surfaces of the sample. The temperature of the sample again is raised to a room temperature by simply putting a beaker filled with water around the U-tube. Thermal conductivity detector

(TCD) detects the amount of trapped nitrogen gas molecules at the exit of the sample container and sends the information to the computer to analyze the surface area.

2.2.6. Temperature programmed techniques

Temperature programmed methods are commonly used chemisorption techniques which produce the information about the reduction/oxidation conditions of a catalyst. We have used three different chemisorption techniques, such as temperature programmed reduction (TPR), temperature programmed oxidation (TPO), and temperature programmed desorption (TPD).

Temperature programmed reduction (TPR) is a process which determines the amount of reducible species existing in the catalyst and the temperature at which the species are reduced. In this method, usually a mixer of hydrogen and argon gas is used and argon which has low thermal conductivity (0.018 W/mK) acts as carrier gas. The thermal conductivity of reducing gas hydrogen is 0.182 W/mK. When mixed gas in a certain proportion is flown through the sample, the detector establishes the baseline based on the thermal conductivity of mixed gas. After rising the temperature, hydrogen starts to react with the catalyst and produces H_2O which is removed at the cold trap. Thus, the amount of hydrogen gas decreases in the gas mixture and therefore, thermal conductivity decreases as well due to the increment of percentage of argon gas. To maintain a constant filament temperature, it requires less electricity due to the increase of low thermal conductive argon gas. The detector detects the change in electrical signal and records it uninterruptedly over a range of temperatures.

To conduct TPR, the sample catalyst is placed in a U-tube which can be connected to the instrument so that reducing gas mixture can be flown through this at a rate of 50 mL/min. In this case, 5% H_2 – 95% Ar mixture is used as the reducing gas mixture. After increasing the temperature with 10^{o}C/min rate, at a certain temperature, reduction occurs or in another way hydrogen is consumed and the composition of the gas mixture is detected by TCD at the exit of U-tube. A schematic representation of TPR process, as described, is shown in Fig. 2.5. We are using Micromeritics AutoChemTM II 2920 to conduct TPR. We used standard Cu_2O sample to calibrate this instrument and to calculate H_2 consumption amount of the catalysts.

Temperature programmed oxidation (TPO) provides information about the oxidation temperature peaks. The TPO experiments are conducted similar way as TPR; only difference is that 5% O_2 – 95% He gas mixture is used for TPO. Thermal conductivity of oxygen and helium gases is 0.027 and 0.151 W/mK. Temperature programmed desorption (TPD) technique is used for determining the strength of active sites accessible at catalyst surfaces. The temperature is increased after flowing pre-adsorbed gas through the catalyst. The pre-adsorbed gas desorbs away with increasing the temperature until the surface is unoccupied with adsorbate gas. In our experiment, the sample in U-tube has been heated from room temperature to 400 ^{o}C under He gas to remove residual moisture. Then the sample has been cooled to room temperature and 5%CO–95%He gas has been flown at 50 mL/min through the sample for 30 mins. The sample has been reheated up to 400 ^{o}C under He gas and the desorption behavior of CO can be analyzed at elevated temperature.

Various masses of standard Cu_2O have been used in TPR where the reaction (4) occurred. From the data, H_2 consumption in μmol per peak area has been calculated for all of the peaks shown in Fig. 2.6. Each sample provided same result for H_2 consumption (22.1 μmol/peak area). Equation (2.4) can be used to calculate H_2 consumption for the catalysts.

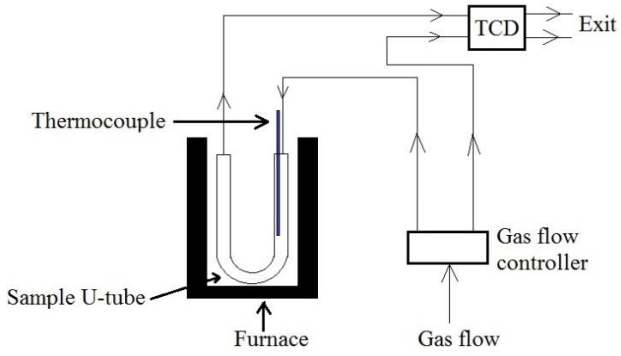

Figure 2.5. Schematical representation of TPR process.

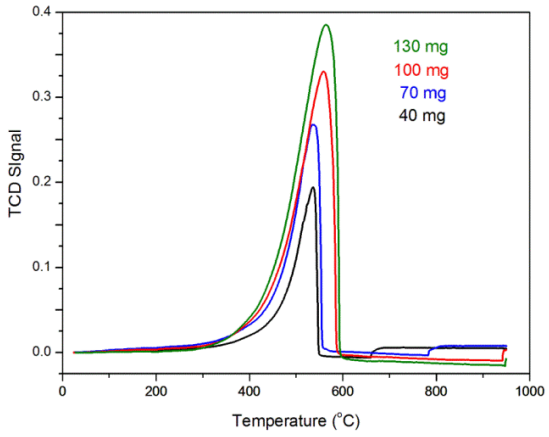

Figure 2.6. Calibration curves of TPR for standard Cu_2O sample.

$$Cu_2O + H_2 = 2Cu + H_2O \qquad (4)$$

$$H_2 \text{ consumption (mmol/g)} = \frac{22.1\ \frac{\mu mol}{peak\ area} \times peak\ area\ of\ catalyst}{mass\ of\ catalyst\ (mg)} \qquad \text{(Eq. 2.4)}$$

Rate of desorption from CO-TPD curve can be calculated using equation (2.5) shown below.

$$\frac{d\theta}{dt} = -\frac{k_d}{\beta}\,\theta^n \qquad \text{(Eq. 2.5)}$$

$$k_d = A \exp\left(-\frac{E_d}{RT}\right) \qquad \text{(Eq. 2.6)}$$

Here, k_d, β, θ, and n are rate of desorption constant, heating rate, surface coverage, and reaction order, respectively. k_d can be found using equation (3.2) where A, E_d, R, and T are rate coefficient, desorption energy, gas constant, and temperature, respectively.

2.2.7. Pulse chemisorption

Pulse chemisorption method is used to measure oxygen storage capacity (OSC) and metal dispersion percentage using Micromeritics AutoChem™ II 2920. The OSC is the measurement of the availability of reactive oxygen near the catalyst surface. It is calculated from the amount of H_2 consumption during H_2 pulse to react with the most active and available oxygen. The detector usually detects the unreacted gas and does the back calculation to determine the amount of reacted gas by using the difference between the volume of unreacted gas and the volume of injected gas. 50 mg of sample is placed in U-tube and a reducing gas (H_2) is injected through the sample for a limited time to measure OSC of the particular catalyst. In this method, the temperature is raised up to 350 ^oC in an inert environment to remove any residual moisture present in the sample. Helium is used as carrier gas which is passed through the sample. 5%H_2-95%He gas is

injected into the U-tube for 5 sec. TCD signal shows a peak for oxygen reduction. H_2 gas injection is done with 3 mins of period till the reduction peak is constant.

Metal dispersion percentage can also be measured during conducting pulse chemisorption method to calculate OSC. This value is needed to calculate turn over frequency (TOF). TOF is a measurement of catalytic activity which shows the number of cycles per unit time. Three types of TOF can be calculated as follows:

$$TOF_1\ (s^{-1}) = X_{CO}\ F_{CO}\ \frac{5\ W_{Cu}}{4\ m_{cat} X_{CuO} D_{CuO}} \quad \text{(Eq. 2.7)}$$

$$TOF_2\ (s^{-1}) = X_{CO}\ F_{CO}\ N\ \frac{m_c}{m_{cat} X_{CuO}} \quad \text{(Eq. 2.8)}$$

$$TOF_3\ (s^{-1}) = \frac{TOF_2}{\frac{\pi}{2d_{Cu-O}}\pi d} = X_{CO}\ F_{CO}\ N\ \frac{m_c}{m_{cat} X_{CuO}} . \frac{2d_{Cu-O}}{\pi^2 d} \quad \text{(Eq. 2.9)}$$

where X_{CO} is the CO conversion at certain temperature; F_{CO} (mol.s^{-1}) is the flow rate of CO; N is the Avogadro's constant; W_{Cu} is the molecular weight of Cu (63.545 g.mol^{-1}); m_{cat} is the weight of catalyst; X_{CuO} is the percentage of CuO loading on the catalyst support; D_{CuO} is the percentage of CuO dispersion; m_c is the weight of a single CuO crystalline and this can be calculated from the volume of assumed semi-spherical CuO and density of CuO (6.45 g.cm^{-3}); d is the crystallite size of CuO; $d_{Cu\text{-}O}$ is distance between Cu and O atom (0.195 nm). TOF_1 calculation is usually based on metal dispersion. TOF_2 contributes the information about the overall activity of Cu atoms on CuO-support periphery and TOF_3 refers to life cycles or turn over frequency of each Cu atom present at interface of CuO-support.

2.2.8. Catalytic activity characterization for CO oxidation

In this method, carbon monoxide (CO) is oxidized to carbon dioxide (CO_2) and this method gives information about the percentage of conversion of CO at a certain temperature. The sample is loaded into the glass tube and placed vertically with the instrument. A mixture of 1% CO, 20% O_2 and 79% He gas is flown through the glass tube at a rate of 70 mL/min. Here, helium gas acts as a carrier gas. The temperature of the sample is programmed from 30 to 350 ^{o}C. Upon exiting the gas mixture from the sample container, gas chromatography (GC) separates the components, and each component exits the column in GC at a different time. Mass spectrometer detects the amount of each component and sends the data to the computer. Fig. 2.7 shows a schematic diagram of CO oxidation process. We have used SRI multiple gas analyzer GC, 8610C chassis. The conversion of CO is calculated using equation (2.8).

$$\%CO\ conversion = [\frac{P_{CO_2}}{P_{CO}+P_{CO_2}}] \times 100\% \qquad \text{(Eq. 2.10)}$$

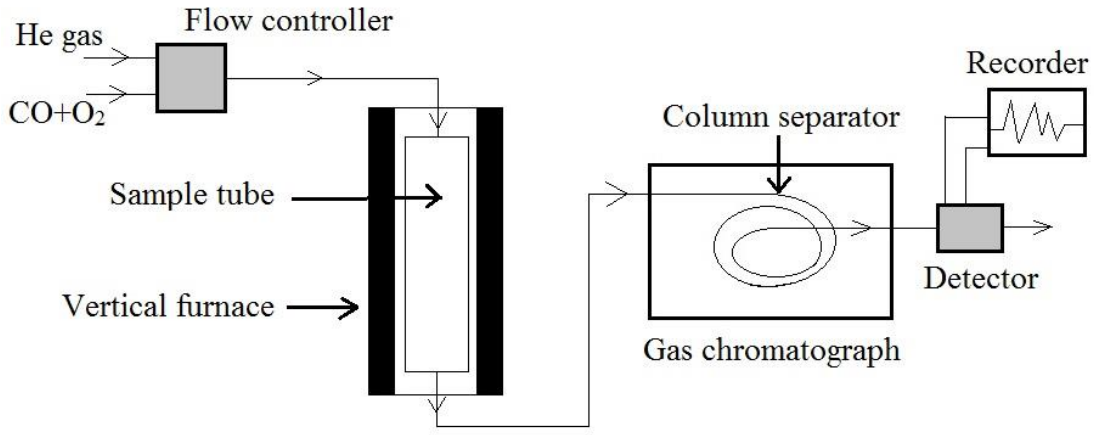

Figure 2.7. Schematic representation of CO oxidation process using gas chromatograph.

Here, P_{CO} and P_{CO2} are the partial pressure of CO and CO_2, respectively, are determined from the relative peak area of the CO and CO_2 peaks normalized to the He standard. Catalytic isothermal stability in function of time can also be established from CO oxidation using gas chromatograph. For this method, the sample temperature is raised up to 350 ^{o}C and then is held for 24 hrs.

2.2.9. Thermogravimetric analysis (TGA)

Thermogravimetric analysis (TGA) is a method in which the mass of any substances is monitored as a function of temperature (with constant heating rate) or as a function of time (with constant temperature). TGA usually consists with sample pan, furnace around the sample, thermocouple and microbalance. It continuously measures the sample weight and temperature. Sample weight changes for decomposition, oxidation, or loss of volatile substances. Change in weight is calculated using the following equations.

$$Weight\ \% = \frac{W_t}{W_i} \times 100 \qquad \text{(Eq. 2.11)}$$

Here, W_i is the initial weight and W_t is the weight at particular time/temperature. In this work, TGA has been used for kinetic study of the sample. At first, aluminum pan is tared and then sample is placed in it. The sample is heated up to 400 ^{o}C at 10 ^{o}C/min rate under inert environment. Any volatile substances or moisture can be removed during heating. Temperature is held at 400 ^{o}C during reduction/oxidation cycles. 5%CO-95%He gas is used to reduce the sample and this gas is passed through the sample at 50 ml/min rate for 30 mins at constant temperature of 400 ^{o}C. The gas is switched to oxygen to oxidize the sample. The flow rate of oxygen gas is 50 ml/min and this gas is flown for 30 mins as

well. One reduction and one oxidation process is called one redox cycle. Total 10 cycles of redox process is conducted for each sample.

Chapter 3: Effect of impregnation methods on CO oxidation over CeO_2 nanorods supported CuO catalysts

In this chapter, copper nitrate and copper carbonate precursors for wet impregnation method and copper nitrate for thermal decomposition method were used to impregnate CuO onto hydrothermally prepared CeO_2 nanorods. Several characterization techniques, such as X-ray diffraction (XRD), Raman spectroscopy, transmission electron microscopy (TEM) and hydrogen temperature programmed reduction (H_2-TPR) confirmed the presence of different copper species (α, β, and γ) interacting with CeO_2 nanorods while forming oxygen vacancies in CeO_2 lattice by compensating the charges between copper and cerium. Furthermore, X-ray photoelectron spectroscopy (XPS) analysis showed a difference in the amount of Ce^{3+}/Ce^{4+} and Cu^{2+}/Cu^{+} couples present in the catalysts. CO oxidation and CO temperature programmed desorption (CO-TPD) were conducted on the catalysts to understand the synergistic effect in CuO/CeO_2 catalysts on their catalytic activity. Rate of desorption was calculated from CO-TPD curves to determine the oxygen mobility in CeO_2 lattice.

3.1. Introduction

Metal-based catalysts, such as Au/TiO_2 [1,2], Au/Fe_2O_3 [3], $Au/\gamma\text{-}Al_2O_3$ [4], Au/CeO_2 [5], Au/ZnO [6], Pt/CeO_2 [7], $Pt/SnO_2–TiO_2$ [8], Pd/CeO_2 [9], Ir/TiO_2 [10], and $Ir/Au\text{-}Al_2O_3$ [11] have been studied for long time, and these catalysts show excellent performance for automotive catalytic application. Nevertheless, these metals, as well as the preparation methods of the catalysts, are expensive which forced researchers to

consider different catalysts with comparable performance. As a consequence, CuO has attracted the attention as one of the most active and cheapest catalysts. On the other side, CeO_2 has fascinated as a catalyst support material due to its ability to take in and release oxygen under oxygen-rich and -lean conditions, respectively [12]. The activity of catalysts depends highly on the preparation method which ensures better contact between copper based particles and CeO_2 support. To prepare CuO/CeO_2 catalyst, researchers have reported several different methods, such as sol-gel method [13], microwave irradiation technique [14], wet chemical methods and thermal decomposition with different precursors [15], co-precipitation [16], and combustion [17]. Yet, these catalysts have been prepared on CeO_2 nanoparticles or octahedral shape. The shape of CeO_2 plays an important role in having a better contact with CuO particles [18]. Different catalyst preparation methods can alter the shape and size of the catalysts, which can have an adverse effect on the catalytic activity. In this chapter, we have compared the catalytic activity towards CO oxidation over CuO/CeO_2 catalysts prepared by three different methods. The presence of various copper species, such as highly-interacted CuO or Cu-Ce-O solid solutions and weakly-interacted CuO, and their influence in increasing catalytic efficiency have been described in this systematic study.

3.2. Experimental

3.2.1. Catalyst preparation

Hydrothermal method was used to prepare CeO_2 nanorods. The 88 mL of 0.1M $Ce(NO_3)_3.6H_2O$ was transferred into a Teflon liner of 200 mL capacity, and 8 mL of 6M NaOH was added into the solution. This solution was stirred for about 15 sec, and then

the lid of Teflon liner was closed. The Teflon liner was put into a stainless steel autoclave and heated at 90 ^{o}C for 48 hrs. Finally, the product was filtered and was washed with 500 mL water and then with 50 mL ethanol. It was dried at 50 ^{o}C for 12 hrs. Later, CuO impregnation onto CeO_2 nanorods was conducted in three different methods as described below.

3.2.1.1. CuO/CeO_2 using $Cu(NO_3)_3$ precursor (CNP)

CeO_2 nanorods and $Cu(NO_3)_3.3H_2O$ were mixed in stoichiometric ratio in 30 mL of water to impregnate 10% CuO on CeO_2. Ammonium hydroxide (NH_4OH) was added dropwise in the solution to get precipitation and was stopped when color of the solution turned into a light blue. After 2 hrs of stirring, it was filtered and washed with water and then ethanol. The sample was dried at 50 ^{o}C for 12 hrs. Finally, the sample was oxidized at 400 ^{o}C for 5 hrs. Then, CuO/CeO_2-CNP catalyst was collected.

3.2.1.2. CuO/CeO_2 using $CuCO_3$ precursor (CCP)

10% CuO was impregnated on CeO_2 using $CuCO_3$ precursor by mixing CeO_2 nanorods and $CuCO_3$ in stoichiometric ratio in 30 mL water. It was stirred for 2 hrs. After filtering the sample and washing with water and ethanol, it was dried at 50 ^{o}C for 12 hrs. The sample was oxidized at 400 ^{o}C for 5 hrs. CuO/CeO_2-CCP catalyst was collected.

3.2.1.3. CuO/CeO_2 using thermal decomposition (TD)

For this method, to impregnate 10% CuO, CeO_2 nanorods and $Cu(NO_3)_3.3H_2O$ were mixed in stoichiometric ratio in 30 mL water. While stirring, it was heated at 120 ^{o}C until

water evaporated. Then, it was oxidized at 400 ^{o}C for 5 hrs. Finally, CuO/CeO_2-TD catalyst was collected.

3.2.2. Catalyst Characterizations

X-ray diffraction (XRD), Raman spectroscopy, X-ray photoelectron spectroscopy (XPS), transmission electron microscopy (TEM), BET surface area measurement, temperature programmed reduction (TPR), temperature programmed desorption (TPD), and CO oxidation were used to characterize the catalysts and their catalytic activity. The description of these techniques can be found in chapter 2.

3.3. Results and Discussions

3.3.1. XRD

The powder XRD was conducted to investigate the structure of CuO/CeO_2 catalysts. The XRD patterns of the samples were shown in Fig. 3.1. The diffraction peaks observed at 2θ of 28.85^{o}, 33.08^{o}, 47.48^{o}, 56.34^{o}, 59.09^{o}, 69.41^{o}, 76.70^{o} and 79.07^{o} can be assigned to fluorite structured CeO_2 (JCPDS 43-1002) as shown in Fig. 3.1a [14]. The diffraction peaks appeared at 2θ of 32.51^{o} 35.46^{o}, 38.73^{o}, 46.24^{o}, 48.73^{o}, 53.45^{o}, 58.34^{o}, 61.54^{o}, 66.24^{o}, 67.94^{o}, 72.37^{o} and 75.22^{o} correspond to monoclinic CuO (JCPDS 45-0937) [14]. For the sample CuO/CeO_2-CCP, the XRD peaks corresponding to CuO nanopowders at 35.46^{o} and 38.73^{o} were observed. These two peaks were also observed for CuO/CeO_2-CNP shown in Fig. 3.1b after magnification. However, these two peaks were not visible for CuO/CeO_2-TD due to high homogeneity. Yang et al. [20] reported that Cu species peaks were not found in $Cu_{0.1}Ce_{0.9}O_2$ sample due to the formation of homogeneous solid

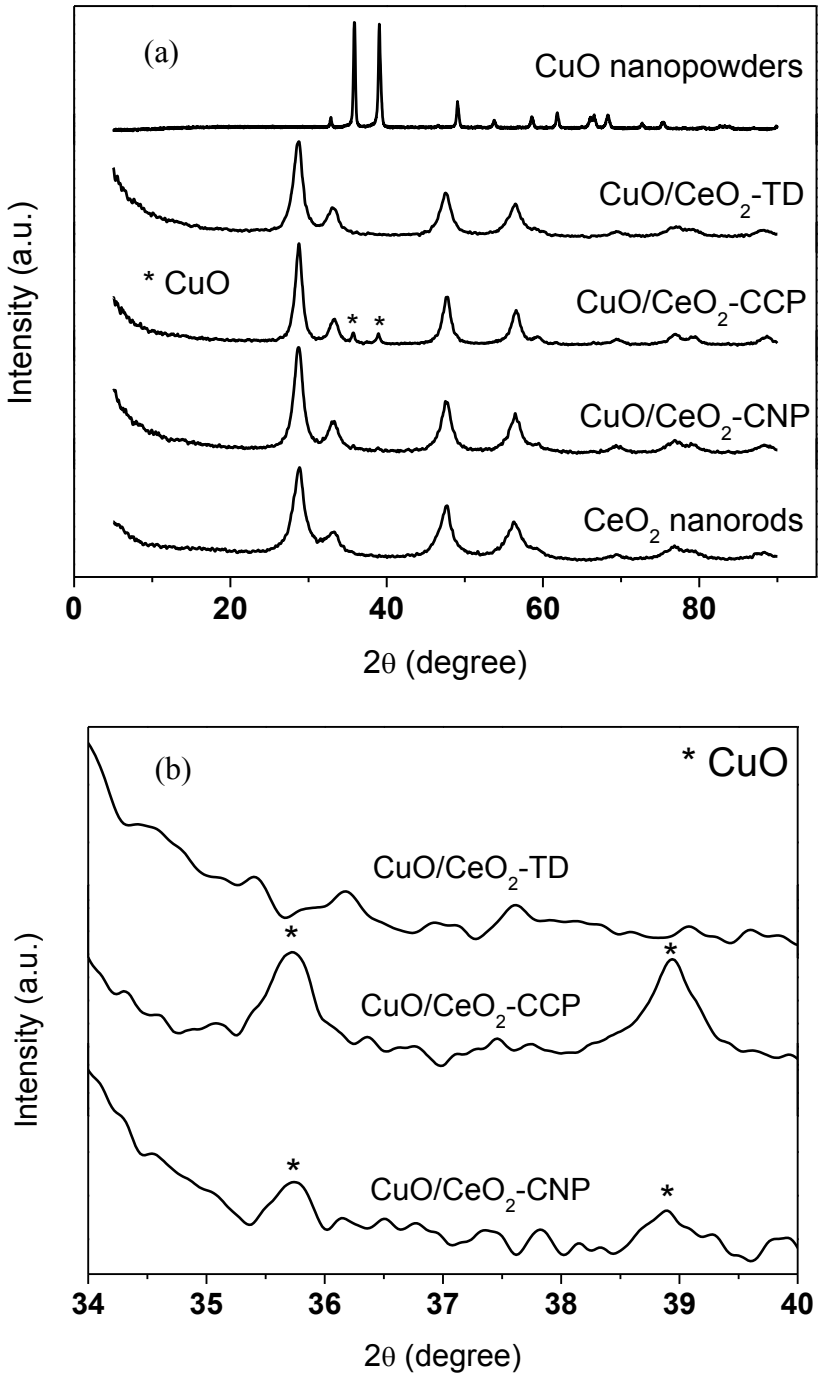

Figure 3.1. XRD patterns of (a) CeO_2 nanorods, various CuO/CeO_2 catalysts and CuO nanopowders, (b) Magnified XRD patterns of various CuO/CeO_2 catalysts.

solution. The presence of CuO peaks indicated that heterodisperse or aggregation of CuO nanoparticles on ceria surfaces can be found in CuO/CeO_2-CCP and CuO/CeO_2-CNP samples. However, the amount of heterodisperse or aggregation of CuO in CuO/CeO_2-CNP could be less than that in CuO/CeO_2-CCP, which can be confirmed from the intensity of CuO peaks. These CuO particles can cover a part of active surfaces of CeO_2, resulting in hamper the catalytic efficiency. On the other hand, XRD pattern of CuO/CeO_2-TD sample showed no visible CuO peaks, providing the evidence of well-dispersed CuO onto ceria surface, Cu-Ce-O solid solutions, or a blend of these two occurrences.

3.3.2. Raman spectroscopy analysis

In Fig. 3.2, Raman spectra of pure CeO_2, various CuO/CeO_2, and pure CuO have been compared. A peak with respectively high intensity observed at 456 cm^{-1} was ascribed to F_{2g} vibration mode of pure CeO_2; however this peak shifted to the lower wavenumber after loading CuO on ceria. The peak shifted from 456 cm^{-1} to 447 cm^{-1}, 444 cm^{-1} and 453 cm^{-1} for CuO/CeO_2-CNP, -TD and -CCP, respectively. The shifting of the peak suggested that Cu^{2+}/Cu^{+} ions incorporated into CeO_2 lattice and formed Cu-Ce-O solid solution [21]. Incorporation of Cu ions creates oxygen vacancies in CeO_2 lattice to compensate the ionic charge difference between Cu^{2+} and Ce^{4+}, resulting a change in lattice parameter as the radius of Cu^{2+} (0.072 nm) is smaller than that of Ce^{4+} (0.101 nm). Copper ions incorporation into CeO_2 lattice can also tempt the lattice distortion of CeO_2, and this leads to the peak deviation by influencing the symmetrical stretching mode. Nevertheless, the peak shifting for CuO/CeO_2-CCP catalyst was very small, which concluded that it had either low amount of solid solution, or there was no solid solution in

it. Shan et al. [21] showed peak shifting toward lower wavenumber in Raman spectra of CuO/CeO_2 catalyst due to the presence of Cu-Ce-O solid solution. In Fig. 3.2, one small and broad peak was observed at 604 cm^{-1} which corresponded to the oxygen vacancies in pure CeO_2. For CuO/CeO_2-CNP, CuO/CeO_2-CCP and CuO/CeO_2-TD, a similar broad peak found at 620 cm^{-1} was a mixture of two separate peaks: one for oxygen vacancies in CeO_2 and another for B_{2g} mode of CuO [22, 23].

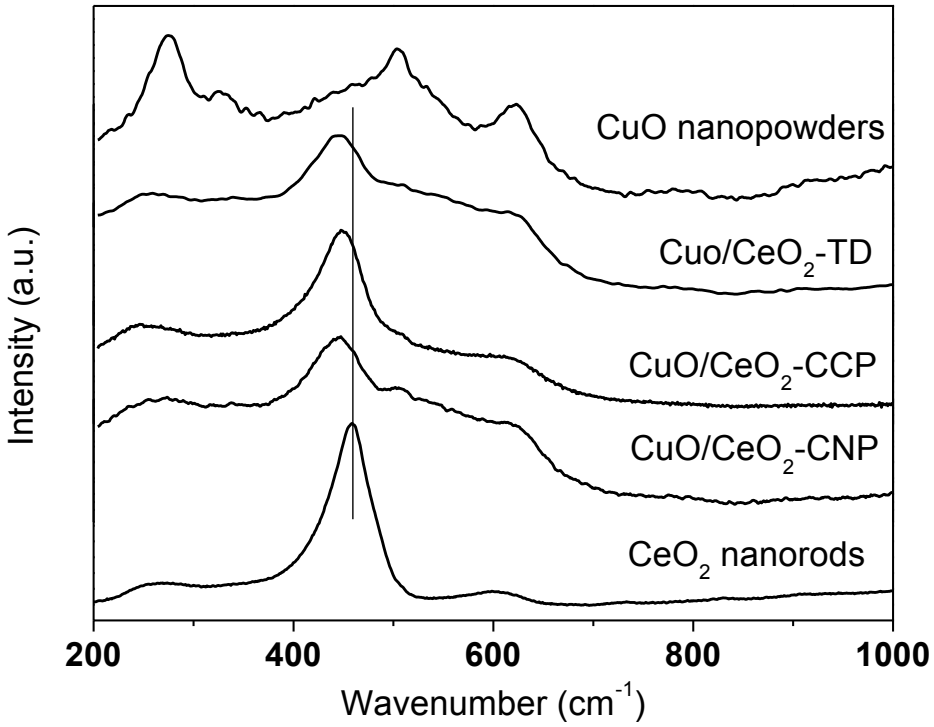

Figure 3.2. Raman spectra of CeO_2 nanorods, different CuO/CeO_2 catalysts and CuO nanopowders.

3.3.3. XPS analysis

XPS spectra of CuO/CeO_2 catalysts were plotted in Fig. 3.3. Spectra for cerium can be seen in Fig. 3.3a where Ce $3d_{3/2}$ and Ce $3d_{5/2}$ peaks were denoted as u and v, respectively. Seven peaks can be found in this order from right to left: v (887.7), v' (890.2), v'' (894.3−893.7), v''' (903.6), u (906.1), u' (908.3−907.2), and u'' (912.7). The

assigned u' and v' peaks belong to Ce^{3+} and the rest five peaks (v, v'', v''', u, u'') correspond to Ce^{4+} [23, 24]. It can easily be distinguished that the amount of Ce^{3+} present in the catalysts in this order: CuO/CeO_2-TD > CuO/CeO_2-CNP > CuO/CeO_2-CCP. The presence of Ce^{3+} produces a chance to form oxygen vacancies in CeO_2 ($2Ce^{4+} \leftrightarrow 2Ce^{3+} + V_{\ddot{o}}^{2+}$) [20]. Thus, the surface of CeO_2 support in CuO/CeO_2-TD sample was enriched with oxygen vacancies compared to other two samples. This defect has an ability to increase oxygen mobility in CeO_2 lattice which is beneficial in enhancing the catalytic activity. Fig. 3.3b showed XPS spectra of Cu $2p_{3/2}$ where low-energy peak was found at 936.2 eV for CuO/CeO_2-CNP and at 934.4 eV for CuO/CeO_2-TD sample. This low-energy peak corresponds to Cu^+ at the surface of catalysts and this suggests a strong interaction of Cu species with CeO_2 [25]. It can be seen that Cu^+ peak was not present in CuO/CeO_2-CCP sample. Thus, it could be reported that CuO was weakly interacted with CeO_2 in CuO/CeO_2-CCP sample. The observation in XPS spectra of Ce and Cu was consistent with Raman analysis. Another peak can be observed in the range of 939.1 – 938.9 eV for all of the samples. This high-energy peak is attributed to Cu^{2+} [24, 25]. XPS spectra of O 1s for different catalysts were shown in Fig. 3.3c. Two peaks can be observed for O 1s where low-energy and high-energy peak were found at 533.5 eV and 536.1–535.0 eV, respectively. It should be pointed out that low-energy peak corresponds to lattice oxygen being present near surface and high-energy peak is attributed to adsorbed oxygen at the surface [20,26]. Li et al. [25] explained that the intensity of adsorbed oxygen peak became stronger after doping Ni in CeO_2 which was a confirmation of increasing oxygen storage capacity. An attempt was made to calculate

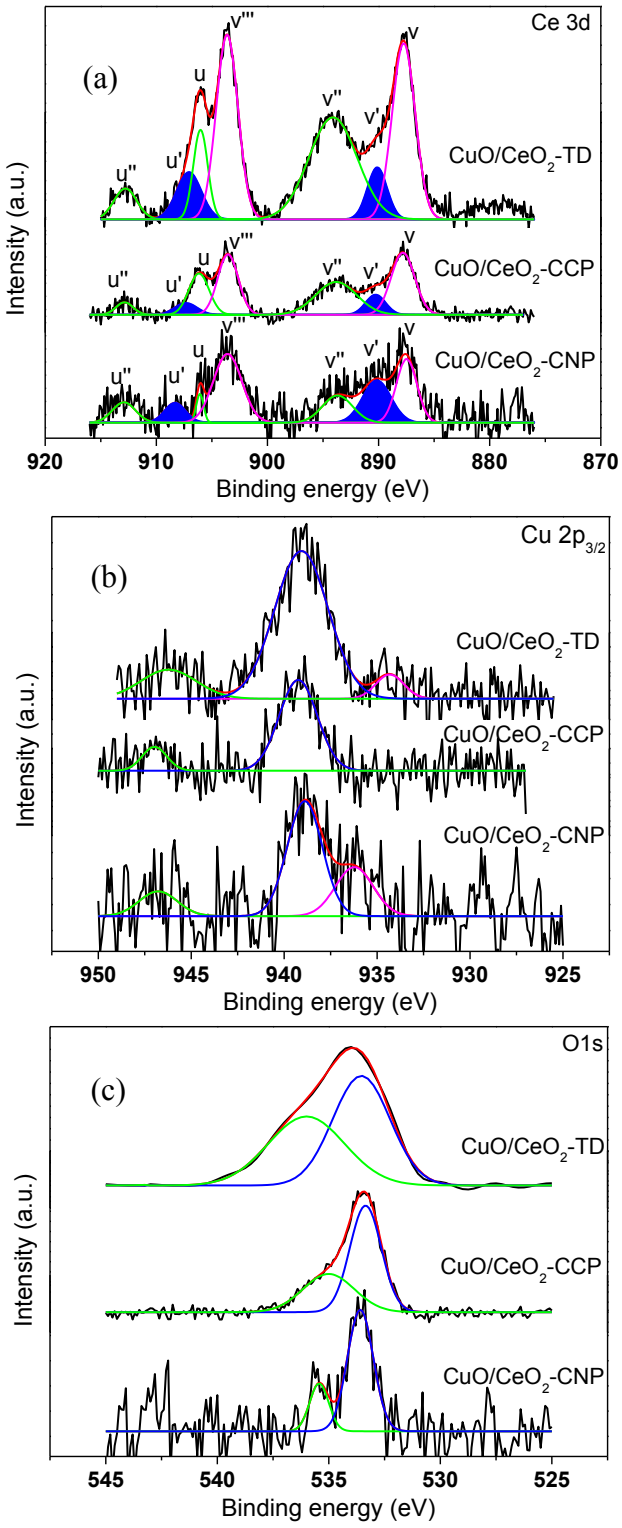

Figure 3.3. XPS spectra of various CuO/CeO_2 catalysts.

the percentage of adsorbed oxygen in all of the samples by using the equation below.

$$\%\ adsorbed\ oxygen = \frac{high\ energy\ peak\ area}{Total\ peak\ area} \times 100 \qquad \text{(Eq. 3.1)}$$

The adsorbed oxygen in CuO/CeO_2-CNP, -CCP, and -TD samples were 37, 36, and 48 %, respectively. The adsorbed oxygen peak suggested that the catalysts could have better capability for oxygen storage [20,25]. Thus, it could be observed that CuO/CeO_2-TD sample had higher oxygen storage capacity which could improve the catalytic activity. A charging effect occurred during the experiment and this caused the peaks to shift toward higher energy compared to the literature [20,23-25].

3.3.4. TEM analysis

Fig. 3.4 showed TEM images of pure CeO_2 and three different catalysts in 100K magnification. Pure CeO_2 nanorods were shown in Fig. 3.4a. CeO_2 nanorods were usually 40-100 nm in length and 5-15 nm in diameter. CeO_2 nanorods with small CuO nanoparticles were agglomerated for CuO/CeO_2-CNP, shown in Fig. 3.4b. Bulk CuO (~ 40 nm) and cluster of small CuO were seen in CuO/CeO_2-CCP catalyst in Fig. 3.4c. Small size CuO particles were dispersed on CeO_2 nanorods in both CuO/CeO_2-CNP and CuO/CeO_2-TD samples, displayed in Fig. 3.4b and 3.4d, respectively. There was no bulk CuO in CuO/CeO_2-TD sample. The TEM images were in agreement with XRD data. Additionally, rough surfaces can be observed in rods of CuO/CeO_2 catalysts, whereas surfaces were smooth in pure CeO_2 rods. High resolution TEM (HRTEM) images of pure CeO_2 nanorods and CuO/CeO_2-CNP catalysts were shown in Fig. 3.5. CeO_2 rods can be seen in Fig. 3.5a and red rectangular portion from Fig. 3.5a was shown separately in Fig. 3.5b after magnifying. CeO_2 rod exposed (111) and (100) planes with d-spacing of 0.31

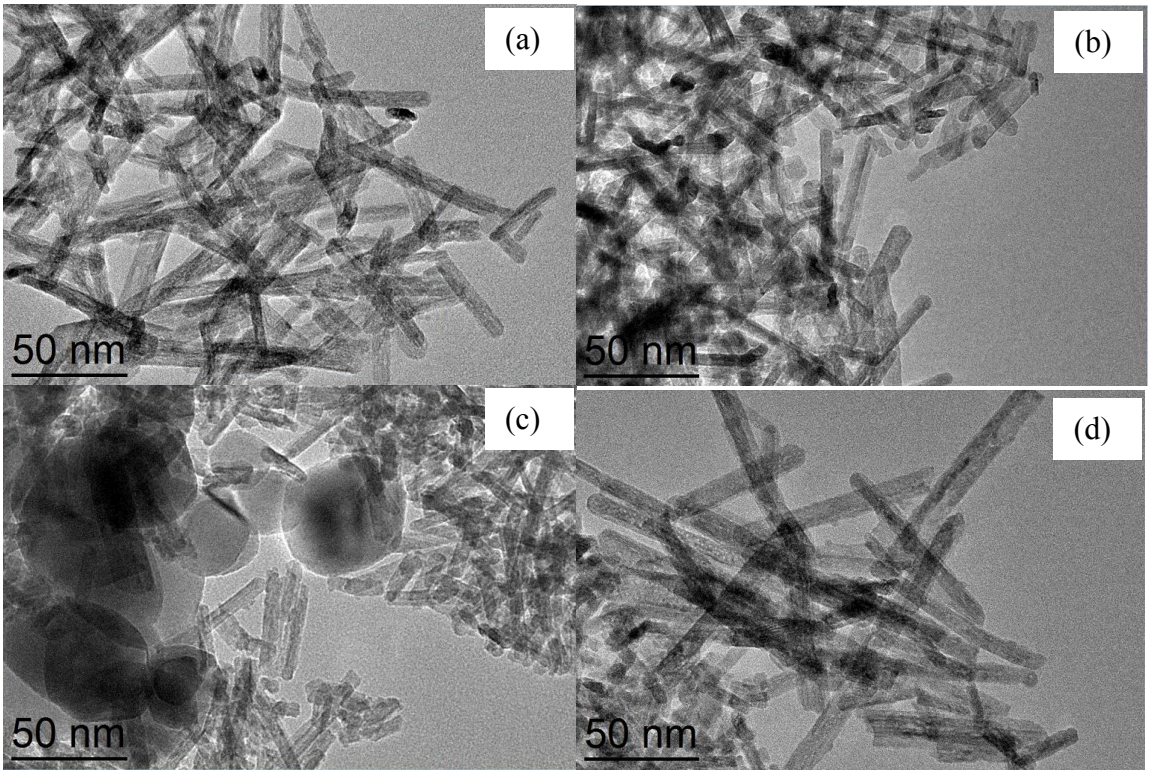

Figure 3.4. TEM images of (a) CeO_2 nanorods, (b) CuO/CeO_2-CNP, (c) CuO/CeO_2-CCP, (d) CuO/CeO_2-TD.

nm and 0.27 nm, respectively. This result was not consistent with the previously reported observations for CeO_2 nanorods as they reported only (100) and (110) planes [18]. However, our group earlier mentioned the presence of (111) planes in CeO_2 nanorods [19,23,27-28]. The inset of Fig. 3.5a displayed the calculated Fast Fourier Transform (FFT) of HRTEM image which confirmed that CeO_2 nanorods were single crystals. For CuO/CeO_2-CNP catalysts, highly interacted CuO nanoparticle (α particle) with CeO_2 was presented in Fig. 3.5c. No definite boundary between CuO and CeO_2 was seen in the inset of Fig. 3.5c. Weakly-interacted CuO (β particle) with CeO_2 and ~10 nm size of bulk CuO (γ particle) was noticed in Fig. 3.5d. CuO nanoparticle was shown in Fig. 3.5e after magnification. The calculate FFT image of CuO particle was shown in Fig. 3.5f and this suggested that CuO nanoparticle was single crystal. It can be seen that CuO particle can

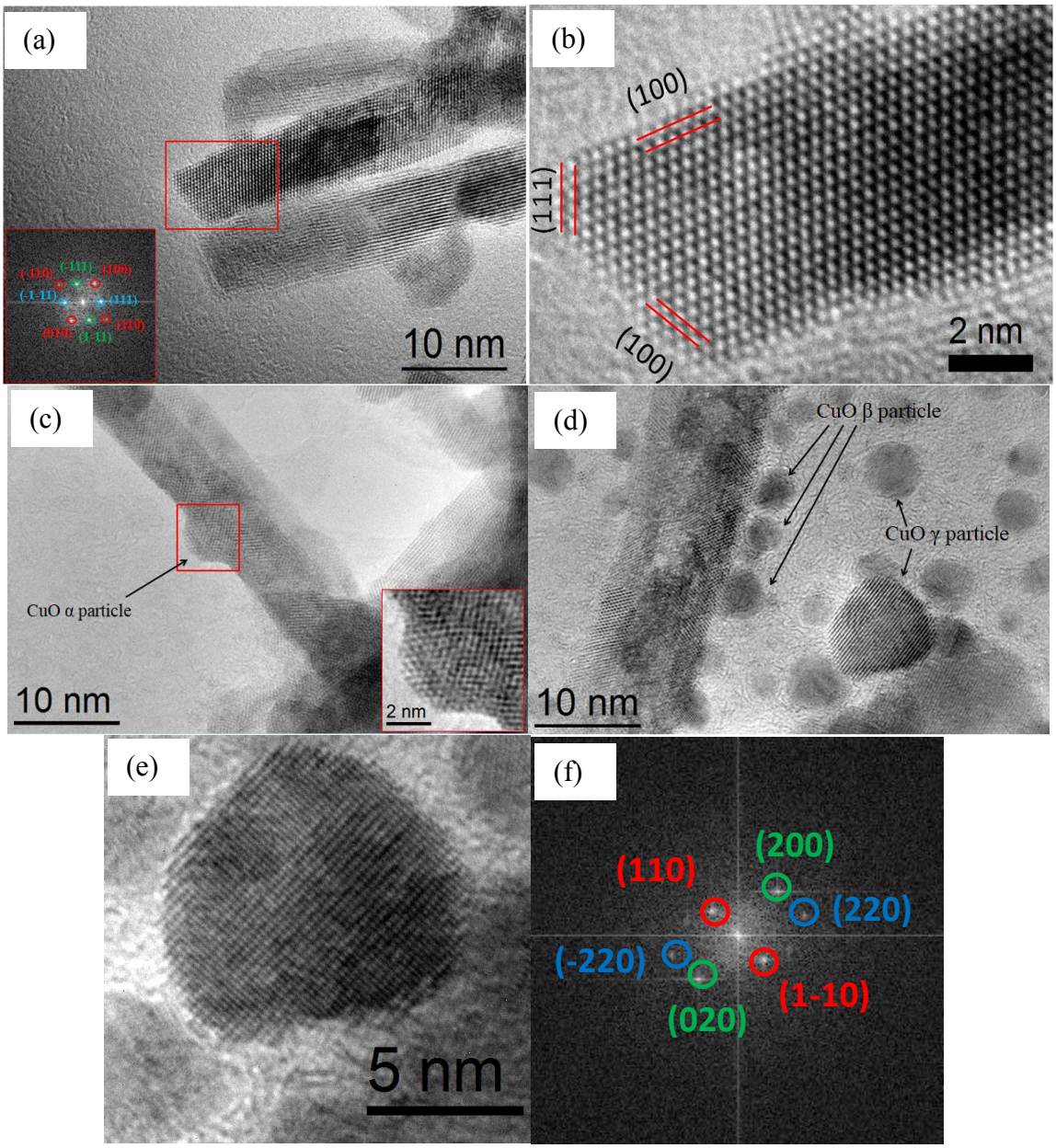

Figure 3.5. HRTEM images of single CeO_2 nanorod (a and b), CuO/CeO_2-CNP (c and d), and single CuO nanoparticle (e). Calculated FFT of CuO nanoparticle (f). Inset of (a): calculated FFT of CeO_2 nanorod.

have (110), (200) and (220) planes. Similar CuO nanoparticles may cover several defects in CeO_2 surface which is not desirable in order to improve the catalytic efficiency.

3.3.5. H_2-TPR

The H_2-TPR profile of pure CeO_2 was shown in Fig. 3.6a and H_2-TPR profiles of various CuO/CeO_2 catalysts were displayed in Fig. 3.6b. Pure CeO_2 showed two reduction peaks at about 474 and 763 ^oC. First peak was assigned to the reduction of surface oxygen of CeO_2, and second peak was assigned for the reduction of bulk oxygen of CeO_2 [29]. Conversely, various CuO/CeO_2 catalysts showed low-temperature reduction compared to pure CeO_2 due to synergistic interaction between CuO and CeO_2 support [30]. Preparation methods could have an effect on the TPR profiles as seen in Fig. 3.6b. CuO/CeO_2-CNP and CuO/CeO_2-CCP catalysts showed three reduction peaks, and CuO/CeO_2-TD catalysts showed two reduction peaks. However, position and size of the peaks were dissimilar for different CuO/CeO_2 catalysts. The reduction peaks were assigned as α, β and γ in order from low to high temperature. The α peaks were allocated to the reduction of strongly-interacted CuO onto CeO_2 surface or Cu-Ce-O solid solution [31]. The β peaks were attributed to the reduction of weakly-interacted CuO on CeO_2 surface [32]. The γ peaks were recognized as the reduction of larger CuO particles and agglomeration of small CuO particles [33]. Fig. 3.7 showed the schematic of $CuO\text{-}CeO_2$ synergistic interactions, where strongly-interacted CuO onto CeO_2 surface were shown in Fig. 3.7a, weakly-interacted CuO on CeO_2 surface was shown in Fig. 3.7b, and Fig. 3.7c presented how a large particle of CuO covered CeO_2 surface without any interaction at the interface. XRD, Raman analysis, XPS and TEM revealed the formation of Cu-Ce-O

solid solution and weakly-interacted CuO onto CeO_2 surface in all catalysts, and bulk CuO in CuO/CeO_2-CCP and CuO/CeO_2-CNP catalysts. Avgouropoulos et al. [34] suggested that it is easy to reduce strongly-interacted CuO. The reducibility of highly-interacted CuO can be enriched by CeO_2. First peaks (α peak) of CuO/CeO_2-CNP, -CCP and -TD were observed at 142, 151 and 142 ^oC, respectively. Second peaks, which were assigned as β peak, were found at 164, 195 and 168 ^oC for CuO/CeO_2-CNP, -CCP and -TD, respectively. Third peaks (γ peaks) for CuO/CeO_2-CNP and CuO/CeO_2-CCP were seen at 176 and 213 ^oC, respectively. It was clear that CuO/CeO_2-TD catalyst showed no γ peak because this catalyst did not have any large CuO particles and this result was consistent with XRD and TEM data. Luo et al. [9] reported two reduction peaks for 10% CuO loading on CeO_2 nanoparticles in which α peak found near 160 ^oC was assigned to highly dispersed CuO particles, and β peak seen near 200 ^oC was attributed as bulk CuO. Shiau et al. [35] and Wang et al. [36] reported three reduction peaks which were similar to our results; however, these peaks were found at over 200 ^oC for their samples. For Cu-Ce-O solid solution, oxygen vacancies are already formed near the surface due to incorporation of Cu^{2+} into CeO_2 lattice to have charge neutrality. Therefore, CeO_2 adsorbs oxygen to fill the vacancies near solid solution and this oxygen can be reduced at a low temperature [34,37-38]. For weakly interacted CuO, firstly CuO near the interface of $CuO\text{-}CeO_2$ reduces to Cu^{1+}/Cu after reacting with H_2. At that moment, CeO_2 supplies oxygen to the reduced Cu species at the interface to re-oxidize these Cu species, and Ce^{4+} reduces to Ce^{3+} itself. Oxygen vacancies are formed near the $CuO\text{-}CeO_2$ interface, which can be filled by adsorbed oxygen. Redox potentials of CuO are decreased due to the electron charge transfer among Cu, O, Ce and oxygen vacancies (or other defect areas)

which aids the diffusion of oxygen from bulk to surface in CeO_2. This ultimately increases the redox action of Ce^{4+}/Ce^{3+} couples [34,37-38].

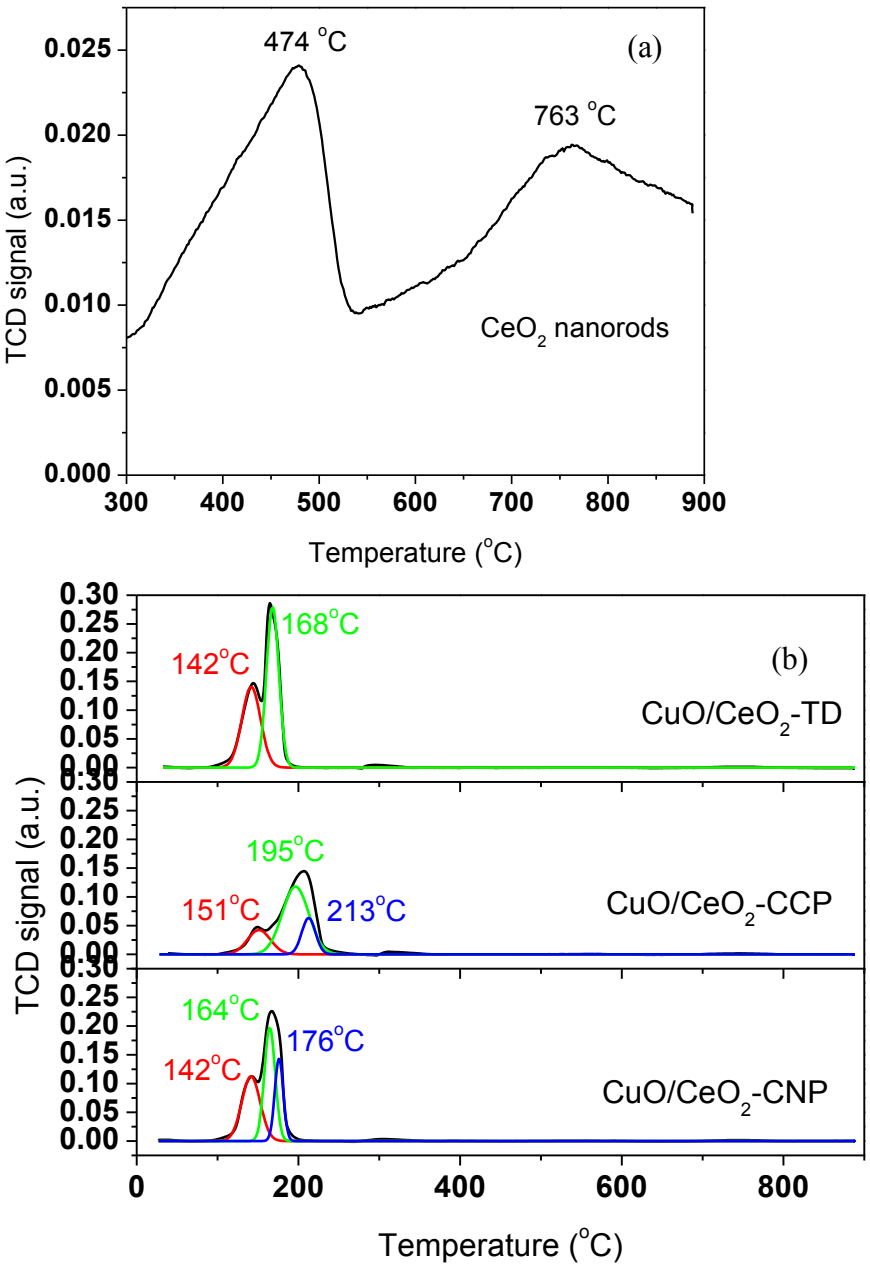

Figure 3.6. H_2-TPR profiles of (a) CeO_2 nanorods, (b) different CuO/CeO_2 catalysts in same scale.

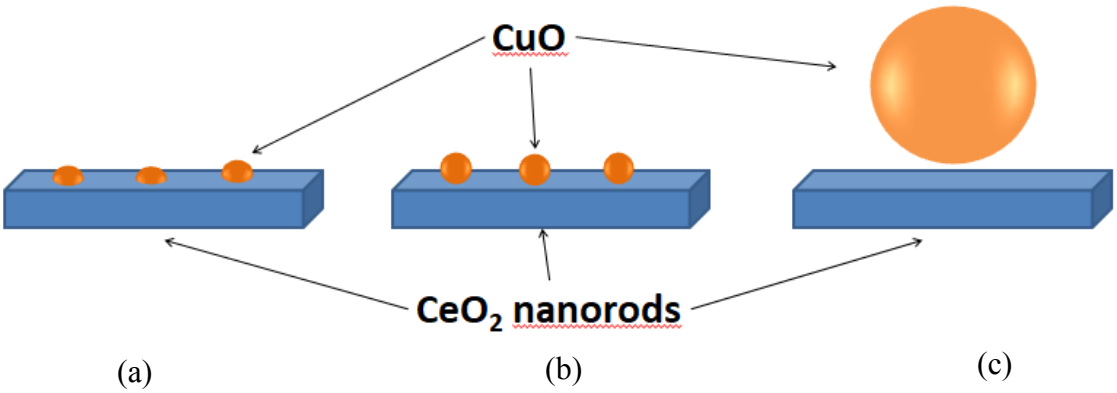

Figure 3.7. Schematic illustration of different Cu^{2+} species interacting with CeO_2 nanorods support. (a) Highly dispersed CuO strongly interacting with CeO_2, (b) well-dispersed weakly-interacted CuO and (c) bulk CuO.

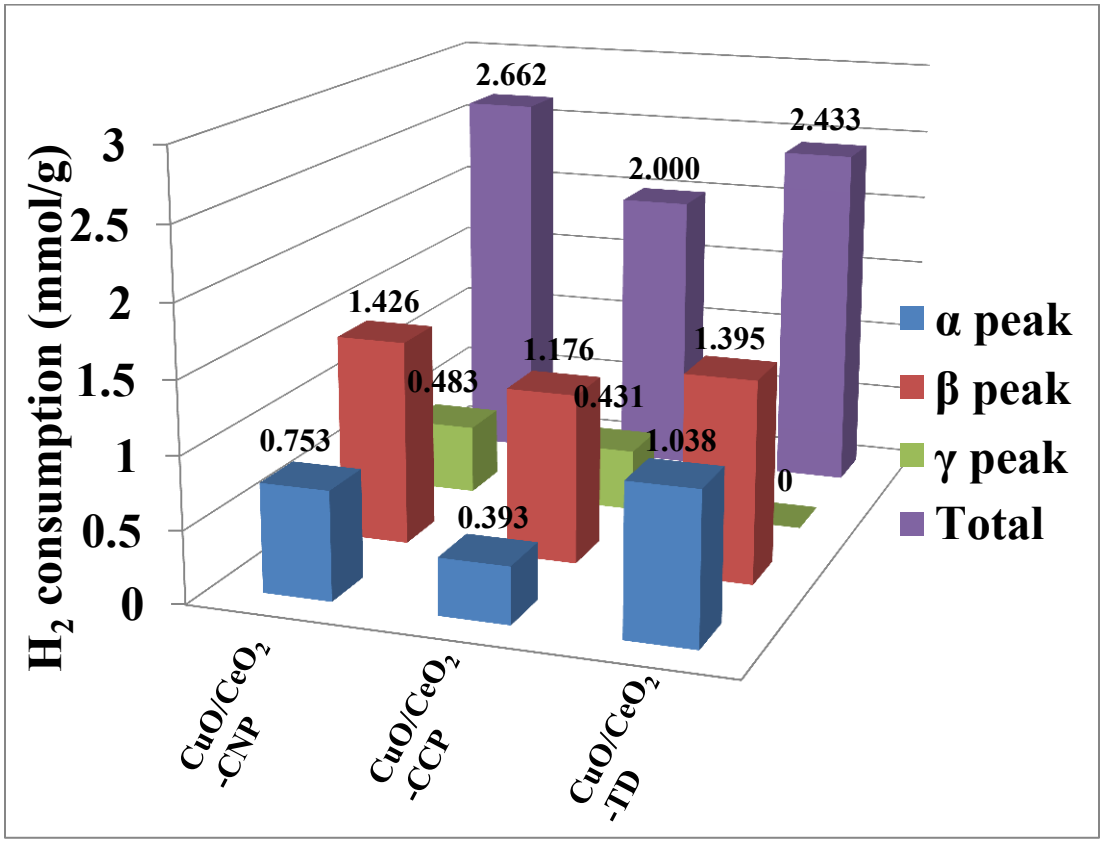

Figure 3.8. The amount of H_2 consumption by the catalysts at different peaks.

Fig. 3.8 showed the amount of H_2 consumption by the catalysts at different peaks. The amount of H_2 consumption by three catalysts at α peak was in the following order: CuO/CeO_2-TD (1.038 mmol/g) > CuO/CeO_2-CNP (0.753 mmol/g) > CuO/CeO_2-CCP (0.393 mmol/g), which suggested that CuO/CeO_2-TD had the highest amount of Cu-Ce-O solid solution. This result was in agreement with Raman analysis. H_2 consumption at β peaks for all of the three catalysts were almost similar which confirmed that similar amount of weakly-interacted CuO nanoparticles were dispersed onto CeO_2 surface for these three samples. CuO/CeO_2-CCP catalyst displayed the lowest amount of H_2 consumption in total (2.0 mmol/g) in comparison with other two catalysts due to the presence of higher amount of bulk CuO particles, consistent with XRD data.

3.3.6. CO TPD

CO-TPD curves of CuO/CeO_2 catalysts were shown in Fig. 3.9a. For instance adsorbed CO molecules desorb away as CO_2 after reacting with lattice oxygen, CO_2 desorption peaks can be found in Fig. 3.9a. First low temperature peak can be seen when adsorbed CO reacted with surface of CeO_2 and produced CO_2. Another peak found at higher temperature is attributed to bidentate carbon species produced from CO reactive sites as mentioned in our previously reported paper [23]. First peaks for CuO/CeO_2-TD, -CNP, and -CCP were observed at 102, 102, and 98 ^oC, respectively. Although, low-temperature peaks were almost at similar position for all of the samples, high-temperature peaks were found at different temperature. For CuO/CeO_2-TD, -CNP, and -CCP second peaks were seen at 142, 312, and 234 ^oC, respectively. By comparison the peak areas, it can be said that CuO/CeO_2-TD can deliver higher quantity of lattice oxygen to react with adsorbed CO. Rate of desorption (ROD) of CO_2 for various

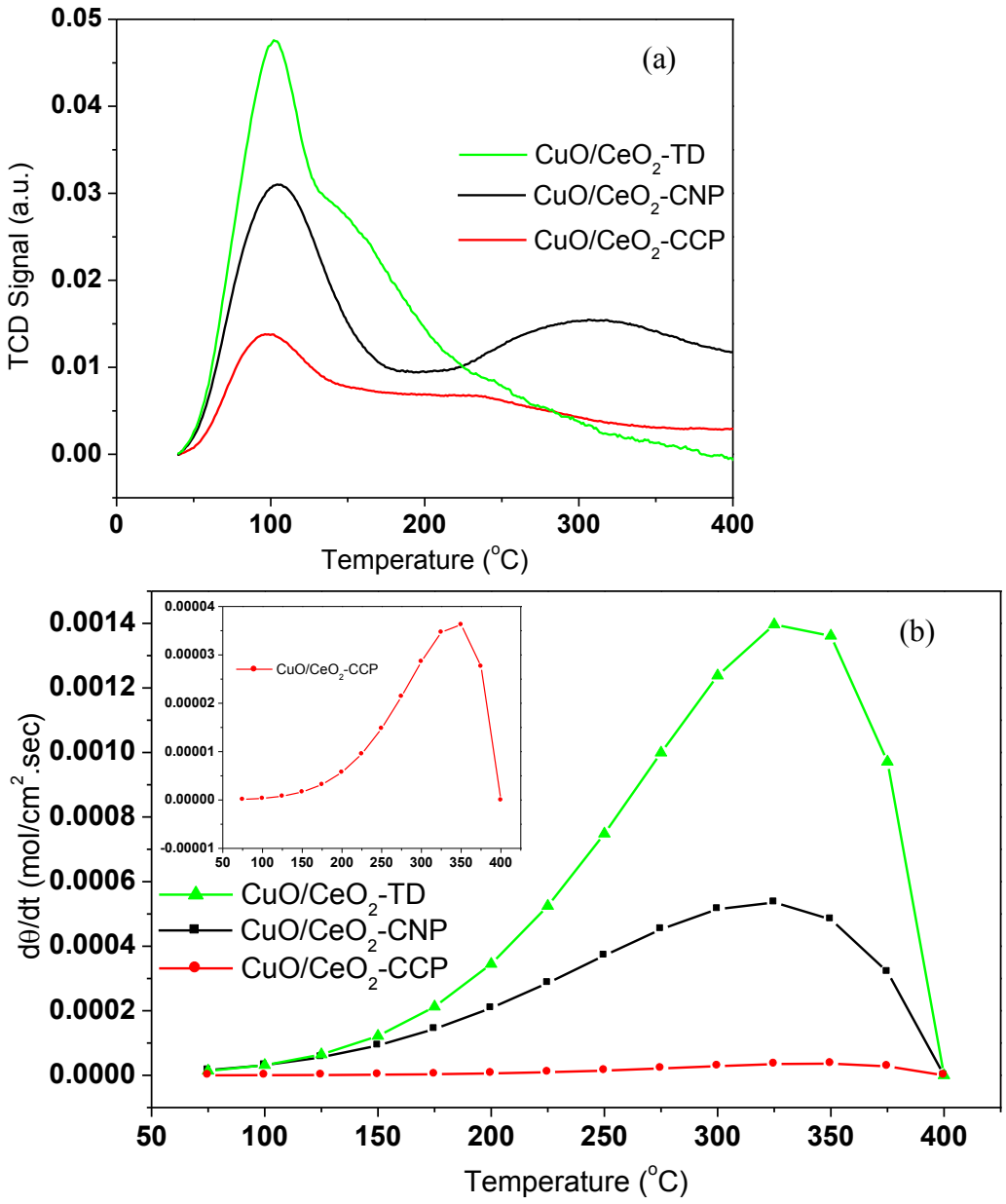

Figure 3.9. (a) CO-TPD and (b) rate of desorption of different CuO/CeO_2 catalysts. Rate of desorption of CuO/CeO_2-CCP in magnified scale shown in the inset of (b).

catalysts were shown in Fig. 3.9b. It can be observed that ROD clearly depends on sample temperature and it changes in three different steps. Firstly, ROD increased slowly with temperature up to 175 °C for both CuO/CeO_2-TD and CuO/CeO_2-CNP, and 225 °C for CuO/CeO_2-CCP. Then at second step, it increased linearly (but faster than previous

step) and the most part of desorption occurred at this step. Second steps for CuO/CeO_2-TD, -CNP, and -CCP were completed at 325, 325, and 350 ^oC, respectively where they reached maximum ROD (13.9×10^{-4}, 5.4×10^{-4}, and 0.37×10^{-4} $mol/cm^2.s$, respectively). In final step, ROD went down rapidly for all the samples due to the presence of low amount of adsorbed CO at this temperature. ROD of various catalysts depends on the mobility of oxygen in CeO_2 lattice and from Fig. 3.9b it can be said that CuO/CeO_2-TD catalyst can have higher oxygen mobility which eventually enhanced the catalytic efficiency. Earlier, through XPS analysis, we mentioned (Fig. 3.3) that CuO/CeO_2-TD sample had higher amount of Ce^{3+} and oxygen vacancies at the surface which can increase oxygen mobility. Thus, CO-TPD was consistent with XPS analysis.

3.3.7. CO oxidation and BET surface area

Fig. 3.10a showed the light-off curves of CO conversion for CuO/CeO_2 catalysts prepared by using various precursors and methods. Table 3.1 showed that the T_{50} (the temperature when the conversion was 50%) for CuO/CeO_2-CNP, -TD and -CCP were 84, 88 and 112 ^oC, respectively. Nonetheless, the total CO conversions for CuO/CeO_2-CNP, -TD and -CCP were achieved at 286, 220 and 278 ^oC, respectively. Although CuO/CeO_2-CNP catalyst showed lower T_{50} value, there were few CuO clusters in CuO/CeO_2-CNP as known from TEM and XRD results, which could be the reason of 100% CO conversion at high temperature for CuO/CeO_2-CNP compared to CuO/CeO_2-TD catalyst. Zheng et al. [12] reported that T_{50} and T_{100} for CuO/CeO_2 catalysts prepared by sol-gel method were 138 and 230 ^oC. Full CO conversion was obtained at 225^oC by Shinde et al. [39] for $Sn_{0.95}Cu_{0.05}O$ catalyst. Activation energy (E_A) for CO oxidation reaction, which is shown in Fig. 3.10b, was calculated using Arrhenius equation. Calculated E_A of CuO/CeO_2-TD,

-CNP, and –CCP were 15.0, 25.7, and 41.9 kJ/mol. CuO/CeO_2-TD sample had the lowest E_A among these three catalysts probably due to the contribution of these phenomenon: (1) the presence Ce^{3+} and oxygen vacancies at the surface, (2) the formation of solid solution near surface, and (3) higher oxygen mobility in CeO_2.

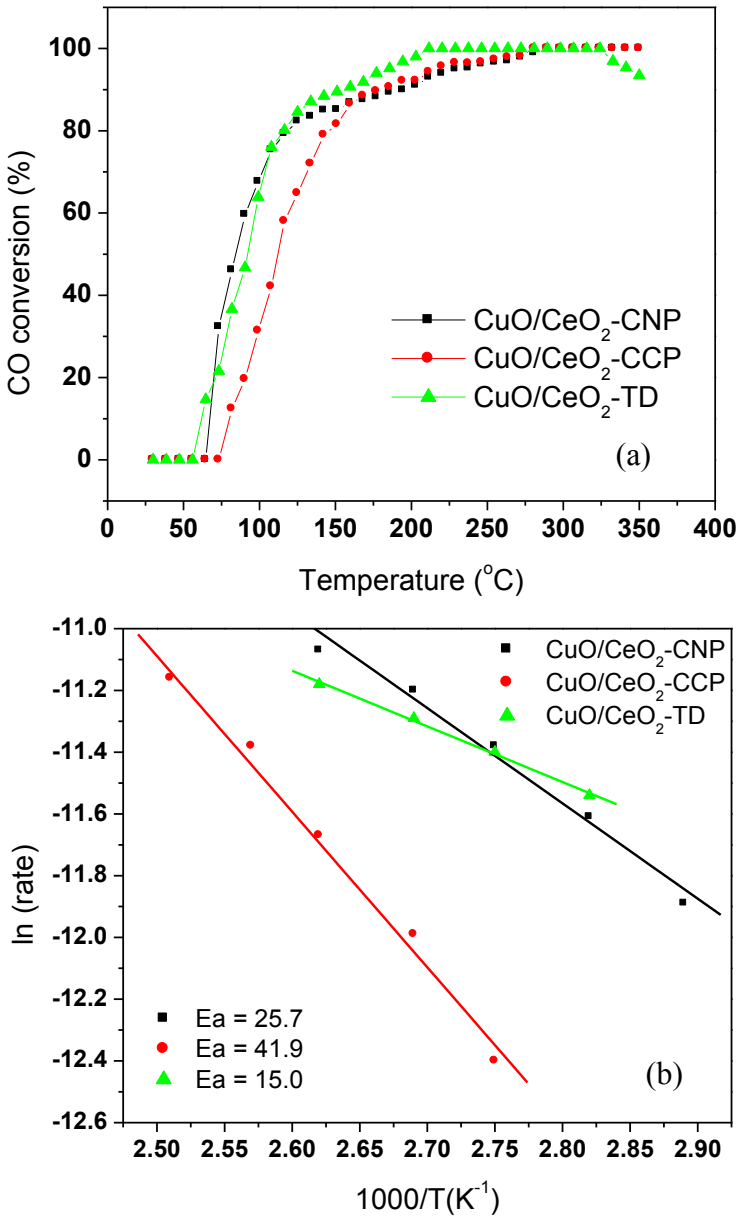

Figure 3.10. (a) Catalytic activity towards CO oxidation and (b) activation energy of different CuO/CeO_2 catalysts.

Table 3.1 showed BET surface area of the catalysts. BET surface area of CuO/CeO_2-TD, -CNP and -CCP were 39.31, 45.70 and 49.95 m^2/g, respectively. The surface area decreased with the increase amount of Cu-Ce-O solid solution in the sample, which was contradictory to the literature [40]. However, Luo et al. [15] showed that CuO impregnation on CeO_2 can decrease the surface area. Low surface area still does not affect the catalytic activity as long as the catalysts have highly synergistic interaction between CuO and CeO_2.

Table 3.1. BET surface area of various CuO/CeO_2 catalysts and temperatures at which 50% and 100% CO conversion by these catalysts.

Sample	Mass (mg)	BET surface area (m^2/g)	T_{50} (^oC)	T_{100} (^oC)
CuO/CeO_2-TD	25.6	39.31	93	211
CuO/CeO_2-CCP	25.2	49.95	112	278
CuO/CeO_2-CNP	24.8	45.70	84	286

3.4. Conclusion

In this study, a series of CuO/CeO_2 catalysts were successfully prepared by using three different CuO impregnation methods. The catalysts were characterized by XRD, Raman spectroscope, XPS, TEM, and H_2-TPR, and their catalytic performances were characterized by CO-TPD and CO oxidation. XRD and TEM confirmed the presence of bulk and agglomerated CuO particles in CuO/CeO_2-CCP and CuO/CeO_2-CNP catalysts. Raman analysis ensured the presence of Cu-Ce-O solid solution in CuO/CeO_2-TD and CuO/CeO_2-CNP catalysts. CuO/CeO_2-CCP catalyst has either less amount of solid

solution or no solid solution at all. XPS spectra advised that higher amount of Ce^{3+} and a strong interaction between Cu species and CeO_2 were present in CuO/CeO_2-TD sample. HRTEM images displayed different types of interactions between CuO and CeO_2 in the catalysts, which have a significant effect on the catalytic activity and lowering the reduction temperature. Among these three catalysts, CuO/CeO_2-TD consumed the highest amount of H_2 at low temperatures (142 and 165 ^oC) and converted 100% CO into CO_2 at low temperature (220 ^oC) in comparison to other two catalysts. Therefore, CuO/CeO_2-TD catalyst showed higher catalytic activity, which was due to the presence of strongly interacted dispersed CuO particles or Cu-Ce-O solid solution, resulting an increase in oxygen mobility in CeO_2 lattice.

3.5. References

1. Wu, S. H.; Li, B. Q.; Huang, W. P.; Zhang, S. M.; Shi, J.; Zheng, X. C. Comparative studies of gold catalysts prepared via solvated metal atom impregnation and conventional impregnation: characterization and low-temperature CO oxidation. *React. Kinet. Catal. Lett*. **2003**, 78, 49-58.

2. Daté, M.; Haruta, M. Moisture effect on CO oxidation over Au/TiO_2 catalyst. *J. Catal*. **2001**, 201, 221-224.

3. Tripathi, A. K.; Kamble, V. S.; Gupta, N. M. Microcalorimetry, adsorption, and reaction studies of CO, O_2, and $CO+O_2$ over Au/Fe_2O_3, Fe_2O_3, and polycrystalline gold catalysts. *J. Catal*. **1999**, 187, 332-342.

4. Lee, S. J.; Gavriilidis, A. Supported Au catalysts for low-temperature CO oxidation prepared by impregnation. *J. Catal*. **2002**, 206, 305-313.

5. Bera, P.; Hegde, M. S. Characterization and catalytic properties of combustion synthesized Au/CeO_2 catalyst. *Catal. Lett*. **2002**, 79, 75-81.

6. Carabineiro, S. A. C.; Machado, B. F.; Bacsa, R. R.; Serp, P.; Drazic, G.; Faria, J. L.; Figueiredo, J. L. Catalytic performance of Au/ZnO nanocatalysts for CO oxidation. *J. Catal*. **2010**, 273, 191-198.

7. Holmgren, A.; Azamoush, F.; Fridell, E. Influence of pre-treatment on the low-temperature activity of Pt/ceria. *Appl. Catal. B-Environ*. **1999**, 22, 49-61.

8. Semon, P. A.; Pt-doped and SnO_2-templated TiO_2: properties and reactivity towards CO. *Solid State Ionics*. **1997**, 101, 673-676.

9. Luo, M. F.; Hou, Z. Y.; Yuan, X. X.; Zheng, X. M. Characterization study of CeO_2 supported Pd catalyst for low-temperature carbon monoxide oxidation. *Catal. Lett*. **1998**, 50, 205-209.

10. Okumura, M.; Masuyama, N.; Konishi, E.; Ichikawa, S.; Akita, T. CO oxidation below room temperature over Ir/TiO_2 catalyst prepared by deposition precipitation method. *J. Catal*. **2002**, 208, 485-489.

11. Song, Y. J.; Lopez-De Jesus, Y. M.; Fanson, P. T.; Williams, C. T. Preparation and characterization of dendrimer-derived bimetallic Ir–Au/Al_2O_3 catalysts for CO oxidation. *J. Phys. Chem. C* **2013**, 117, 10999-11007.

12. Zheng, X. C.; Wu, S. H.; Wang, S. P.; Wang, S. R.; Zhang, S. M.; Huang, W. P. The preparation and catalytic behavior of copper–cerium oxide catalysts for low-temperature carbon monoxide oxidation. *Appl. Catal. A-Gen*. **2005**, 283, 217-223.

13. Sedmak, G.; Hocevar, S.; Levec, J. Kinetics of selective CO oxidation in excess of H_2 over the nanostructured $Cu_{0.1}Ce_{0.9}O_{2-y}$ catalyst. *J. Catal*. **2003**, 213, 135-150.

14. Xu, D.; Cheng, F.; Lu, Q.; Dai, P. Microwave enhanced catalytic degradation of methyl orange in aqueous solution over CuO/CeO_2 catalyst in the absence and presence of H_2O_2. *Ind. Eng. Chem. Res.*, **2014**, 53, 2625–2632.

15. Luo, M. F.; Zhong, Y. J.; Yuan, X. X.; Zheng, X. M. TPR and TPD studies of catalysts for low temperature CO oxidation. *Appl. Catal. A-Gen*. **1997**, 162, 121-131.

16. Aunbamrung, P.; Wongkaew, A. Effect of Cu loading to catalytic selective CO oxidation of CuO/CeO_2 –Co_3O_4. *Adv. Chem. Eng. Sci.*, **2013**, 3, 15-19.

17. Delimaris, D.; Loannides, T. VOC oxidation over CuO–CeO_2 catalysts prepared by a combustion method. *Appl. Catal. B-Environ.* **2009**, 89, 295-302.

18. Zabilskiy, M.; Djinović, P.; Tchernychova, E.; Tkachenko, O. P.; Kustov, L. M.; Pintar, A. Nanoshaped CuO/CeO_2 materials: Effect of the exposed ceria surfaces on catalytic activity in N_2O decomposition reaction. *ACS Catal.* **2015**, 5, 5357−5365.

19. Wang, R.; Dangerfield, R. Seed-mediated hydrothermal synthesis of shape-controlled CeO_2 nanocrystals. *RSC Adv.*, **2014**, 4(7), 3615-3620.

20. Yang, F.; Wei, J.; Liu, W.; Guo, J.; Yang, Y. Copper doped ceria nanospheres: surface defects promoted catalytic activity and a versatile approach. *J. Mater. Chem. A*, **2014**, 2, 5662-5667.

21. Shan, W.; Shen, W.; Li, C. Structural characteristics and redox behaviors of $Ce_{1-x}Cu_xO$ solid solutions. *Chem. Mater*. **2003**, 15, 4761-4767.

22. Zhong, K.; Xue, J.; Mao, Y.; Wang, C.; Zhai, T.; Liu, P.; Xia, X.; Li, H.; Tong, Y. Facile synthesis of CuO nanorods with abundant adsorbed oxygen concomitant with high surface oxidation states for CO oxidation. *RSC. Adv*., **2012**, 2, 11520-11528.

23. Hossain, S. T.; Almesned, Y.; Zhang, K.; Zell, E. T.; Bernard, D. T.; Balaz, S.; Wang, R. Support structure effect on CO oxidation: A comparative study on SiO_2 nanospheres and CeO_2 nanorods supported CuOx catalysts. *Appl. Surf. Sci.* **2018**, 428, 598-608.

24. Shen, W.; Mao, D.; Luo, Z.; Yu, J. CO oxidation on mesoporous SBA-15 supported CuO-CeO_2 catalyst prepared by a surfactant-assisted impregnation method. *RSC. Adv.* **2017**, 7, 27689-27698.

25. Zheng, Y.; Mao, D.; Sun, S.; Fu, G. CO oxidation on CuO/CeO_2 catalyst prepared by solvothermal synthesis: influence of catalyst activation temperature. *J. Nanopart. Res*. **2015**, 17, 471 (1-12).

26. Li, T.; Xiang, G.; Zhuang, J.; Wang, X. Enhanced catalytic performance of assembled ceria necklace nanowires by Ni doping. *Chem. Commun*. **2011**, 47, 6060-6062.

27. Mock, S. A.; Sharp, S. E.; Stoner, T. R.; Radetic, M. J.; Zell, E. T.; Wang, R. CeO_2 nanorods-supported transition metal catalysts for CO oxidation. *J. Colloid Interface Sci.* **2016**, 466, 261-267.

28. Mock, S. A.; Zell, E. T.; Hossain, S. T.; Wang, R. Effect of reduction treatment on CO oxidation with CeO_2 nanorod-supported CuO_x catalysts. *ChemCatChem*. **2017**. doi:10.1002/cctc.201700972

29. Wang, Z.; Wang, Q.; Liao, Y.; Shen, G.; Gong, X.; Han, N.; Liu, H.; Chen, Y. Comparative study of CeO_2 and doped CeO_2 tailored oxygen vacancies for CO oxidation. *ChemPhysChem* **2011**, 12, 2763-2770.

30. Chen, J.; Zhan, Y.; Zhu, J.; Chen, C.; Lin, X.; Zheng, Q. The synergetic mechanism between copper species and ceria in NO abatement over Cu/CeO_2 catalysts. *Appl. Catal. A* **2010**, 377, 121−127.

31. Xiaoyuan, J.; Guanglie, L.; Renxian, Z.; Jianxin, M.; Yu, C.; Xiaoming, Z. Studies of pore structure, temperature-programmed reduction performance, and micro-structure of CuO/CeO_2 catalysts. *Appl. Surf. Sci.*, **2001**, 173, 208–220.

32. Zeng, S.; Zhang, W.; Sliwa, M.; Su, H. Comparative study of CeO_2/CuO and CuO/CeO_2 catalysts on catalytic performance for preferential CO oxidation. *Int. J. Hydrogen Energ*. **2013**, 38, 3597-3605.

33. Zhu, P.; Liu, M.; Zhou, R. Effect of interaction between CuO and CeO_2 on the performance of $CuO\text{-}CeO_2$ catalysis for selective oxidation of CO in H_2 rich streams. *Indian J. Chem.* **2012**, 51, 1529-1537.

34. Avgouropoulos, G.; Ioannides, T. Effect of synthesis parameters on catalytic properties of CuO-CeO_2. *Appl. Catal. B-Environ*., **2006**, 67, 1-11.

35. Shiau, C. Y.; Ma, M. W.; Chuang, C. S. CO oxidation over CeO_2-promoted Cu/γ-Al_2O_3 catalyst: Effect of preparation method. *Appl. Catal. A-Gen*., **2006**, 301, 89-95.

36. Wang, J. B.; Shih, W. H.; Huang, T. J. Study of Sm_2O_3-doped CeO_2/Al_2O_3-supported copper catalyst for CO oxidation. *Appl. Catal. A-Gen*., **2000**, 203, 191-199.

37. Liu, W.; Flytzani-Stephanopoulos, M. Total oxidation of carbon monoxide and methane over transition metal fluorite oxide composite catalysts: Catalyst composition and activity. *J. Catal*. **1995**, 153, 304−316.

38. Martinez-Arias, A.; Fernandez-Garcia, M.; Soria, J.; Conesa, J. C. Spectroscopic study of a Cu/CeO_2 catalyst subjected to redox treatments in carbon monoxide and oxygen. *J. Catal*. **1999**, 182, 367−377.

39. Shinde, V. M.; Madras, G. Kinetics of carbon monoxide oxidation with $Sn_{0.95}M_{0.05}O_{2-d}$ (M = Cu, Fe, Mn, Co) catalysts. *Catal. Sci. Technol.*, **2012**, 2, 437–446.

40. Luo, M. F.; Song, Y. P.; Lu, J. Q.; Wang, X. Y.; Pu, Z. Y. Identification of CuO species in high surface area CuO-CeO_2 catalysts and their catalytic activities for CO oxidation. *J. Phys. Chem. C* **2007**, 111, 12686-12692.

Chapter 4: A comparative study of CO oxidation over Cu-O-Ce solid solutions and CuO/CeO_2 nanorods catalysts

The distribution of copper species (on the surface or in the bulk of CeO_2 support) and the interfacial interactions between CuO and CeO_2 are critical in understanding the synergistic effect on the catalytic activity of CeO_2 supported CuO catalysts. In this chapter, Cu-O-Ce solid solutions and CuO impregnated on CeO_2 nanorods catalysts (CuO/CeO_2) with various compositions were prepared using thermal decomposition and hydrothermal methods, to understand the distribution effect of copper species on low temperature CO oxidation. The incorporation of copper ions into CeO_2 lattice in both types of catalysts was confirmed by X-ray diffraction (XRD), Raman spectroscopy, and hydrogen temperature programmed reduction (H_2-TPR) analysis, indicating a strong $CuO\text{-}CeO_2$ interfacial interaction and formation of oxygen vacancies which compensates the charge difference between copper (I/II) and cerium (III/IV) ions. A series of temperature programmed reduction-temperature programmed oxidation (TPR-TPO) thermal cycling studies were conducted to understand the interactions between three assigned copper species (α, β, and γ) with CeO_2 support and the corresponding catalytic performance of the catalysts. In addition, an improved low temperature catalytic performance for the CuO/CeO_2 nanorods catalysts was observed, which was attributed to stronger interactions between copper species and CeO_2 nanorods enriched with surface defects (steps and voids etc.).

4.1. Introduction

Cerium oxide (CeO_2) supported CuO catalyst has been considered as an economically favorable material for various catalytic reactions, such as automotive three-way catalytic conversions [1,2], water gas shift reaction [3], oxidation of volatile organic compounds [4,5], and SO_2 reduction [6] etc. Researchers have approached various ways to investigate and improve the catalytic performance of CuO-CeO_2 catalysts for low-temperature reduction of nitrogen oxides and carbon monoxide oxidation. Zabilsky et al. [7] reported the effect of CeO_2 support shapes on the catalytic efficiency, and they concluded that CeO_2 nanorods presented a better catalytic performance in N_2O decomposition reaction due to exposing {100} and {110} high-energy surface planes. Avgouropoulos et al. [8] showed that the preparation method of CuO-CeO_2 catalysts can affect the catalytic activity in the selective oxidation of CO. They explored several different preparation methods, such as co-precipitation, urea-nitrates combustion, and citrate-hydrothermal method, to synthesize CuO-CeO_2 catalysts. The catalysts prepared by urea-nitrates combustion method showed the best catalytic activity in the selective oxidation of CO, which was contributed to the well-dispersed copper oxide species strongly interacting with CeO_2 surface. Zhou et al. [9] and Liu et al. [10] used deposition-precipitation method and wet impregnation method (thermal decomposition of $Cu(NO_3)_2$), respectively, to prepare CuO-CeO_2 nanorods catalysts. They investigated the support shape and crystal plane effect, and concluded that the coordination environment of copper ions is different on {111}, {110} and {100} planes of CeO_2 surfaces. Zheng et al. [11] demonstrated that both thermal decomposition temperature of $Ce(NO_3)_3$ and calcination temperature of CuO-CeO_2 catalysts have a significant impact on the physical

texture and catalytic activity of catalysts for low temperature CO oxidation. Avgouropoulos et al. [12] also reported that the hydrothermal treatment of citrate precursors promoted the mixing of Cu^{2+} and Ce^{4+} and the intimate interaction between CuO and CeO_2 which led to the improved structural and thermal stabilization of the catalysts.

These previous investigations pointed out the importance of mixing or interaction between CuO catalyst and CeO_2 support either on the CeO_2 surface or in the form of Cu-O-Ce solid solution phases during the catalysts preparation. CeO_2 nanorods have demonstrated as a highly reducible and active support for CuO catalysts compared to CeO_2 nanocubes and nanoctahedra. To further explore the roles of copper species distribution (on the surface or in the bulk of CeO_2 support), CeO_2 nanorods with significant surface roughness and defects were chosen as support of CuO catalyst to understand the synergistic effect in CuO-CeO_2 catalysts for low-temperature CO oxidation. In this chapter, Cu-O-Ce solid solutions and CuO impregnated CeO_2 nanorods catalysts (CuO/CeO_2) with various compositions were prepared and a systematic comparison study was conducted to advance our understanding of the effects of copper distribution and thermal cycling treatments on the catalytic behavior in CuO-CeO_2 catalysts.

4.2. Experimental

4.2.1. Catalyst preparation

To prepare the Cu-O-Ce solid solution catalyst samples with 2-12 wt% Cu addition, $Ce(NO_3)_3 \cdot 6H_2O$ and $Cu(NO_3)_2 \cdot 3H_2O$ were mixed with the stoichiometric ratios in 30 mL

deionized water. The mixture solution in a beaker was stirred and heated at 120 ^{o}C on a hot plate until water evaporated completely. The collected samples were then oxidized at 400 ^{o}C for 5 hrs in air. These samples were called as Cu-O-Ce solid solutions and were denoted as x-Cu-O-Ce, where x was the weight percentage of Cu (wt%). For example, 2-Cu-O-Ce stands for 2 wt% Cu addition in Cu-O-Ce solid solution. Reduction-oxidation (redox) thermal cycling treatments were conducted on the 10-Cu-O-Ce catalyst sample. The catalyst was reduced in a tube furnace t at 400 ^{o}C for 1 hr under 5%H_2-95%Ar gas environment. After cooling down to room temperature, the sample was then oxidized in a box furnace at 400 ^{o}C for 1 hr in air. This two-step process is called one redox treatment.

Hydrothermal method is a common way to prepare CeO_2 nanorods [1], which was used in this study. 8 mL of 6 M NaOH was added into 88 mL of 0.1 M $Ce(NO_3)_3 \cdot 6H_2O$ solution in Teflon liner of 200 mL capacity. After stirring the solution for about 15 sec, the lid of Teflon liner was closed. The Teflon liner along with stainless steel autoclave was heated and kept at 90 ^{o}C for 48 hrs. After cooling down to room temperature, a filtration of the suspension solution was conducted. The filtered product was washed with 500 mL water, and then with 50 mL ethanol to remove any Na^+ ion remained in the product and most of water to avoid hard agglomeration during drying. Then the sample was dried at 50 ^{o}C for 12 hrs.

To prepare the CuO/CeO_2 catalyst samples with 6-10 wt% Cu addition (CuO impregnated CeO_2 nanorods catalysts), the as-synthesized CeO_2 nanorods powder and $Cu(NO_3)_2 \cdot 3H_2O$ solution were mixed first with the stoichiometric ratios in 30 mL of deionized water. The suspension solution was heated and kept at 120 ^{o}C until water evaporated completely. Finally, the samples were oxidized at 400 ^{o}C for 5 hrs in air. The

samples were denoted as x-CuO/CeO_2, where x is Cu wt%. For example, 6-CuO/CeO_2 stands for 6 wt% Cu loaded onto CeO_2 nanorods.

4.2.2. Catalyst Characterizations

X-ray diffraction (XRD), Raman spectroscopy, X-ray photoelectron spectroscopy (XPS), transmission electron microscopy (TEM), BET surface area measurement, temperature programmed reduction (TPR),), temperature programmed oxidation (TPO), temperature programmed desorption (TPD), pulse chemisorption to calculate oxygen storage capacity (OSC), and CO oxidation were used to characterize the catalysts and their catalytic activity. The description of these techniques can be found in chapter 2.

4.3. Results and discussion

4.3.1. XRD and BET surface area

For comparison, Fig. 4.1a showed the XRD patterns of the as-synthesized CeO_2 nanorods and CuO powder. Typical diffraction peaks for fluorite structured CeO_2 were observed at 2θ of 28.8°, 33.1°, 47.5°, 56.3°, 59.1°, 69.4°, 76.7° and 79.1° (JCPDS 43-1002) [13]. Two strong and sharp diffraction peaks for monoclinic CuO were observed at 2θ of 35.6° and 38.8° which correspond to (-111) and (111) planes (JCPDS 45-0937), respectively [14,15]. Fig. 4.1b displayed the XRD patterns of the Cu-O-Ce solid solutions samples where the Cu content varied from 2 to 12 wt%. Fluorite structure CeO_2 phase was observed clearly in all six samples. The disappearance of the CuO diffraction peaks below 8 wt% Cu addition indicated a formation of Cu-O-Ce solid solution. There could be a possibility that amorphous or small-sized copper species could anchor onto the

surface of CeO_2 support, which was also invisible in XRD patterns. But a continuous CeO_2 (111) diffraction peak shift was observed as shown in Fig. 4.2a, indicating the incorporation of Cu^{2+} into CeO_2 concluded that the disappearance of CuO diffraction was at least partially due to the formation of Cu-O-Ce solid solution. The characteristic (-111)/(111) CuO diffraction peaks were visible starting for 8 wt% Cu addition and more in the solid solution samples, as shown in Fig. 4.1b. The intensities of these two peaks were low in the 8-Cu-O-Ce sample and became progressively stronger with increasing the Cu content to 10 wt% and 12 wt%. The XRD patterns of the CuO/CeO_2 nanorods samples with 6-10 wt% Cu addition were shown in Fig. 4.1c, where the characteristic peaks of CeO_2 were visible for all three samples. Interestingly, no CuO diffraction peaks were detected for these three CuO/CeO_2 nanorods samples, which suggested a different distribution of copper species over CeO_2 nanorods compared to the 6-10 wt% Cu-O-Ce solid solution samples (Fig. 4.1b). Some possible reasons why CuO phase was not detected in XRD analysis were the following: poor crystallization, formation of Cu-O-Ce solid solution, and highly dispersed small copper species on CeO_2 nanorods, and/or a mixture of these. It was also found that when the Cu content increased, the characteristic XRD peaks of CeO_2 became broader for both Cu-O-Ce solid solution and CuO/CeO_2 nanorods samples. The peak broadening was due to decrease in crystallite size and increase in compositional heterogeneity with increasing the Cu amount. Table 4.1 showed that the crystallite size of the Cu-O-Ce samples decreased with increasing the Cu content up to 8 wt% Cu addition, and then increased with further Cu addition. For the CuO/CeO_2 samples, the crystallite size showed a continuous decrease from 6 wt% to 10 wt% Cu addition.

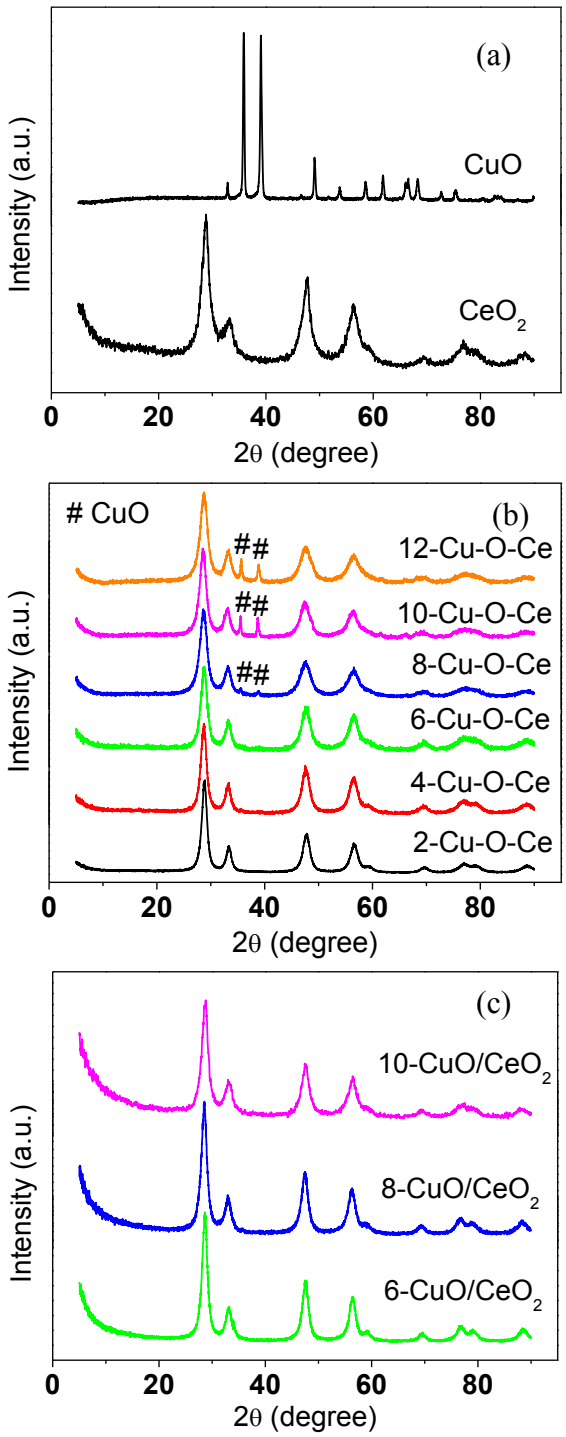

Figure 4.1. XRD patterns of (a) CeO_2 and CuO, (b) Cu-O-Ce samples, and (c) CuO/CeO_2 samples.

Table 4.1. Crystallite size and lattice parameter measured from CeO_2 (111) peak, and BET surface area of Cu-O-Ce and CuO/CeO_2.

Cu contents (%)	Cu-O-Ce solid solution			CuO/CeO_2 nanorods		
	Crystallite size (nm)	Lattice parameter (Å)	S_{BET} (m^2/g)	Crystallite size (nm)	Lattice parameter (Å)	S_{BET} (m^2/g)
0	-	-	-	5.6	5.4142 (±0.0004)	64.32
2	6.6	5.4212 (±0.0005)	48.12	-	-	-
4	6.1	5.4274 (±0.0006)	29.36	-	-	-
6	5.5	5.4358 (±0.0003)	18.69	6.3	5.4254 (±0.0003)	55.39
8	4.9	5.4468 (±0.0002)	15.20	5.8	5.4398 (±0.0003)	43.86
10	5.2	5.4548 (±0.0002)	13.68	5.4	5.4747 (±0.0005)	39.31
12	5.4	5.4324 (±0.0003)	12.01	-	-	-

Fig. 4.2a and 4.2b illustrated that the characteristic (111) peak of CeO_2 for both Cu-O-Ce solid solutions and CuO/CeO_2 nanorods samples shifted towards lower angle with increasing the Cu content. This peak shifting towards lower diffraction angle indicated a lattice expansion of CeO_2 according to the Scherrer equation ($2d \sin\theta = n\lambda$). The ionic radius of Cu^{2+} and Ce^{4+} were 0.072 nm and 0.103 nm, respectively [16,17]. As the radius of Cu^{2+} was smaller than that of Ce^{4+}, the incorporation of Cu^{2+} in CeO_2 would cause lattice contraction leading to the peak shifting towards higher diffraction angle. Most likely, the addition of Cu^{2+} in CeO_2 created oxygen vacancies accompanied by reduction of Ce^{4+} ions in their vicinity into Ce^{3+} ($2Ce^{4+} \leftrightarrow 2Ce^{3+} + V_{\ddot{O}}^{2+}$) to compensate the change difference between Cu^{2+} and Ce^{4+}. Since the ionic radius of Ce^{3+} (0.111 nm) is about 7.8% larger than that of Ce^{4+} (0.103 nm), the diffraction peak shifted to lower diffraction angle due to the lattice expansion observed in the samples. The change in

CeO_2 lattice parameter with the Cu addition was shown in Table 4.1. The lattice constant in CeO_2 increased with increasing the Cu content for both Cu-O-Ce solid solution and CuO/CeO_2 nanorods samples, except for the 12-Cu-O-Ce sample. It has been reported that Cu^{2+} ions can incorporate into CeO_2 lattice to form $CuO\text{-}CeO_2$ solid solution [18]. As a result, oxygen vacancies are formed which leads to the formation of

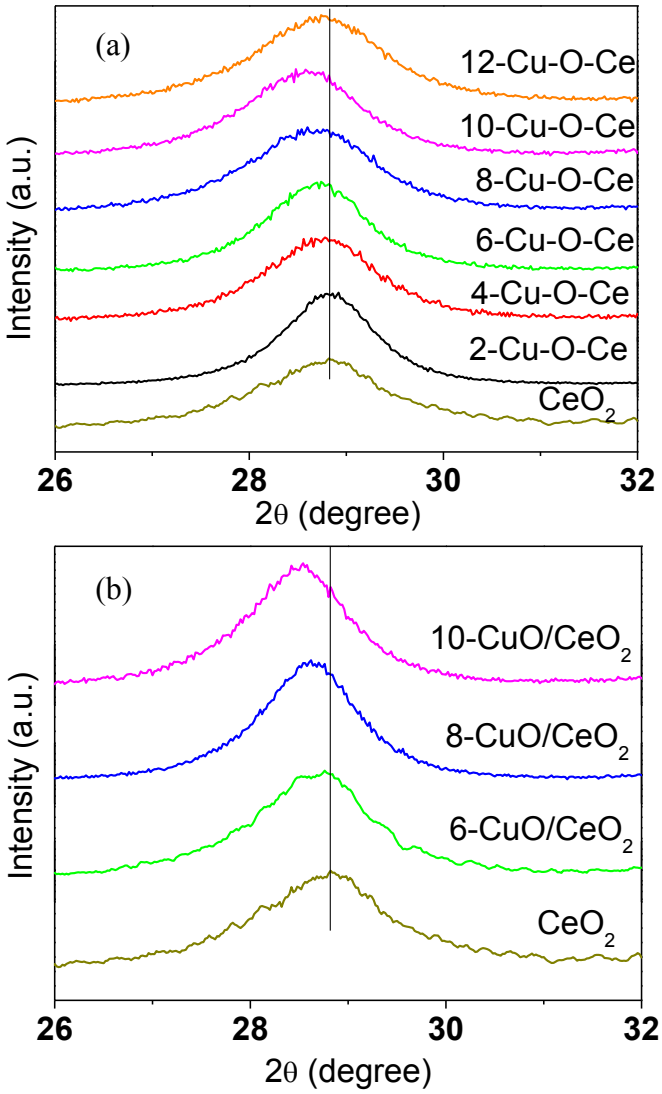

Figure 4.2. XRD patterns of CeO_2 (111) peak in (a) Cu-O-Ce and (b) CuO/CeO_2 samples.

substoichiometric fluorite-structured CeO_{2-y} ($0 \leq y < 0.5$). By comparing between the Cu-O-Ce solid solutions and CuO/CeO_2 nanorods samples for 6-10 wt% Cu addition, it was found in Table 4.1 that the 10-CuO/CeO_2 nanorods sample showed the largest lattice constant due to possibly the presence of highest amount of Ce^{3+} ions and oxygen vacancies in CeO_2 lattice. It also should be noted that another possible explanation for the lattice expansion is the size effect, and generally smaller particle size causes an expanded lattice due to the high concentration of defects. The particle size of these samples is in the range of 4~6 nm with evident defects shown in Fig. 4.5. Table 4.1 also showed that the BET surface area of the Cu-O-Ce solid solutions and CuO/CeO_2 nanorods samples decreased with increasing the Cu content. In principle, the surface area of the samples would increase if the crystallite size decreased. But it should be noted that the crystallite size was estimated by the CeO_2 (111) peak, but the BET surface areas was measured on both CeO_2 and copper based particles and species in the samples by N_2 adsorption. It was reported previously that surface area of the samples decreased due to increasing the amount of Cu ions incorporation into CeO_2 lattice [16].

4.3.2. Raman analysis

Raman spectra of CeO_2 nanorods and CuO were shown in Fig. 4.3a. The characteristic peak of CeO_2 observed at 456 cm^{-1} corresponded to F_{2g} vibrational mode [19]. Two peaks found at 258 and 605 cm^{-1} were attributed to oxygen vacancies in CeO_2 nanorods [19]. CuO showed the typical peaks at 271, 326, 506, and 625 cm^{-1}, which corresponded to A_g, B_{1g}, B_{2u}, and B_{2g} mode, respectively [20-22]. According to Debbichi et al., [23] the peak found at 506 cm^{-1} corresponded to E_g mode of Cu_4O_3. However, no evidence of Cu_4O_3 phase was found in the XRD patterns and thus, this peak was assumed

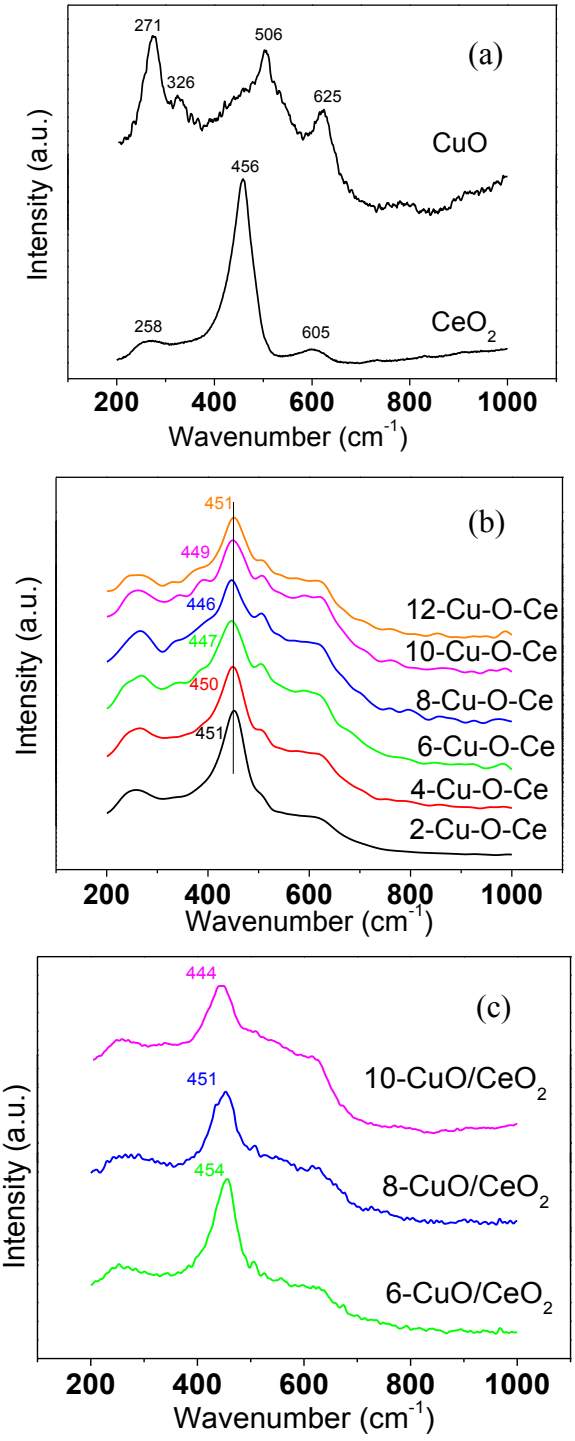

Figure 4.3. Raman spectra of (a) CeO_2 and CuO, (b) Cu-O-Ce samples, and (c) CuO/CeO_2 samples.

as B_{2u} mode of CuO. Fig. 4.3b showed the Raman spectra of the Cu-O-Ce solid solutions samples, where it was clear that the characteristic F_{2g} peak of CeO_2 started shifting to the left (from 456 cm^{-1} to 446 cm^{-1}) with increasing the Cu content till 8 wt%, and then the peak started shifting to the right (from 446 cm^{-1} to 451 cm^{-1}) with further increasing the Cu content. Such peak shifting to the lower wavenumber in Raman analysis occurred for two possible reasons: (i) lattice distortions in CeO_2 due to Cu addition, and (ii) decrease in crystallite size [24,25]. The incorporation of Cu ions into CeO_2 lattice led to the formation of Cu-O-Ce solid solutions. In the meantime, oxygen vacancy was created to compensate the charge discrepancy between Cu^{2+} and Ce^{4+}. However, oxygen vacancy was not restricted in one single site, but instead this spread to further adjacent oxygen positions. Thus, the incorporation of Cu ions into CeO_2 lattice increased the chance of forming substoichiometric CeO_{2-y} due to the generation of many oxygen vacancies. The oxygen vacancy defect disrupted the O-Ce-O lattice, which eventually caused the Raman peak shifting. The decrease in crystallite size along with the Cu incorporation created more lattice distortion and defects. For the Cu-O-Ce solid solutions, the CeO_2 F_{2g} peak for the 10-Cu-O-Ce and 12-Cu-O-Ce samples started shifting to the right with respect to the same peak of the 8-Cu-O-Ce sample. For the 10-Cu-O-Ce sample, although the XRD pattern showed the lattice expansion due to the presence of Ce^{3+} and oxygen vacancies, CeO_2 F_{2g} peak shifted to the right due to the increment of crystallite size as shown in Table 4.1. Fig. 4.3c showed that CeO_2 F_{2g} peak for the CuO/CeO_2 nanorods samples shifted to the left (from 456 cm^{-1} to 444 cm^{-1}) with increasing the Cu content. The 10-CuO/CeO_2 nanorods sample showed the largest peak shifting to the left due to the existence of oxygen vacancies and Ce^{3+} as discussed above, which was in line with the

XRD analysis (Fig. 4.2). Shan et al. [16] reported a similar peak shift due to the formation of CuO-CeO_2 solid solution.

4.3.3. XPS analysis

Fig. 4.4 compared the XPS spectra of the 10-Cu-O-Ce solid solution and 10-CuO/CeO_2 nanorods samples. Fig. 4.4a showed spectra of Ce 3d which was used to assess the fraction of Ce^{3+} state. The fitted Ce 3d spectrum was overlaid on top of the experimental data. v (882.7 eV), v″(888.5 eV), v‴(898.3 eV), u (901.3 eV), and u″(907.3 eV) referred to Ce^{4+} state, while v′(885.2 eV), and u′(903.4 eV) referred to Ce^{3+} state [26,27]. The marked differences in v′(885.2 eV) and u′(903.4 eV) intensity indicated the higher concentration of Ce^{3+} in the 10-CuO/CeO_2 nanorods sample, which was consistent with the XRD and Raman analysis above. XPS spectra of Cu $2p_{3/2}$ were shown in Fig. 4.4b where one peak with high intensity can be observed at 938.9 eV for the 10-CuO/CeO_2 nanorods and 939.0 eV for the 10-Cu-O-Ce sample. This peak corresponded to Cu^{2+} [27]. A shoulder peak can be found at low energy for both samples (at 936.0 eV for 10-CuO/CeO_2 and at 934.3 eV for 10-Cu-O-Ce). The shoulder peak referred to the presence of Cu^{+} which was considered as a strong interaction of Cu types with CeO_2 [27,28]. As the intensity of shoulder peak in 10-CuO/CeO_2 was higher than that in 10-Cu-O-Ce, it suggested that 10-CuO/CeO_2 had larger amount of highly-interacted Cu species with CeO_2. Two peaks for O 1s were found in Fig. 4.4c. First peak found at 536.1 eV for 10-CuO/CeO_2 and 535.1 eV for 10-Cu-O-Ce was attributed to the presence of adsorbed oxygen at the surface and this adsorbed oxygen was easy to be reduced at low-temperature [29,30]. Yang et al. [29] reported that the presence of strong shoulder peak

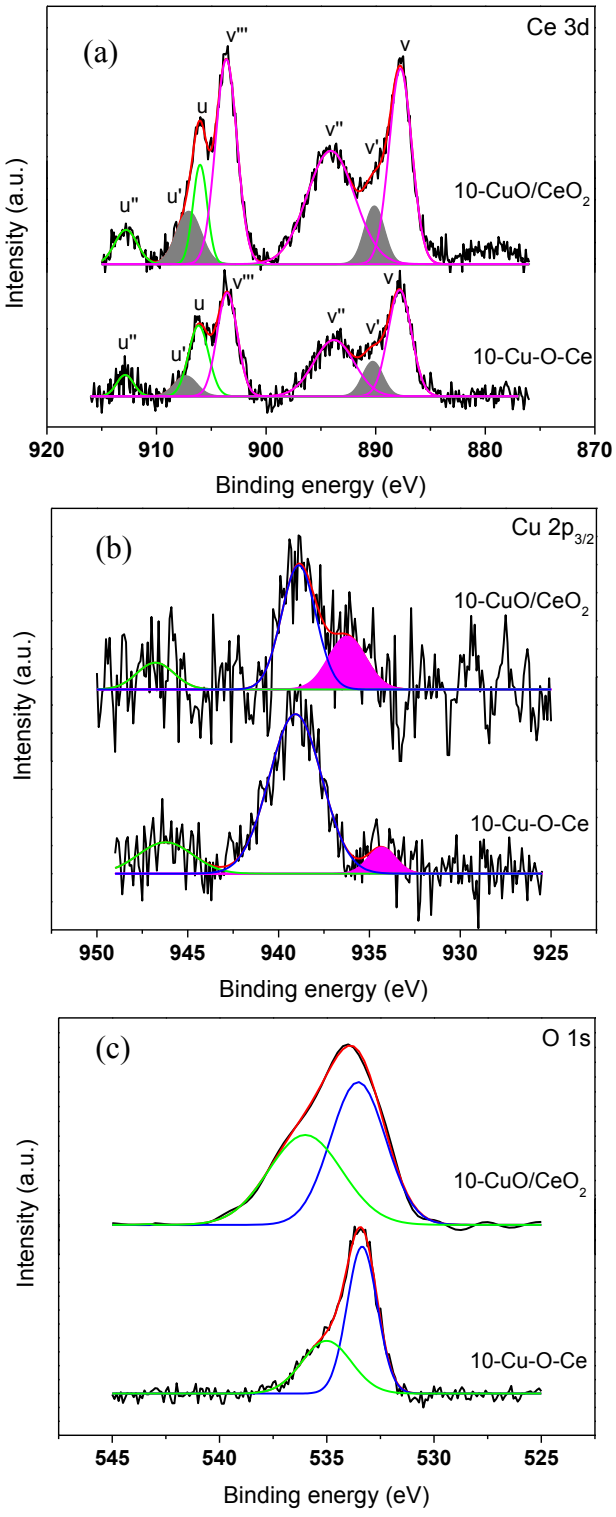

Figure 4.4. XPS spectra of 10-Cu-O-Ce solid solution and 10-CuO/CeO_2 nanorods samples.

of $Cu_{0.1}Ce_{0.9}O_2$ suggested an increase in oxygen storage capacity. By comparing the intensity, it could be easily concluded that the 10-CuO/CeO_2 sample could adsorb more oxygen from the environment which eventually helped in increasing the catalytic efficiency. Another peak, which was found at 533.4 eV for both samples, corresponds to lattice oxygen of metal oxides. Charging effect during experiment caused the peak shift compared to other literatures [26-30].

4.3.4. TEM analysis

TEM analysis was performed to investigate the microstructural characteristics of the catalysts. Fig. 4.5 showed the TEM and HRTEM images of the 10-Cu-O-Ce (Fig. 4.5a

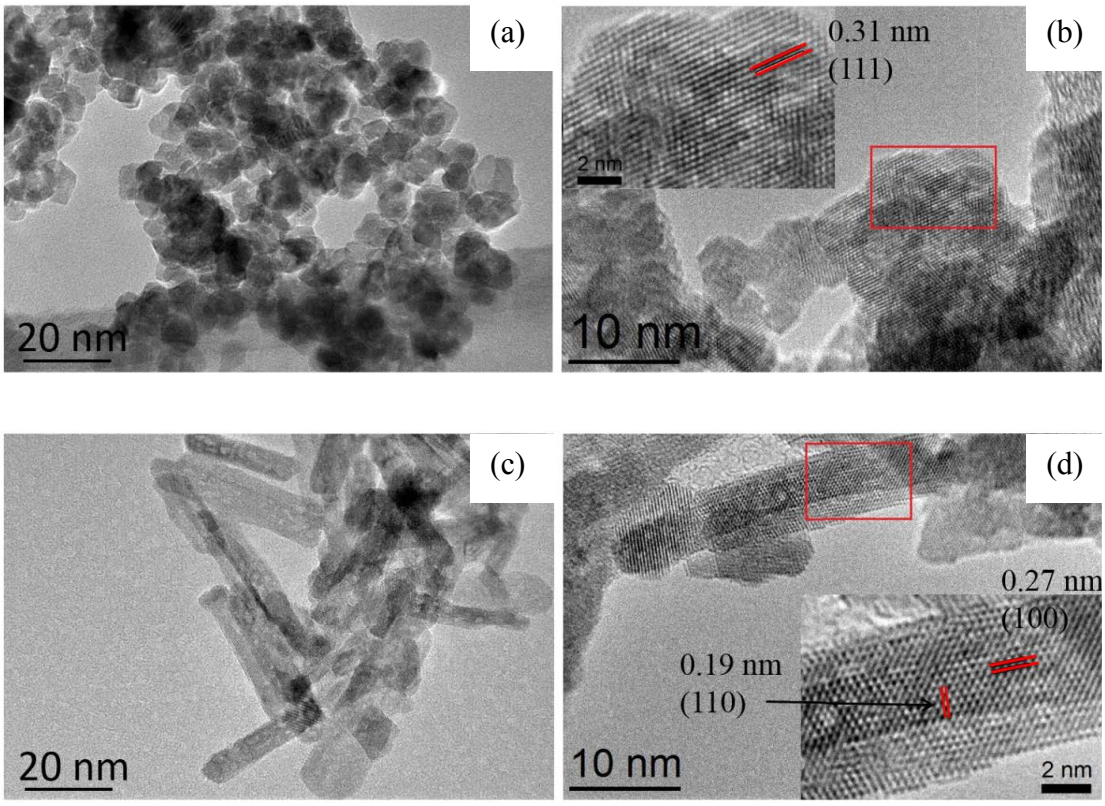

Figure 4.5. (a) TEM and (b) HRTEM images of 10-Cu-O-Ce, and (c) TEM and (d) HRTEM images of 10-CuO/CeO_2.

and 4.5b) and 10-CuO/CeO_2 (Fig. 4.5c and 4.5d) samples. The TEM image of the 10-Cu-O-Ce sample, shown in Fig. 4.5a, revealed an average particle size smaller than 10 nm. In the inset of Fig. 4.5b, HRTEM image analysis of red rectangular portion indicated that the nanoparticle exposed lattice fringes with a d-spacing at 0.31 nm, which was close to CeO_2 (111) planes. Typical TEM image of the 10-CuO/CeO_2 nanorods was shown in Fig. 4.5c, confirming the thermal stability of CeO_2 nanorods after Cu addition and calcination at 400 ^oC for 5 hrs. These nanorods were 5-10 nm in width and 50-100 nm in length. The HRTEM image in Fig. 4.5d showed relatively large number of rough surfaces and defects on CeO_2 nanorods, which is consistent with the previous Raman and XRD analysis. The inset in Fig. 4.5d demonstrated that CeO_2 nanorods exposed both (100) and (110) planes.

4.3.5. H_2-TPR

H_2-TPR was conducted to determine the reduction temperature and amount of H_2 consumption at each peak. Fig. 4.6 showed the H_2-TPR profiles of the Cu-O-Ce solid solutions and CuO/CeO_2 nanorods samples, respectively. After fitting the peak profiles, it appeared the presence of two reduction peaks for 2-8 wt% Cu addition in the Cu-O-Ce solid solution samples shown in Fig. 4.6a. Whereas, there were three reduction peaks identified for the 10 and 12 wt% Cu-O-Ce solid solution samples. In literature of CuO-CeO_2, the first peak was designated as α peak, which corresponded to the reduction of solid solutions or highly interacted CuO with CeO_2 [31]. The second peak was assigned as β peak, which related to the reduction of highly dispersed CuO particles on CeO_2 [32]. The third peak, γ peak, was attributed to the reduction of bulk CuO [33]. However, the specific reduction temperature for these three assignments (α, β, and γ) was quite diverse in literature. For example, Shiau et al. [34] and Wang et al. [35] reported three H_2

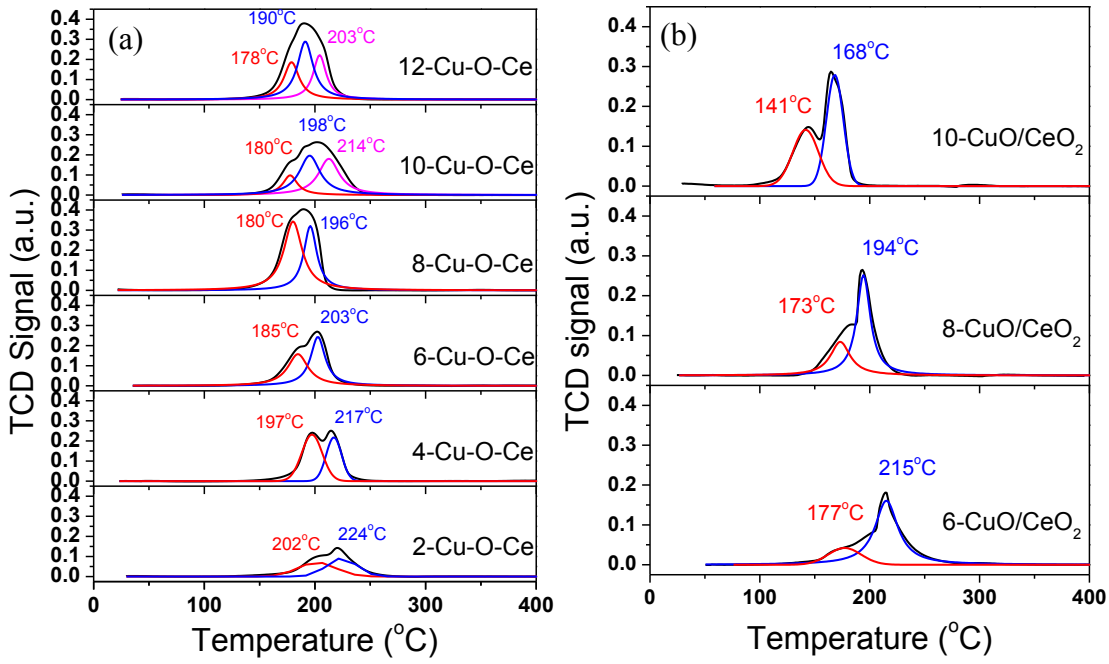

Figure 4.6. H_2-TPR profiles of (a) Cu-O-Ce solid solutions and (b) CuO/CeO_2 nanorods.

reduction peaks at over 200 °C. Luo et al. [36] stated that two reduction peaks for 10 wt% CuO loading were found near 160 and 200 °C. In our samples, for the 2-Cu-O-Ce sample, both α and β peaks were found over 200 °C and for the rest of the Cu-O-Ce samples, α peak were shown at less than 200 °C. Both α and β peaks progressively shifted to lower temperature as the Cu content increased, revealing the promoting synergistic effect of CuO addition on the low temperature reducibility in the Cu-O-Ce samples. A similar peak shifting could also be seen for the CuO/CeO_2 nanorods as shown in Fig. 4.6b. For the 10-CuO/CeO_2 sample, both α and β peaks shifted to the lowest temperature in all nine samples in this study probably because this sample had the highest lattice expansion with Ce^{3+} along with a large amount of oxygen vacancies and lattice distortion in CeO_2 as discussed in XRD and Raman/XPS analysis. The CuO/CeO_2 nanorods samples did not

show γ peak due to absence of bulk CuO, which was in agreement with XRD analysis (Fig. 4.1c).

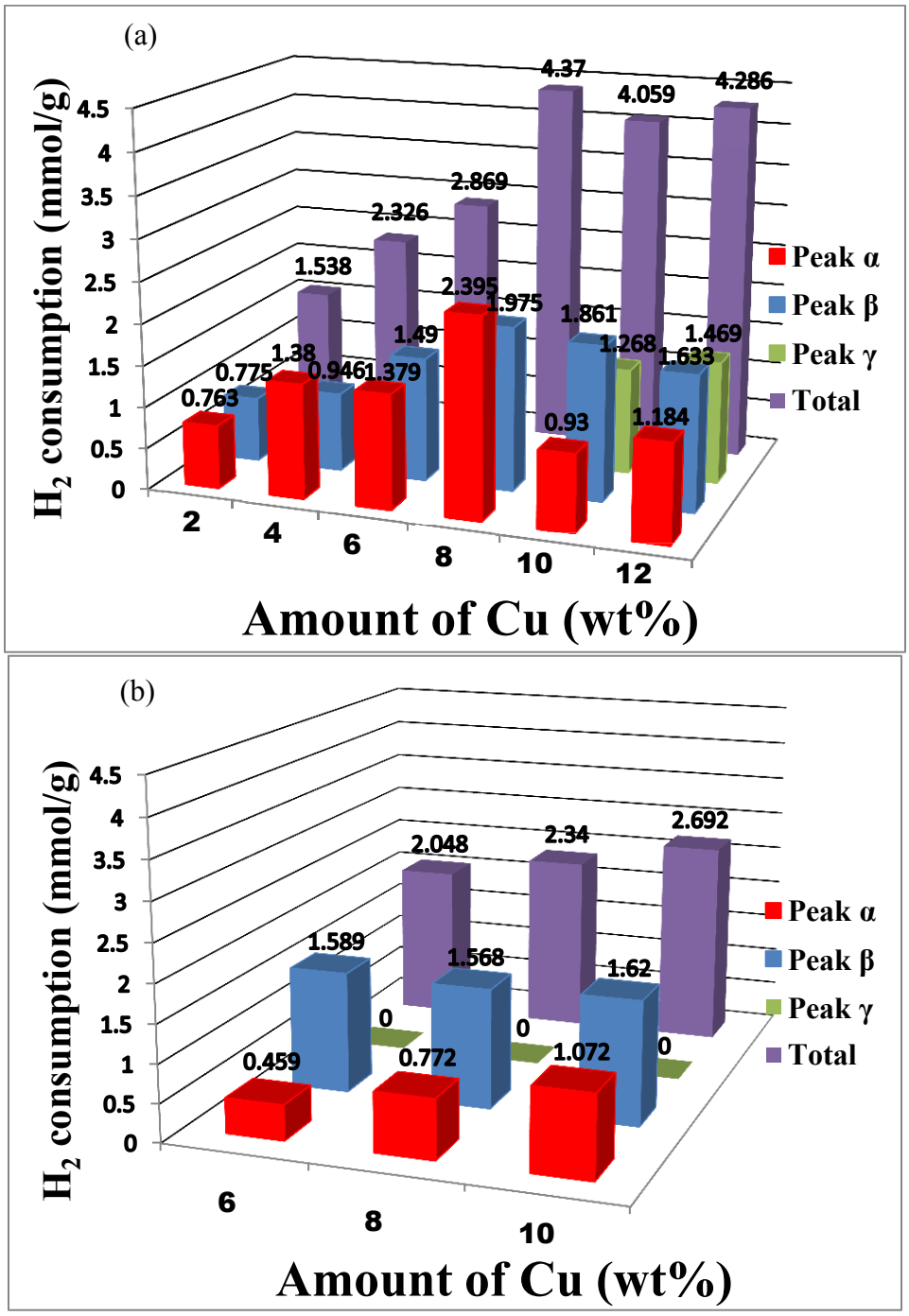

Figure 4.7. H_2 consumption at each peak of (a) Cu-O-Ce solid solutions and (b) CuO/CeO_2 nanorods.

Fig. 4.7 showed the H_2 consumption at each TPR peak and total H_2 consumption ($\alpha+\beta+\gamma$) for the Cu-O-Ce and CuO/CeO_2 samples. For the Cu-O-Ce catalysts, H_2 consumption at α peak increased from 2 to 8 wt% Cu addition as shown in Fig. 4.7a. H_2 consumption at α peak (0.930 mmol/g) of the 10-Cu-O-Ce sample was lower than that (2.395 mmol/g) of the 8-Cu-O-Ce sample, and this happened due to the presence of more CuO particles on CeO_2 surface. CuO particles could cover up CeO_2 surface where Cu-O-Ce solid solution was formed. The proof of having higher amount of bulk CuO in the 10-Cu-O-Ce and 12-Cu-O-Ce samples could be seen from both XRD (Fig. 4.1b) and the presence of γ peak in H_2-TPR (Fig. 4.6a). For the CuO/CeO_2 catalysts, the H_2 consumption at β peak for all three samples was very close as shown in Fig. 4.7b. H_2 consumption at α peak increased with increasing the Cu addition possibly due to the increment of oxygen vacancies in CeO_2 lattice as discussed in Raman analysis. The theoretical H_2 consumptions of 2, 4, 6, 8, 10, and 12 wt% CuO addition in $CuO\text{-}CeO_2$ are 252, 504, 756, 1008, 1260, and 1512 μmol/g, respectively. It could be seen from Fig. 4.7 that the experimental H_2 consumptions for both Cu-O-Ce solid solutions and CuO/CeO_2 nanorods samples were higher (3 to 6 times for Cu-O-Ce and 2 to 3 times for CuO/CeO_2) than the corresponding theoretical H_2 consumptions. Sun et al. [37] also reported that 1 wt% and 5 wt% CuO impregnated CeO_2 consumed ~10 times and 2.5 times respectively higher H_2 consumption than the theoretical values. Thus, it could be concluded that CeO_2 support contributed significantly to the total H_2 consumption. It has been reported that the interfacial structure plays a role in easy reduction of $CuO\text{-}CeO_2$ due to a synergistic effect [33,38]. Our results indicated that the interfacial structure formed in CeO_2 nanorods supported CuO (CuO/CeO_2) was more favorable for reduction compared to the formation

of Cu-O-Ce solid solution. The detailed interfacial structure and composition study of CuO/CeO_2 is ongoing.

4.3.6. TPR-TPO cycling

Redox thermal cycling treatments are essential steps for the preparation and long-term applications of supported high surface area catalysts. TPR-TPO thermal cycling experiments were conducted on the 10-Cu-O-Ce solid solution and 10-CuO/CeO_2 nanorods samples to investigate the correlation of redox treatments with the change in their structure and catalytic activity. Fig. 4.8 showed the TPR profiles of the pristine sample and the sample after each TPR-TPO cycle, and the XRD patterns and Raman spectra of as-synthesized and after each TPR-TPO cycle for the 10-Cu-O-Ce sample. In the TPR profiles (Fig. 4.8a), both α and β peaks shifted to the lower temperatures after each TPR-TPO cycle with respect to the previous TPR profile. In Fig. 4.8b, the XRD patterns showed that the characteristic CeO_2 (111) peak shifted to lower diffraction angle after each TPR-TPO cycle and thus, the lattice parameter of CeO_2 increased after each cycle due to the increment of concentration of Ce^{3+} and oxygen vacancies in the sample. It was expected that the sample would be fully re-oxidized during the TPO treatment at 350 ^{o}C [39]. However, it appeared that the re-oxidation did not affect the lattice parameter of CeO_2, confirmed from the data shown in Fig. 4.10. Table 4.2 displayed the change in crystallite size and lattice parameter determined by CeO_2 (111) XRD diffraction peak and OSC of the10-Cu-O-Ce sample with the redox treatments. The OSC of the 10-Cu-O-Ce sample increased from 1.98 to 2.27 μmol O_2/g after 3 TPR-TPO

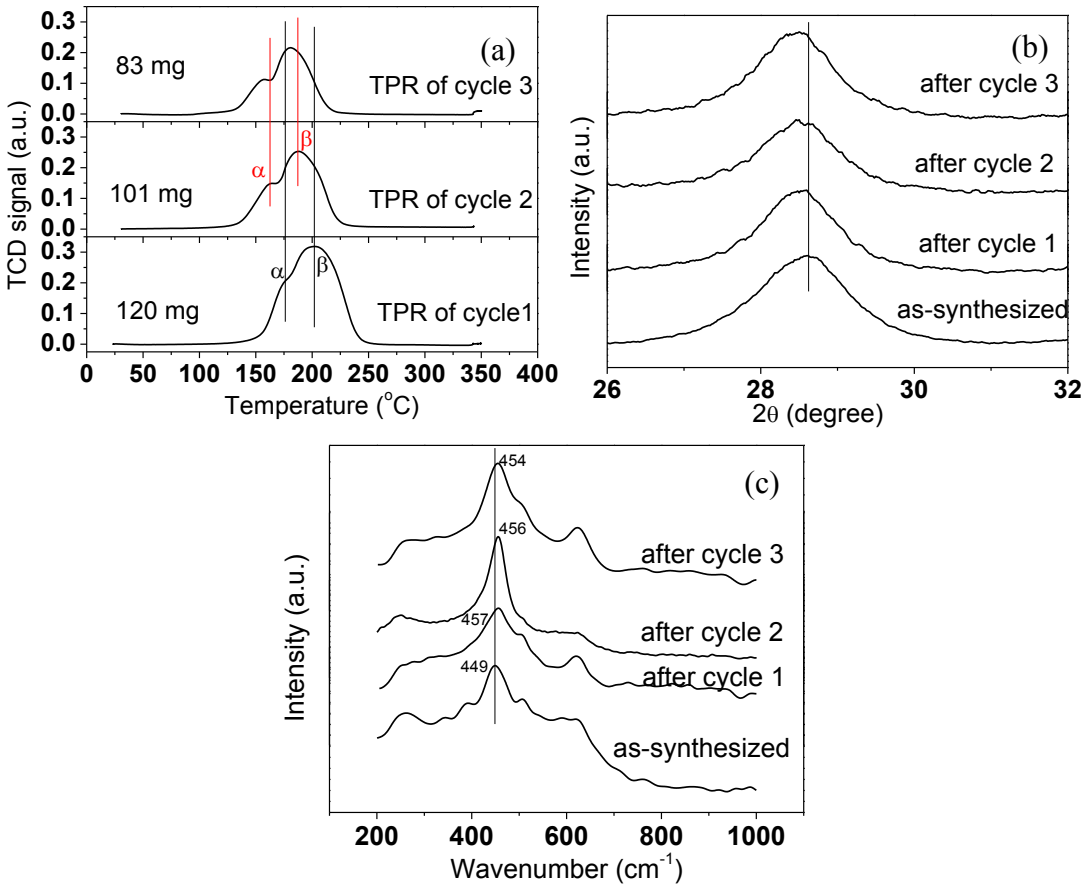

Figure 4.8. (a) H_2-TPR profiles, (b) XRD patterns, and (c) Raman spectra after each TPR-TPO cycling for the sample of 10-Cu-O-Ce.

cycles as shown in Table 4.2. Fig. 4.8c showed the Raman spectra of the Cu-O-Ce sample after each cycle of TPR-TPO treatment, and the CeO_2 F_{2g} peak of the 10-Cu-O-Ce sample shifted to the right after each cycle possibly due to a combination effect of lattice distortion and crystallite size as mentioned earlier. A similar study was conducted and shown in Fig. 4.9 for the 10-CuO/CeO_2 nanorods sample. The TPR profiles in Fig. 4.9a displayed that α peaks which correspond to the solid solution copper species, remained at the same position at each cycle. No change in peak position was observed which was consistent with the XRD data. The CeO_2 (111) peaks in XRD presented in

Fig. 4.9b, did not change their position and thus, the lattice parameter of CeO_2 tabulated in Table 4.3 did not change as well. Similarly, no change in the position of CeO_2 (111) peak was found in Fig. 4.10 after TPR and after TPR-TPO with compared to as-synthesized sample. This explained that the concentration of Ce^{3+} and oxygen vacancies in the 10-CuO/CeO_2 sample may have already reached its maximum during the synthesis. On the other hand, the crystallite size increased with number of redox cycles, and this was the reason for shifting the Raman peak of CeO_2 to the right as shown in Fig. 4.9c. Table 4.3 showed that the OSC of the 10-CuO/CeO_2 sample remained constant (2.38 $\mu molO_2/g$) before and after redox treatments.

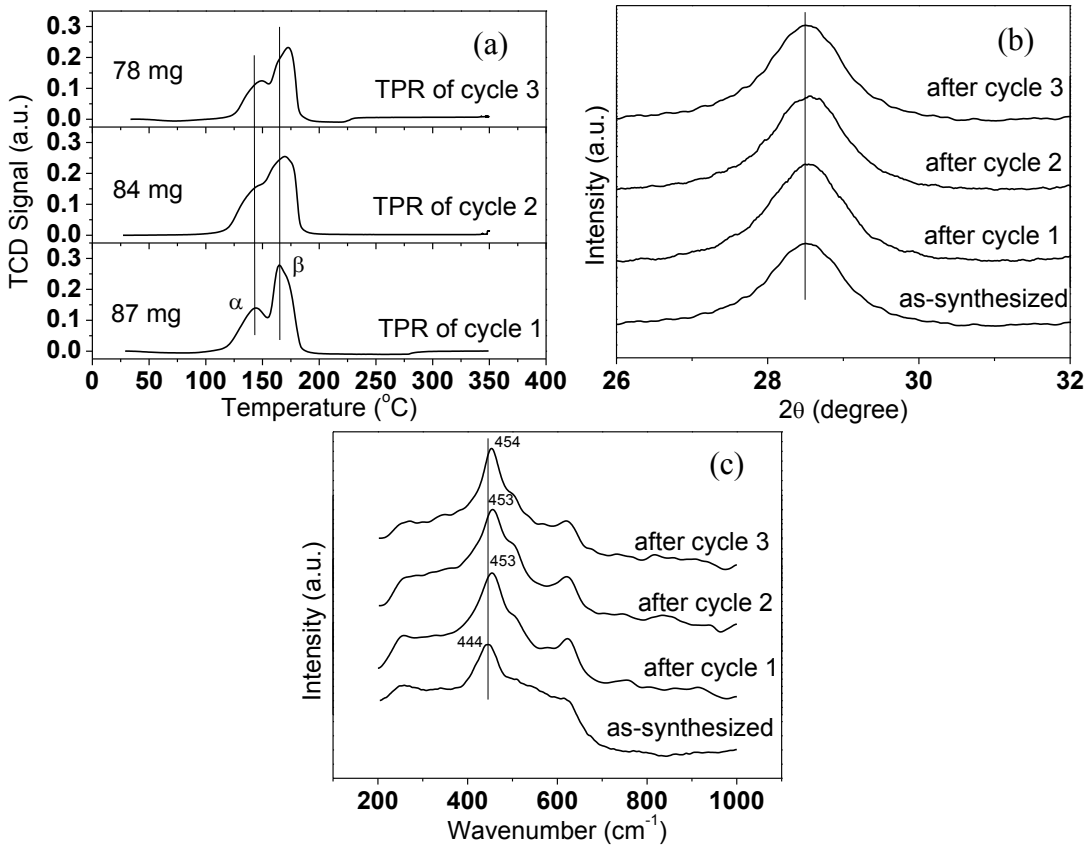

Figure 4.9. (a) H_2-TPR profiles, (b) XRD patterns, and (c) Raman spectra after each TPR-TPO cycling for the sample of 10-CuO/CeO_2.

Table 4.2. Crystallite size and lattice parameters of 10-Cu-O-Ce after each TPR-TPO cycling.

TPR-TPO cycle number	Crystallite size (nm)	Lattice parameters (Å)	OSC (μmol O_2/g)
0	5.2	5.4548 (±0.0002)	1.98
1	6.5	5.4787 (±0.0004)	-
2	6.8	5.4807 (±0.0003)	-
3	6.9	5.4939 (±0.0004)	2.27

Table 4.3. Crystallite size and lattice parameters of 10-CuO/CeO_2 after each TPR-TPO cycling.

TPR-TPO cycle number	Crystallite size (nm)	Lattice parameters (Å)	OSC (μmolO_2/g)
0	5.4	5.4747 (±0.0005)	2.38
1	6.0	5.4739 (±0.0002)	-
2	6.3	5.4711 (±0.0003)	-
3	6.4	5.4742 (±0.0003)	2.39

4.3.7. CO-TPD

The CO-TPD profiles of both the 10-Cu-O-Ce and 10-CuO/CeO_2 samples were shown in Fig. 4.11a. In this experiment, CO usually adsorbs on the surface of the catalysts and desorbs away as CO_2 after reacting with surface oxygen. A large difference in the intensity of the CO-TPD curves for the two samples could be observed in Fig. 4.11a. We previously reported that two desorption peaks were seen for CuO/CeO_2 catalyst [26]. The first peak found at around 100 ^oC corresponded to desorption of CO_2 which was the product of reaction between adsorbed CO and CeO_2 surface. The second peak seen at 150-160 ^oC was attributed to desorption of CO_2 produced from the transformation of adsorbed CO into bidentate carbon species at the reactive sites. Two similar peaks (at 105 and 180 ^oC) with much lower intensity were found for the 10-Cu-O-

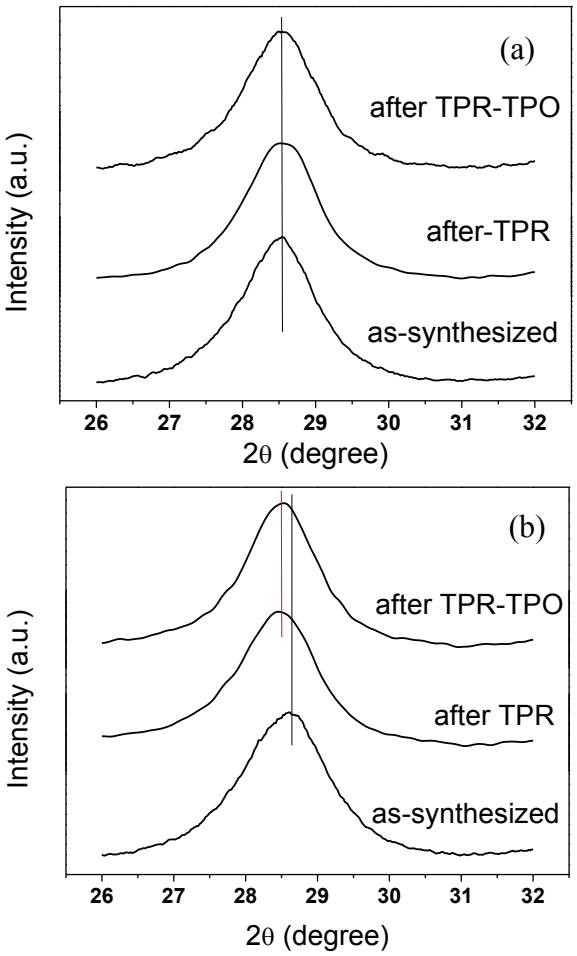

Figure 4.10. XRD patterns of as-synthesized, after first TPR and after first TPR-TPO cycle of both (a) 10-CuO/CeO_2 and (b) 10-Cu-O-Ce.

Ce sample. This data suggested that the 10-CuO/CeO_2 sample provided higher amounts of lattice oxygen compared to the 10-Cu-O-Ce sample. Fig. 4.11b showed the rate of desorption (ROD) of CO_2 for both 10-Cu-O-Ce and 10-CuO/CeO_2 samples. The rate of desorption (ROD) for the 10-CuO/CeO_2 sample increased with increasing temperature and the maximum ROD (~ 0.0014 mol cm^{-2} s^{-1}) was achieved at 325 ^{o}C. After reaching the maximum, the ROD decreased rapidly because most of the adsorbed CO already desorbed away from the surface. A similar trend of the ROD can be seen for the10-Cu-O-

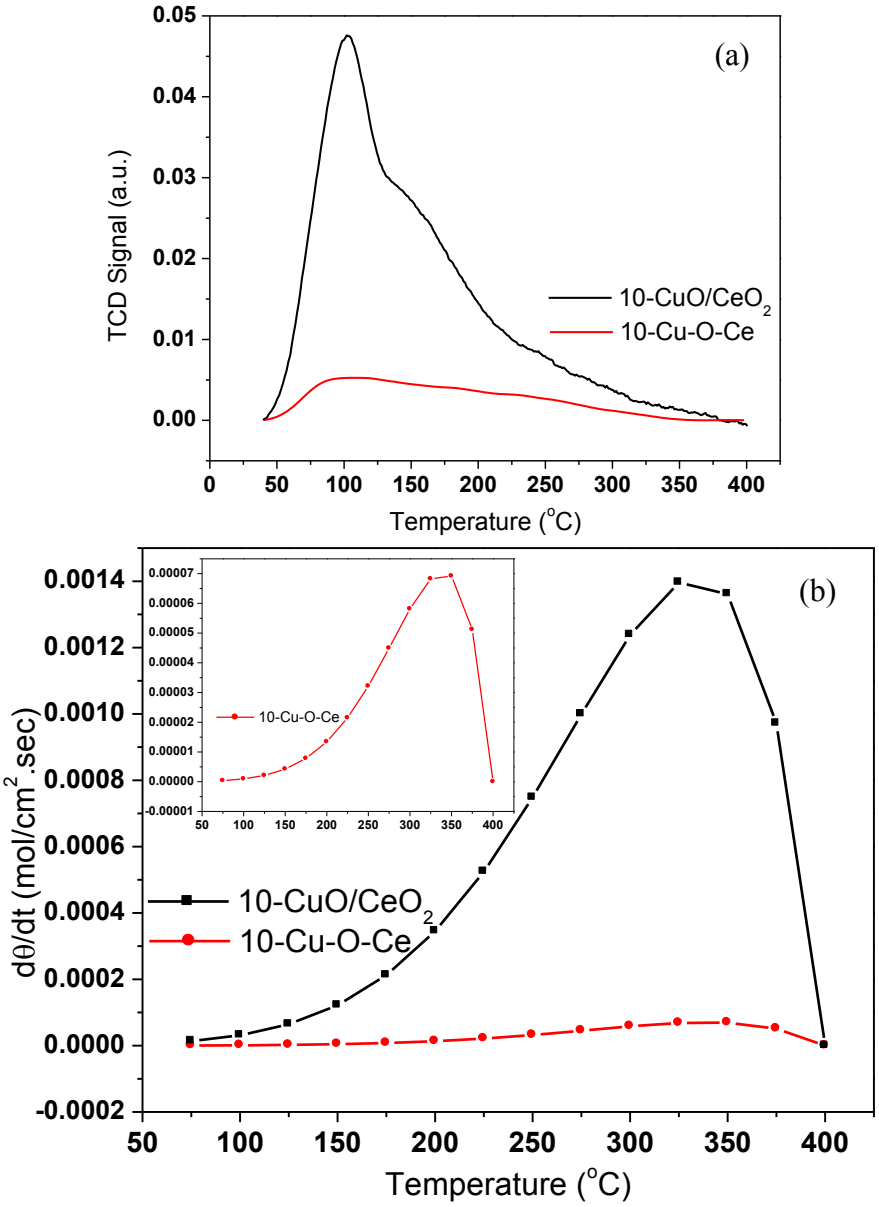

Figure 4.11. (a) CO-TPD and (b) rate of desorption of 10-Cu-O-Ce solid solution and 10-CuO/CeO_2 nanorods samples. Rate of desorption of 10-Cu-O-Ce in magnified scale shown in the inset of (b).

Ce sample as well in the inset of Fig. 4.11b. However, the maximum ROD (~ 6.9×10^{-5} mol cm^{-2} s^{-1}) for the 10-Cu-O-Ce sample was found at 350 °C. The maximum ROD for the 10-CuO/CeO_2 sample was almost 20 times larger than that for the 10-Cu-O-Ce

sample. This observation advised that more CO was absorbed on the surface in the 10-CuO/CeO_2 sample during the flow of 5%CO-95%He gas, which resulted in the high rate of CO_2 desorption. In other words, more CO adsorption sites were available on the surface of the 10-CuO/CeO_2 sample. Also, the 10-CuO/CeO_2 sample had a lower desorption energy (29.3 kJ/mol) in comparison with the 10-Cu-O-Ce sample (39.5 kJ/mol) calculated from the equation (4.2).

4.3.8. CO oxidation

Fig. 4.12 compared the light-off curves over the Cu-O-Ce solid solutions and CuO/CeO_2 nanorods samples toward CO oxidation. It showed that the Cu-O-Ce catalysts converted less than 90% CO up to 350 ^oC with the addition of 2-12 wt% Cu. It was clear that the 10-CuO/CeO_2 nanorods sample exhibited the highest activity with 100% CO conversion to CO_2 at around 220 ^oC. Table 4.4 displayed the T_{50} temperature (the temperature at which the CO conversion reaches 50% is taken as a measurement of catalytic activity), maximum CO conversion percentage (up to 350 ^oC), and the T_{max} temperature (the temperature at which the maximum CO conversion is achieved). The Cu-O-Ce samples achieved maximum ~88% CO conversion in the range of temperature from 220 to 270 ^oC. Comparing the six Cu-O-Ce catalysts studied, T_{50} decreased with increasing Cu addition up to 6 wt%, and this enhancement of the catalytic activity could be attributed to the increased oxygen vacancy concentration due to the Cu ions substitutions of Ce ions in CeO_2 lattice as discussed earlier. The addition of higher amounts of Cu (> 6 wt%) into CeO_2 led to the formation of CuO as shown in Fig. 4.1b. It appeared that T_{50} increased for the 8-Cu-O-Ce, 10-Cu-O-Ce, and 12-Cu-O-Ce samples.

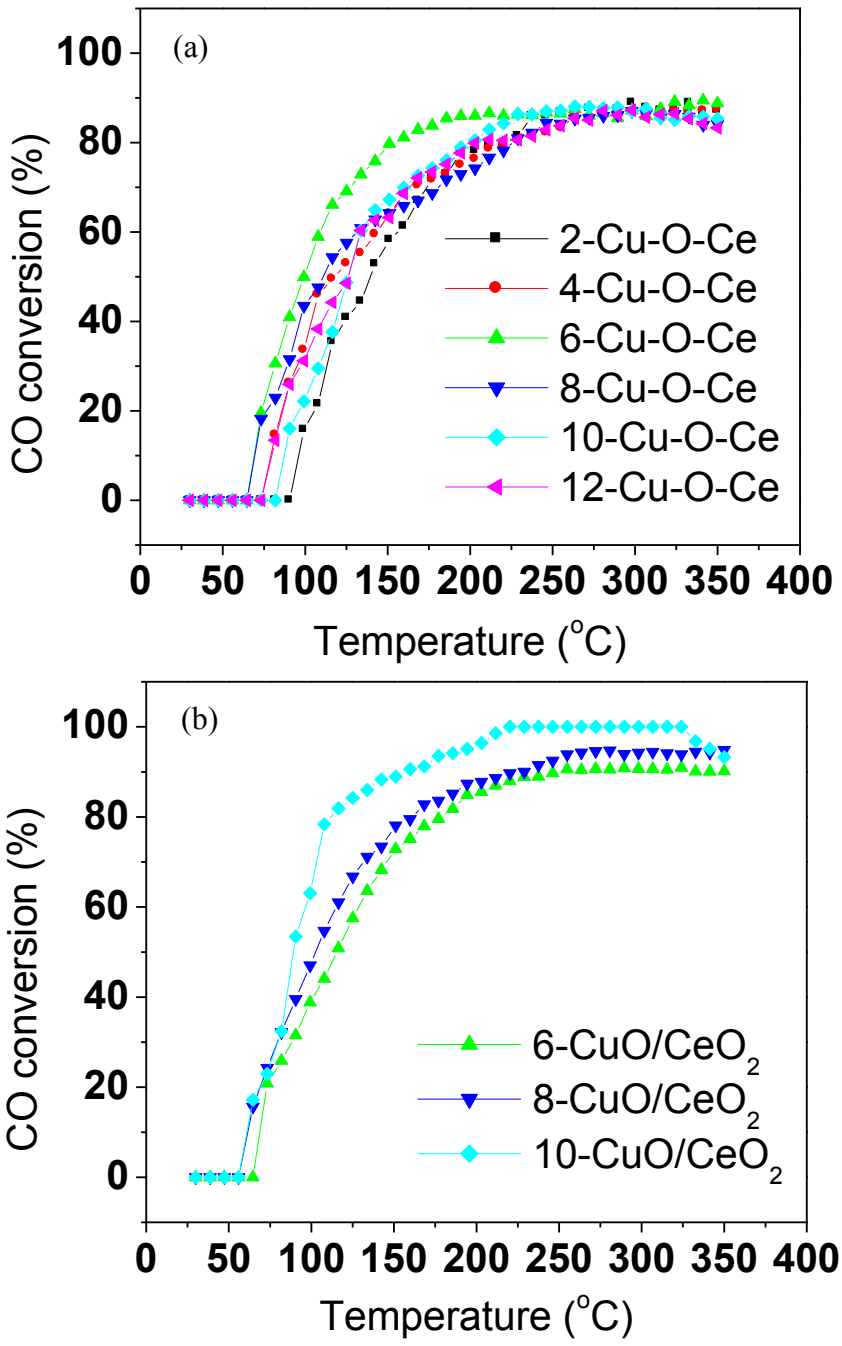

Figure 4.12. CO oxidation curves of (a) Cu-O-Ce and (b) CuO/CeO_2.

Probably the presence of bulk CuO with large particle size covered up the active surface sites on the Cu-O-Ce solid solution particles, which was not in favor the access of the reactant to the active sites. On the other hand, the $6\text{-}CuO/CeO_2$ and $8\text{-}CuO/CeO_2$

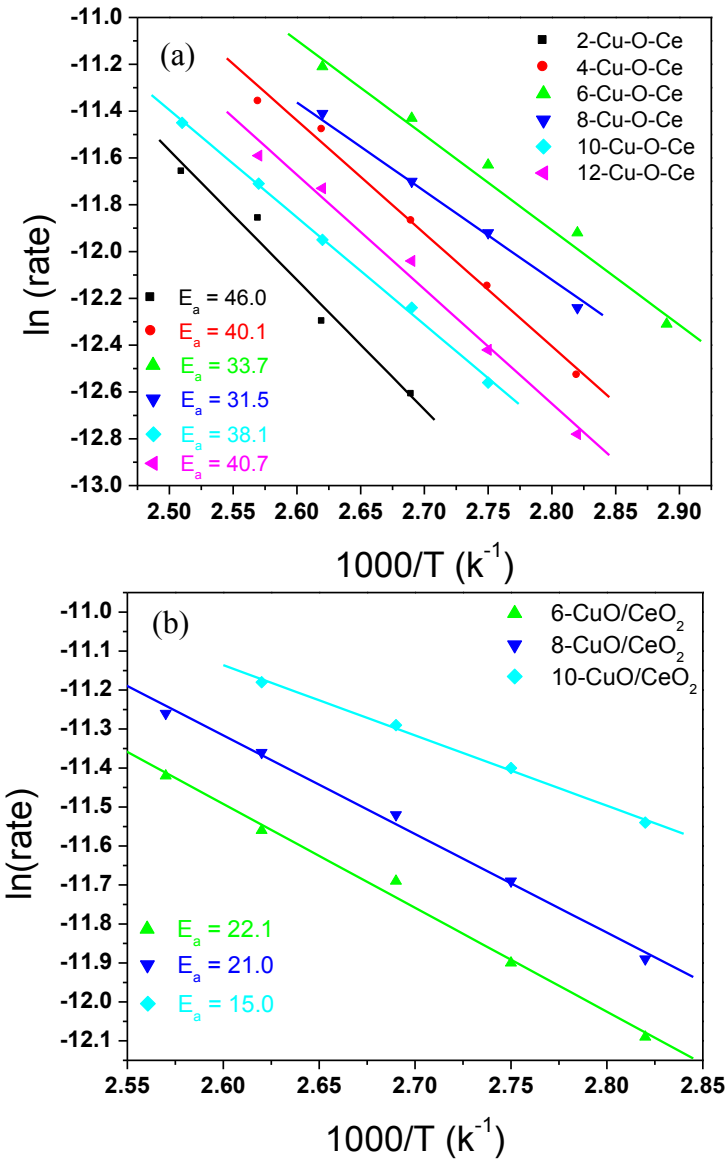

Figure 4.13. Ln(rate) vs. 1000/T curves for calculating activation energies of (a) Cu-O-Ce and (b) CuO/CeO_2.

nanorods converted 90 and 94% CO to CO_2 at 254 ^oC, respectively. T_{50} of CuO/CeO_2 nanorods samples gradually decreased with increasing Cu addition from 6 to10 wt%. As mentioned earlier, no bulk CuO was found in the CuO/CeO_2 nanorods samples from XRD analysis shown in Fig. 4.1c. This result suggested the addition Cu in CeO_2 lattice or

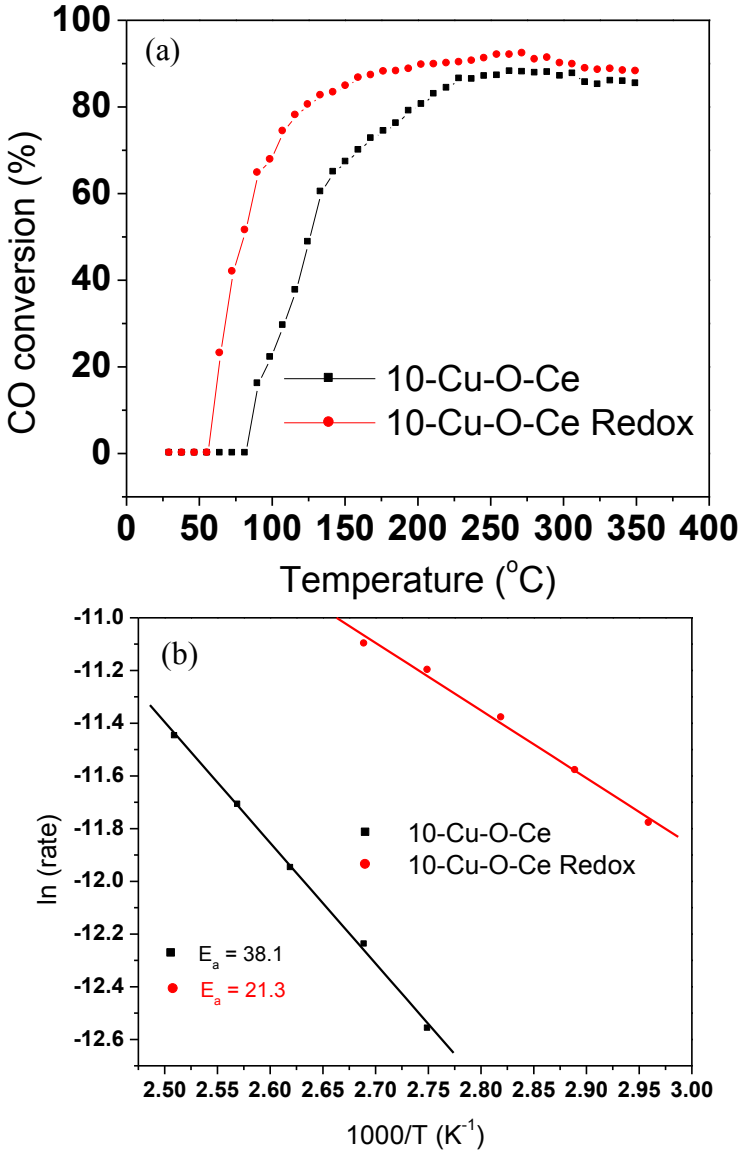

Figure 4.14. (a) CO oxidation and (b) ln(rate) vs. 1000/T curves of 10-Cu-O-Ce before and after redox treatment.

well-dispersed strongly-interacted small CuO favoring the low-temperature CO conversion. Zheng et al. [40] reported that T_{50} and T_{100} for CuO/CeO_2 catalysts prepared by sol-gel method were 138 and 230 °C, respectively. Zheng et al. [40] and Liu et al. [41] remarked that finely dispersed CuO on CeO_2 was primarily responsible for low-temperature CO oxidation and bulk CuO had no significant contributions to this

conversion. Fig. 4.13 showed activation energy of various catalysts and it can be seen that 10-CuO/CeO_2 which achieved an enhanced catalytic activity had the lowest activation energy (15.0 KJ/mol) among all the prepared catalysts. Fig. 4.14a compared the light-off curves of 10-Cu-O-Ce solid solutions before and after the redox treatment. It was clear that the 10-Cu-O-Ce sample after the redox treatment displayed higher catalytic activity and lower activation energy (21.3 KJ/mol shown in Fig. 4.14b), indicating a reduction activation of the sample. The T_{50} of 10-Cu-O-Ce-Redox was 82 ^oC, and this catalyst could convert maximum 92% CO at 272 ^oC, as tabulated in Table 4.5.

Table 4.4. The catalytic activity toward CO oxidation over Cu-O-Ce and CuO/CeO_2.

Cu contents (%)	Cu-O-Ce solid solution			CuO/CeO_2 nanorods		
	T_{50} (^oC)	Max conversion (%)	T_{max} (^oC)	T_{50} (^oC)	Max conversion (%)	T_{max} (^oC)
2	140	88	263	-	-	-
4	115	88	263	-	-	-
6	100	88	220	115	90	254
8	109	87	246	102	94	254
10	124	87	227	88	100	220
12	124	86	263	-	-	-

Table 4.5. The catalytic activity toward CO oxidation over 10-Cu-O-Ce before and after redox treatment, and 10-CuO/CeO_2.

Sample	T_{50} (^oC)	Max conversion (%)	T_{max} (^oC)
10-Cu-O-Ce	124	87	227
10-Cu-O-Ce-Redox	82	92	272
10-CuO/CeO_2	88	100	220

4.4. Conclusion

Cu-O-Ce solid solutions (2~12 wt%) and CuO/CeO_2 nanorods (6~10 wt%) samples were successfully prepared using thermal decomposition method and hydrothermal methods. It could be concluded that the amount of Cu incorporation into CeO_2 lattice depended on the preparation methods of the catalysts and CeO_2 structure (shape and surface defects etc.). The different distribution and interactions of copper species with CeO_2 in these samples led to varied hydrogen consumption behaviors (temperature and amount). In the CuO/CeO_2 nanorods samples, two reduction TPR profiles were observed for the compositions from 6 wt% to 10 wt% CuO with a continuous decrease in the reduction temperature. While for the Cu-O-Ce samples, a transition from two (2~8 wt% CuO) to three (10~12 wt% CuO) reduction profiles was observed, which was explained by the formation of bulk CuO phase due to the solid solution limitation of CuO in CeO_2. The TPR-TPO thermal cycling treatments suggested an increase of oxygen vacancy concentration and improved low temperature reducibility over the 10-Cu-O-Ce samples after each cycle, which was further supported by the CO oxidation analysis. H_2 pulse chemisorption analysis showed that the OSC of the 10-Cu-O-Ce sample increased after redox treatments and 10-CuO/CeO_2 had the same OSC value before and after redox treatments.

4.5. References

1. Mock, S. A.; Sharp, S. E.; Stoner, T. R.; Radetic, M. J.; Zell, E. T.; Wang, R. CeO_2 nanorods-supported transition metal catalysts for CO oxidation. *J. Colloid Interface Sci*., **2016**, 466, 261-267.

2. Zhang, S. M.; Huang, W. P.; Qiu, X. H.; Li, B. Q.; Zheng, X. C.; Wu, S. H. Comparative study on catalytic properties for low-temperature CO oxidation of Cu/CeO_2 and CuO/CeO_2 prepared via solvated metal atom impregnation and conventional impregnation. *Catal. Lett*., **2002**, 80, 41-46.

3. Yao, S. Y.; Xu, W. Q.; Johnston-Peck, A. C.; Zhao, F. Z.; Liu, Z. Y.; Luo, S.; Senanayake, S. D.; Martinez-Arias, A.; Liu, W. J.; Rodriguez, J. A. Morphological effects of the nanostructured ceria support on the activity and stability of CuO/CeO_2 catalysts for the water gas shift reaction. *Phys. Chem. Chem. Phys*., **2014**, 16, 17183-17195.

4. Zhuan, H. D.; Bai, S. F.; Liu, X. M.; Yan, Z. F. Structure and performance of Cu/ZrO_2 catalyst for the synthesis of methanol from CO_2 hydrogenation. *J. Fuel Chem. Technol*., **2010**, 38, 462-467.

5. Hu, C.; Zhu, Q.; Jiang, Z.; Zhang, Y.; Wang, Y. Preparation and formation mechanism of mesoporous $CuO–CeO_2$ mixed oxides with excellent catalytic performance for removal of VOCs. *Microporous Mesoporous Mater*., **2008**, 113, 427-434.

6. Flytzani-Stephanopoulos, M.; Zhu, T.; Li, Y. Ceria-based catalysts for the recovery of elemental sulfur from SO_2-laden gas streams. *Catal. Today*, **2000**, 62, 145–158.

7. Zabilsky, M.; Djinovic, P.; Tchernychova, E.; Tkachenko, O. P.; Kustov, L. M.; Pintar, A. Nanoshaped CuO/CeO_2 materials: Effect of the exposed ceria surfaces on catalytic activity in N_2O decomposition reaction. *ACS Catal*., **2015**, 5, 5357−5365

8. Avgouropoulos, G.; Ioannides, T.; Matralis, H. Influence of the preparation method on the performance of CuO-CeO_2 catalysts for the selective oxidation of CO. *Appl. Catal. B: Environ*., **2005**, 56, 87-93.

9. Zhou, K.; Xu, R.; Sun, X.; Chen, H.; Tian, Q.; Shen, D.; Li, Y. Favorable synergistic effects between CuO and the reactive planes of ceria nanorods. *Catal. Lett*., **2005**, 101, 169–173

10. Liu, L.; Yao, Z.; Deng, Y.; Gao, F.; Liu, B.; Dong, L. Morphology and crystal-place effects of nanoscale ceria on the activity of CuO/CeO_2 for NO reduction by CO. *ChemCatChem*, **2011**, 3, 978–989.

11. Zheng, X.; Zhang, X.; Wang, X.; Wang, S.; Wu, S. Preparation and characterization of CuO/CeO_2 catalysts and their applications in low-temperature CO oxidation. *Appl. Catal. A: Gen*., **2005**, 295, 142–149.

12. Avgouropoulos, G.; Ioannides, T. Effect of synthesis parameters on catalytic properties of CuO-CeO_2. *Appl. Catal. B: Environ*., **2006**, 67, 1–11.

13. Xu, D.; Cheng, F.; Lu, Q.; Dai, P. Microwave enhanced catalytic degradation of methyl orange in aqueous solution over CuO/CeO_2 catalyst in the absence and presence of H_2O_2. *Ind. Eng. Chem. Res.*, **2014**, 53, 2625–2632.

14. Xu, J. F.; Ji, W.; Shen, Z. X.; Tang, S. H. Preparation and characterization of CuO nanocrystals. *J. Solid State Chem*., **1999**, 147, 516-519.

15. Yao, W. T.; Yu, S. H.; Zhou, Y.; Jiang, J.; Wu, Q. S.; Zhang, L.; Jiang, J. Formation of uniform CuO nanorods by spontaneous aggregation: Selective synthesis of CuO, Cu_2O and Cu nanoparticles by a solid-liquid phase arc discharge process. *J. Phys. Chem. B*, **2005**, 109, 14011-14016.

16. Shan, W.; Shen, W.; Li, C. Structural characteristics and redox behaviors of $Ce_{1-x}Cu_xO_y$ solid solutions. *Chem. Mater*., **2003**, 15, 4761-4767.

17. Sun, S.; Zhao, X.; Lu, H.; Zhang, Z.; Wei, J.; Yang, Y. Unusual properties of nanostructured $Ce_{1-x}Co_xO_{2-y}$, $Ce_{1-x}Ni_xO_{2-y}$ and $Ce_{1-(x+y)}Co_xNi_yO_{2-z}$: structural studies and catalytic activity. *CrystEngComm*., **2013**, 15, 1370-1376.

18. Shan, W.; Feng, Z.; Li, Z.; Zhang, J.; Shen, W.; Li, C. Oxidative steam reforming of methanol on $Ce_{0.9}Cu_{0.1}O_Y$ catalysts prepared by deposition-precipitation, coprecipitation, and complexation-combustion method. *J. Catal*., **2004**, 228, 206-217.

19. Wu, Z.; Li, M.; Howe, J.; Meyer III, H. M.; Overbury, S. H. Probing defect sites on CeO_2 nanocrystals with well-defined surface planes by Raman spectroscopy and O_2 adsorption. *Langmuir*, **2010**, 26, 16595-16606.

20. Zhong, K.; Xue, J.; Mao, Y.; Wang, C.; Zhai, T.; Liu, P.; Xia, X.; Li, H.; Tong, Y. Facile synthesis of CuO nanorods with abundant adsorbed oxygen concomitant with high surface oxidation states for CO oxidation. *RSC. Adv*., **2012**, 2, 11520-11528.

21. Kliche, G.; Popovic, Z. V. Far-infrared spectroscopic investigations on CuO. *Phys. Rev. B*, **1990**, 42, 10060-10066.

22. Li, Z.; Tong, K.; Shi, R.; Shen, Y.; Zhang, Y.; Yao, Z.; Fan, J.; Thwaites, M.; Shao, G. Reactive plasma deposition of high quality single phase CuO thin films suitable for metal oxide solar cells. *J. Alloy Comp.,* **2017**, 695, 3116-3123.

23. Debbichi, L.; Marco de Lucas, M. C.; Pierson, J. F.; Kruger, P. Vibrational properties of CuO and Cu_4O_3 from first-principles calculations, and Raman and infrared spectroscopy. *J. Phys. Chem. C*, **2012**, 116, 10232-10237.

24. Popovic, Z. V.; Dohcevic-Mitrovic, Z.; Cros, A.; Cantarero, A. Raman scattering study of the anharmonic effects in CeO_{2-y} nanocrystals. *J. Phys.: Condens. Matter*, **2007**, 19, 496209 (9pp).

25. Zhang, F.; Chan, S. W.; Spanier, J. E.; Apak, E.; Jin, Q.; Robinson, R. D.; Herman, I. P. Cerium oxide nanoparticles: Size-selective formation and structure analysis. *Appl. Phys. Lett*., **2002**, 80, 127-129.

26. Hossain, S. T.; Almesned, Y.; Zhang, K.; Zell, E. T.; Bernard, D. T.; Balaz, S.; Wang, R. Support structure effect on CO oxidation: A comparative study on SiO_2 nanospheres and CeO_2 nanorods supported CuO_x catalysts. *Appl. Surf. Sci.,* **2018**, 428, 598-608.

27. Shen, W.; Mao, D.; Luo, Z.; Yu, J. CO oxidation on mesoporous SBA-15 supported CuO-CeO_2 catalyst prepared by a surfactant-assisted impregnation method. *RSC. Adv.* **2017**, 7, 27689-27698.

28. Zheng, Y.; Mao, D.; Sun, S.; Fu, G. CO oxidation on CuO/CeO_2 catalyst prepared by solvothermal synthesis: influence of catalyst activation temperature. *J. Nanopart. Res*. **2015**, 17, 471 (1-12).

29. Yang, F.; Wei, J.; Liu, W.; Guo, J.; Yang, Y. Copper doped ceria nanospheres: surface defects promoted catalytic activity and a versatile approach. J. Mater. Chem. A, **2014**, 2, 5662-5667.

30. Li, T.; Xiang, G.; Zhuang, J.; Wang, X. Enhanced catalytic performance of assembled ceria necklace nanowires by Ni doping. Chem. Commun. **2011**, 47, 6060-6062.

31. Jiang, X.; Lu, G.; Zhou, R.; Miao, J.; Yu, C.; Zheng, X. Studies of pore structure, temperature-programmed reduction performance, and micro-structure of CuO/CeO_2 catalysts. *Appl. Surf. Sci*., **2001**, 173, 208–220.

32. Zeng, S.; Zhang, W.; Sliwa, M.; Su, H. Comparative study of CeO_2/CuO and CuO/CeO_2 catalysts on catalytic performance for preferential CO oxidation. *Int. J. Hydrogen Energ*., **2013**, 38, 3597-3605.

33. Zhu, P.; Liu, M.; Zhou, R. Effect of interaction between CuO and CeO_2 on the performance of $CuO\text{-}CeO_2$ catalysis for selective oxidation of CO in H_2 rich streams. *Indian J. Chem*., **2012**, 51, 1529-1537.

34. Shiau, C. Y.; Ma, M. W.; Chuang, C. S. CO oxidation over CeO_2-promoted $Cu/\gamma\text{-}Al_2O_3$ catalyst: Effect of preparation method. *Appl. Catal. A: Gen.,* **2006**, 301, 89-95.

35. Wang, J. B.; Shih, W. H.; Huang, T. J. Study of Sm_2O_3-doped CeO_2/Al_2O_3-supported copper catalyst for CO oxidation. *Appl. Catal. A: Gen.,* **2000**, 203, 191-199.

36. Luo, M. F.; Hou, Z. Y.; Yuan, X. X.; Zheng, X. M. Characterization study of CeO_2 supported Pd catalyst for low-temperature carbon monoxide oxidation. *Catal. Lett*., **1998**, 50, 205-209.

37. Sun, J.; Zhang, L.; Ge, C.; Tang, C.; Dong, L. Comparative study on the catalytic CO oxidation properties of CuO/CeO_2 catalysts prepared by solid state and wet impregnation. *Chin. J. Catal*, **2014**, 35, 1347-1358.

38. Zhu, P.; Li, J.; Huang, Q.; Yan, S.; Liu, M.; Zhou, R. High performance $CuO\text{-}CeO_2$ catalysts for selective oxidation of CO in excess hydrogen: Effect of hydrothermal preparation conditions. *J. Nat. Gas Chem.,* **2009**, 18, 1-8.

39. Caputo, T.; Lisi, L.; Pirone, R.; Russo, G. On the role of redox properties of CuO/CeO_2 catalysts in the preferential oxidation of CO in H_2-rich gases. *Appl. Catal. A: Gen*., **2008**, 348, 42-53.

40. Zheng, X. C.; Wu, S. H.; Wang, S. P.; Wang, S. R.; Zhang, S. M.; Huang, W. P. The preparation and catalytic behavior of copper–cerium oxide catalysts for low-temperature carbon monoxide oxidation. *Appl. Catal. A: Gen*., **2005**, 283, 217-223.

41. Liu, W.; Flytzani-Stephanopoulos, M. Total oxidation of carbon monoxide and methane over transition metal fluorite oxide composite catalysts: catalyst composition and activity. *J. Catal*., **1995**, 153, 304-316.

Chapter 5: Support structure effect on CO oxidation: A comparative study on SiO_2 nanospheres and CeO_2 nanorods supported CuO_x catalysts

The effect of support reducibility and reduction treatment has been studied in SiO_2 nanospheres and CeO_2 nanorods supported CuO_x ($0 \leq x \leq 1$) catalysts on CO oxidation. CuO nanoparticles were impregnated on SiO_2 nanospheres and CeO_2 nanorods using thermal decomposition method and then the samples were oxidized in air at different temperatures (400-600 ^oC). The sample oxidized at 400 ^oC was also further reduced under hydrogen atmosphere to compare the effect of reduction treatment on the catalytic activity. Detailed XRD, Raman, H_2-TPR, and CO oxidation analyses were carried out to understand the effect of CuO_x-support interaction and different CuO_x species on the catalytic performance. In comparison to SiO_2 nanospheres supported CuO_x catalysts, both CuO/CeO_2 and reduced CuO_x/CeO_2 catalysts exhibited superior catalytic performance in terms of CO conversion and low-temperature hydrogen consumption. The enhanced activity of CeO_2 nanorods supported CuO_x catalysts was correlated strongly to the surface defects on CeO_2 nanorods and interfacial structures.

5.1. Introduction

Various oxides (SiO_2, TiO_2, ZrO_2, CeO_2, and Al_2O_3) have been extensively assessed and used as catalyst support materials in heterogeneous catalysis [1-4]. It has been widely recognized that some of these oxide supports not only can promote the dispersion and thermal stability of catalyst nanoparticles, but also benefit the catalyst activity and

selectivity via a synergistic effect or catalyst-support interaction. The oxide supports can usually be divided into two categories: reducible (CeO_2 and TiO_2) and non-reducible (SiO_2, ZrO_2, and Al_2O_3). The catalytic activity can be significantly influenced by the reducibility of oxide support and catalyst-support interaction at the interface [2-4]. For example, Wang et al. [5] presented that reducible TiO_2 support promoted CO oxidation over Au/TiO_2 catalyst by affecting the charge state of Au and the charge transfer at the interface. Non-noble metal catalyst CuO on rutile TiO_2 support prepared by Kang et al. [6] showed 100% CO conversion at ~200 ^oC due to the contribution of reduction of Ti^{4+} to Ti^{3+}. Venezia et al. [7] reported that Au deposited on non-reducible SiO_2 supports converted 100% CO at over 450 ^oC due to the presence of weak metal-support interaction. Another reducible oxide, CeO_2, has also been investigated considerably as a great catalyst support candidate due to its distinctive feature as high oxygen storage and release capacity [8-10]. A possible explanation for the promotion role is reducible oxides are used as support due to charge transfer and oxygen exchange at the catalyst-support interface under reaction conditions [8, 9]. One of difficulties to study the catalyst-support interactions and the resulting catalytic activity is that preparing model catalyst systems, consisting of catalyst clusters deposited on shape well-defined support with specific crystal planes, is still challenging. In addition, catalyst preparation methods and thermal treatments also play a significant role on the catalyst-support interfacial structures [11-15]. CeO_2 nanorods support has been reported to present a superior low temperature surface lattice oxygen release and storage capacity compared to other CeO_2 shapes (octahedral and nanocube) [8]. In this chapter, a comparative study was conducted on shape-controlled non-reducible SiO_2 nanospheres and highly reducible CeO_2 nanorods

supported CuO_x ($0 \leq x \leq 1$) catalysts to understand the effect of support reducibility and thermal treatments (oxidation and reduction treatments) on the catalytic activity of CO oxidation. The results will further improve our understanding of the interfacial interactions between catalyst and support, and possible synergistic effect for low-temperature CO conversion.

5.2. Experimental

5.2.1. Catalyst preparation

Silica (SiO_2) nanospheres were prepared using a hydrolysis method. First, 2 mL of Tetraethoxysilane (TEOS 99%) was dissolved in a mixture of 9 mL of deionized water and 38.2 mL of ethanol. Then, 50 mL of 28-30% NH_4OH was added dropwise to the solution under vigorous magnetic stirring. The reaction was kept for 4 hrs under continuous magnetic stirring. The suspension solution was centrifuged, and then washed with DI water and ethanol. The sample was dried at 60 ^oC overnight. CeO_2 nanorods were synthesized using the hydrothermal method. The 88 mL of 0.1 M $Ce(NO_3)_3 \cdot 6H_2O$ and 8 mL of 6 M NaOH solutions were added in a Teflon liner of 200 mL capacity. The mixture was stirred for about 15 seconds, and then the lid of Teflon liner was closed. After putting the Teflon liner into a stainless-steel autoclave, it was heated and kept at 90 ^oC for 48 hrs. Finally, the sample was filtered and then was washed with 500 mL DI water and 50 mL ethanol. It was dried at 50 ^oC for 12 hrs. 10wt.% CuO was impregnated in both CeO_2 nanorods and SiO_2 nanospheres using thermal decomposition method. $Cu(NO_3)_2 \cdot 3H_2O$ and the oxide supports (CeO_2 nanorods or SiO_2 nanospheres) were mixed in a stoichiometric ratio in 30 mL DI water. The solution was stirred continuously

and was heated at 120 ^{o}C until the water evaporated completely. The collected samples were calcined at 400, 500 and 600 ^{o}C for 5 hrs in air. These samples were denoted as CuO/CeO_2-X and CuO/SiO_2-X, where X stands for the oxidation temperature (X=400, 500 and 600 ^{o}C). The reduction treatment was conducted on CuO/CeO_2-400 and CuO/SiO_2-400 samples at 400 ^{o}C for 5 hrs under 5%H_2-95%Ar environment. These samples were denoted as CuO/CeO_2-400R and CuO/SiO_2-400R.

5.2.2. Catalyst characterizations

X-ray diffraction (XRD), Raman spectroscopy, X-ray photoelectron spectroscopy (XPS), transmission electron microscopy (TEM), BET surface area measurement, temperature programmed reduction (TPR), temperature programmed desorption (TPD), and CO oxidation were used to characterize the catalysts and their catalytic activity. The description of these techniques can be found in chapter 2.

5.3. Results

5.3.1. The effect of oxidation temperature

The XRD patterns of CeO_2 nanorods, SiO_2 nanospheres, and CuO nanopowders were shown in Fig. 5.1a. The diffraction pattern of as-synthesized CeO_2 nanorods was consistent with the standard fluorite-type CeO_2 reported in JCPDS data (JCPDS 43-1002). A broad diffraction peak was observed in the XRD pattern of SiO_2 nanospheres, indicating that as-synthesized SiO_2 nanospheres were amorphous [16]. The XRD pattern of CuO nanopowders displayed two sharp peaks at 2θ of 35.6^{o} and 38.8^{o} corresponding to (-111) and (111) planes (JCPDS 45-0937) [17]. Fig. 1b displayed the XRD patterns of CuO/SiO_2 samples oxidized at different temperatures (400 ^{o}C-600 ^{o}C). One broad peak

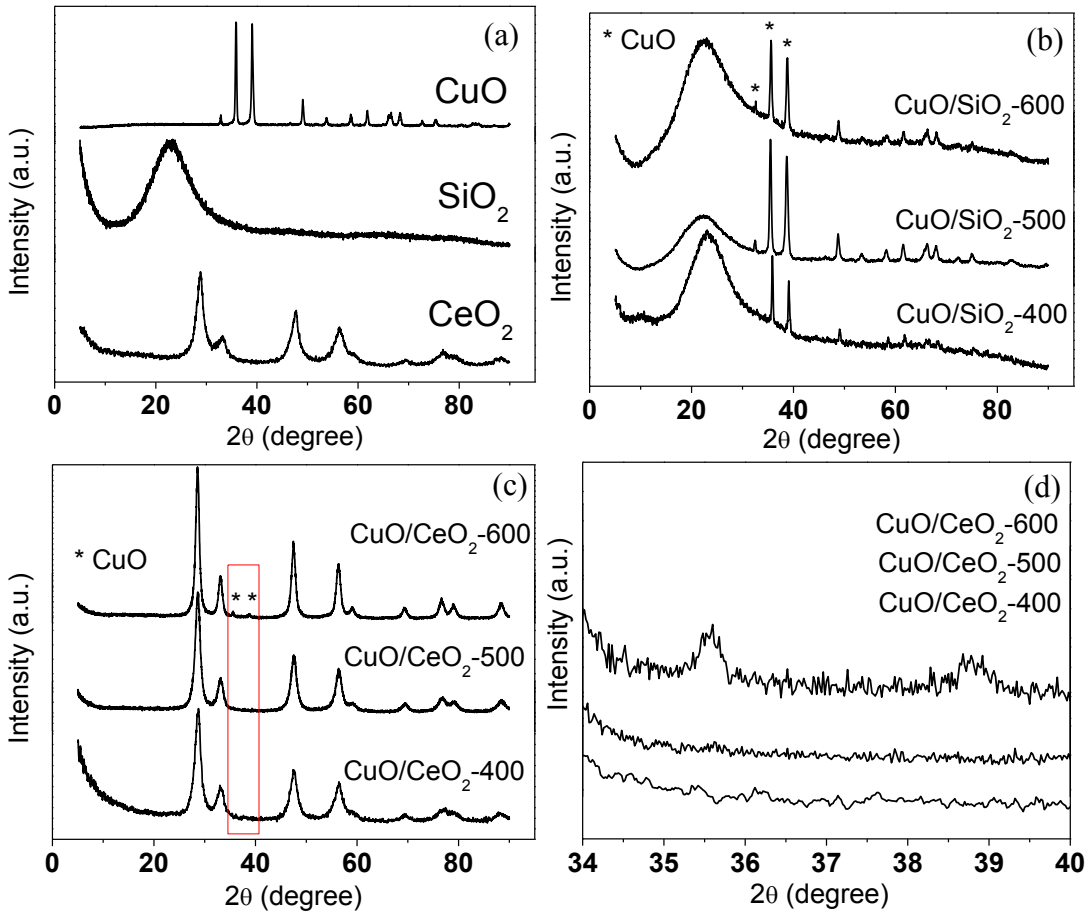

Figure 5.1. XRD patterns of (a) CuO nanopowders, SiO_2 nanospheres and CeO_2 nanorods, and (b) CuO/SiO_2 nanospheres and (c) CuO/CeO_2 nanorods oxidized at various temperatures. (d) Magnified XRD patterns of CuO/CeO_2 nanorods of red rectangular portion shown in (c).

for amorphous SiO_2 and other sharp peaks for CuO were easily visible for all three CuO/SiO_2 samples. For the CuO/CeO_2 samples, the diffraction peaks of CuO were not visible for the CuO/CeO_2-400 and CuO/CeO_2-500 samples (Fig. 5.1c and 5.1d). When the CuO/CeO_2 sample was oxidized at 600 ^oC, small (-111) and (111) diffraction peaks of CuO emerged in the XRD pattern, as shown in Fig. 5.1c, which were much evident in the magnified patterns shown in Fig. 5.1d. The presence of CuO peaks indicated that a phase separation of CuO from Cu-O-Ce solid solution occurred in these samples at elevated

oxidation temperature, and/or well-dispersed small CuO nanoparticles started to grow and sinter at a higher oxidation temperature. Table 5.1 showed the average crystallite size of CuO estimated from (-111) and (111) diffraction peaks of XRD and BET surface area of the CuO/SiO_2 samples. The calculated crystallite size of CuO in the CuO/SiO_2 samples increased with increasing the oxidation temperature from 16.2 nm (400 °C) to 20.7 nm (600 °C). The BET surface area of CuO/SiO_2-400 was 6.71 m^2/g which was very close to an average (6.92 m^2/g) of BET surface area of pure CuO (4.12 m^2/g) and SiO_2 nanospheres (9.72 m^2/g). For CuO/SiO_2-500 and CuO/SiO_2-600, the measured surface area was almost twice as that of CuO/SiO_2-400 possibly due to better decomposition and crystallization of copper precursor at higher oxidation temperatures [18]. In Table 5.2, the crystallite size of CeO_2, which was calculated using (111) peak of XRD in the CuO/CeO_2 samples, also increased with increasing the oxidation temperature [19, 20]. The BET surface area of the CuO/CeO_2 samples slightly decreased with increasing the oxidation temperatures.

Table 5.1. Average crystallite size measured using CuO (-111) and (111) peaks, BET surface area, T_{50}, and maximum CO conversion along with temperatures of CuO/SiO_2 samples oxidized at different temperatures and reduced at 400 ^oC.

Sample	Crystallite size (nm)	BET surface area (m^2/g)	T_{50} (^oC)	Max CO conversion (%)	T_{max} (^oC)
CuO/SiO_2-400	16.2	6.71	241	72	324
CuO/SiO_2-500	18.2	12.62	234	77	298
CuO/SiO_2-600	20.7	11.42	194	89	280
CuO/SiO_2-400R	18.6	13.24	246	68	298

Table 5.2. Crystallite size measured using CeO_2 (111) peak, BET surface area, T_{50}, and maximum CO conversion along with temperatures of CuO/CeO_2 samples oxidized at different temperatures and reduced at 400 ^oC.

Sample	Crystallite size (nm)	BET surface area (m^2/g)	T_{50} (^oC)	Max CO conversion (%)	T_{max} (^oC)
CuO/CeO_2-400	5.4	39.42	88	100	220
CuO/CeO_2-500	6.4	39.22	94	95	237
CuO/CeO_2-600	7.9	37.33	117	92	263
CuO/CeO_2-400R	6.6	38.72	94	92	280

Fig. 5.2a showed the Raman spectra of CeO_2 nanorods, SiO_2 nanospheres, and CuO nanopowders. For CeO_2 nanorods, typical CeO_2 peak at 456 cm^{-1} corresponded to F_{2g} vibrational mode and two other peaks at 276 and 605 cm^{-1} were assigned to oxygen vacancies in CeO_2 lattice [21]. A small peak of SiO_2 nanospheres, observed at 504 cm^{-1}, was attributed to the vibrations of four-membered ring structures called D_1 vibrational mode [22, 23]. A broad peak near 440 cm^{-1} corresponded to symmetric vibrations of oxygen atoms [24]. Two other peaks at 290 and 350 cm^{-1} were attributed to D_3 and D_4 bands [25]. The characteristic CuO peaks were found at 276, 326 and 625 cm^{-1} which corresponded to A_g, B_{1g}, and B_{2g} mode, respectively [26]. Another peak found at 506 cm^{-1} in Raman spectrum of CuO sample was assigned to either E_g mode of Cu_4O_3 or B_{2u} mode of CuO in literature [27-29]. In our case, this peak was assigned to CuO because there was no evidence of the presence of Cu_4O_3 gathered from the XRD analysis (Fig. 5.1a).

Fig. 5.2b showed the Raman spectra of the CuO/SiO_2 samples oxidized at different temperatures (400 °C-600 °C). A sharp peak with large intensity observed at 506 cm^{-1} for all three CuO/SiO_2 samples was probably a blend of two different peaks: one for D_1 band of SiO_2 (at 504 cm^{-1} in Fig. 5.2a) and the other for B_{2u} mode of CuO (at 506 cm^{-1} in Fig.

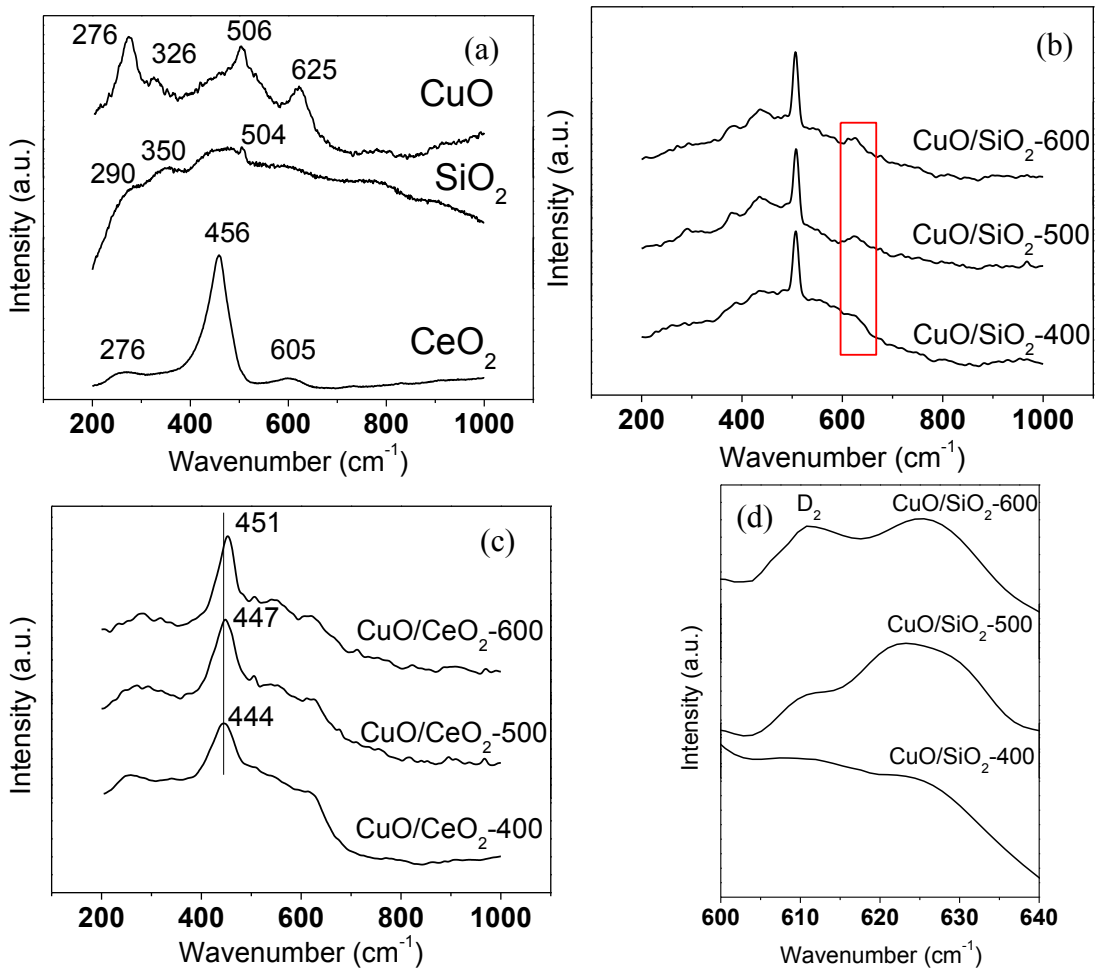

Figure 5.2. Raman spectra of (a) CuO nanopowders, SiO_2 nanospheres and CeO_2 nanorods, and (b) CuO/SiO_2 nanospheres and (c) CuO/CeO_2 nanorods oxidized at various temperatures. (d) Magnified Raman spectra of CuO/SiO_2 nanospheres of red rectangular portion shown in (b).

5.2a). A broad peak centered near 620 cm^{-1} (in the range of 600~640 cm^{-1}) for CuO/SiO_2-400 became sharper with increasing the oxidation temperature and finally, for CuO/SiO_2-600 this peak split into two separate peaks (Fig. 5.2b: red rectangular portion). These two peaks could be assigned as one from B_{2g} mode of CuO and the other one from D_2 band of SiO_2. This D_2 peak of SiO_2 was not seen in Raman spectrum of pure SiO_2, corresponding to the planar threefold $[SiO_3]^{2-}$ rings [23, 30-32]. The formation of threefold $[SiO_3]^{2-}$ rings was further demonstrated in magnified Raman spectra in Fig. 5.2d with increasing the oxidation temperature. In comparison, Fig. 5.2c illustrated the Raman spectra of the CuO/CeO_2 samples oxidized from 400 °C to 600 °C. The characteristic CeO_2 F_{2g} peak shifted from 456 cm^{-1} for CeO_2 nanorods (Fig. 5.2a) to 444 cm^{-1} for CuO/CeO_2-400 (Fig. 5.2c) possibly due to the lattice distortion occurred during incorporation of Cu ions into CeO_2 lattice to form solid solution [20]. With increasing oxidation temperature, this F_{2g} peak in CuO/CeO_2 continuously shifted from 444 cm^{-1} in CuO/CeO_2-400 to 451 cm^{-1} in CuO/CeO_2-600. This result also supported the XRD observation in Fig. 5.1c and 5.1d that CuO emerged in CuO/CeO_2-600. This suggested a phase separation of CuO from the Cu-O-Ce solid solution, which resulted in the Raman peak shifting to close to the value of CeO_2 (456 cm^{-1}) as shown in Fig. 5.2c [20]. A broad peak seen at 625 cm^{-1} was a mixture of two peaks, including oxygen vacancy peak of CeO_2 at 605 cm^{-1} and B_{2g} mode of CuO at 625 cm^{-1}. This peak became stronger with increasing the oxidation temperature due to the formation of CuO as discussed earlier. XPS spectra of CuO/CeO_2-400 and CuO/SiO_2-400 were shown in Fig. 5.3a-c and 5.4a-c, respectively, to study the chemical state of various elements at the catalyst surface. Cu 2p XPS spectra can be seen in Fig. 5.3a. It can be observed that Cu^{2+} component peak was present at 939.6 eV (peak shifted

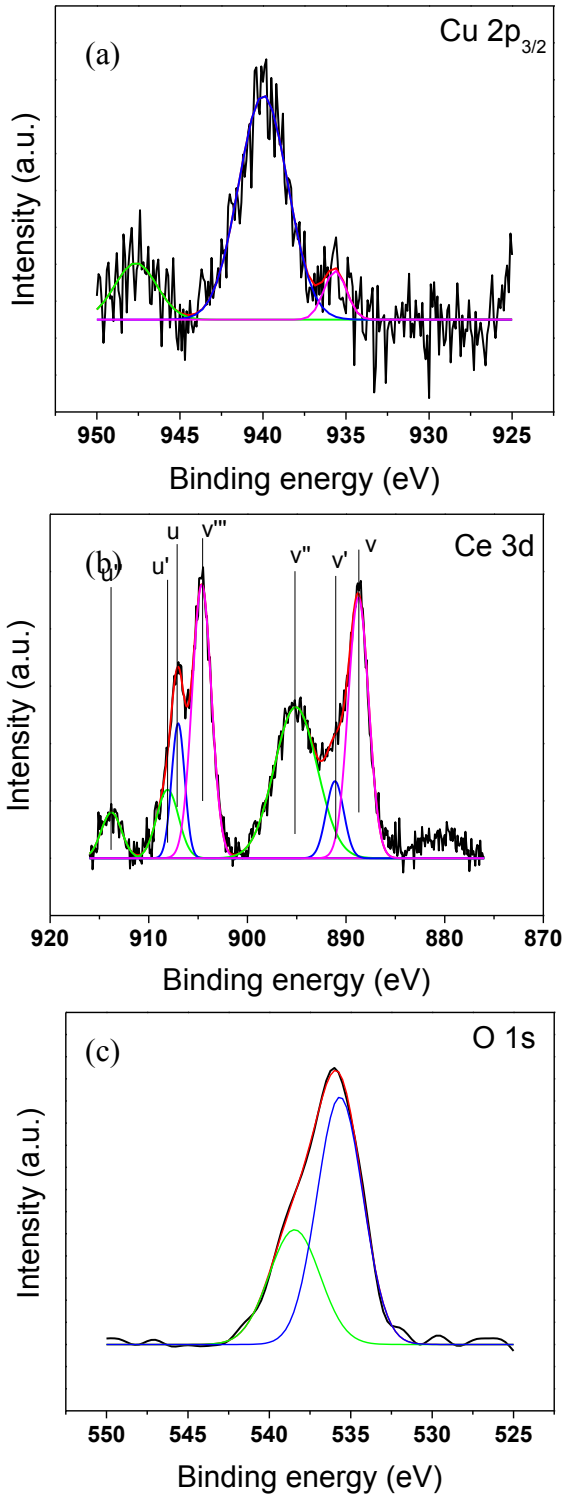

Figure 5.3. XPS spectra of (a) Cu $2p_{3/2}$, (b) Ce 3d, and (c) O 1s for CuO/CeO_2-400.

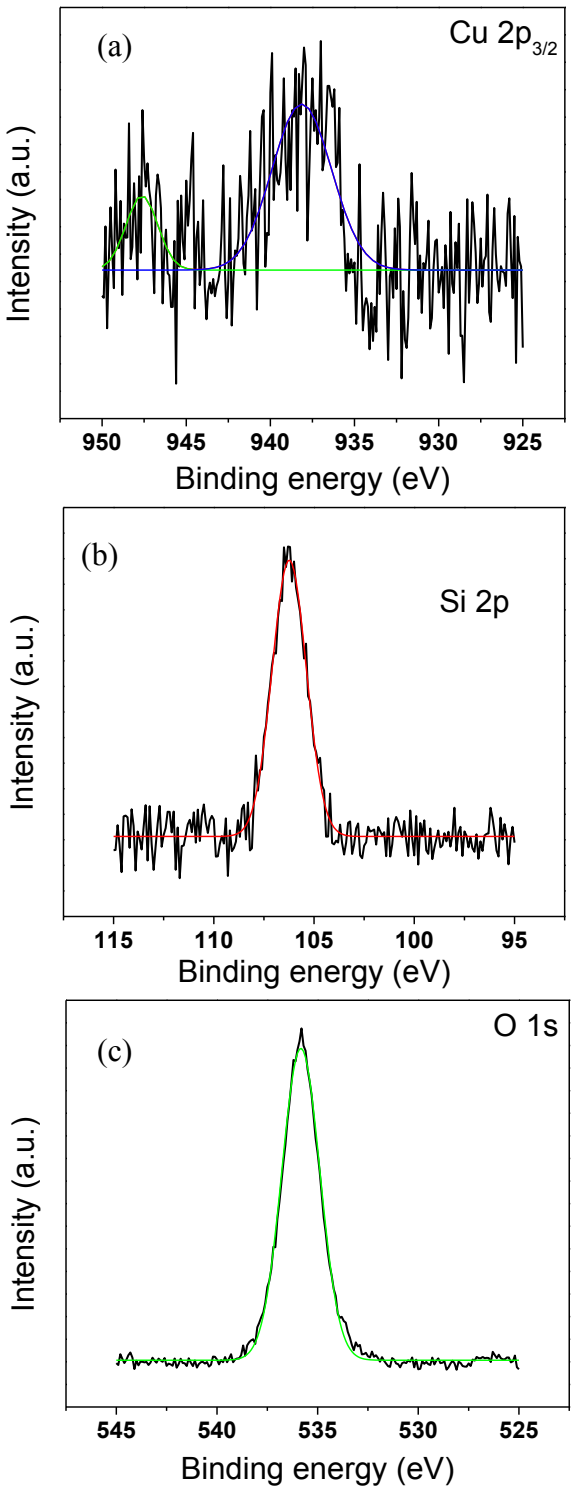

Figure 5.4. XPS spectra of (a) Cu $2p_{3/2}$, (b) Si 2p, and (c) O 1s for CuO/SiO_2-400.

by +6 eV) [15, 33, 34]. Another small peak found at 935.6 eV (peak shifted by +4 eV) represented Cu^{+}, which implied strong interaction between CeO_2 and copper species [33, 34]. Fig. 5.3b showed Ce 3d XPS spectra where $3d_{3/2}$ and $3d_{5/2}$ peaks were labeled as u and v, respectively. There were seven peaks: u (907.1), u' (908.2), u'' (913.8), v (888.8), v' (891.1) and v'' (895.1) of Ce 3d in CuO/CeO_2-400. The peaks u, u'', v, v'' and v''' can be assigned to Ce^{4+} and the peaks u' and v' can be assigned to Ce^{3+} [33, 34]. The presence of Ce^{3+} is beneficial for attaining outstanding performance in CO oxidation [33, 34]. In Fig. 5.3c, O 1s XPS spectra can be seen where two peaks were observed at 538.4 (peak shifted by +7 eV) and 535.6 eV (peak shifted by +6 eV). Higher energy peak (538.4) corresponded to adsorbed oxygen species at surface and lower energy peak (535.6) was assigned to lattice oxygen of metal oxides [33, 34]. Clearly, the intensity of lower energy peak was higher, which suggested that a large amount of lattice oxygen from CeO_2 was present at the surface. Cu 2p XPS spectra of CuO/SiO_2-400 can be seen in Fig. 5.4a where Cu^{2+} peak was observed at 938.1 eV. There was no Cu^{+} peak for this sample, suggesting weak interaction between SiO_2 and copper species. Si 2p peak was found at 106.2 eV as shown in Fig. 5.4b. In Fig. 5.4c, one strong peak for O 1s can be found at 535.8 eV (peak shifted by +4 eV) which corresponded to lattice oxygen at the surface of catalyst. All of the peaks shifted to higher energy compared to the literature [34] due to charging effect in the sample during conducting the experiments.

The H_2-TPR profiles of SiO_2 nanospheres and CeO_2 nanorods were shown in Fig. 5.5a. Two major reduction peaks of CeO_2 nanorods were visible at 470 and 824 ^{o}C, which correspond to the reduction of surface and bulk CeO_2, respectively. On the other hand, SiO_2 nanospheres did not show any reduction peak as expected. The H_2-TPR

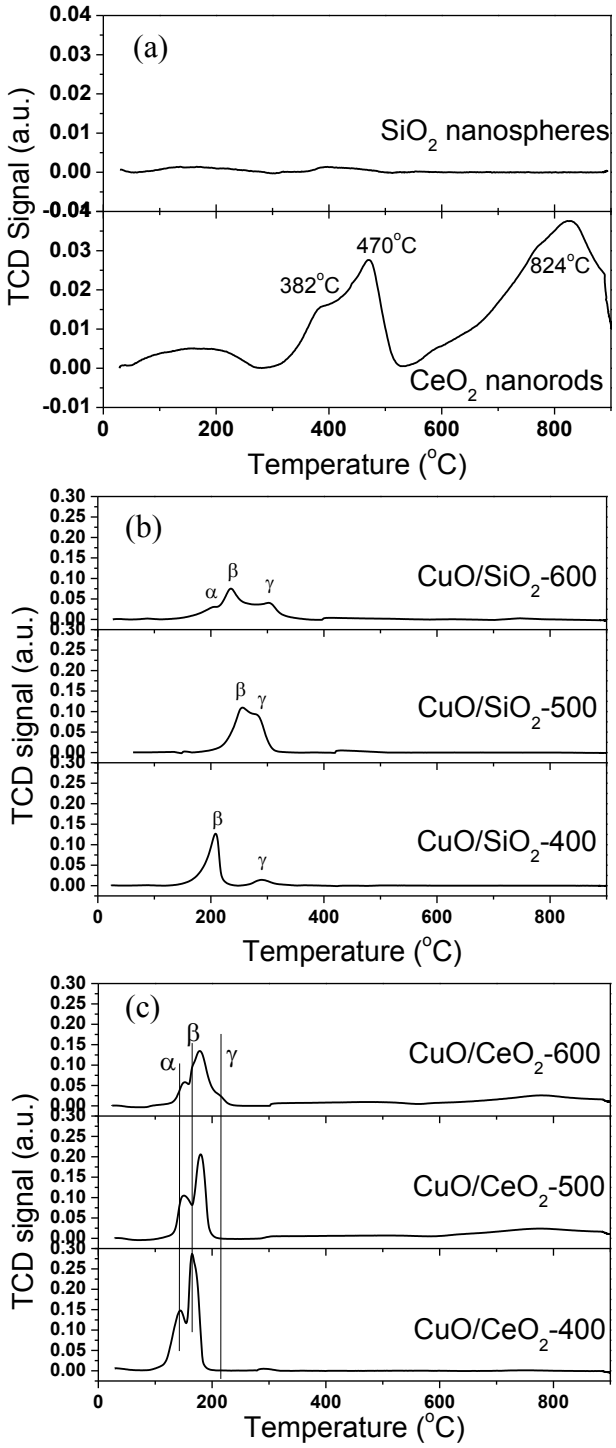

Figure 5.5. H_2 TPR profiles of (a) SiO_2 nanospheres and CeO_2 nanorods, and (b) CuO/SiO_2 and (c) CuO/CeO_2 oxidized at various temperatures.

profiles of the CuO/SiO_2 samples were shown in Fig. 5.5b. Two well-separated reduction peaks at 207 and 288 ^oC can be found for CuO/SiO_2-400. According to the peak assignments of supported CuO catalysts in literature [35], the first peak at 207 ^oC, called β peak, corresponded to the reduction of CuO nanoparticles dispersed onto SiO_2 surface. The peak found at 288 ^oC, called γ peak, was attributed to the reduction of small amount of bulk CuO (larger particles). For CuO/SiO_2-500, the β peak shifted to a higher reduction temperature (254 ^oC) while γ peak remained at the same position. The γ peak for CuO/SiO_2-600 shifted to a higher temperature (304 ^oC) due to the growth and sintering of bulk CuO at higher oxidation temperature. Another peak found at 195 ^oC was attributed to α peak and this peak corresponded to the reduction of incorporated copper species into SiO_2 support which will be explained in details later. The H_2-TPR profiles of the CuO/CeO_2 samples were presented in Fig. 5.5c. It should be noted that the same TCD signal scales and similar sample weight (~90 mg) in all six supported CuO samples in Fig. 5.5b and 5.5c were used to make the hydrogen consumption calculation comparable. The TPR profiles of the CuO/CeO_2-400 sample showed two reduction peaks. The first peak (called α peak) found at 142 ^oC was assigned to Cu-O-Ce solid solution or strongly interacting copper species [36-38]. The β peak at 165 ^oC was attributed to the reduction of well-dispersed CuO onto CeO_2 surface. For the CuO/CeO_2-500 sample, both α and β peaks shifted a little to higher reduction temperatures at 146 and 170 ^oC, respectively. The α and β reduction peaks in the CuO/CeO_2-600 sample showed a continuous shift to a higher temperature (150 and 175 ^oC) due to the increased crystallite size (Table 5.2). Meanwhile, another peak (γ peak) was found at 210 ^oC which corresponded to bulk CuO reduction. Fig. 5.6 illustrated the H_2 consumption of the CuO/SiO_2 and CuO/CeO_2

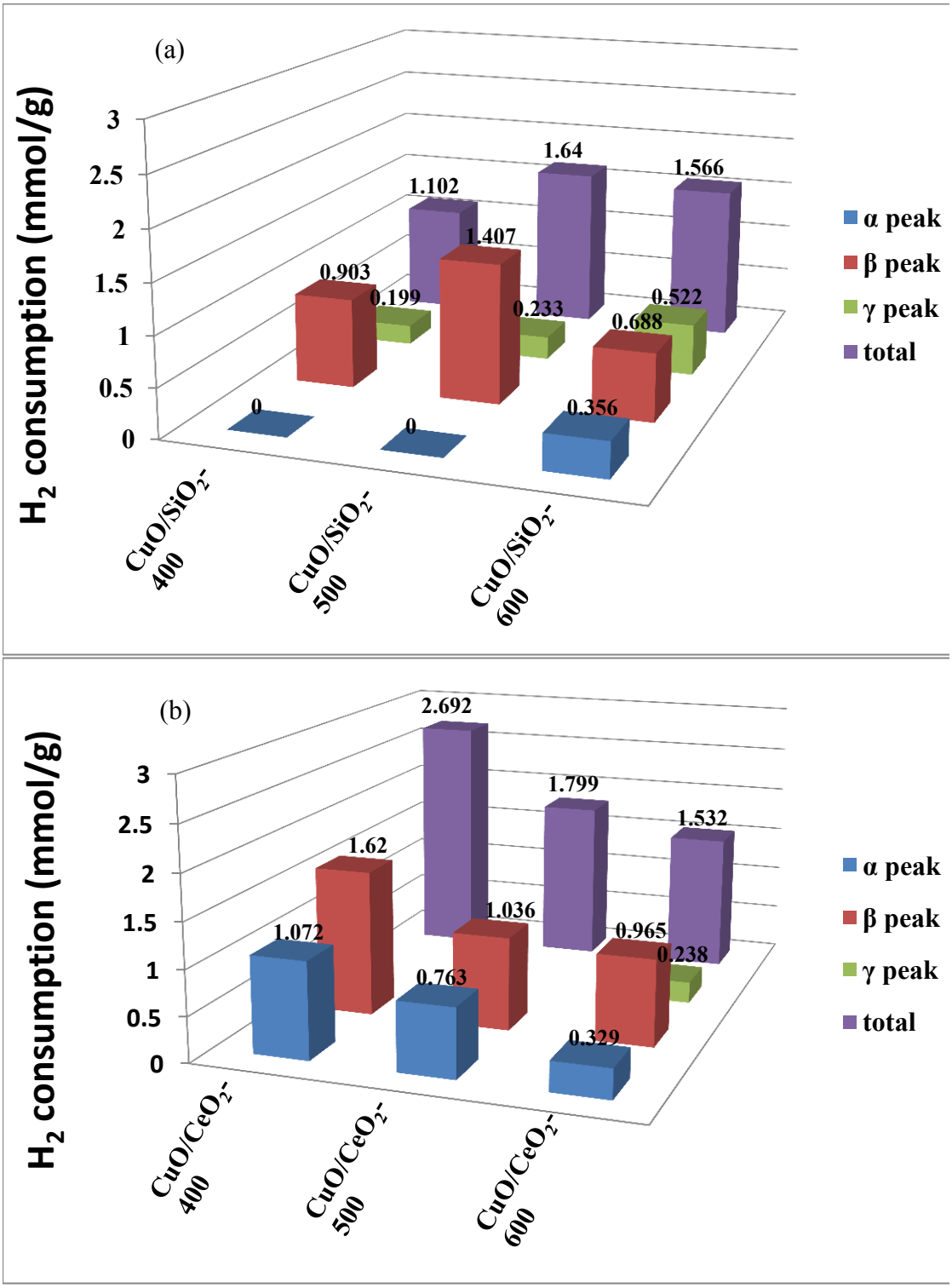

Figure 5.6. H_2 consumption of (a) CuO/SiO_2 and (b) CuO/CeO_2 oxidized at various temperatures.

samples. In the temperature range of 150 to 400 ^{o}C, the H_2 consumptions in the CuO/CeO_2 samples were all higher than the counterpart in the CuO/SiO_2 samples. This confirmed the advantage of reducible CeO_2 support compared to the non-reducible SiO_2 support for H_2 consumption. The calculated H_2 consumption for the γ peak increased with increasing the oxidation temperature in the CuO/SiO_2 samples as shown in Fig. 5.6a. The CuO/SiO_2-500 and CuO/SiO_2-600 samples demonstrated a similar total amount of H_2 consumption in the range of 150 to 400 ^{o}C. The H_2 consumption of the CuO/CeO_2 samples decreased with increasing the oxidation temperature as shown in Fig. 5.6b. The H_2 consumption for both the α and β peaks clearly decreased with increasing the oxidation temperature, which is probably due to the CuO and CeO_2 phase separation at higher oxidation temperature as discussed earlier. These results support the hypothesis that the reducible CeO_2 support favors the low-temperature reduction and H_2 consumption in CeO_2 nanorods supported CuO catalysts [39].

The light-off curves for CO oxidation conversion of the CuO/SiO_2 and CuO/CeO_2 samples were plotted in Fig. 5.7. The T_{50} temperatures where 50% CO conversion occurred for CuO/SiO_2-400, CuO/SiO_2-500, and CuO/SiO_2-600 were 241, 234 and 194 ^{o}C, respectively, as shown in Table 5.1. These samples did not achieve 100% CO conversion up to 350 ^{o}C. The CuO/SiO_2-400, CuO/SiO_2-500, and CuO/SiO_2-600 samples converted maximum 72, 77, and 89 % CO at 324, 298, and 280 ^{o}C, respectively, indicating that the catalytic efficiency of CuO/SiO_2 increased with increasing the oxidation temperatures. The CuO/CeO_2 samples presented an opposite trend toward CO conversion. The T_{50} of the CuO/CeO_2-400, CuO/CeO_2-500, and CuO/CeO_2-600 samples were found at 88, 94, and 117 ^{o}C, respectively, as displayed in Table 5.2. The CuO/CeO_2-

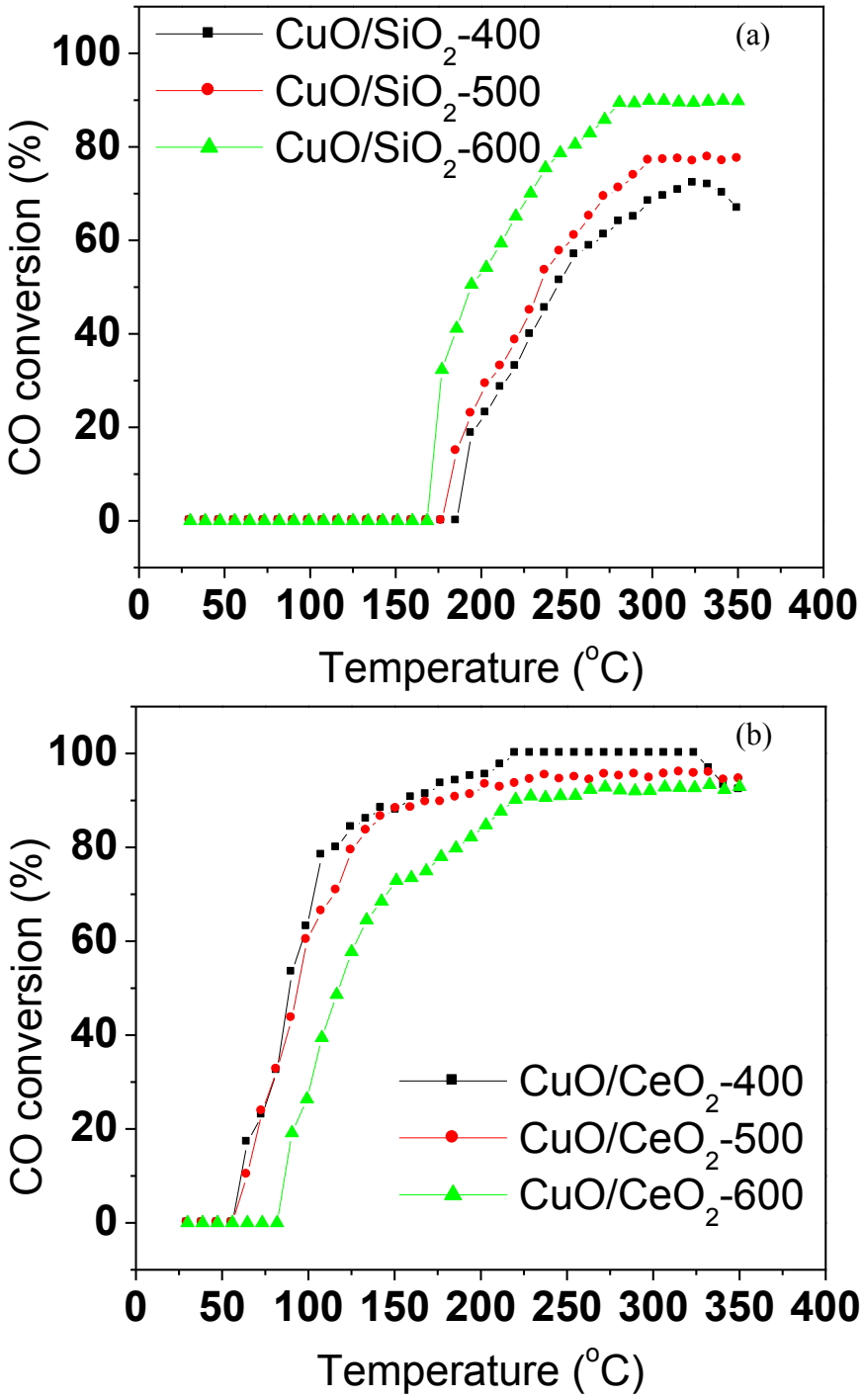

Figure 5.7. CO conversion curves of (a) CuO/SiO_2 and (b) CuO/CeO_2 oxidized at different temperatures.

400 sample was the only sample which achieved 100% CO conversion at 220 ^{o}C among all of the prepared samples. The CuO/CeO_2-500 and CuO/CeO_2-600 samples attained maximum 95 and 92 % CO conversion at 237 and 263 ^{o}C, respectively.

5.3.2. Reduction treatment effect

Fig. 5.8a illustrated the XRD patterns of the CuO/CeO_2-400 and CuO/SiO_2-400 catalysts before and after reduction treatment at 400 ^{o}C in 5% H_2-95% Ar. The XRD patterns of CuO/CeO_2-400 and CuO/CeO_2-400R only showed the presence of fluorite-structured CeO_2, but no copper-containing phases were detected in both samples. The possible reasons that no copper-containing phases (CuO_x, $0 \leq x \leq 1$) were found from XRD analysis were due to the presence of small well dispersed CuO_x on CeO_2 nanorods, Cu-O-Ce solid solutions or a mixture of both cases. The presence of small well-dispersed CuO_x on CeO_2 was supported by XRD and Raman analysis as shown in Fig. 5.1c/5.1d and 5.2c, respectively. CuO_x was clearly visible from XRD patterns and Raman spectra in the CuO/CeO_2-600 sample with a higher thermal treatment temperature (at 600 ^{o}C). The formation of Cu-O-Ce solid solution was supported by the peak shifting in Raman spectra for the samples heat-treated from 400 ^{o}C to 600 ^{o}C, as shown in Fig. 5.2c [39]. After the reduction treatment, the crystallite size of CeO_2 in CuO/CeO_2-400R increased from 5.4 nm to 6.6 nm.

The XRD patterns of CuO/SiO_2-400 and CuO/SiO_2-400R exhibited the presence of a monoclinic CuO phase (JCPDS 45-0937) and metallic Cu (JCPDS 04-0836), respectively, as shown in Fig. 5.8a. Thus, after the reduction treatment, CuO existed in CuO/SiO_2-400 was reduced to metallic Cu in CuO/SiO_2-400R. Except for the peak

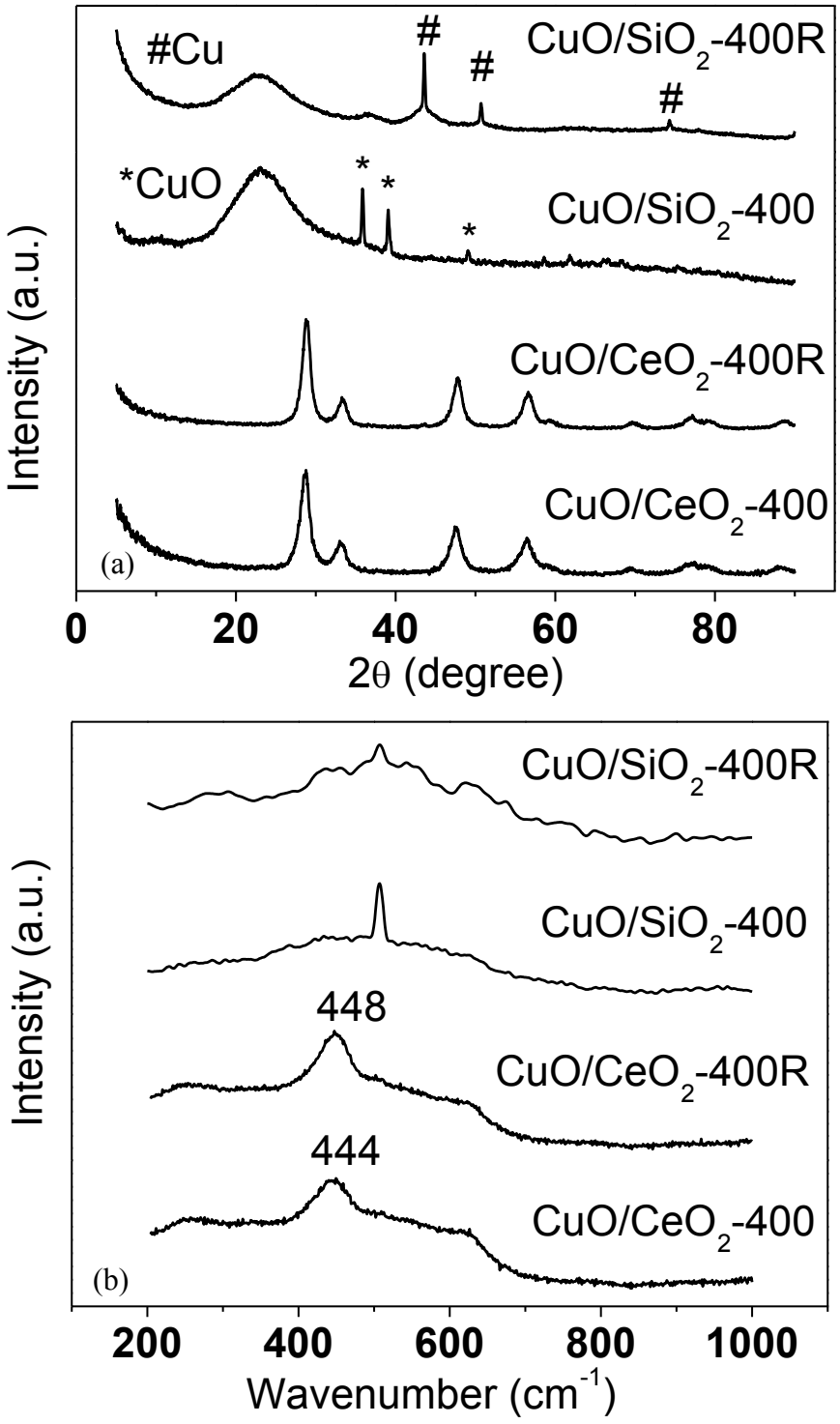

Figure 5.8. (a) XRD patterns and (b) Raman spectra of CuO/SiO_2-400 and CuO/CeO_2-400 before and after reduction treatment.

broadness, no evident change was observed for amorphous SiO_2 support. Although negligible changes were found for both CeO_2 and SiO_2 supports from the XRD profiles before and after the reduction treatment, the visibility and reduction behavior of copper species were completely different on them, suggesting that support kind/structure had a critical impact on the structure, texture, and distribution of CuO_x catalyst.

Raman spectra of the CuO/CeO_2-400 and CuO/SiO_2-400 samples before and after the reduction treatment were shown in Fig. 5.8b. For the CuO/CeO_2-400 sample, the characteristic CeO_2 F_{2g} peak shifted to 444 cm^{-1} from 456 cm^{-1} in CeO_2 due to incorporation of Cu ions into CeO_2 to form solid solution as discussed earlier. After the reduction treatment, this peak shifted to 448 cm^{-1} due to either a phase separation of CuO from Cu-O-Ce solid solution or increment of crystallite size of CeO_2 [20]. For both CuO/CeO_2-400 and CuO/CeO_2-400R samples showed two peaks at 270 and 624 cm^{-1}. These two peaks were assigned to the combination of oxygen vacancies in CeO_2 and CuO B_{2g} mode.

For the CuO/SiO_2-400 sample, the peak corresponded to D_1 vibrational mode of SiO_2 (at 504 cm^{-1} in Fig. 5.2a) and the B_{2u} mode peak of CuO (at 506 cm^{-1} in Fig. 5.2a) were overlapped, and then they became one sharp peak at around 506 cm^{-1}[22-23, 27]. After the reduction treatment, a similar peak at 506 cm^{-1} in CuO/SiO_2-400R became much weaker. Since CuO was reduced to metallic Cu after the reduction treatment (Fig. 5.8a), the remaining peak at around 506 cm^{-1} was assigned to D_1 mode of SiO_2.

Fig. 5.9a showed the H_2-TPR profiles of both CuO/CeO_2 and CuO/SiO_2 samples before and after the reduction treatment. The CuO/CeO_2-400 sample displayed two

reduction peaks at 142 and 164 ^{o}C which corresponded to α and β peak, respectively, as discussed earlier. For the CuO/CeO_2-400R sample, the α and β peaks were found at 137 and 157 ^{o}C. Two reduction peaks at 208 and 291 ^{o}C were found for the CuO/SiO_2-400 sample. For this case, the first peak was assigned to the β peak which was attributed to the reduction of dispersed CuO, and the second peak was the γ peak which corresponded to bulk CuO reduction. There was no α peak for this case, indicting no strong interaction between CuO and SiO_2 during the oxidation treatment at 400 ^{o}C. However, one α peak was found at 165 ^{o}C for CuO/SiO_2-400R. This α peak probably corresponded to the copper species diffused and incorporated into threefold SiO_3 rings during the reduction treatment. There was no β or γ peak for the CuO/SiO_2-400R sample, indicating the dispersed and bulk CuO particles were reduced to metallic Cu. The most remarkable fact was that surprisingly H_2 consumption peaks were still found for both CuO/CeO_2-400R and CuO/SiO_2-400R samples. This may have happened due to the presence of Cu-O-Ce solid solution and CuO_x ($1 \geq x > 0$) at the interface for the CuO/CeO_2-400R sample, and the presence of copper species in threefold SiO_3 rings for the CuO/SiO_2-400R sample. Fig. 5.9b displayed that the H_2 consumption in the CuO/CeO_2-400 and CuO/CeO_2-400R samples are 2.692 and 1.487 mmol/g, respectively. On the other hand, the CuO/SiO_2-400 and CuO/SiO_2-400R samples consumed 1.102 and 0.342 mmol/g of H_2, respectively. The H_2 consumption at β peak for CuO/CeO_2-400R decreased abruptly after the reduction treatment due to the reduction of dispersed CuO to metallic Cu. However, the H_2 consumption at α peak remained constant. BET surface areas of both CuO/SiO_2-400 and CuO/CeO_2-400 samples before and after reduction treatment were tabulated in Table 5.1 and 5.2, respectively. It was found that surface area of CuO/SiO_2-400R increased

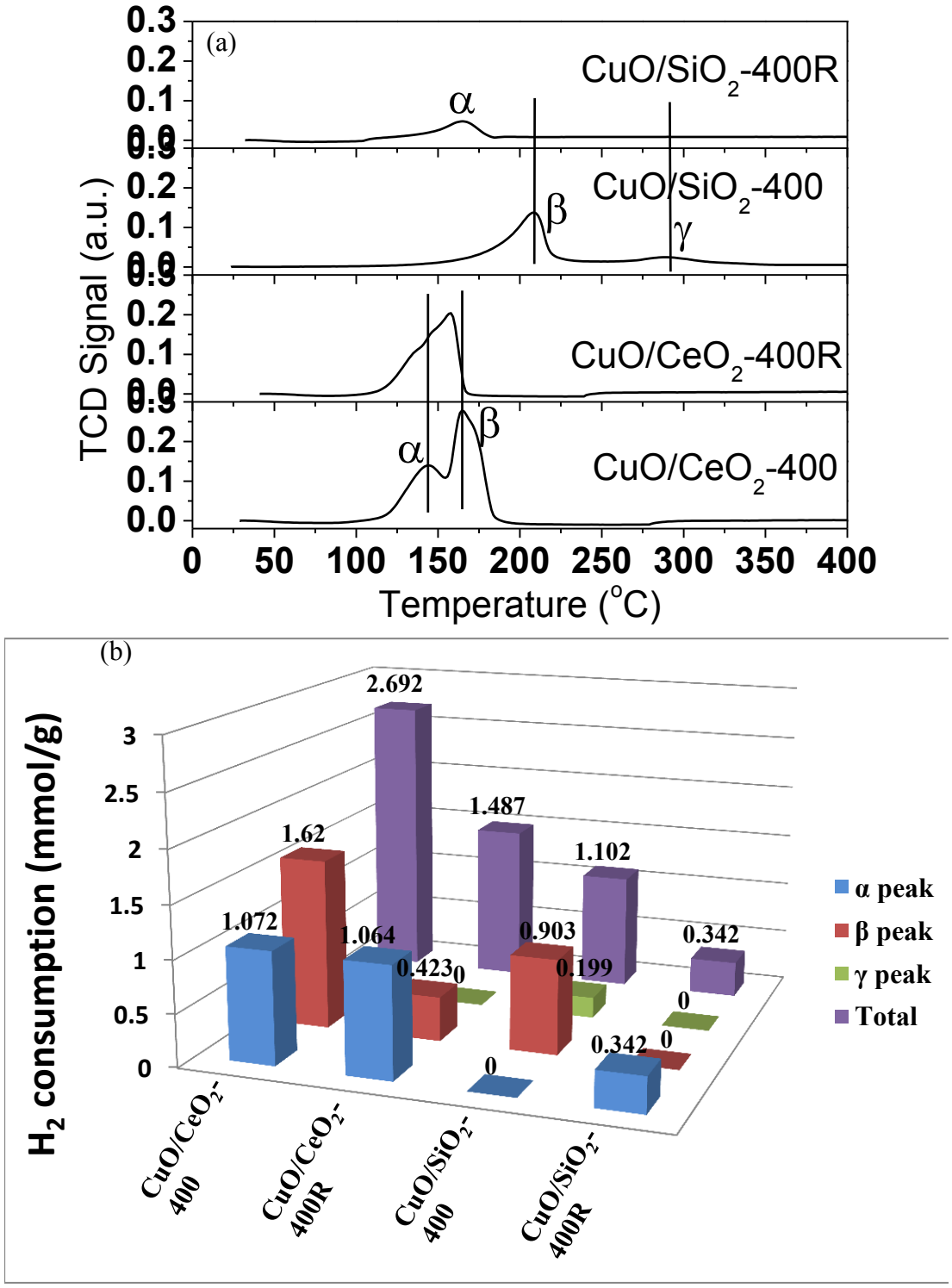

Figure 5.9. (a) H_2-TPR profiles and (b) H_2 consumption of CuO/CeO_2-400 and CuO/SiO_2-400 before and after reduction treatment.

significantly after the reduction treatment and surface area of CuO/CeO_2-400R decreased after the reduction treatment.

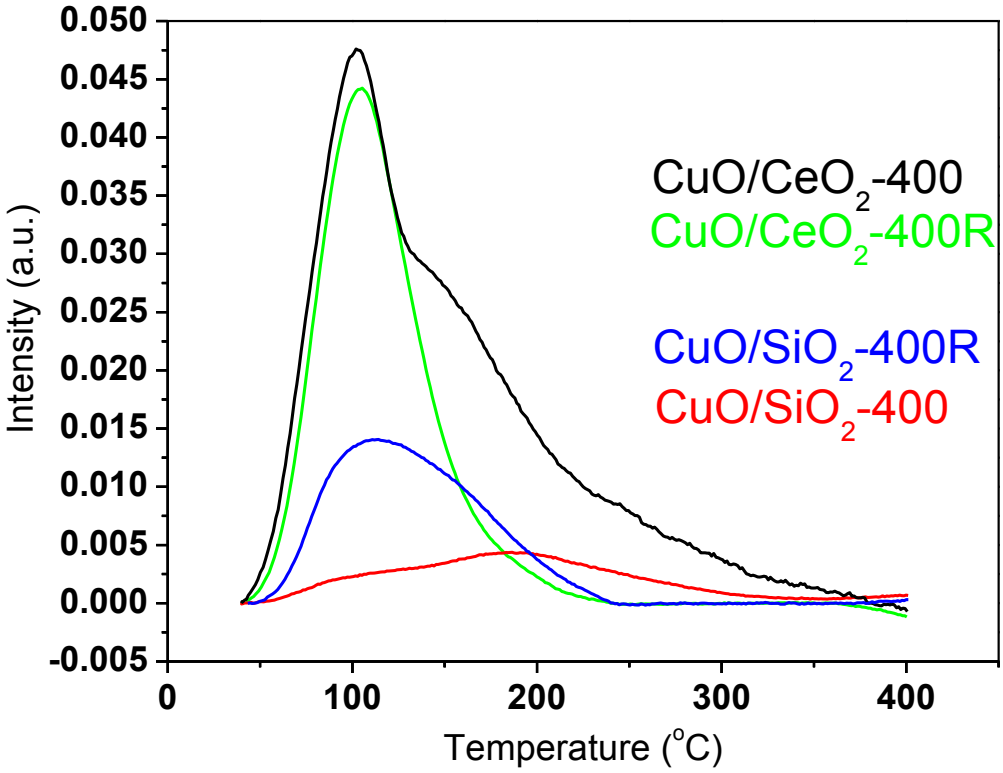

Figure 5.10. CO-TPD of CuO/CeO_2 and CuO/SiO_2 before and after reduction treatment.

Typical CO-TPD profiles of CuO/CeO_2-400 and CuO/SiO_2-400 before and after reduction were shown in Fig. 5.10. Generally, CO desorbs as CO_2 during the heating process produced by the reaction of adsorbed CO with lattice oxygen. CuO/CeO_2-400 showed two desorption peaks; one peak at 100 ^oC and another peak at 150-160 ^oC. The first peak was attributed to desorption of CO_2 produced from the reaction of adsorbed CO with CeO_2 surface [33, 34]. The second peak was assigned to desorption of CO_2, which was formed by adsorbed CO developing into bidentate carbonate species on the reactive sites [33, 34]. CuO/SiO_2-400 also showed two desorption peaks at 95 and 192 ^oC;

however, the intensity of these two peaks was very low in comparison to the peaks of CuO/CeO_2-400. After the reduction of CuO/CeO_2-400, only one peak at 104 ^oC was observed for CuO/CeO_2-400R because only CeO_2 lattice could be available for CO reaction after CuO being reduced to metallic Cu. Surprisingly, CuO/SiO_2-400R still showed one peak at 106 ^oC with higher intensity compared to that of CuO/SiO_2-400, implying that more CO_2 could desorb at a lower temperature. A possible explanation is that after the reduction treatment, the presence of $[SiO_3]^{2-}$ rings increased suggesting that there was more active oxygen formed in SiO_3 rings [23].

For the CuO/CeO_2-400 and CuO/SiO_2-400 catalysts before and after reduction, the light-off curves of CO conversion as a function of temperature were shown in Fig. 5.11. The temperatures (T_{50}) where 50% CO conversion occurred for the CuO/CeO_2-400 and CuO/CeO_2-400R samples were at 88 and 94 ^oC respectively as shown in Table 5.2. The CuO/CeO_2-400 sample converted 100% CO at 220 ^oC, and the CuO/CeO_2-400R sample converted maximum 92% CO at 280 ^oC. On the other hand, 50% CO conversion for both CuO/SiO_2-400 and CuO/SiO_2-400R samples were found at ~240 ^oC. The maximum CO conversions for the CuO/SiO_2-400 and CuO/SiO_2-400R samples were 72% at 324 ^oC and 68% at 298 ^oC, respectively. Clearly, the CuO/CeO_2-400 sample showed the best performance of CO oxidation conversion, indicating the effect of reducible CeO_2 support on the catalytic efficiency. Again, an unexpected result could be seen that both of the reduced catalysts could still convert CO into CO_2 due to the reducibility of CeO_2 support ($2CeO_2 + CO \rightarrow Ce_2O_3 + CO_2$) and the presence of Cu-O-Ce solid solution at the interface for the CuO/CeO_2-400R sample, and the presence of copper species in threefold SiO_3 rings for the CuO/SiO_2-400R sample.

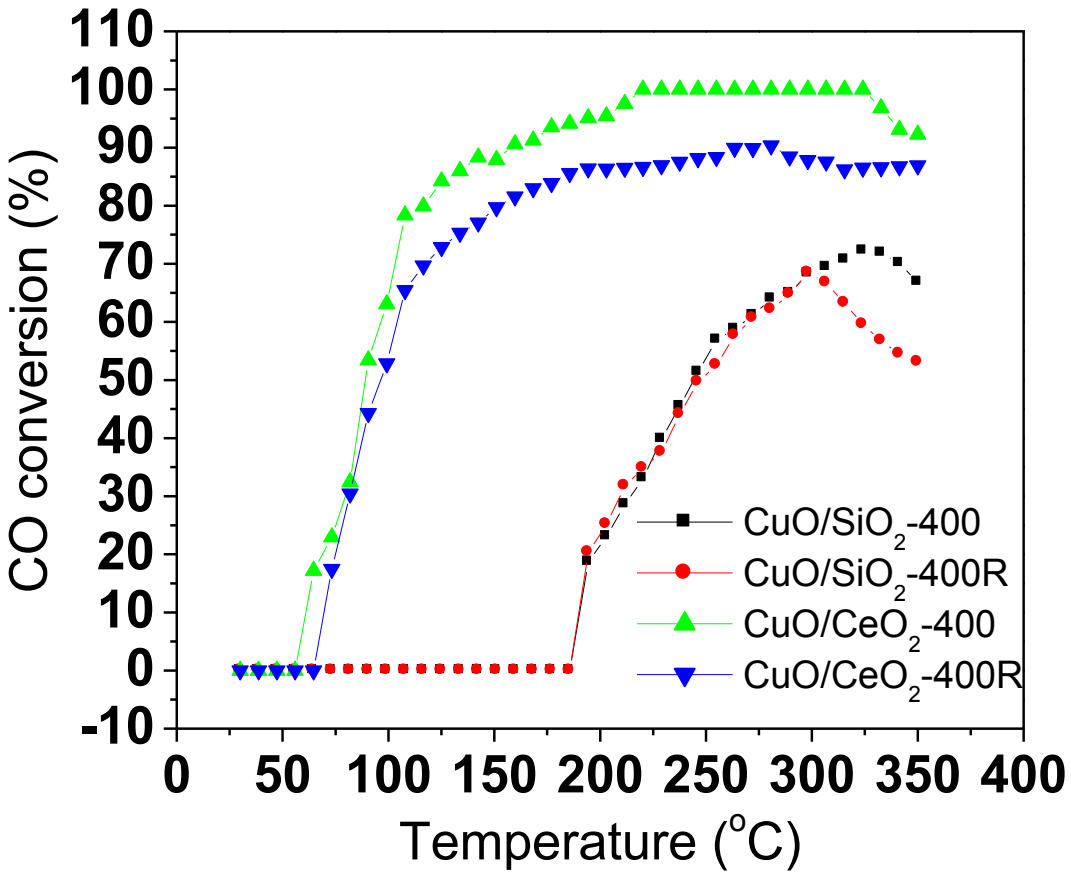

Figure 5.11. CO conversion of CuO/CeO_2-400 and CuO/SiO_2-400 before and after reduction treatment.

5.3.3. TEM analysis

Fig. 5.12 exhibited typical TEM images of CeO_2 nanorods and SiO_2 nanospheres samples before and after CuO loading. In Fig. 5.12a, as-synthesized CeO_2 nanorods were 50-150 nm long and 5-20 nm in width. Fig. 5.12b showed that SiO_2 nanospheres were ~300 nm in diameter. After CuO loading, no visible size/shape change was observed for

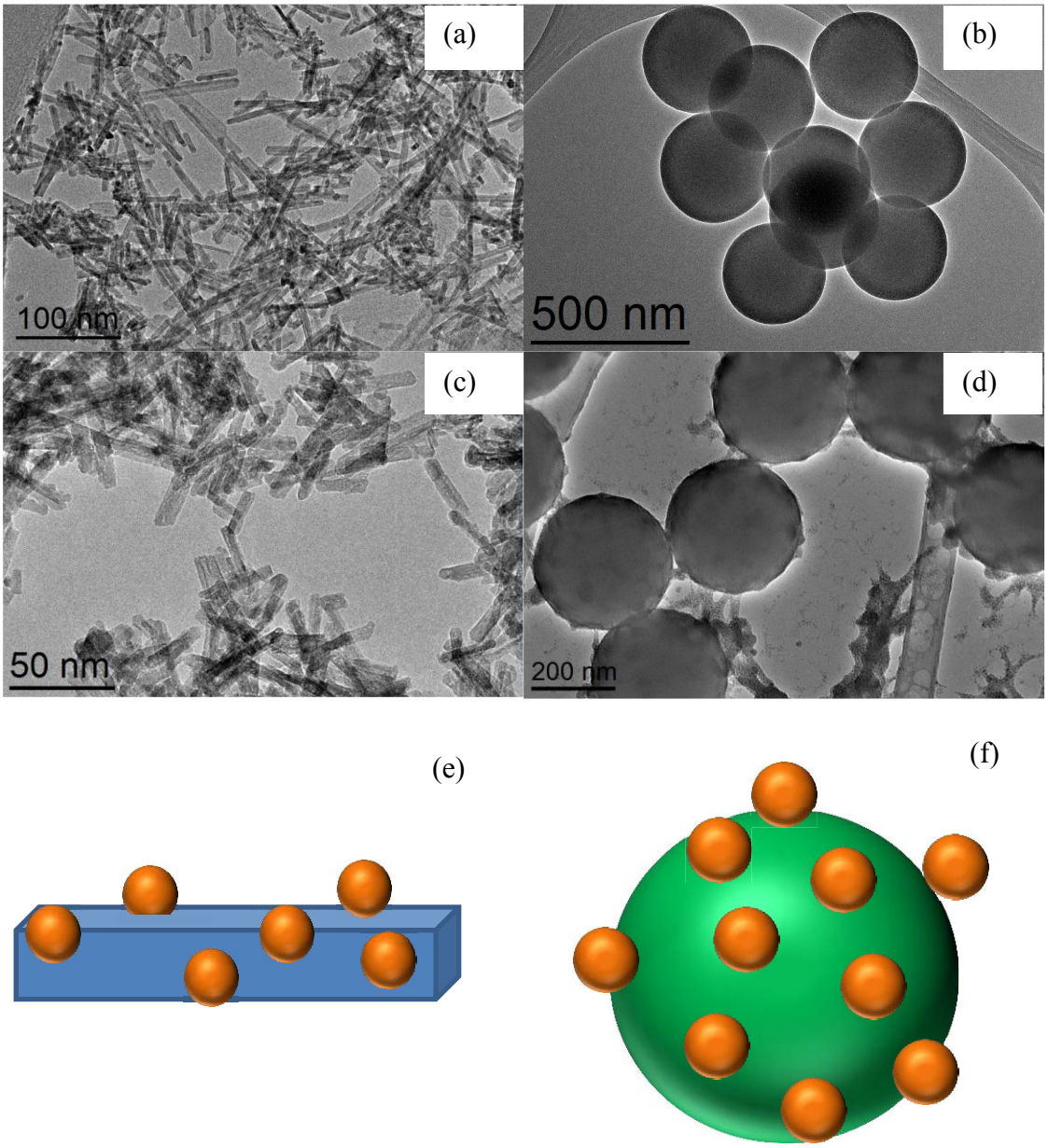

Figure 5.12. TEM images of (a) CeO_2 nanorods, (b) SiO_2 nanospheres, (c) CuO/CeO_2-400, and (d) CuO/SiO_2-400. Schematical representations of (e) CuO/CeO_2 and (f) CuO/SiO_2.

SiO_2 nanospheres. These results are consistent with XRD and BET surface area analysis about the particle size. Fig. 5.12 c and d revealed TEM images of the CuO/CeO_2-400 and CuO/SiO_2-400 samples after CuO loading. A uniform dispersion of CuO on SiO_2 was

clearly shown, while no apparent CuO was found on CeO_2 nanorods consistent with the XRD analysis (Fig. 5.1c). Fig. 5.12e and 5.12f schematically showed how CuO particles were attached onto CeO_2 nanorods and SiO_2 nanoshperes, respectively.

In high resolution TEM (HRTEM) image of the CuO/SiO_2-400 sample, it appears that some small CuO nanoparticles were attached with SiO_2 nanosphere with a partially embedded CuO as shown in Fig. 5.13a. In the inset of Fig. 5.13a, HRTEM image of SiO_2 provided an evidence for their amorphous structure. The boundary of CuO particle can easily be separated from SiO_2, indicating that CuO and SiO_2 did not make very strong bond or interaction and this was the main reason of β peak observed in H_2-TPR. Fig. 5.13b showed HRTEM image of CuO/CeO_2-400 where CuO particle interacted with CeO_2 nanorod can be seen. In the inset of Fig. 5.13b, the interface between CuO and CeO_2 showed non-distinguishable boundary of CuO and CeO_2, leading to the conclusion of strong CuO-CeO_2 interaction. This type of strong interaction caused α peak in H_2-TPR. Fig. 5.13c showed HRTEM image of CuO/CeO_2-400 where a CeO_2 nanorod was presented and oriented along [011] projection. In the inset of Fig. 5.13c, the calculated Fast Fourier Transform (FFT) pattern from HRTEM image of CeO_2 nanorod was shown, which indicated that CeO_2 nanorod was a single crystal with [011] growth direction and [001] surface termination along this projection. Fig. 5.13d and 5.13e showed that CeO_2 nanorods exposed (111), (110), and (100) planes with d-spacing of 3.1 Å, 1.9 Å, and 2.7 Å, respectively. Zhou et al. [40] and Pan et al. [41] reported that CeO_2 nanorods prepared by a similar hydrothermal method have dominantly (100) and (110) planes. Our group previously reported the presence of (111) planes in CeO_2 nanorods [42]. Fig. 5.13f

illustrated a schematic representation of CeO_2 nanorod exposing (111), (110) and (100) planes from [10-1] projection.

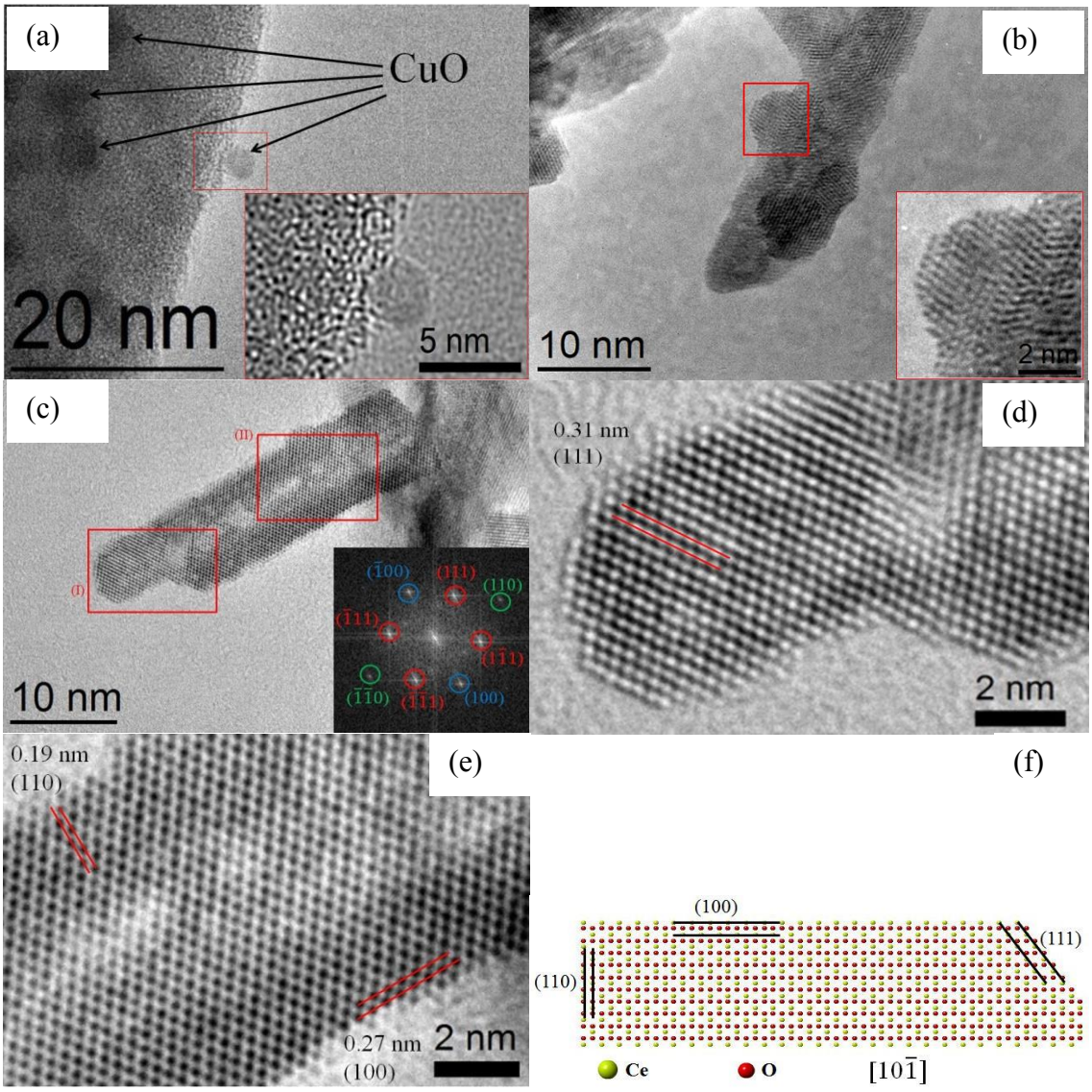

Figure 5.13. HRTEM images of (a) CuO/SiO_2-400, and (b) and (c) CuO/CeO_2-400. FFT of CuO/CeO_2-400 in the inset of (c). HRTEM images of red rectangular section I and II shown in (d) and (e) respectively. (f) Schematic representation of atomic structure of CeO_2 nanorods.

5.4. Discussion

The results discussed above demonstrated that the CuO/CeO_2-400 nanorods sample showed the best catalytic performance toward both H_2 consumption and CO oxidation. It also showed that the catalytic efficiency of CuO/CeO_2 nanorods decreased with increasing the oxidation temperatures, which was ascribed to the phase separation of CuO and CeO_2 at elevated temperature. The presence of CuO in CuO/CeO_2-600 was exhibited in Fig. 5.1c and 5.1d. The XRD result agreed with the H_2-TPR analysis because the γ peak corresponded to bulk CuO can be found in CuO/CeO_2-600 (Fig. 5.5c). The bulk CuO had higher reduction temperature and also could cover up the surfaces of CeO_2 where Cu-O-Ce solid solution was formed, which has a negative effect on the catalytic activity. In the Cu-O-Ce solid solution, Cu^{2+} or Cu^{+} ions replace Ce^{4+}, resulting in oxygen vacancies in CeO_2 structure to reach the charge neutrality [39]. The catalysts with oxygen vacancies can adsorb oxygen from the environment near the solid solution surface. The adsorbed oxygen, which is loosely bonded with the catalysts, can be easily accessible to H_2 or CO for conversion reaction at low temperature. Fig. 5.2c illustrated that the characteristic CeO_2 peak shifted to a lower wavenumber at 444 cm^{-1} for the CuO/CeO_2-400 sample due to the incorporation of Cu ions into CeO_2 to form solid solution. This peak continuously shifted to the right with increasing the oxidation temperature in the CuO/CeO_2 samples. This Raman peak shifting attests a lower concentration of Cu ions incorporated into CeO_2 lattice for the samples treated at higher oxidation temperature. For further verification, the amount of H_2 consumption at α peak (shown in Fig. 5.5b) decreased with increasing the oxidation temperature in the CuO/CeO_2 catalysts, and this result was in agreement with Raman and XRD analysis as discussed above.

The CuO/SiO_2 samples showed an opposite catalytic activity trend in comparison with the CuO/CeO_2 samples as the catalytic efficiency of the CuO/SiO_2 samples increased with increasing the oxidation temperature. A probable mechanism was suggested based on the presence of threefold $[SiO_3]^{2-}$ rings as Raman spectra showed a gradual increase of D_2 peak with increasing the oxidation temperature of the CuO/SiO_2 samples as shown in Fig. 5.2d.

5.5. Conclusion

The reducibility and surface structure of oxide supports showed a significant effect on the catalytic activity toward CO oxidation and hydrogen consumption in supported CuO_x catalysts. The CuO/CeO_2 nanorods exhibited a great enhancement in catalytic efficiency than the CuO/SiO_2 nanospheres. Incorporation of Cu ions in CeO_2 lattice promoted the lower reduction temperature and enhanced the catalytic efficiency by increasing oxygen mobility via redox reaction at the catalyst-support interface. Increasing the oxidation temperature of CuO/CeO_2 decreased the catalytic activity by lowering the amount of incorporation of Cu in CeO_2 lattice. Conversely, increasing oxidation temperature of CuO/SiO_2 increased the presence of threefold SiO_3 rings, and incorporating Cu into these rings enhanced the catalytic efficiency. Both CuO/CeO_2-400R and CuO/SiO_2-400R samples after reduction treatment still displayed H_2 consumption and CO conversion even although CuO was not detected in XRD analysis. The activity of the CuO/CeO_2 and CuO/SiO_2 catalysts highly depends on the catalyst-support interaction in which reducible oxide support acts a significant role through redox reaction.

5.6. References

1. Aguila, C.; Gracia, F.; Araya, P. CuO and CeO_2 catalysts supported on Al_2O_3, ZrO_2 and SiO_2 in the oxidation of CO at low temperature. *Appl. Catal. A: Gen.*, **2008**, 343, 16-24.

2. Sun, S.; Mao, D.; Yu, J.; Yang, Z.; Lu, G.; Ma, Z. Low-temperature CO oxidation on CuO/CeO_2 catalysts: the significant effect of copper precursor and calcination temperature. *Catal. Sci. Technol*., **2015**, 5, 3166-3181.

3. Snapkauskienė, V.; Valinčius, V.; Valatkevičius, P. Experimental study of catalytic CO oxidation over CuO/Al_2O_3 deposited on metal sheets. *Catal. Today*, **2011**, 176, 77-80.

4. Mallick, K.; Scurrell, M. S. CO oxidation over gold nanoparticles supported on TiO_2 and TiO_2-ZnO: catalytic activity effects due to surface modification of TiO_2 with ZnO. *Appl. Catal. A: Gen*., **2003**, 253, 527-536.

5. Wang, Y. G.; Yoon, Y.; Glezakou, V. A.; Li, J.; Rousseau, R. The Role of reducible oxide-metal cluster charge transfer in catalytic processes: new insights on the catalytic mechanism of CO oxidation on Au/TiO_2 from ab Initio molecular dynamics. *J. Am. Chem. Soc*., **2013**, 135, 10673-10683.

6. Kang, M. Y.; Yun, H. J.; Yu, S.; Kim, W.; Kim, N. D.; Yi, J. Effect of TiO_2 crystalline phase on CO oxidation over CuO catalysts supported on TiO_2. *J. Mol. Catal. A: Chem.*, **2013**, 368-369, 72-77.

7. Venezia, A. M.; Liotta, L. F.; Pantaleo, G.; La Parola, V.; Deganello, G.; Beckc, A.; Koppány, Z.; Frey, K.; Horváth, D.; Guczi, L. Activity of SiO_2 supported gold-palladium catalysts in CO oxidation. *Appl. Catal. A: Gen*. **2003**, 251, 359-368.

8. Mai, H. X.; Sun, L. D.; Zhang, Y. W.; Si, R.; Feng, W.; Zhang, H. P.; Liu, H. C; Yan, C. H. Shape-selective synthesis and oxygen storage behavior of ceria nanopolyhedra, nanorods, and nanocubes. *J. Phys. Chem. B,* **2005**, 109, 24380-24385.

9. Shen, M.; Wang, X.; An, Y.; Wen, D.; Zhao, M.; Wang, J. Dynamic oxygen storage capacity measurements on ceria-based material. *J. Rare Earth*, **2007**, 25, 48-52.

10. Porsin, A. V.; Alikin, E. A.; Bukhtiyarov, V. I. A low-temperature method for measuring oxygen storage capacity of ceria-containing oxides. *Catal. Sci. Technol*. **2016**, 6, 5891-5898.

11. Maciel, C. G.; Silva, T. D. F.; Hirooka, M. I.; Belgacem, M. N.; Assaf, J. M. Effect of nature of ceria support in CuO/CeO_2 catalyst for PROX-CO reaction. *Fuel* **2012**, 97, 245-252.

12. Gurbani, A.; Ayastuy, J. L.; Gonzalez-Marcos, M. P.; Herrero, J. E.; Guil, J. M.; Gutierrez-Ortiz, M. A. Comparative study of $CuO\text{-}CeO_2$ catalysts prepared by wet-impregnation and deposition-precipitation. *Int. J. Hydrogen Energ.* **2009**, 34, 547-553.

13. Marino, F.; Schonbrod, B.; Moreno, M.; Jobbagy, M.; Baronetti, G.; Laborde, M. CO preferential oxidation over $CuO\text{-}CeO_2$ catalysts synthesized by the urea thermal decomposition method. *Catal. Today* **2008**, 133-135, 735-742.

14. Avgouropoulos, G.; Ioannides, T. Selective CO oxidation over CuO-CeO_2 catalysts prepared via the urea-nitrate combustion method. *Appl. Catal. A: Gen.* **2003**, 244, 155-167.

15. Avgouropoulos, G.; Ioannides, T. Effect of synthesis parameters on catalytic properties of CuO-CeO_2. *Appl. Catal. B: Environ*. **2006**, 67, 1-11.

16. Nandanwar, R.; Singh, P.; Haque, F. Z. Synthesis and characterization of SiO_2 nanoparticles by sol-gel process and its degradation of methylene blue. *ACS J*. **2015**, 5, 1-10.

17. Xu, J. F.; Ji, W.; Shen, Z. X.; Tang, S. H. Preparation and characterization of CuO nanocrystals. *J. Solid State Chem*., **1999**, 147, 516-519.

18. Homaunmir, V.; Tohidi, S. H.; Grigoryan, G. Characterization of sol-gel derived CuO@SiO_2 nano catalysts towards gas phase reactions. *Iran J. Chem. Chem. Eng.*, **2013**, 32, 37-44.

19. Zheng, X.; Wang, S.; Wang, S.; Zhang, S.; Huang, W.; Wu, S. Copper oxide catalysts supported on ceria for low-temperature CO oxidation. *Catal. Commun*. **2004**, 5, 729-732.

20. Shan, W.; Shen, W.; Li, C. Structural characteristics and redox behaviors of $Ce_{1-x}Cu_xO_y$ solid solutions. *Chem. Mater*., **2003**, 15, 4761-4767.

21. Wu, Z.; Li, M.; Howe, J.; Meyer III, H. M.; Overbury, S. H. Probing defect sites on CeO_2 nanocrystals with well-defined surface planes by Raman spectroscopy and O_2 adsorption. *Langmuir*, **2010**, 26, 16595-16606.

22. Malinovsky, V. K.; Novikov, V. N.; Surovtsev, N. V.; Shebanin, A. P. Investigation of amorphous states of SiO_2 by Raman scattering spectroscopy. *Phys. Solid State*, **2000**, 42, 65-71.

23. Perez-Robles, F.; Garcia-Rodriguez, F. J.; Jimenez-Sandoval, S.; Gonzalez-Hernandez, J. Raman study of copper and iron oxide particles embedded in an SiO_2 matrix. *J. Raman Spectrosc*. **1999**. 30, 1099-1104.

24. Chen, K.; Bao, Z.; Shen, J.; Wu, G.; Zhou, B.; Sandhage, K. H. Freestanding monolithic silicon aerogels. *J. Mater. Chem*. **2012**, 22, 16196-16200.

25. Borowicz, P.; Latek, M.; Rzodkiewicz, W.; Laszcz, A.; Czerwinski, A.; Ratajczak, J. Deep-ultraviolet Raman investigation of silicon oxide: thin film on silicon substrate versus bulk material. *Adv. Nat. Sci.: Nanosci. Nanotechnol*. **2012**, 3, 045003 (7 pp).

26. Zhong, K.; Xue, J.; Mao, Y.; Wang, C.; Zhai, T.; Liu, P.; Xia, X.; Li, H.; Tong, Y. Facile synthesis of CuO nanorods with abundant adsorbed oxygen concomitant with high surface oxidation states for CO oxidation. *RSC. Adv*. **2012**, 2, 11520-11528.

27. Debbichi, L.; Marco de Lucas, M. C.; Pierson, J. F.; Kruger, P. Vibrational properties of CuO and Cu_4O_3 from first-principles calculations, and Raman and infrared spectroscopy. *J. Phys. Chem. C*, **2012**, 116, 10232-10237.

28. Kliche, G.; Popovic, Z. V. Far-infrared spectroscopic investigations on CuO. *Phys. Rev. B*, **1990**, 42, 10060-10066.

29. Li, Z.; Tong, K.; Shi, R.; Shen, Y.; Zhang, Y.; Yao, Z.; Fan, J.; Thwaites, M.; Shao, G. Reactive plasma deposition of high quality single phase CuO thin films suitable for metal oxide solar cells. *J. Alloy Comp*., **2017**, 695, 3116-3123.

30. Galeener, F. L.; Geissberger, A.E. Vibrational dynamics in 30Si-substituted vitreous SiO_2. *Phys. Rev. B*, **1983**, 27, 6199-6204.

31. Brinker, C. J.; Brow, R. K.; Tallant, D. R.; Kirkpatrick, R. J. Surface structure and chemistry of high surface area silica gels. *J. Non-Cryst. Solids*, **1990**, 120, 26-33.

32. Yuan, P.; He, H. P.; Wu, D. Q.; Wang, D. Q.; Chen, L. J. Characterization of diatomaceous silica by Raman spectroscopy. *Spectrochim. Acta A*, **2004**, 60, 2941-2945.

33. Shen, W.; Mao, D.; Luo, Z.; Yu, J. CO oxidation on mesoporous SBA-15 supported CuO-CeO_2 catalyst prepared by a surfactant-assisted impregnation method. *RSC. Adv*. **2017**, 7, 27689-27698.

34. Zheng, Y.; Mao, D.; Sun, S.; Fu, G. CO oxidation on CuO/CeO_2 catalyst prepared by solvothermal synthesis: influence of catalyst activation temperature. *J. Nanopart. Res*. **2015**, 17, 471 (1-12).

35. Song, C.; Wang, C.; Zhu, H.; Wu, X. Dong, L; Chen, Y. Preparation, characterization and catalytic activity for CO oxidation of SiO_2 hollow spheres supporting CuO catalysts. *Catal. Lett*., **2008**, 120, 215-220.

36. Jiang, X.; Lu, G.; Zhou, R.; Mao, J.; Chen, Y.; Zheng, X. Studies of pore structure, temperature-programmed reduction performance, and micro-structure of CuO/CeO_2 catalysts. *Appl. Surf. Sci*., **2001**, 173, 208–220.

37. Wang, Z.; Wang, Q.; Liao, Y.; Shen, G.; Gong, X.; Han, N.; Liu, H.; Chen, Y. Comparative study of CeO_2 and doped CeO_2 tailored oxygen vacancies for CO oxidation. *ChemPhysChem*, **2011**, 12, 2763-2770.

38. Zeng, S.; Zhang, W.; Sliwa, M.; Su, H. Comparative study of CeO_2/CuO and CuO/CeO_2 catalysts on catalytic performance for preferential CO oxidation. *Int. J. Hydrogen Energ*., **2013**, 38, 3597-3605.

39. Shan, W.; Feng, Z.; Li, Z.; Zhang, J.; Shen, W.; Li, C. Oxidative steam reforming of methanol on $Ce_{0.9}Cu_{0.1}O_y$ catalysts prepared by deposition-precipitation, coprecipitation, and complexation-combustion methods. *J. Catal*., **2004**, 228, 206-217.

40. Zhou, K.; Wang, X.; Sun, X.; Peng, Q.; Li, Y. Enhanced catalytic activity of ceria nanorods from well-defined reactive crystal planes. *J. Catal*., **2005**, 229, 206-212.

41. Pan, C.; Zhang, D.; Shi, L.; Fang, J. Template-Free Synthesis, Controlled Conversion, and CO Oxidation Properties of CeO_2 Nanorods, Nanotubes, Nanowires, and Nanocubes. *Eur. J. Inorg. Chem*., **2008**, 2429-2436.

42. Mock, S. A.; Sharp, S. E.; Stoner, T. R.; Radetic, M. J.; Zell, E. T.; Wang, R. CeO_2 nanorods-supported transition metal catalysts for CO oxidation. *J. Colloid Interface Sci*. **2016**, 466, 261-267.

43. Liu, W.; Flytzani-Stephanopoulos, M. Total oxidation of carbon monoxide and methane over transition metal fluorite oxide composite catalysts: Catalyst composition and activity. *J. Catal*. **1995**, 153, 304−316.

Chapter 6: CeO_2 nanorods and SiO_2 nanospheres composite supported CuO catalysts for the application of CO oxidation

In this chapter, synthesized CeO_2 nanorods and SiO_2 nanospheres were mixed in various ratios and 10 wt% CuO nanoparticles were impregnated onto CeO_2-SiO_2 composite using thermal decomposition method. X-ray diffraction and Raman spectroscopy were used to confirm the presence of CeO_2, SiO_2, and CuO. Agglomeration of CeO_2 nanorods were stopped by introducing SiO_2 nanospheres in the catalyst system and this phenomenon increased the chance to expose CeO_2 surface to CuO nanoparticles in order to form higher amount of surface defects (incorporation of Cu ions and oxygen vacancies) and to have higher synergistic interaction between CuO and CeO_2. H_2 temperature programmed reduction (TPR) and CO oxidation experiments suggested an enhanced low-temperature catalytic performance for 1:1 ratio mixture of CeO_2 and SiO_2 due to a strong interfacial interaction among SiO_2-CeO_2-CuO.

6.1. Introduction

Cerium oxide (CeO_2) and silica (SiO_2) have been widely used as substrates in supported-metal catalysts for many industrial applications, such as catalytic converter [1, 2], water-gas shift reactions [3], SO_2 reduction [4], ethanol reforming [5, 6], and photosynthesis [7], etc. Compared to the unsupported catalysts, both CeO_2 and SiO_2 supports can significantly increase the dispersion and thermal stability of catalyst nanoclusters; however, CeO_2 is also considered as an active support due to oxygen storage capacity and strong interactions in supported-metal catalysts. For example, Huang

et al. [8] reported that CeO_2 supported Au catalyst achieved 100% CO conversion at 170 ^oC due to the presence of reactive oxygen at the surface of CeO_2 and a synergistic strong interaction between support Au and CeO_2. On the other hand, Venezia et al. [9] showed that SiO_2 supported Au catalyst attained 100% CO conversion over 450 ^oC, indicating a weak metal-support interaction. A mix of these oxide supports can act differently as there can be a synergistic interaction between the oxide supports due to the formation of Si-O-Ce bond at the interface [10]. Xi et al. [11] mixed CeO_2, Fe_2O_3, and MnO_2 with SiO_2 support for better catalytic activity. They reported that SiO_2 supported CuO catalyst achieved 100% CO at 280 ^oC, and after introducing Fe_2O_3, MnO_2, and CeO_2 separately in the catalyst system a complete CO conversion occurred at 240, 200, and 160 ^oC respectively, which were 40, 80, and 120 ^oC correspondingly lower than CuO/SiO_2. They suggested that these added metal oxides increased the oxygen mobility of catalyst by promoting Cu^+ species in copper oxides. CeO_2-SiO_2 composite supported gold catalyst was reported by Huili et al. [12], and they mentioned that CeO_2 enriched oxygen mobility to exhibit high CO conversion activity and SiO_2 promoted the thermal stability of gold catalysts. Controlling the shape and size of oxide supports can affect the catalytic activity due to different exposed surfaces [13]. CeO_2 nanorods exposed highly reactive {110} and {100} planes and CeO_2 nanoparticles have stable {111} planes [13, 14]. Wang et al. [13] presented that CeO_2 nanorods supported CuO catalysts can obtain higher catalytic efficiency than CeO_2 nanoparticles or nanospheres supported CuO catalysts due to the presence of highly reactive planes in CeO_2 nanorods. In this chapter, we synthesized CeO_2 nanorods and SiO_2 nanospheres composite with varied compositions and impregnated 10 wt% CuO in shape-controlled oxide composites. A systematic study was

conducted to understand the synergistic interaction among CeO_2, SiO_2, and CuO and to investigate the effect of various composition of oxide composite support on low-temperature CO oxidation.

6.2. Experimental

6.2.1. Catalyst preparation

A hydrolysis method (modified Stober method) was used to synthesize silica (SiO_2) nanospheres. First, a mixture of 9 mL of deionized water and 38.2 mL of ethanol was prepared in which 2 mL of Tetraethoxysilane (TEOS 99%) was added. Then, 50 mL of 28-30% NH_4OH was added dropwise to the solution while it was stirred vigorously. After adding NH_4OH, it was held under continuous magnetic stirring for 4 hrs to complete the reaction. The suspension solution was centrifuged to collect the solid silica. It was then washed with DI water and ethanol. The sample was dried at 60 ^oC overnight. Hydrothermal method was used to synthesize CeO_2 nanorods as reported previously [15]. 0.1 M $Ce(NO_3)_3 \cdot 6H_2O$ and 6 M NaOH solutions were added in 11:1 ratio in a Teflon liner of 200 mL capacity. Before closing the lid of Teflon liner, the mixture was stirred for about 15 seconds. A stainless-steel autoclave along with Teflon liner was heated and kept at 90 ^oC for 48 hrs. When the autoclave cooled down to room temperature, the precipitates were collected via filtration. After filtration, the sample was washed with 500 mL DI water and 50 mL ethanol. It was then dried at 50 ^oC for 12 hrs.

Thermal decomposition method was used to impregnate 10 wt% CuO on CeO_2-SiO_2 composite. The as-synthesized CeO_2 nanorods and SiO_2 nanospheres were mixed in various compositions (0-100 wt%) in 30 mL DI water. It was stirred for 30 mins. Then,

$Cu(NO_3)_2 \cdot 3H_2O$ was added in a stoichiometric ratio in the solution. The composite mixtures were stirred continuously and were heated at 120 ^oC until the water evaporated completely. The collected samples were calcined at 500 ^oC for 5 hrs in air.

6.2.2. Catalyst characterization

X-ray diffraction (XRD), Raman spectroscopy, X-ray photoelectron spectroscopy (XPS), transmission electron microscopy (TEM), BET surface area measurement, temperature programmed reduction (TPR), temperature programmed desorption (TPD), pulse chemisorption to calculate oxygen storage capacity (OSC), and CO oxidation were used to characterize the catalysts and their catalytic activity. The description of these techniques can be found in chapter 2

6.3. Results and discussions

6.3.1. XRD and BET surface area

The XRD patterns of CeO_2-SiO_2 composite supported 10 wt% CuO catalysts were shown in Fig. 6.1. A broad peak with a center at 2θ of 21.7^o confirmed the presence of amorphous SiO_2 in the SiO_2 supported 10 wt% CuO catalysts ($100SiO_2$) [16]. Except for the broad peak at around 21.7^o for amorphous SiO_2 support, all other diffraction peaks can be assigned to monoclinic CuO phase (JCPDS 45-0937) in $100SiO_2$ [17]. Two very sharp peaks at 2θ of 35.6^o and 38.8^o found in $100SiO_2$ sample corresponded to (-111) and (111) planes of CuO. Although the amount of CuO addition was kept constant at 10wt% in all of the eleven catalyst samples, the intensity of CuO peaks became smaller with increasing CeO_2 amount; and finally, these peaks completely disappeared for the CeO_2

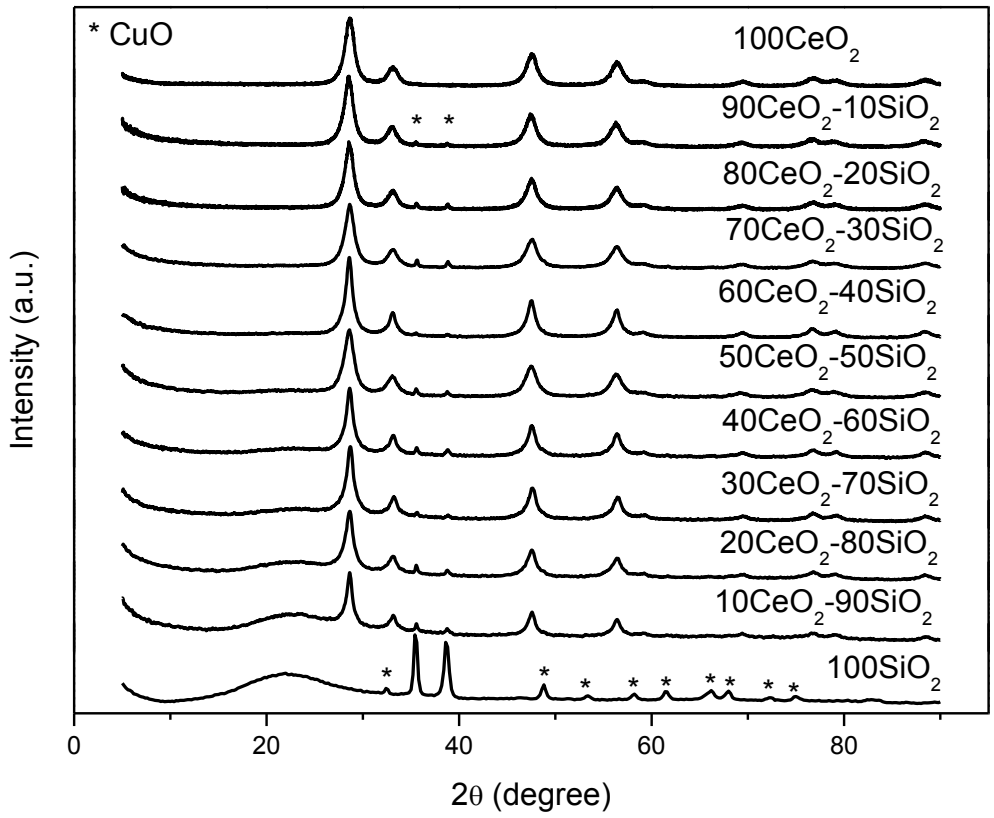

Figure 6.1. XRD patterns of CeO_2-SiO_2 supported CuO catalysts.

supported 10 wt% CuO catalysts ($100CeO_2$). The intensity of SiO_2 peak found at 21.7^o in $100SiO_2$ decreased with increasing the amount of CeO_2 in the samples. For the rest of the samples from $10CeO_2$-$90SiO_2$ ($xCeO_2$-$(100-x)SiO_2$ referred to $xCeO_2$-$(100-x)SiO_2$ supported 10 wt% CuO catalyst) to $100CeO_2$, the observed CeO_2 diffraction peaks were consistent with fluorite-structured CeO_2 reported in JCPDS data (JCPDS 43-1002). The intensity of those peaks increased with increasing the amount of CeO_2 in the composite samples. This occurrence happened, as reported previously [18], because CuO nanoclusters can form strong interactions with CeO_2 support or even Cu-O-Ce solid solution. Due to the strong CuO-CeO_2 interactions (α, β, γ phases), tiny CuO cluster can be well dispersed on CeO_2 nanorods [2]. Both the high dispersion and formation of Cu-

O-Ce solid solutions could lead to the decreased intensity of CuO phase or even disappearance in the diffraction patterns of CeO_2-SiO_2 composites samples.

Fig. 6.2 showed that BET surface area of the synthesized composite catalysts increased in a fine trend from 12.6 to 39.2 m^2/g with increasing the weight percentage of CeO_2. BET surface area of pure SiO_2 nanospheres, CeO_2 nanorods and CuO nanopowders were 9.72, 64.65 and 4.12 m^2/g, respectively. Thus, the increased surface area of the composite catalysts was due to the addition of CeO_2 in the composite samples.

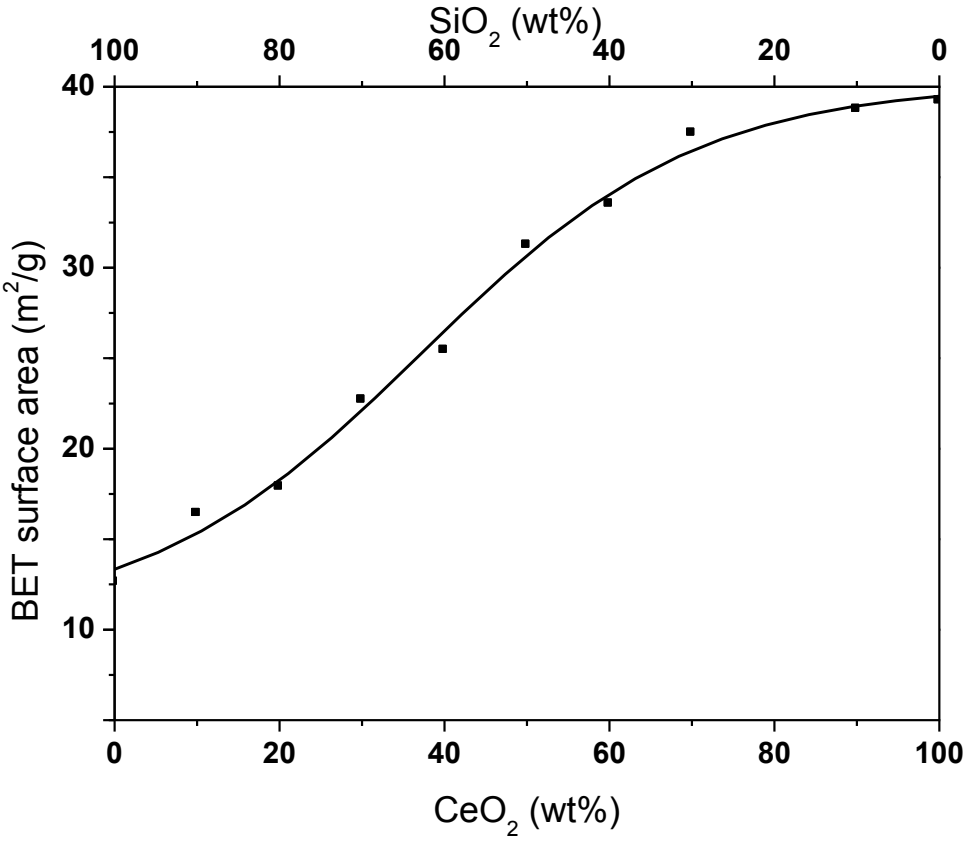

Figure 6.2. BET surface area of CeO_2-SiO_2 supported CuO catalysts.

6.3.2. Raman analysis

Fig. 6.3 showed Raman spectra of CeO_2-SiO_2 composite supported 10 wt% CuO catalysts. One sharp peak observed at 508.6 cm^{-1} for $100SiO_2$ sample which was a mixture of D_1 mode of SiO_2 and B_{2u} mode of CuO [19, 20]. D_1 vibrational mode is due to vibrations of four-membered ring structures of SiO_2. This mixed peak started decreasing with increasing the amount of CeO_2 in the composite catalysts and finally for $100CeO_2$ sample, only B_{2u} mode of CuO peak was observed at 505.5 cm^{-1}. Other Raman peaks found at 288, 379, and 436 cm^{-1} were attributed to D_3, D_4 and symmetric vibrations of oxygen atoms in SiO_2, respectively [21]. Another CuO peak could be seen at 623 cm^{-1} which corresponded to B_{2g} mode [22]. After addition of CeO_2 in the composite catalysts, a peak appeared at 459 cm^{-1} corresponded to F_{2g} vibrational mode of CeO_2 [23]. This peak gradually shifted to the lower frequency with increasing the amount of CeO_2 in the composite catalysts. At first, this F_{2g} peak for $10CeO_2$-$90SiO_2$ sample shifted from 459 cm^{-1} to 452 cm^{-1} for $50CeO_2$-$50SiO_2$. Then this F_{2g} peak of CeO_2 was found at 455 cm^{-1} for $60CeO_2$-$40SiO_2$. This peak again started gradually shifting to the lower frequency from 455 cm^{-1} for $60CeO_2$-$40SiO_2$ to 447 cm^{-1} for $100CeO_2$. The peak shifting was also observed in CeO_2 supported CuO catalysts by several other groups, which was attributed to the strong interactions between CuO and CeO_2 [24, 25]. For example, Shan et al. [26] reported previously that a peak shifting happened due to the presence of oxygen vacancies, leading to the formation of substoichiometric structured CeO_{2-y} ($0 \leq y < 0.5$), which was associated with the formation of solid solution in the presence of copper species. Incorporation of Cu species into CeO_2 lattice can disrupt the Ce-O bond due to the charge and coordination number difference between Cu^{2+} and Ce^{4+}. With the

increased CeO_2 content in the composite samples, the amount of highly interacted CuO or Cu-O-Ce solid solution increases, resulting in a continuous F_{2g} peak shift to the lower frequency. The incorporation of Cu into CeO_2 lattice is also verified by both the decreased intensity of CuO B_{2u} and the broadening of F_{2g} of CeO_2 with the increased CeO_2 content in the composite catalysts. As shown in Fig. 6.3, among all of the composite ($xCeO_2$-$(100-x)SiO_2$) samples, $50CeO_2$-$50SiO_2$ possessed the lowest frequency of F_{2g} peak of CeO_2 found at 452 cm^{-1}, indicating a highest Cu substitution and lattice disruption.

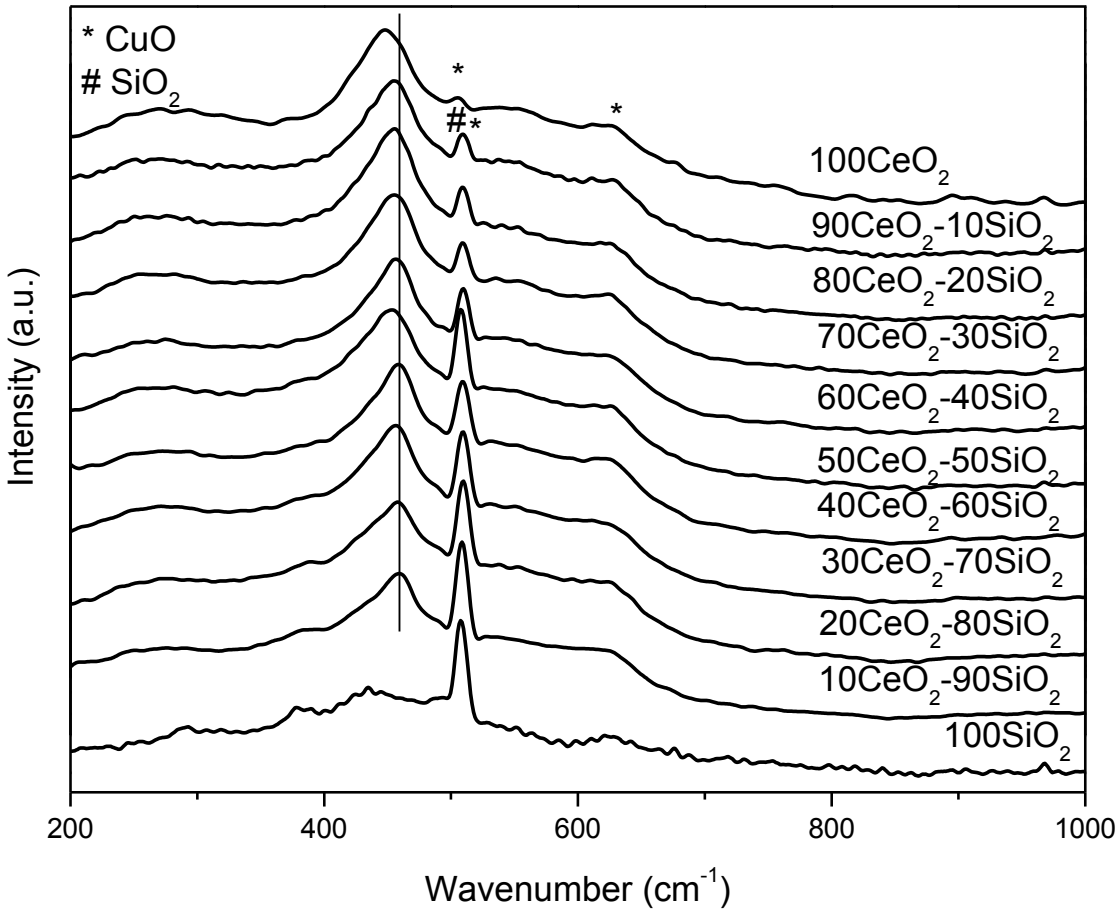

Figure 6.3. Raman spectra of CeO_2-SiO_2 supported CuO catalysts.

6.3.3. XPS analysis

XPS spectra of $10CeO_2$-$90SiO_2$, $50CeO_2$-$50SiO_2$ and $90CeO_2$-$10SiO_2$ were shown in Fig. 6.4. In Fig. 6.4a, $90CeO_2$-$10SiO_2$ sample displayed 7 peaks for Ce 3d at 889.0, 891.5, 895.1, 904.6, 907.4, 910.1, and 913.6 eV, which were called as v, v', v'', v''', u, u', and u'', respectively. Among these peaks, u' and v' were attributed to Ce^{3+} and rest of the 5 peaks were recognized as Ce^{4+} [27, 28]. The peaks (u' and v'), which belong to Ce^{3+}, were not visible for $10CeO_2$-$90SiO_2$ sample, and one peak (u') was not visible for $50CeO_2$-SiO_2 sample. Visibility of only v' peak suggested a low amount of Ce^{3+} present in $50CeO_2$-$50SiO_2$, and non-visibility of these two peaks (u' and v') advised that there was no Ce^{3+} in $10CeO_2$-$90SiO_2$. The intensity of Ce 3d peaks became smaller, and this suggested that the amount of Ce at the surface decreased with decreasing the amount of CeO_2 in the sample. Fig. 6.4b presented spectra of Cu $2p_{3/2}$ where one peak for $10CeO_2$-$90SiO_2$ found at 938 eV corresponded to Cu^{2+} [27]. This peak can also be seen for $50CeO_2$-$50SiO_2$ and $90CeO_2$-$10SiO_2$ samples. Another shoulder peak was observed at 935 – 933 eV for $50CeO_2$-$50SiO_2$ and $90CeO_2$-$10SiO_2$ samples, and this peak was attributed to Cu^{+} [27, 28]. It can be observed that the amount of Cu^{+} was higher in $50CeO_2$-$50SiO_2$ than in $90CeO_2$-$10SiO_2$, and this can happen due to a strong synergistic interaction among Ce, Si, and Cu. Spectra of O 1s were shown in Fig. 6.4c. Only one peak was found at 536 eV for $10CeO_2$-$90SiO_2$; whereas two peaks were seen at 538 – 536 eV and 535 – 534 eV for $50CeO_2$-$50SiO_2$ and $90CeO_2$-$10SiO_2$ samples. Higher energy peak was attributed to adsorbed oxygen, and lower energy peak corresponded to lattice oxygen [29]. Clearly, SiO_2 did not provide any lattice oxygen because there was no low energy peak for $10CeO_2$-$90SiO_2$. In this case, the adsorbed oxygen peak may also come

from –OH present on the surface of SiO_2. Spectra of Si 2p were seen in Fig. 6.4d and one broad peak can be observed for all of the samples. This peak was found at 109.0, 108.4, and 107.8 eV for $90CeO_2$-$10SiO_2$, $50CeO_2$-$50SiO_2$ and $10CeO_2$-$90SiO_2$, respectively. These peaks corresponded to Si^{4+} [30]. All of the peaks in Fig. 6.4 may shift to higher energy compared to the literatures due to the charging effect during the execution of the experiment [27-30].

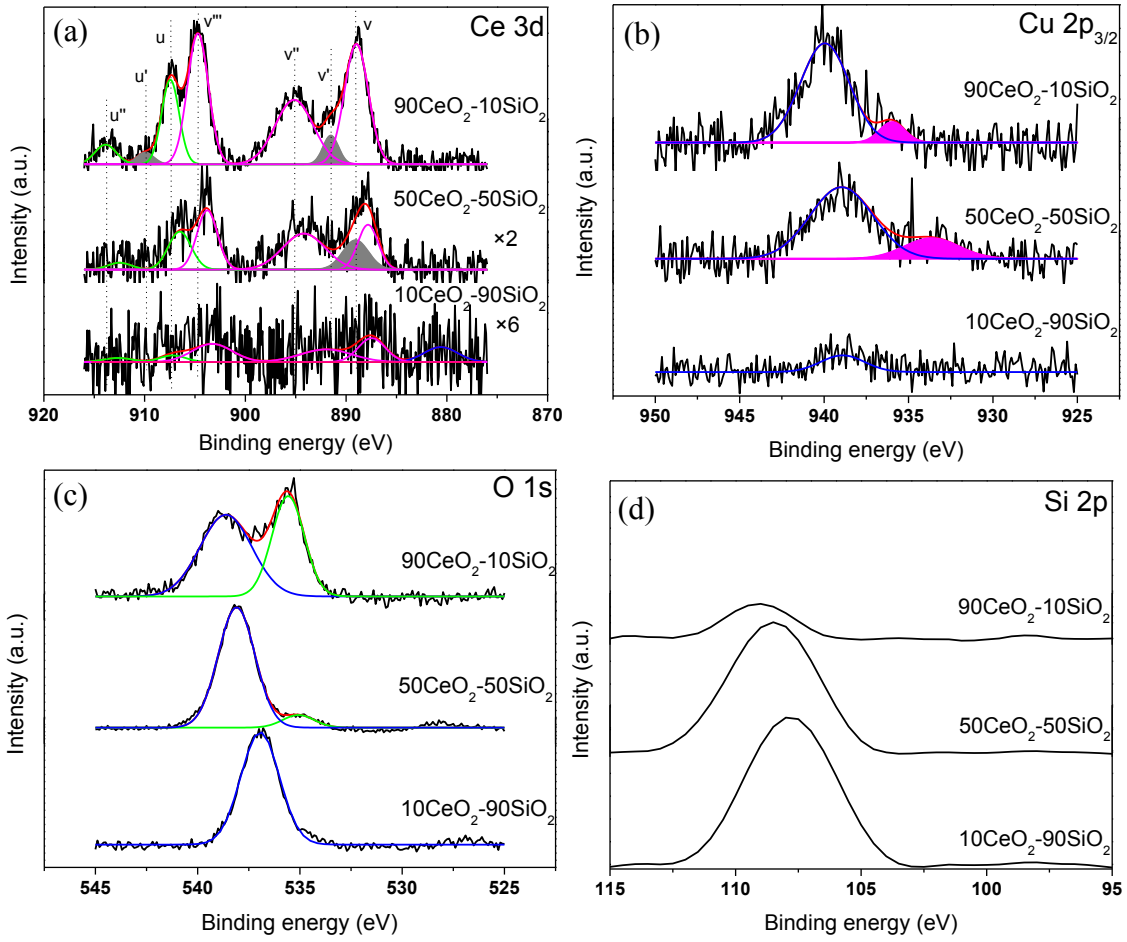

Figure 6.4. XPS spectra of CeO_2-SiO_2 supported CuO catalysts.

6.3.4. TEM analysis

TEM images of CuO on CeO_2-SiO_2 composites were shown in Fig. 6.5. It can be seen in Fig. 6.5a that CeO_2 nanorods were agglomerated in $100CeO_2$ samples and agglomeration of CeO_2 can be harmful to the catalytic efficiency due to lowering the chance of exposing of active surface. After introducing 10 wt % of SiO_2 nanospheres, a part of CeO_2 nanorods was separated by SiO_2 as seen in Fig. 6.5b. Similar agglomerated CeO_2 nanorods could still be found near SiO_2 nanospheres in $70CeO_2$-$30SiO_2$ shown in Fig. 6.5c. CeO_2 nanorods spread out well onto SiO_2 nanospheres in $50CeO_2$-$50SiO_2$ sample observed in Fig. 6.5d, and this increased CeO_2 active surfaces to be exposed. For $30CeO_2$-$70SiO_2$ and $10CeO_2$-$90SiO_2$, a very few CeO_2 nanorods were observed onto SiO_2 nanospheres as shown in Fig. 6.5e and 6.5f, respectively. Fig. 6.5g showed SiO_2 nanospheres, which were 200 – 250 nm in diameter for $100SiO_2$ samples. Although $100SiO_2$ had CuO particles, it cannot be visible because CuO particles were usually almost 5 – 15 nm, which were very small compared to SiO_2 nanospheres. Thus, they were hard to observe at this magnification. CeO_2 nanorods were usually 5 – 15 nm in width and 100 – 150 nm in length and SiO_2 nanospheres had 200 – 250 nm diameter for all of the samples. Fig. 6.6 presented TEM and HRTEM images of $50CeO_2$-$50SiO_2$. In Fig. 6.6a, the surface of SiO_2 nanospheres were not smooth, and few SiO_2 nanospheres were broken. These defects may help in improving the catalytic activity. Fig. 6.6b showed that a single CeO_2 nanorod stayed in between two SiO_2 nanospheres, and Fig. 6.6c showed one CeO_2 nanorod onto SiO_2 nanosphere. As CuO nanoparticles were placed near the interface of SiO_2 and CeO_2, there can be a charge transfer among Ce, O, Cu, and Si due to synergistic interaction among SiO_2, CuO, and CeO_2. HRTEM image shown in

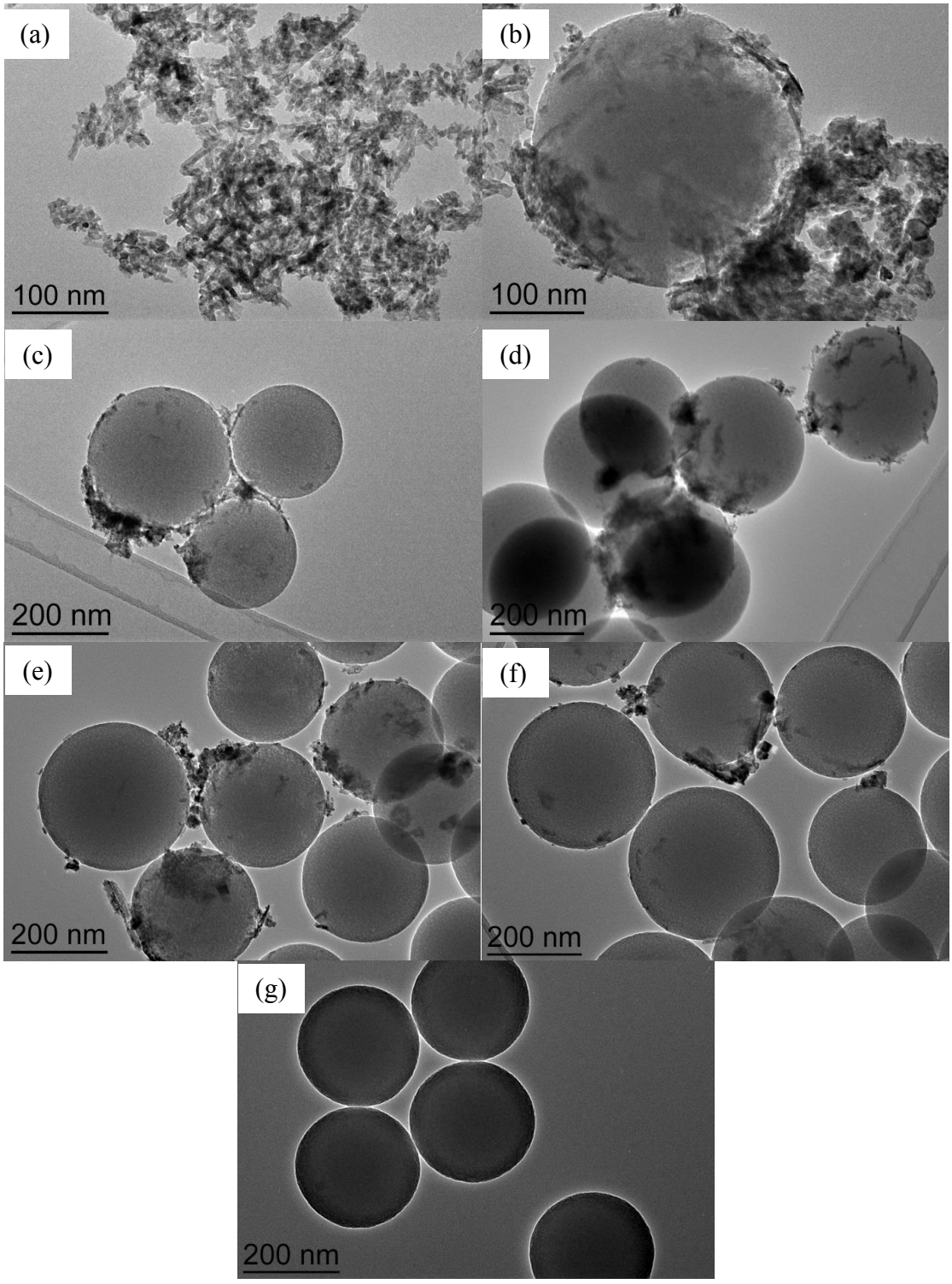

Figure 6.5. TEM images of (a) 100CeO_2, (b) 90CeO_2-10SiO_2, (c) 70CeO_2-30SiO_2, (d) 50CeO_2-50SiO_2, (e) 30CeO_2-70SiO_2, (f) 10CeO_2-90SiO_2, and (g) 100SiO_2.

Fig. 6.6d presented a clear distinguishable boundary between CeO_2 and SiO_2. It can also be seen that CeO_2 nanorods were single crystal and SiO_2 nanospheres were amorphous.

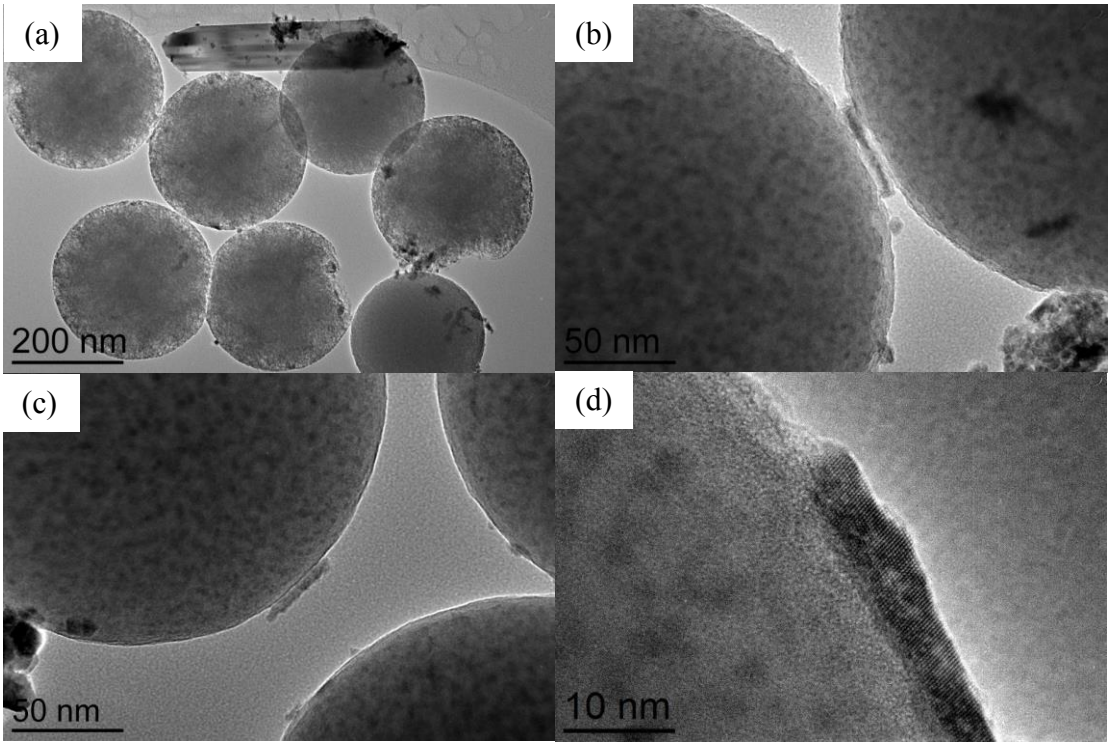

Figure 6.6. TEM (a-c) and HRTEM (d) images of $50CeO_2$-$50SiO_2$ sample.

6.3.5. H_2-TPR

H_2-TPR of CeO_2-SiO_2 composite supported 10 wt% CuO catalysts were observed in Fig. 6.7. Two reduction peaks were found at 250 and 285 ^oC for $100SiO_2$. First peak seen at 250 ^oC was called β peak, which corresponded to reduction of weakly interacted small CuO particles with SiO_2 [31]. The peak (γ peak) found at higher temperature was attributed to reduction of bulk CuO [31]. After introducing 10 wt% CeO_2 in the catalyst system, these peaks shifted to lower temperature (180 and 228 ^oC). This clearly suggested

that there was an effect of CeO_2 on reduction behavior. In this case, β peak corresponded to reduction of small CuO particles, which may have interacted weakly with either SiO_2 nanospheres or CeO_2 nanorods or at the interface of SiO_2-CeO_2. Further addition of CeO_2 caused an appearance of another low-temperature reduction peak (α peak). This peak could be found at 151 ^oC for $20CeO_2$-$80SiO_2$. The α peak corresponded to reduction of strongly interacted small CuO particles with CeO_2 [32]. We previously reported that CuO/SiO_2 nanospheres oxidized at 500 ^oC did not show any α reduction peak [33]. The α and β peak intensity started increasing and γ peak started decreasing with increasing the amount of CeO_2 up to 50 wt%. Increasing of the peak intensity can be associated with the surface oxygen availability. For $50CeO_2$-$50SiO_2$, the α, β, and γ peak were observed at 150, 179, and 227 ^oC, respectively. A large amount of highly-interacted CuO with CeO_2 were present in $50CeO_2$-$50SiO_2$ sample as described in Raman analysis (Fig. 6.3) and many CeO_2 nanorods were not agglomerated (seen in Fig. 6.5d), which increased the chances of exposing active surface of CeO_2. Thus, H_2-TPR was clearly in agreement with Raman and TEM analysis. Table 6.1 represented that the OSC of catalysts increased with increasing CeO_2 until 50 wt% addition and then decreased for further addition of CeO_2. Here, 50-CeO_2-$50SiO_2$ catalyst achieved maximum OSC of 1.56 μmol[O_2]/g. Trovarelli et al. [34] reported that mixing of CeO_2 and SiO_2 at 500-700 ^oC produced a mixture of crystalline CeO_2, amorphous SiO_2 and residual $Ce_{9.33}(SiO_4)_6O_2$. After reoxidation, this complex compound decomposed into amorphous SiO_2 and small CeO_2 crystallites, which increased OSC of the catalyst. With further addition of CeO_2 in our samples, all of the reduction peaks progressively shifted to higher temperature up to 70 wt% CeO_2 additions and then again gradually shifted to the lower temperature up to $100CeO_2$. For $70CeO_2$-

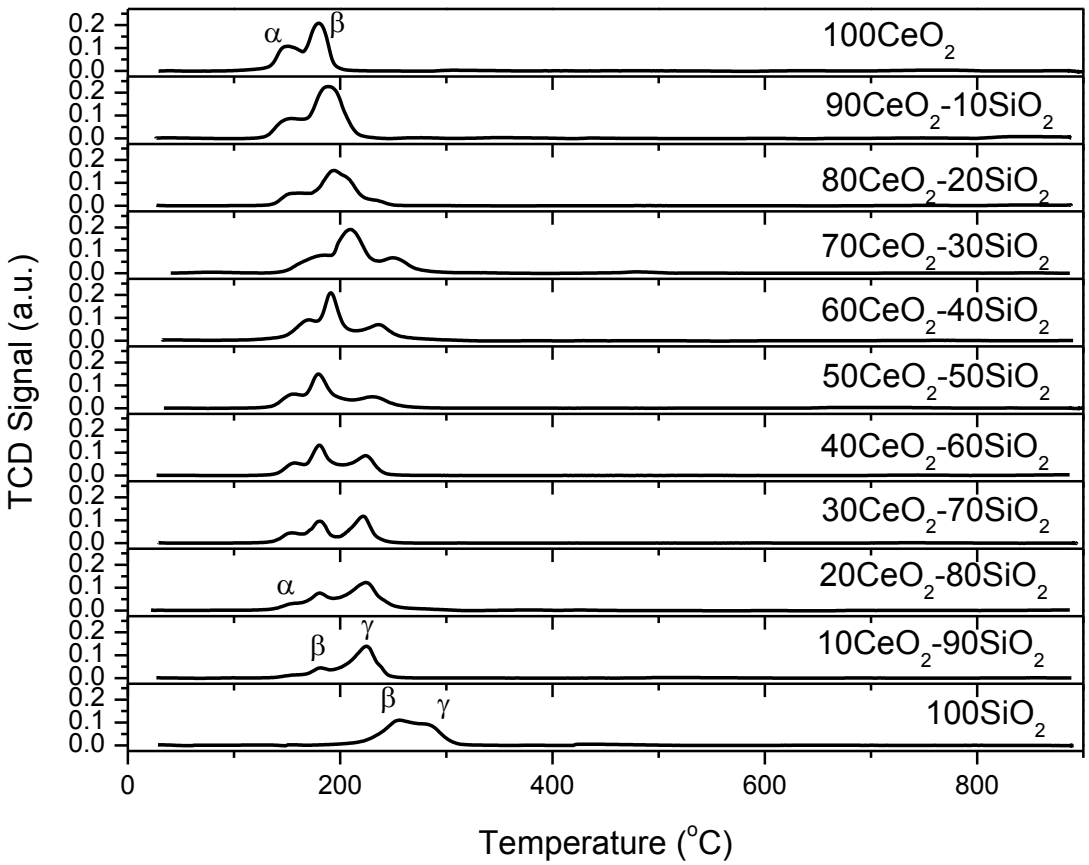

Figure 6.7. H_2-TPR profiles of CeO_2-SiO_2 supported CuO catalysts.

$30SiO_2$ sample, a large part of CeO_2 nanorods were still agglomerated as seen in Fig. 6.5c and thus, the peaks shifted to higher temperatures. The α, β, and γ peak were found at 179, 204, and 249 ^oC respectively for $70CeO_2$-$30SiO_2$. With further increasing the amount of CeO_2 nanorods, the percentage of agglomeration increased (Fig. 6.5a and 6.5b). However, the presence of Cu-O-Ce solid solutions of highly interacted CuO increased in $80CeO_2$-$20SiO_2$, $90CeO_2$-$10SiO_2$ and $100CeO_2$ as reported in Raman analysis (Fig. 6.3), and this surpassed the effect of CeO_2 agglomeration, causing the peaks shifting back to the lower temperature. The γ peak intensity decreased for 80 wt% CeO_2 addition in the catalyst system, and this peak completely disappeared for $90CeO_2$-$10SiO_2$ due to the absence of bulk CuO as in agreement with XRD analysis (Fig. 6.1).

The α and β peak could be observed at 147 and 179 ^{o}C for 100CeO_2. Table 6.1 showed the H_2 consumption of the catalysts at different peaks, and it could be seen that it did not follow any particular trend. That happened because H_2 consumptions usually depended on the total amount of available various oxygen species, such as adsorbed oxygen, lattice oxygen of CeO_2, and lattice oxygen of CuO. On the other hand, reduction peaks could be seen at different temperature due to different activation energies of various oxygen species.

Table 6.1. H_2 consumptions and OSC of CeO_2-SiO_2 supported CuO catalysts.

Samples	α peak (mmol/g)	β peak (mmol/g)	γ peak (mmol/g)	Total (mmol/g)	OSC (μmol/g)
100CeO_2	0.763	1.036	0	1.799	0.86
90CeO_2-10SiO_2	0.602	1.826	0	2.428	1.07
80CeO_2-20SiO_2	0.359	1.435	0.083	1.878	-
70CeO_2-30SiO_2	0.672	1.220	0.621	2.513	1.18
60CeO_2-40SiO_2	0.903	0.504	0.715	2.123	-
50CeO_2-50SiO_2	0.338	0.661	0.679	1.677	1.56
40CeO_2-60SiO_2	0.248	0.686	0.650	1.584	-
30CeO_2-70SiO_2	0.223	0.478	0.717	1.418	0.72
20CeO_2-80SiO_2	0.169	0.447	1.050	1.667	-
10CeO_2-90SiO_2	0.000	0.530	0.771	1.300	0.48
100SiO_2	0	1.407	0.233	1.64	0.29

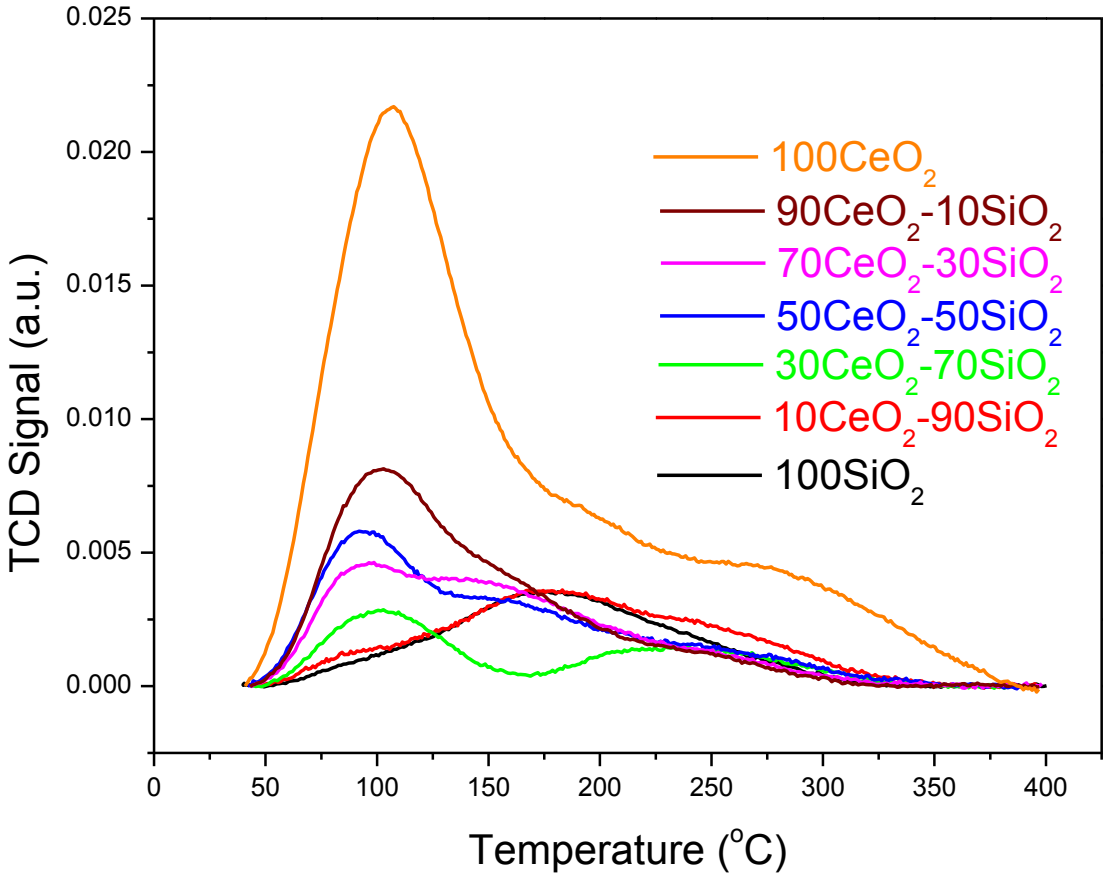

Figure 6.8. CO-TPD profiles of CeO_2-SiO_2 supported CuO catalysts.

6.3.6. CO-TPD

In this method, after CO molecules are being adsorbed, they react with lattice oxygen of metal oxides during heating and desorb away as CO_2. Fig. 6.8 presented CO_2 desorption peaks of various CeO_2-SiO_2 composite supported CuO catalysts. $100SiO_2$ showed a broad desorption peak centered at 180 ^oC. This peak may have corresponded to CO_2 produced by the reaction between adsorbed CO and surface oxygen of SiO_2 and/or CuO [27, 28, 33]. As SiO_2 support was inactive, the intensity of desorption peak was very low. As the amount of CeO_2 was increased, desorption peak intensity increased and the

peak shifted to lower temperature due to the presence of surface oxygen of CeO_2. The support CeO_2 takes part in the reaction by providing oxygen and reducing itself ($4CeO_2 = 2Ce_2O_3 + O_2$). Oxygen vacancies in CeO_2 lattice help in increasing the oxygen mobility to reach at the surface, and this surface oxygen reacts with adsorbed CO easily.

6.3.7. CO oxidation

The light-off curves of CO oxidation for CeO_2-SiO_2 composite supported 10 wt% CuO catalysts were shown in Fig. 6.9. It can be seen that only two catalysts ($40CeO_2$-$60SiO_2$ and $50CeO_2$-$50SiO_2$) achieved 100% CO conversion to CO_2 at 306 and 263 ^oC, respectively. Table 6.2 displayed T_{50}, T_{Max} and maximum CO conversion up to 350 ^oC. T_{50} is the temperature at which 50% CO conversion is achieved and T_{Max} is the temperature at which maximum CO conversion is achieved. As displayed in Table 6.2, T_{50} of $100SiO_2$ was at 234 ^oC and it gradually decreased with increasing CeO_2 amount in the CeO_2-SiO_2 composite supported 10 wt% CuO catalysts. $100SiO_2$ sample only achieved a maximum 77% CO conversion at 350 ^oC, and this conversion value rapidly increased to over 90% by introducing CeO_2 in CeO_2-SiO_2 composite supported 10 wt% CuO catalysts. In the CeO_2-SiO_2 composite supported 10wt% CuO catalysts, SiO_2 nanospheres not only offer support to increase the dispersion of CuO, but also can separate CeO_2 nanorods so that CeO_2 nanorods do not agglomerate. Fig. 6.10a showed a schematic of agglomerated CeO_2 supported CuO and SiO_2 nanospheres schematic was seen in Fig. 6.10b. After mixing CeO_2 nanorods and SiO_2 nanospheres, CeO_2 nanorods spread out and lie on SiO_2 surface as shown in Fig. 6.10c and CuO nanoparticles lie on the interface of CeO_2-SiO_2 (shown in Fig. 6.10d). It was confirmed earlier in TEM images as shown in Fig. 6.5. This effect usually helped to expose maximum surface area

of CeO_2 nanorods and created more chances to form Cu-O-Ce solid solutions and/or CuO onto the interface of SiO_2-CeO_2. $100CeO_2$ can convert maximum 95% CO up to 350 ^oC due to the presence of agglomeration of CeO_2 nanorods. We previously reported that CuO impregnated CeO_2 nanorods oxidized at 400 ^oC showed 100% CO conversion at 220 ^oC [33]. Small CuO particles became larger at high temperature calcination (500 ^oC), and this affected the catalytic efficiency for $100CeO_2$ sample. Qian et al. [35] and Dekkers et al. [36] reported that CeO_2-SiO_2 supported Au catalysts achieved 50% CO conversion at 110 and 115 ^oC, respectively. On the other hand, T_{50} for our $50CeO_2$-$50SiO_2$ sample was 100 ^oC, which confirmed an enhanced catalytic activity without using noble metal catalyst.

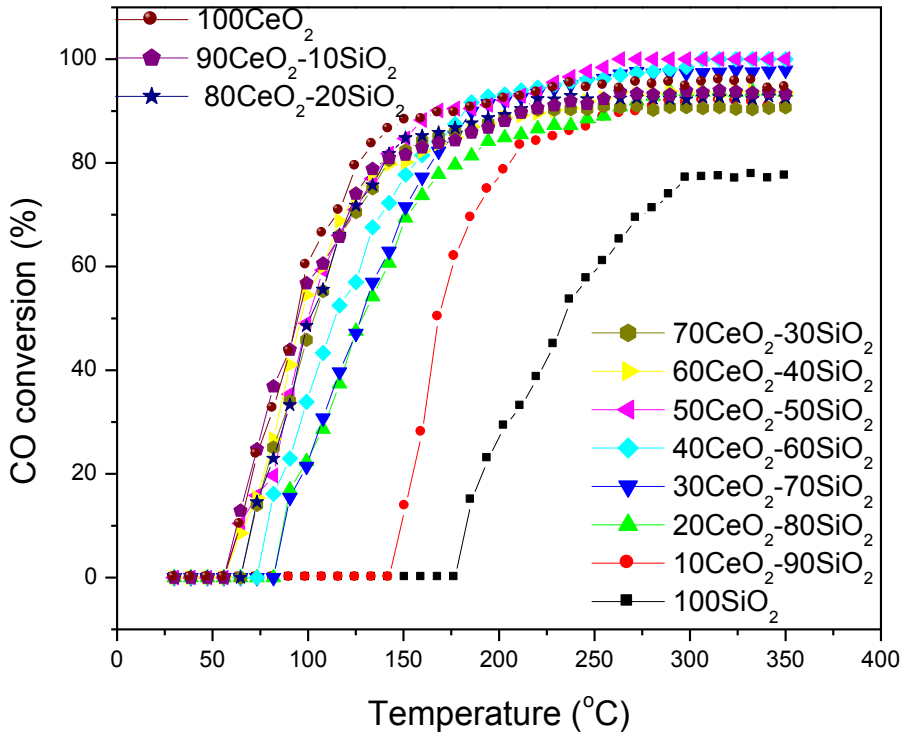

Figure 6.9. CO oxidation curves of CeO_2-SiO_2 supported CuO catalysts.

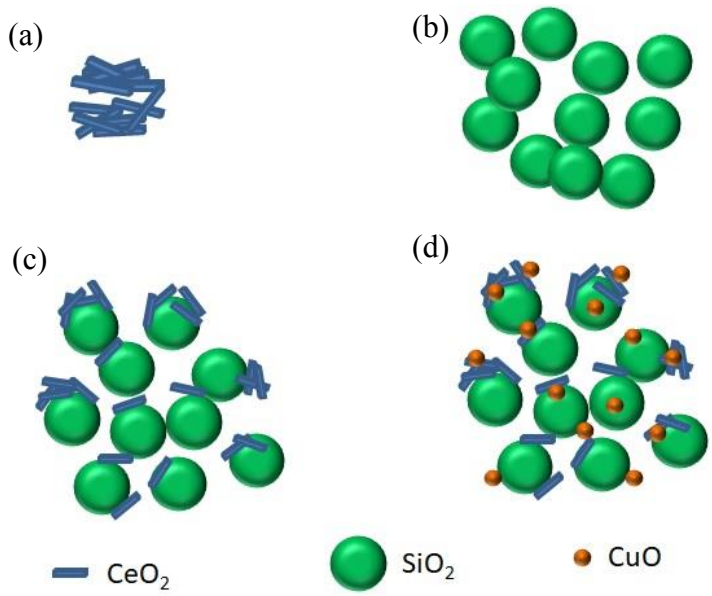

Figure 6.10. Schematical representation of (a) agglomerated CeO_2 nanorods, (b) SiO_2 nanospheres, (c) CeO_2 nanorods sperated by SiO_2 nanospheres, and (d) CuO nanoparticles impregnated on CeO_2-SiO_2.

Table 6.2. Catalytic activity toward CO oxidation over CeO_2-SiO_2 supported CuO catalysts.

Samples	T_{50} (^oC)	T_{Max} (^oC)	Max CO conversion (%)
100 CeO_2	94	237	95
90CeO_2-10SiO_2	95	263	93
80CeO_2-20SiO_2	100	220	92
70CeO_2-30SiO_2	102	220	90
60CeO_2-40SiO_2	98	263	93
50CeO_2-50SiO_2	100	263	100
40CeO_2-60SiO_2	114	306	100
30CeO_2-70SiO_2	127	263	97
20CeO_2-80SiO_2	127	280	93
10CeO_2-90SiO_2	168	289	91
100SiO_2	234	298	77

6.4. Conclusion

The composite of shape-controlled CeO_2-SiO_2 supported 10 wt% CuO catalysts were successfully synthesized for low-temperature CO oxidation applications. Both $100SiO_2$ and $100CeO_2$ samples did not achieve 100% CO conversion. However, a mixture of CeO_2 nanorods and SiO_2 nanospheres changed the catalytic activity depending on the percentage of CeO_2 or SiO_2 in the catalyst mixture. $50CeO_2$-$50SiO_2$ showed low-temperature (150, 179, and 227 ^oC) H_2 reduction peaks with total of 1.677 mmol H_2 consumption. This sample also converted 100% CO at 263 ^oC. When comparing with rest of the prepared catalysts, it can be concluded that $50CeO_2$-$50SiO_2$ achieved higher catalytic activity, and this happened because 50% SiO_2 reduced agglomeration of CeO_2 nanorods, leading to an increase of oxygen availability by increasing CuO dispersion on both CeO_2 nanorods and the interface of SiO_2-CeO_2.

6.5. References

1. Mock, S. A.; Sharp, S. E.; Stoner, T. R.; Radetic, M. J.; Zell, E. T.; Wang, R. CeO_2 nanorods-supported transition metal catalysts for CO oxidation. *J. Colloid Interface Sci.,* **2016**, 466, 261-267.

2. Mock, S. A.; Zell, E. T.; Hossain, S. T.; Wang, R. Effect of reduction treatment on CO oxidation with CeO_2 nanorod-supported CuO_x catalysts. *ChemCatChem*. **2018**. 10, 311-319.

3. Yao, S. Y.; Xu, W. Q.; Johnston-Peck, A. C.; Zhao, F. Z.; Liu, Z. Y.; Luo, S.; Senanayake, S. D.; Martinez-Arias, A.; Liu, W. J.; Rodriguez, J. A. Morphological

effects of the nanostructured ceria support on the activity and stability of CuO/CeO_2 catalysts for the water gas shift reaction. *Phys. Chem. Chem. Phys*., **2014**, 16, 17183-17195.

4. Flytzani-Stephanopoulos, M.; Zhu, T.; Li, Y. Ceria-based catalysts for the recovery of elemental sulfur from SO_2-laden gas streams. *Catal. Today*, **2000**, 62, 145–158.

5. Kugai, J.; Velu, S.; Song, C. Low-temperature reforming of ethanol over CeO_2-supported Ni-Rh bimetallic catalysts for hydrogen production. *Catal. Lett*., **2005**, 101, 255-264.

6. Vicente, J.; Erena, J.; Montero, C.; Ajkoiti, M. J.; Bilbao, J.; Gayubo, A. G. Reaction pathway for ethanol steam reforming on a Ni/SiO_2 catalyst including coke formation. *Int. J. Hydrogen Energ*., **2014**, 39, 18820-18834.

7. Liu, S. Q.; Zhou, S. S.; Chen, Z. G.; Liu, C. B.; Chen, F.; Wu, Z. Y. An artificial photosynthesis system based on CeO_2 as light harvester and N-doped graphene Cu(II) complex as artificial metalloenzyme for CO_2 reduction to methanol fuel. *Catal. Commun*., **2016**, 73, 7-11.

8. Huang, P. X.; Wu, F.; Zhu, B. L.; Gao, X. P.; Zhu, H. Y.; Yan, T. Y.; Huang, W. P.; Wu, S. H.; Song, D. Y. CeO_2 nanorods and gold nanocrystals supported on CeO_2 nanorods as catalyst. *J. Phys. Chem. B* **2005**, 109, 19169-19174.

9. Venezia, A. M.; Liotta, L. F.; Pantaleo, G.; La Parola, V.; Deganello, G.; Beckc, A.; Koppány, Z.; Frey, K.; Horváth, D.; Guczi, L. Activity of SiO_2 supported gold-palladium catalysts in CO oxidation. *Appl*. Catal. A: Gen. **2003**, 251, 359-368.

10. Reddy, B. M.; Khan, A.; Yamada, Y.; Kobayashi, T.; Loridant, S.; Volta, J. S. Surface characterization of CeO_2/SiO_2 and $V_2O_5/CeO_2/SiO_2$ catalysts by Raman, XPS, and other techniques. *J. Phys. Chem. B*, **2002**, 106, 10964-10972.

11. Xi, X.; Ma, S.; Chen, J. F.; Zhang, Y. Promotional effects of Ce, Mn and Fe oxides on CuO/SiO_2 catalysts for CO oxidation. *J. Environ. Chem. Eng*. **2014**, 2, 1011-1017.

12. Huili, Z.; Lihui, R.; Anhui, L.; Wencui, L. Role of CeO_2 in three-component $Au/CeO_2/SiO_2$ composite catalyst for low temperature CO oxidation. *Chin. J. Catal*. **2012**, 33, 1125-1132.

13. Wang, W. W.; Yu, W. Z.; Du, P. P.; Xu, H.; Jin, Z.; Si, R.; Ma, C.; Shi, S.; Jia, C. J.; Yan, C. H. Crystal plane effect of ceria on supported copper oxide cluster catalyst for CO oxidation: importance of metal-support interaction. *ACS Catal*. **2017**, 7, 1313-1329.

14. Zhou, K.; Wang, X.; Sun, X.; Peng, Q.; Li, Y. Enhanced catalytic activity of ceria nanorods from well-defined reactive crystal planes. *J. Catal*. **2005**, 229, 206-212.

15. Wang, R.; Dangerfield, R. Seed-mediated hydrothermal synthesis of shape-controlled CeO_2 nanocrystals. *RSC Adv.*, **2014**, 4(7), 3615-3620.

16. Nandanwar, R.; Singh, P.; Haque, F. Z. Synthesis and characterization of SiO_2 nanoparticles by sol-gel process and its degradation of methylene blue. *ACS J*. **2015**, 5, 1-10.

17. Xu, J. F.; Ji, W.; Shen, Z. X.; Tang, S. H. Preparation and characterization of CuO nanocrystals. *J. Solid State Chem*., **1999**, 147, 516-519.

18. Shan, W.; Shen, W.; Li, C. Structural characteristics and redox behaviors of $Ce_{1-x}Cu_xO_y$ solid solutions. *Chem. Mater*., **2003**, 15, 4761-4767.

19. Malinovsky, V. K.; Novikov, V. N.; Surovtsev, N. V.; Shebanin, A. P. Investigation of amorphous states of SiO_2 by Raman scattering spectroscopy. *Phys. Solid State*, **2000**, 42, 65-71.

20. Perez-Robles, F.; Garcia-Rodriguez, F. J.; Jimenez-Sandoval, S.; Gonzalez-Hernandez, J. Raman study of copper and iron oxide particles embedded in an SiO_2 matrix. *J. Raman Spectrosc*. **1999**. 30, 1099-1104.

21. Chen, K.; Bao, Z.; Shen, J.; Wu, G.; Zhou, B.; Sandhage, K. H. Freestanding monolithic silicon aerogels. *J. Mater. Chem*. **2012**, 22, 16196-16200.

22. Zhong, K.; Xue, J.; Mao, Y.; Wang, C.; Zhai, T.; Liu, P.; Xia, X.; Li, H.; Tong, Y. Facile synthesis of CuO nanorods with abundant adsorbed oxygen concomitant with high surface oxidation states for CO oxidation. *RSC. Adv*. **2012**, 2, 11520-11528.

23. Wu, Z.; Li, M.; Howe, J.; Meyer III, H. M.; Overbury, S. H. Probing defect sites on CeO_2 nanocrystals with well-defined surface planes by Raman spectroscopy and O_2 adsorption. *Langmuir*, **2010**, 26, 16595-16606.

24. Popovic, Z. V.; Dohcevic-Mitrovic, Z.; Cros, A.; Cantarero, A. Raman scattering study of the anharmonic effects in CeO_{2-y} nanocrystals. *J. Phys.: Condens. Matter*, **2007**, 19, 496209 (9pp).

25. Zhang, F.; Chan, S. W.; Spanier, J. E.; Apak, E.; Jin, Q.; Robinson, R. D.; Herman, I. P. Cerium oxide nanoparticles: Size-selective formation and structure analysis. *Appl. Phys. Lett*., **2002**, 80, 127-129.

26. Shan, W.; Shen, W.; Li, C. Structural characteristics and redox behaviors of $Ce_{1-x}Cu_xO_y$ solid solutions. *Chem. Mater*., **2003**, 15, 4761-4767.

27. Shen, W.; Mao, D.; Luo, Z.; Yu, J. CO oxidation on mesoporous SBA-15 supported CuO-CeO_2 catalyst prepared by a surfactant-assisted impregnation method, *RSC. Adv*. **2017**, 7, 27689–27698.

28. Zheng, Y.; Mao, D.; Sun, S.; Fu, G. CO oxidation on CuO/CeO_2 catalyst prepared by solvothermal synthesis: influence of catalyst activation temperature, *J. Nanopart. Res*. **2015**, 17, 471 (1–12).

29. Wang, Q.; Jia, W.; Liu, B.; Dong, A.; Gong, X.; Li, C.; Jing, P.; Li, Y.; Xu, G.; Zhang, J. Hierarchical structure based on Pd(Au) nanoparticles grafted onto magnetite cores and double layered shells: enhanced activity for catalytic applications. *J. Mater. Chem. A*, **2013**, 1, 12732-12741.

30. Ulgut, B.; Suzer, S. XPS Studies of SiO_2/Si System under External Bias. *J. Phys. Chem. B*, **2003**, 107, 2939-2943.

31. Song, C.; Wang, C.; Zhu, H.; Wu, X.; Dong, L.; Chen, Y. Preparation, characterization and catalytic activity for CO oxidation of SiO_2 hollow spheres supporting CuO catalysts, *Catal. Lett*., **2008**, 120, 215–220.

32. Jiang, X.; Lu, G.; Zhou, R.; Miao, J.; Yu, C.; Zheng, X. Studies of pore structure, temperature-programmed reduction performance, and micro-structure of CuO/CeO_2 catalysts. *Appl. Surf. Sci*., **2001**, 173, 208–220.

33. Hossain, S. T.; Almesned, Y.; Zhang, K.; Zell, E. T.; Bernard, D. T.; Balaz, S.; Wang, R. Support structure effect on CO oxidation: A comparative study on SiO_2 nanospheres and CeO_2 nanorods supported CuO_x catalysts. *Appl. Surf. Sci.,* **2018**, 428, 598-608.

34. Trovarelli, A.; Boaro, M.; Rocchini, E.; Leitenburg, C.; Dolcetti, G. Some recent developments in the characterization of ceria-based catalysts. *J. Alloy Comp*., **2001**, 323-324, 584-591.

35. Qian, K.; Lv, S.; Xiao, X.; Sun, H.; Lu, J. Influences of CeO_2 microstructures on the structure and activity of $Au/CeO_2/SiO_2$ catalysts in CO oxidation. *J. Mol. Catal. A: Chem.*, **2009**, 306, 40-47.

36. Dekkers, M. A. P.; Lippits, M. J.; Nieuwenhuys, B. E. Supported gold/MO_x catalysts for NO/H_2 and CO/O_2 reactions. *Catal. Today*, **1999**, 54, 381-390.

Chapter 7: Kinetic study of CeO_2 supported CuO catalyst toward CO oxidation reaction

This chapter investigates the redox kinetics of CeO_2 nanorods supported CuO catalyst prepared by thermal decomposition method. 5%CO-95%He and O_2 gases were used to reduce and oxidize CuO/CeO_2 catalyst respectively at a constant temperature of 400 ^oC (isothermal process). Mathematical formulas for power law, diffusion, nucleation and contraction models have been used to compare with the experimental data collected during the reduction and oxidation process of the catalyst to determine the best fitted reaction mechanism.

7.1. Introduction

CO oxidation reaction is one of the most studied catalytic reactions and has gotten more attention due to industrial concern for treatment of automotive exhaust and in the preferential oxidation of CO in the excess H_2 (PROX reaction) for hydrogen fuel cells [1]. Researchers have been trying to synthesize various metal oxide supported catalysts for low-temperature CO oxidation. Metal oxides, such as Al_2O_3, SiO_2, CeO_2, TiO_2, SnO_2, and ZrO_2 have been used as support for noble metals (i.e. Pt, Au, Pd, and Rh) and/or transition metal oxides (i.e. NiO, CuO, ZnO, and MnO_2) catalysts [1-12]. Among various catalyst systems, CeO_2 supported CuO is one of the most active transition metal catalysts for low-temperature CO oxidation application; and thus, this catalyst system has been studied extensively. However, the reaction mechanism of CO oxidation over CuO/CeO_2 catalyst is still unclear. Compared to vast majority of publications on synthesis and

catalytic activity of CuO/CeO_2, there is relatively small number of publications on kinetic study of CO oxidation reaction over CuO/CeO_2 catalyst, even though the kinetic study can aid important information on the reaction mechanism. In literature, several kinetic models, including Langmuir-Hinshelwood (L-H) [13], Mars-Van Krevelen (MVK) [14], and Liu and Flytzani-Stephanopoulos (LFS) [15] mechanisms, are often used to understand CO oxidation over CuO/CeO_2 catalysts. L-H model predicted that the reaction occurs at noble metal catalyst, where adsorbed oxygen and CO react and lattice oxygen does not take part in the reaction. On the other hand, MVK model has been explained based on involving lattice oxygen of CeO_2 in the reaction. LFS model exhibited a different view because they reported that the reaction occurs at the interface of CuO and CeO_2. In this chapter, we have attempted a distinct way for kinetic study of CO oxidation over CuO/CeO_2 and various solid state kinetic models, such as contraction, power, nucleation and diffusion models, have been used to determine reaction mechanism and activation energy for CO oxidation.

7.2. Experimental

7.2.1. Catalyst preparation

Hydrothermal method was used to prepare CeO_2 nanorods. The 88 mL of 0.1 M $Ce(NO_3)_3.6H_2O$ was transferred into Teflon liner of 200 mL capacity, and 8 mL of 6 M NaOH was added into the solution. This solution was stirred for about 15 sec, and then the lid of Teflon liner was closed. The Teflon liner was put into a stainless steel autoclave and heated at 90 ^oC for 48 hrs. Finally, the product was filtered and was washed with 500 mL water and then with 50 mL ethanol. It was dried at 50 ^oC for 12 hrs. To impregnate

10% CuO, CeO_2 nanorods and $Cu(NO_3)_3.3H_2O$ were mixed in stoichiometric ratio in 30 mL water. While stirring, it was heated at 120 ^oC until water evaporated. Then, it was oxidized at 400 ^oC for 5 hrs. Finally, CuO/CeO_2 catalyst was collected.

7.2.2. Catalyst characterizations

The X-ray diffraction of powder samples were carried out on Mini-Flex II diffractometer. The diffraction patterns were recorded with Cu Kα source ($\lambda = 0.154$ nm) in the range of 2θ between 5^o and 90^o. Raman spectroscopy analysis on the samples was done using the Horiba iHR-320 Raman spectrometer with a laser at an excitation wavelength of 532 nm. Exposure time of 5 sec and accumulation number of 10 were used for all of the samples. The Raman spectrometer was calibrated before testing the catalyst samples. Silicon single crystal wafer was used to calibrate with a reference peak at 520 cm^{-1}. TEM was performed on the samples to analyze the morphology and size of the catalysts using JEOL 2100 TEM. 400 mesh copper grid (from Ted Pella) was used to prepare TEM sample. At first, the catalysts powder sample was mixed with ethanol in a beaker, and the suspension was sonicated for 1 min. Samples were taken from the solution by a small pipette, and one or two drops of sample were poured on the hydrocarbon copper grid. Oxygen storage capacity (OSC) of the catalysts and metal dispersion percentage were measured by H_2 pulse chemisorption using Micromeritics Autochem^{TM} II 2920. Prior to the measurement, the sample loaded in U-tube was pre-treated at 350 ^oC in 5%O_2-95%He for 30 mins. After cooling down to room temperature, He gas was flown for 30 mins to take excess oxygen out of the system. Then the sample was again heated to 350 ^oC and 5%H_2-95%Ar gas was injected into the sample U-tube every 3 mins until the intensity of the hydrogen consumption peaks was nearly equal. The

OSC was expressed as μmol of O_2 per gram catalyst sample. For CO temperature programmed desorption (TPD), the sample was heated up to 400 ^oC under inert environment (He gas) with a flow rate of 50 mL/min to remove residual moisture. After cooling down to room temperature, 5% CO – 95% He gas with 50 mL/min rate was flown through the sample for 30 mins. Helium gas was flown again for 30 mins. Then the sample was reheated up to 400 ^oC under inert environment. Rate of desorption was calculated using equation (7.1) shown below.

$$\frac{d\theta}{dt} = -\frac{k_d}{\beta}\theta^n \qquad \text{(Eq. 7.1)}$$

$$k_d = A\exp\left(-\frac{E_d}{RT}\right) \qquad \text{(Eq. 7.2)}$$

Here, k_d, β, θ, and n are rate of desorption constant, heating rate, surface coverage, and reaction order, respectively. k_d can be found using equation (7.2) where A, E_d, R, and T are rate coefficient, desorption energy, gas constant, and temperature, respectively. The CO oxidation was performed in a quartz reactor inserted in a vertical furnace. The mixture gases consisted with 1% CO, 20% O_2 and the rest He. The flow rate of the mixture gas was 70 mL/min. The reaction was done between room temperature and 350^oC. The CO conversion was calculated using the following equation:

$$\%CO\ conversion = \left[\frac{P_{CO_2}}{P_{CO}+P_{CO_2}}\right] \times 100\%, \qquad \text{(Eq. 7.3)}$$

Here, P_{CO} and P_{CO_2} are the partial pressure of CO and CO_2, respectively, are determined from the relative peak area of the CO and CO_2 peaks normalized to the He standard. Turnover frequency (TOF) is a measurement of catalytic activity which shows the number of cycles per unit time. Three types of TOF can be calculated as follows [16, 17]:

$$TOF_1\ (s^{-1}) = X_{CO}\ F_{CO}\ \frac{5\ W_{Cu}}{4\ m_{cat} X_{CuO} D_{CuO}} \quad \text{(Eq. 7.4)}$$

$$TOF_2\ (s^{-1}) = X_{CO}\ F_{CO}\ N\ \frac{m_c}{m_{cat} X_{CuO}} \quad \text{(Eq. 7.5)}$$

$$TOF_3\ (s^{-1}) = \frac{TOF_2}{\frac{\pi}{2d_{Cu-O}}\pi d} = X_{CO}\ F_{CO}\ N\ \frac{m_c}{m_{cat} X_{CuO}} . \frac{2d_{Cu-O}}{\pi^2 d} \quad \text{(Eq. 7.6)}$$

Here, X_{CO} is the CO conversion percentage (%) at certain temperature; F_{CO} (mol·s^{-1}) is the flow rate of CO; N is the Avogadro's constant; W_{Cu} is the molecular weight of Cu (63.545 g·mol^{-1}); m_{cat} is the weight of catalyst; X_{CuO} is the percentage of CuO loading on the catalyst support; D_{CuO} is the percentage of CuO dispersion; m_c is the weight of a single CuO crystalline and this can be calculated from the volume of assumed semi-spherical CuO and density of CuO (6.45 g·cm^{-3}); d is the crystallite size of CuO; d_{Cu-O} is distance between Cu and O atom (0.195 nm). TOF_1 calculation is usually based on metal dispersion. TOF_2 contributes the information about the overall activity of Cu atoms on CuO-support periphery and TOF_3 refers to life cycles or turn over frequency of each Cu atom present at interface of CuO-support. Thermogravimetric analyzer (TGA) under different atmosphere was used for kinetic study of the catalyst in this study. At first, an aluminum pan was tared and then sample was placed in it. The sample was heated up to 400 ^{o}C at 10 ^{o}C/min rate under inert environment (He gas). Any volatile substances or moisture can be removed during heating. Temperature was held at 400 ^{o}C during reduction/oxidation cycles. 5%CO-95%He gas was used to reduce the sample and this mixture gas was passed through the sample at 50 mL/min rate for 30 mins at a constant temperature of 400 ^{o}C. The gas was switched to pure oxygen to oxidize the sample. The flow rate of oxygen gas was 50 mL/min and this gas was flown for 30 mins as well. The

pair of one reduction and one oxidation processes is mutually called one redox cycle. In total, 10 cycles of redox process was conducted for the catalyst. Sample weight changed for decomposition, oxidation, or loss of volatile substances.

7.3. Results and Discussion

7.3.1. Structural analysis

XRD and Raman analysis were conducted to determine the presence of CeO_2 and CuO in the catalyst. Fig. 7.1a showed XRD pattern of CuO/CeO_2 catalyst. The peaks for fluorite structured CeO_2 were observed, and these peaks matched with JCPDS data (JCPDS 43-1002) [18]. CuO peak was not present in the XRD pattern due to the presence of small CuO nanoparticles or Cu-O-Ce solid solutions [19]. We previously showed that increasing the oxidation temperature causes to increase the particle size of CuO as well as the possibility of CuO phase separation from solid solutions [20]. Thus, CuO peaks can be visible in XRD profiles for higher oxidation temperature. Raman analysis in Fig. 7.1b confirmed the presence of CuO in the catalyst. The peaks found at 271 and 625 cm^{-1} corresponded to A_g and B_{2g} mode of CuO [18]. One peak with large intensity can be seen at 444 cm^{-1}, and this peak was associated with F_{2g} mode of CeO_2. According to the literature, this peak was usually found at 456 cm^{-1} [20]. For this catalyst, CeO_2 peak shifted to lower wavenumber due to the presence of oxygen vacancies in CeO_2 lattice. TEM and HRTEM images of CuO/CeO_2 were presented in Fig. 7.2. CeO_2 nanorods of 50-100 nm long and 10-20 nm width can be observed in Fig. 7.2a. CuO nanoparticle was attached onto the surface of CeO_2 nanorods as shown in Fig. 7.2b.

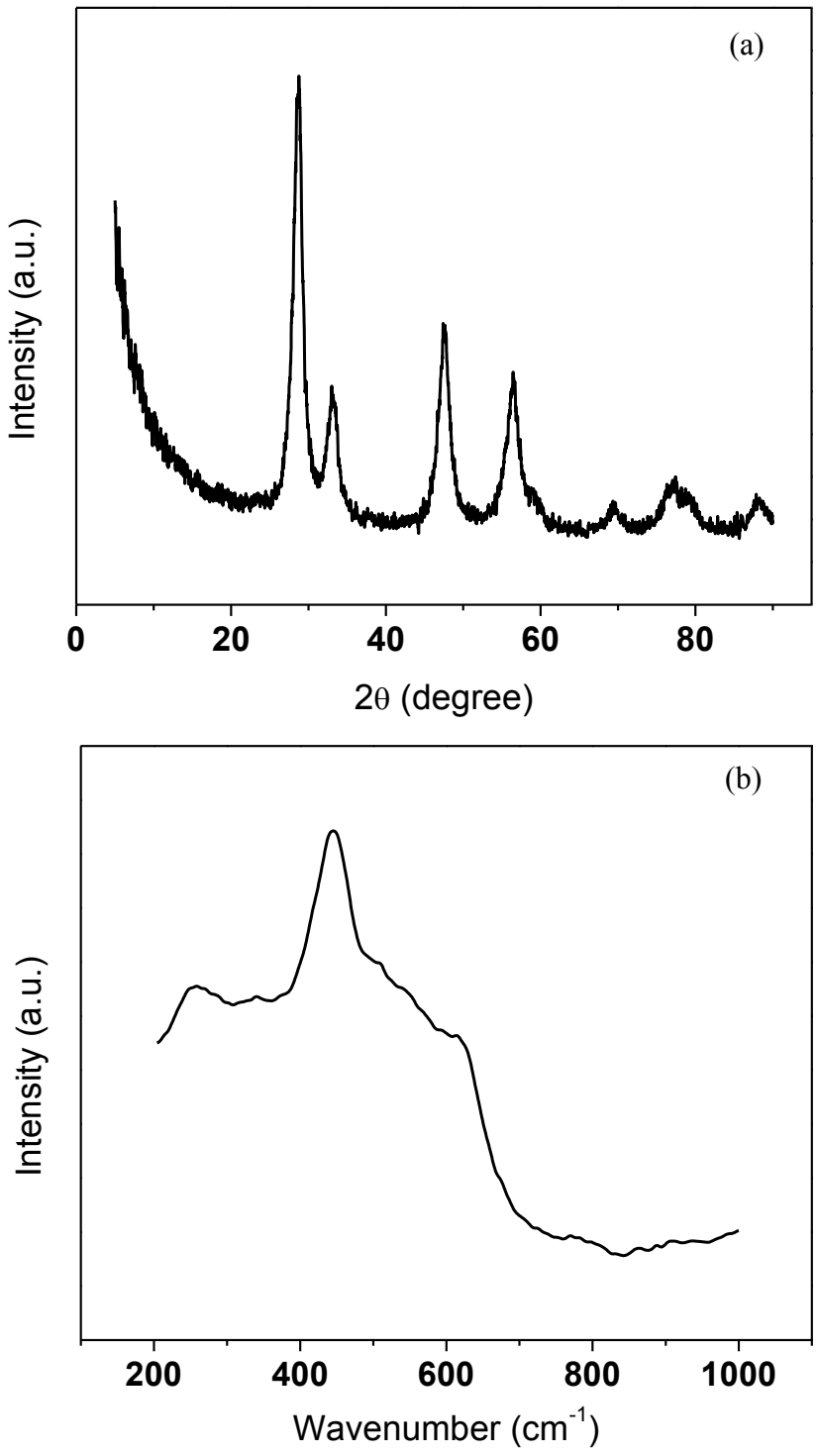

Figure 7.1. XRD pattern (a) and Raman spectrum (b) of CuO/CeO_2 catalyst.

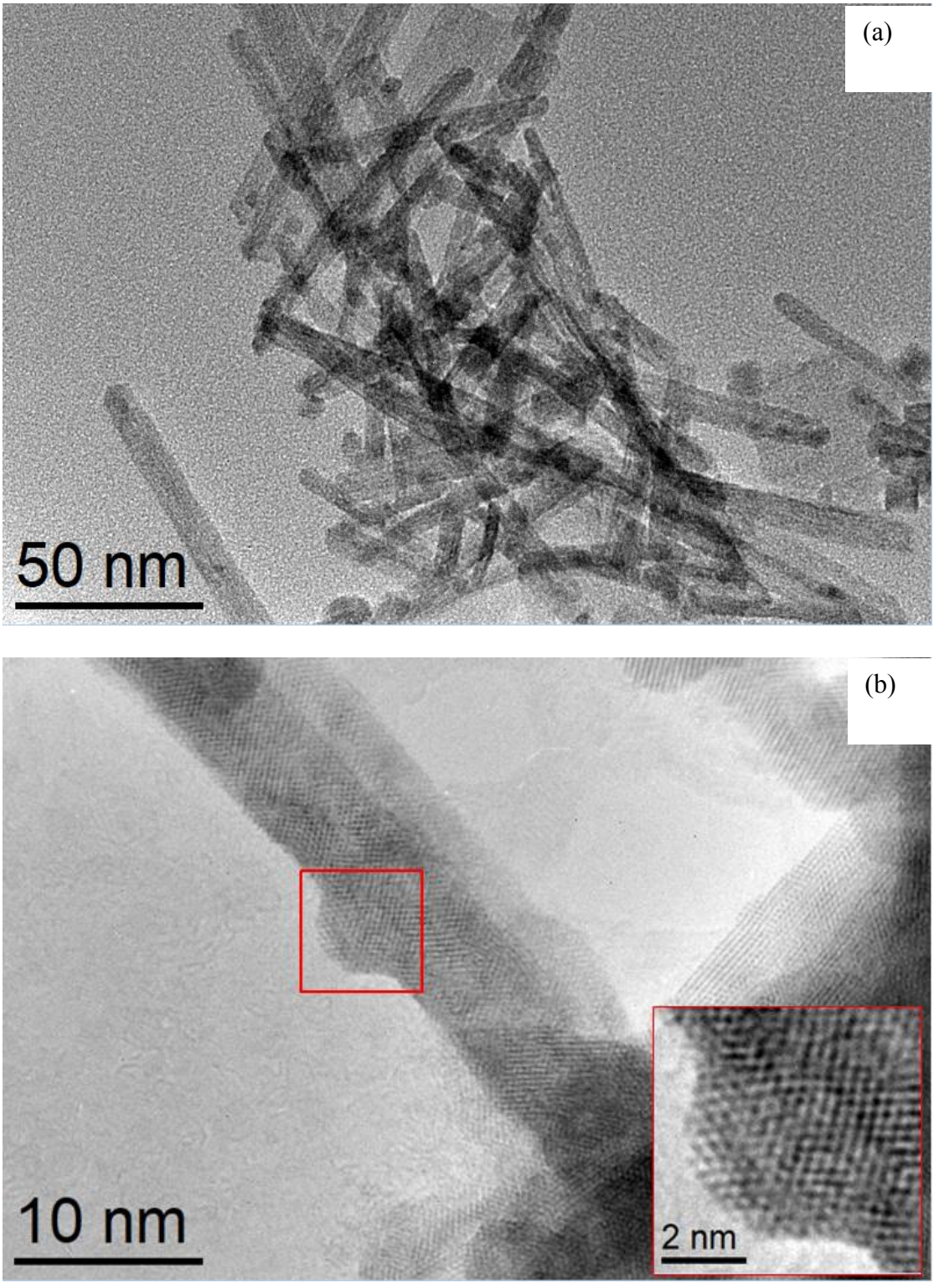

Figure 7.2. TEM (a) and HRTEM (b) of CuO/CeO_2 catalyst.

7.3.2. CO oxidation and pulse chemisorption

The light-off curves of CO oxidation over CuO/CeO_2 catalysts were shown in Fig. 7.3a. The weight of the catalysts was varied from 23.7 to 124.3 mg for this experiment, and it can be seen that rate of reaction changed with increasing the weight of the sample. The T_{50} (the temperature when 50% CO was converted) of the samples were 119, 101, 97, 93, and 87 ^{o}C for 23.7, 49.0, 73.7, 100.0, and 124.3 mg of sample, respectively. An attempt was conducted to calculate activation energy of prepared CuO/CeO_2 catalyst. We considered that W is weight of the sample and F_{CO} is fraction of CO conversion. Fig. 7.3b showed the changes of W/F_{CO} ratio with fraction of CO conversion at different temperatures. As the temperature increased, the conversion ratio lost the linearity with W/F_{CO}. The reaction rate was calculated, using the slope of curves up to 0.40 fraction of CO conversion from Fig. 7.3b. Arrhenius plot for CO oxidation was shown in Fig. 7.3c. Activation energy of CuO/CeO_2 for CO conversion reaction was calculated and the value was 20.2 KJ/mol. Using CO oxidation light-off curves shown in Fig. 7.3a, three different TOFs were calculated at 50% CO conversion. Calculated TOF_1, TOF_2 and TOF_3 were 0.8605, 0.136, and 11.94×10^{-4} s^{-1}, respectively. Lu et al. [16] presented $TOF_1 = 0.00852$ s^{-1}, $TOF_2 = 5.22$ s^{-1}, and $TOF_3 = 30.02 \times 10^{-4}$ s^{-1} for CuO/CeO_2. Our calculated TOF_1 was 100 times higher than the reported data due to well dispersed CuO nanoparticles onto CeO_2 surface. However, our calculated TOF_2 and TOF_3 were lower than the reported data and Lu et al. [16] explained that smaller CuO particles could give low TOF_2 and TOF_3 values and this was consistent with our XRD data.

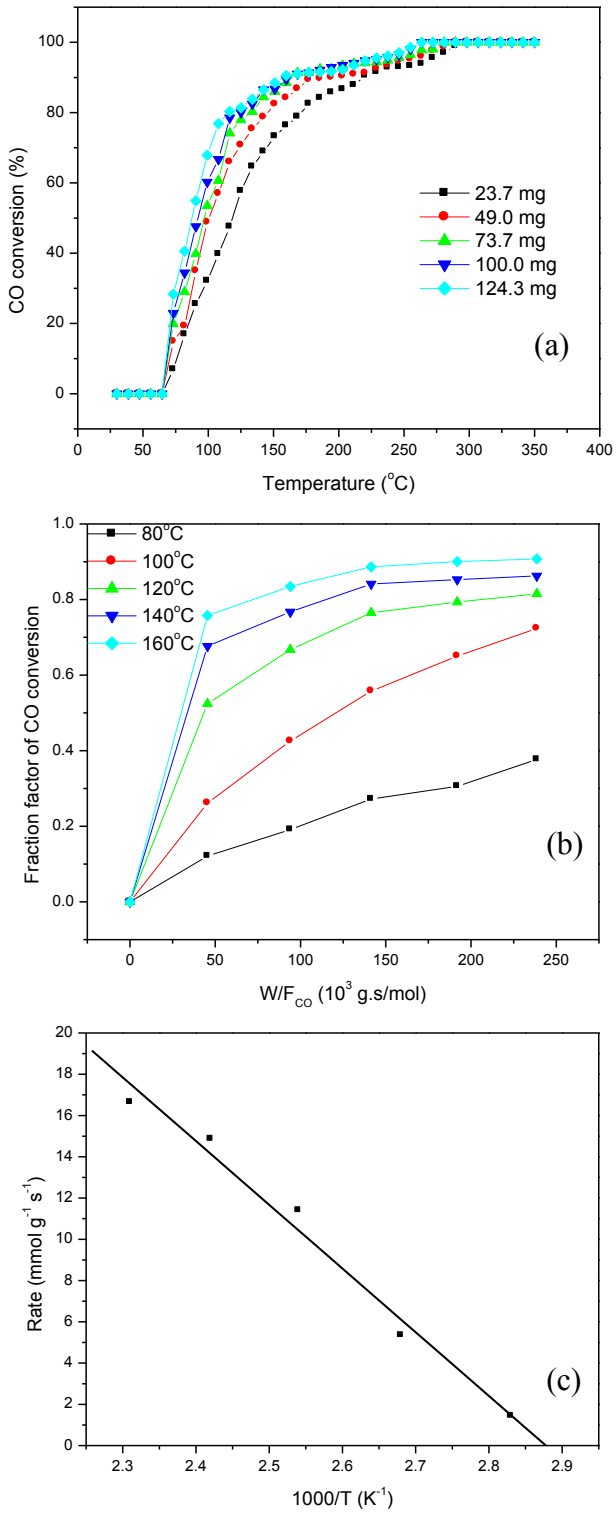

Figure 7.3. Light-off curves of CO oxidation (a), W/F ratio vs CO fraction (b), and Arrhenious plot (c).

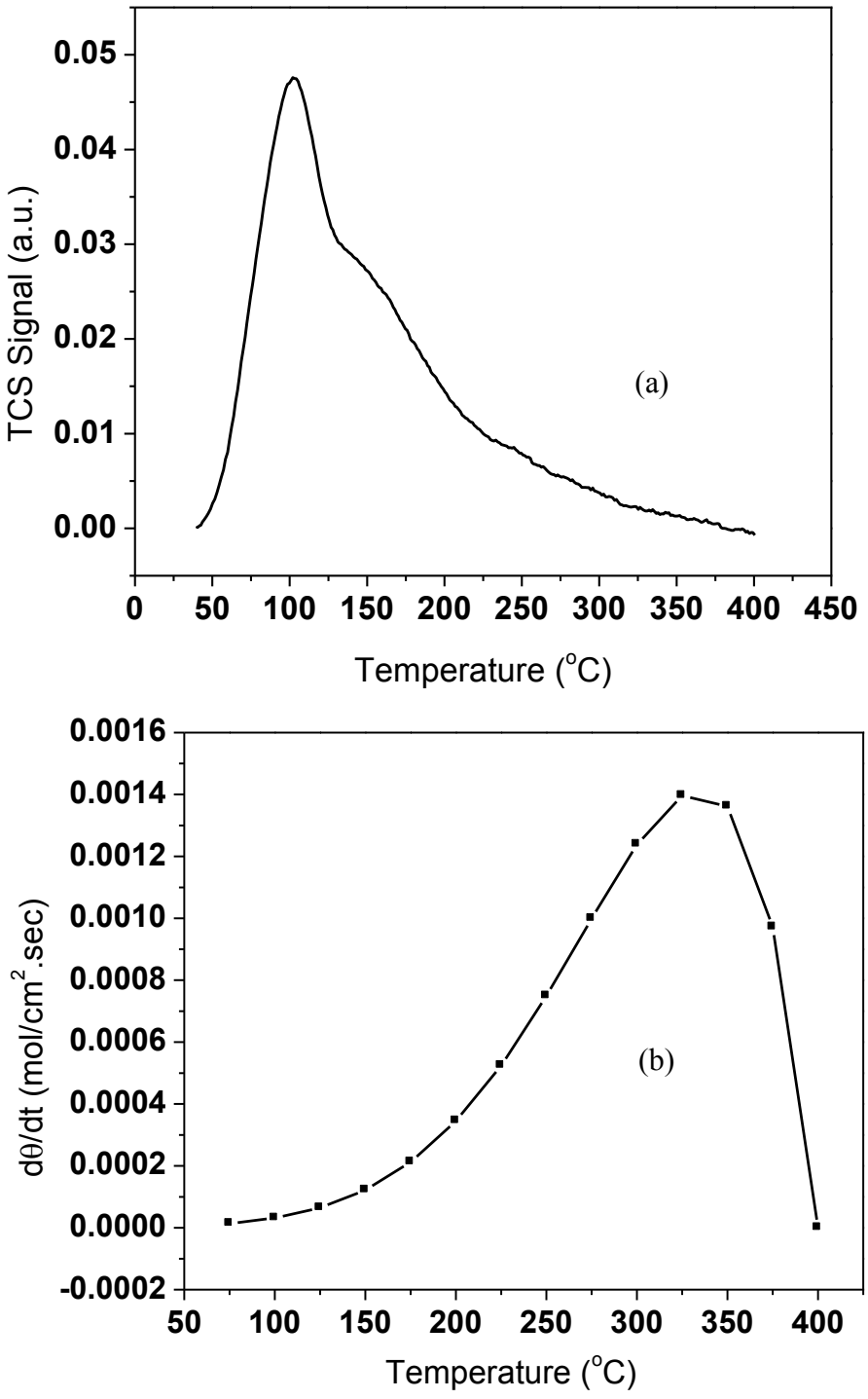

Figure 7.4. CO-TPD (a) and rate of desorption (b) of CuO/CeO_2 catalyst.

7.3.3. CO TPD

CO-TPD profile of CuO/CeO_2 was shown in Fig. 7.4a. Two desorption peaks were found at 100 and 150 ^oC. These peaks are fundamentally for CO_2 produced from the reaction between adsorbed CO and the surface of CeO_2. Lattice oxygens at the interface of CuO-CeO_2 may take part in the reaction. Rate of desorption (ROD) of CO_2 was measured from CO-TPD curve and was shown in Fig. 7.4b. It can be observed that the temperature affected ROD. At first, desorption increased with temperature up to 175 ^oC. Then at latter step, it still increased linearly, however quicker than the former step; and this step was completed at 325 ^oC where it showed maximum ROD (13.9×10^{-4} $mol/cm^2.s$). In final step, ROD started going down rapidly probably due to the presence of low amount of adsorbed CO at this temperature.

7.3.4. Kinetic model

As mentioned earlier, TGA was used to conduct kinetic study on CO oxidation reaction over CuO/CeO_2 catalyst. Reduction degree and oxidation degree were calculated using the change in weight from TGA measurements. The equations were used as follows.

$$Reduction\ degree\ (RD)\ \% = \frac{W_i - W_t}{W_i - W_f} \times 100 \qquad \text{(Eq. 7.7)}$$

$$Oxidation\ degree\ (OD)\ \% = \frac{W_t - W_i}{W_f - W_i} \times 100 \qquad \text{(Eq. 7.8)}$$

Here, W_i, W_f, and W_t are initial weight before reduction or oxidation reaction, final weight after reduction or oxidation reaction and weight at time t, respectively. For solid-state kinetics, a series of mathematical models was compared with experimental data collected

during redox reaction in order to find an appropriate one. Statistical parameters were used for ideal selection. Now, gas-solid reaction rate can be expressed as follows [21].

$$\frac{dX}{dt} = k(T).f(X) \qquad \text{(Eq. 7.9)}$$

Here, X is the reduction/oxidation degree, k is reaction rate or Arrhenius parameter, T is reaction temperature, t is time and $f(X)$ is the empirical function for solid-state kinetics. Now, equation 7.9 can be rewritten which is shown in equation 7.10 and 7.11.

$$g(X) = \int_0^X \frac{dX}{f(X)} = k(T) \int dt \qquad \text{(Eq. 7.10)}$$

$$g(X) = \int_0^X \frac{dX}{f(X)} = kt \qquad \text{(Eq. 7.11)}$$

The Arrhenius parameter k can vary with temperature T and this can be shown in equation 7.12.

$$k = k_o \exp\left(-\frac{E_a}{RT}\right) \qquad \text{(Eq. 7.12)}$$

Here, k_o pre-exponential factor, E_a is activation energy, and R is universal gas constant. Ipsakis et al. mentioned that $f(X)$ usually depends on the reaction mechanism and it can be expressed as follows [20]:

$$f(X) = X^m.(1-X)^n.[-\ln(1-X)]^p \qquad \text{(Eq. 7.13)}$$

where m, n, and p are empirical dependence parameters.

Various empirical models for gas-solid kinetics were shown in Table 7.1 [21, 22]. The experimental data were compared with the simulated data calculated using these kinetic models. The error between experimental and simulated data was minimized using equation 7.14 and then R^2 values were calculated to determine the fitting result.

$$Minimized\ error = (Y_{Sim} - Y_{Exp})^2 \qquad \text{(Eq. 7.14)}$$

where Y_{Sim} and Y_{Exp} were simulated and experimental data of reduction or oxidation degree respectively at normalized range of 0-1.

Table 7.1 Basic solid state kinetic models of f(X) and g(X).

Model	*f(X)*	*g(X)*	Model name
M1	$3.(1-X)^{\frac{2}{3}}$	$1-(1-X)^{\frac{1}{3}}$	Contraction
M2	$(1-X)$	$-ln(1-X)$	Kinetic order
M3	$2.(1-X)^{\frac{1}{2}}$	$1-(1-X)^{\frac{1}{2}}$	Contraction
M4	$\frac{3}{2}.(1-X)^{\frac{1}{3}}$	$1-(1-X)^{\frac{2}{3}}$	Contraction
M5	$4.(1-X)^{\frac{3}{4}}$	$1-(1-X)^{\frac{1}{4}}$	Contraction
M6	$\frac{2}{3}.(X)^{-\frac{1}{2}}$	$(X)^{\frac{3}{2}}$	Power law
M7	$X(1-X)$	$ln\left(\frac{X}{1-X}\right)$	Power law
M8	$n(1-X).(-ln(1-X))^{\left(1-\frac{1}{n}\right)}$	$(-ln(1-X))^{\frac{1}{n}}$	Nucleation /Avramai-Erofeev
M9	$\frac{3.(1-X)^{\frac{1}{3}}}{2.(1-X)^{-\frac{1}{3}}-1}$	$\frac{1}{2}[(1-X)^{\frac{2}{3}}-4(1-X)^{\frac{1}{3}}+3]$	Diffusion
M10	$\frac{3}{2.(1-X)^{-\frac{1}{3}}-1}$	$\frac{1}{2}-\frac{1}{2}(1-X)^{\frac{4}{3}}-\frac{1}{3}X$	Diffusion

Fig. 7.5 showed TGA profile of reduction and oxidation reaction over CuO/CeO_2 catalyst. First 40 mins, moisture in catalysts evaporated as the temperature was increased from room temperature to 400 ^{o}C. Then, weight of the catalyst decreased again rapidly in almost 1 min due to reduction reaction under CO environment. Weight of the catalyst stopped changing after completing the reduction reaction with all available oxygen in the catalyst. When oxygen gas was started flowing, the catalyst restored oxygen and gained weight. As it fully restored all of the available sites with oxygen, weight of the catalyst became constant. The redox reaction was conducted for total 10 cycles.

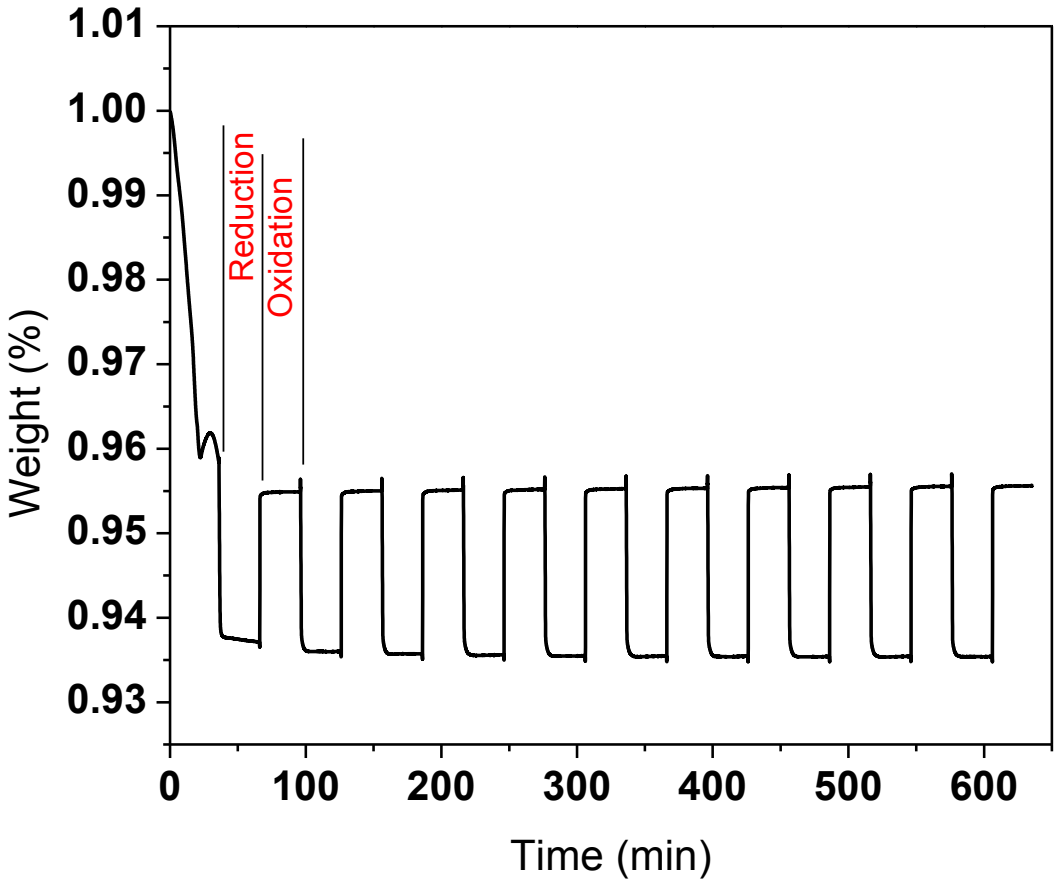

Figure 7.5. TGA profile of reduction and oxidation reactions over CuO/CeO_2 catalysts.

For kinetic analysis of CuO/CeO_2 catalyst, cycle 1, 2, 3, 5, and 10 for reduction and oxidation stages were selected. The mathematical models mentioned earlier in Table 7.1 were used to find out the best fitted model with the experimental data. Table 7.2 showed an overview of fitting results for reduction reaction kinetic models. Here, R^2 values varied from 0.24 to 0.99 for most of the kinetic models. It can also be seen that some of the kinetic models totally rejected this reaction and thus there was no R^2 values for them.

Table 7.2. Overview of fitted data (R^2) for kinetic models at reduction stages.

Model		Cycle 1	Cycle 2	Cycle 3	Cycle 5	Cycle 10
M1		0.9904	0.8138	0.5103	0.4730	0.4058
M2		0.9746	0.6861	0.3827	0.3441	0.2746
M3		0.9827	0.8653	0.5779	0.5418	0.4765
M4		-	-	-	-	-
M5		0.9897	0.7841	0.4733	0.4396	0.3717
M6		0.9752	0.1999	-	-	-
M7		-	-	-	-	-
M8	n = 1.5	0.9903	0.9908	0.9928	0.9922	0.9924
	n = 2	0.8226	0.9380	0.9904	0.9935	0.9941
	n = 3	0.6465	0.8432	0.9007	0.9081	0.9203
	n = 4	0.5308	0.7861	0.8351	0.8435	0.8575
M9		-	-	-	-	-
M10		-	-	-	-	-

From the comparison among all the kinetic models, it can be visible that M8 model or Avrami-Erofeev model for n = 1.5 fitted the best for this reduction reaction. Fig. 7.6 represented the reduction profile of CuO/CeO_2 catalyst using the optimal fitting result which was 1.5^{th} order of Avrami-Erofeev or nucleation model; and here the change in reduction degree as function of time was shown for 5 different cycles (1, 2, 3, 5, and 10). Cycle 1 took relatively longer reduction time (0.8 min) to stabilize RD value at 90%. Higher cycles (2 to 10) took 0.66 – 0.63 min to stabilize at 90% RD. Constant stabilized RD value (90%) for all cycles suggested that the amount of available oxygen in the catalyst did not change with increasing redox cycles. However, after cycle 1 the reduction time decreased due to the increment in oxygen mobility in CeO_2 lattice. We earlier showed in Chapter 4 that oxygen storage capacity (OSC) of CuO/CeO_2 was 2.39 μmol/g and this value did not vary after 3 redox cycles. In Fig. 7.6, the reaction initially started with faster and constant reduction rate up to 67% reduction for cycle 1 and 78% reduction for cycle 2-10. In this stage, CO gas reacted with the most easily-reducible oxygen species, which possibly originated from adsorbed oxygen near Cu-O-Ce solid solution and/or oxygen at the interface of CuO and CeO_2. At the next stage, the reaction rate slowly decreased. In this case, we assumed that oxygen needs to travel within CeO_2 lattice to reach near the surface or at the interface of CuO and CeO_2. Depending on the mobility of oxygen in CeO_2 lattice, the reaction rate may vary at different cycles. This reduction profile was the best fitted with 1.5^{th} order of Avrami-Erofeev model or nucleation model where both point defects (oxygen vacancy) and nucleation need to be considered. In this case, random nucleation and significant growth of Cu^0 possibly occurred during reduction. However, this model failed to show exact reduction pathways

and/or timeline of reduction reaction, Cu^0 nucleation and Cu^0 growth. Table 7.3 represented that reaction rate increased from 2.33 to 2.72 with increasing the redox cycle from 1 to 10. This data was retrieved using 1.5^{th} order of Avrami-Erofeev kinetic model.

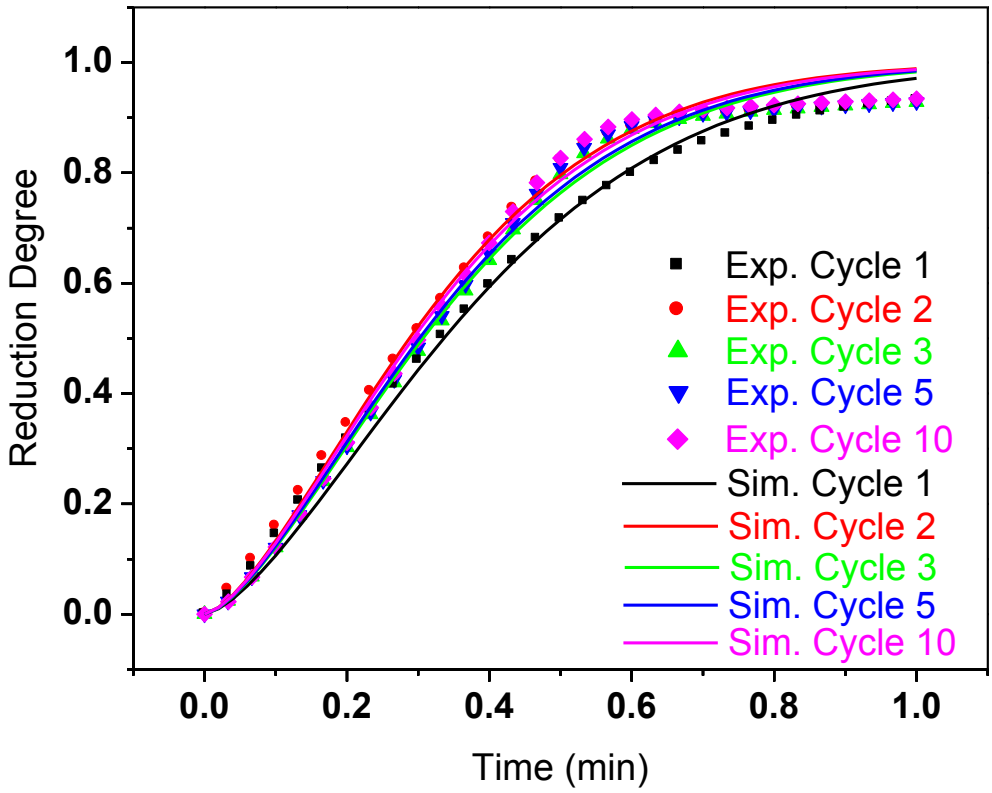

Figure 7.6. Reduction degree profile of CuO/CeO_2 catalysts using optimal kinetic results.

Table 7.3. Reaction rate at different cycles of reduction stages.

	Cycle 1	Cycle 2	Cycle 3	Cycle 5	Cycle 10
R^2	0.9903	0.9908	0.9928	0.9922	0.9924
k	2.33	2.55	2.59	2.67	2.72

The oxidation analysis was conducted with same principle as the reduction stage. The mathematical models used for the reduction stage were also used for the oxidation stage. In this case, R^2 values varied from 0.5452 to 0.9948 at different cycles as shown in Table 7.4. After comparison, it can be concluded that 4^{th} order of Avrami-Erofeev model fitted the oxidation reactions. Oxidation degree (OD) as a function of time was represented in Fig. 7.7. The stabilized experimental OD value was found at 96% for all of the cycles. However, the reaction rate was different at different cycles. It can be seen that oxidation reaction at first cycle occurred faster than rest of the cycles. At first cycle, 88% OD was achieved in 0.13 min, and then the reaction rate continuously decreased up to stabilized 96% OD at 0.24 min. For other cycles, it took 0.16 min to achieve 88% OD before stabilizing at 96% OD in 0.24 min. The mathematical reaction rate k values retrieved from 4^{th} order of Avrami-Erofeev or nucleation model were listed in Table 7.5. This model employed that during oxidation, Cu^{2+} nucleation perhaps occurred on specific sites, such as grain boundaries or impurities and saturated rapidly. Due to unhindered growth of the nuclei, 3-dimensional growth can be assumed. A part of CeO_{2-x} can also be oxidized to transform into CeO_2 during oxidation process. With compared to the reduction profile, it can be seen that reaction rates of oxidation reaction were much higher (~ 2.75 times) than those of reduction reaction, and this can happen due to unhindered 3-D growth Cu^{2+} during oxidation reaction. However, this model failed to predict the timeline for oxidation of Cu^0 and CeO_{2-x}.

Table 7.4. Overview of fitted data (R^2) for kinetic models at oxidation stages.

Model		Cycle 1	Cycle 2	Cycle 3	Cycle 5	Cycle 10
M1		0.9442	0.8675	0.8755	0.8752	0.8734
M2		0.9169	0.8352	0.8341	0.8333	0.8312
M3		0.9538	0.8938	0.8928	0.9456	0.9466
M4		-	-	-	-	-
M5		0.9386	0.8668	0.9318	0.9316	0.9306
M6		0.8581	0.8501	0.9233	0.9236	0.9225
M7		0.5452	0.6958	0.6949	-	-
M8	n = 1.5	0.9758	0.9297	0.9273	0.9283	0.9267
	n = 2	0.9926	0.9700	0.9694	0.9693	0.9681
	n = 3	0.9705	0.9836	0.9734	0.9541	0.9538
	n = 4	0.9895	0.9932	0.9934	0.9943	0.9948
M9		-	-	-	-	-
M10		-	-	-	-	-

Table 7.5. Reaction rate at different cycles of oxidation stages.

	Cycle 1	Cycle 2	Cycle 3	Cycle 5	Cycle 10
R^2	0.9895	0.9932	0.9934	0.9943	0.9948
k	11.25	8.08	8.07	8.12	8.15

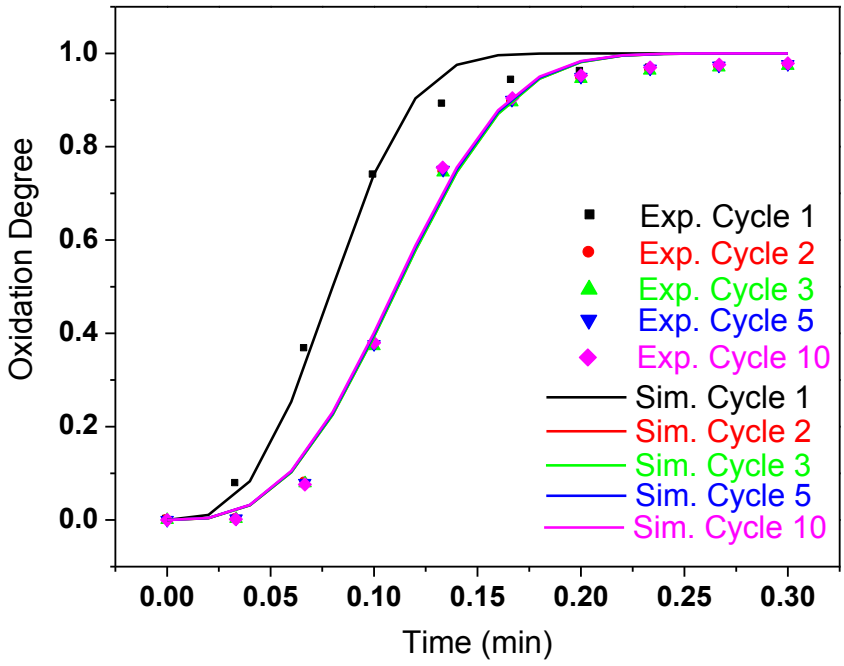

Figure 7.8. Oxidation degree profile of CuO/CeO_2 catalysts using optimal kinetic results.

7.4. Conclusion

CeO_2 nanorods were successfully synthesized using hydrothermal method, and then CuO nanoparticles were incorporated on CeO_2 using thermal decomposition method. Solid state kinetic study of CuO/CeO_2 presented the effect of increasing the cycle number of reduction and oxidation reactions. Both reactions followed Avrami-Erofeev or nucleation model. Reduction reactions proceeded via 1.5^{th} order nucleation model in which possible random Cu^0 nucleation and growth occurred. On the other hand, oxidation reactions progressed likely via 3-dimensional growth of Cu^{2+}.

7.5. References

1. Gamarra, D.; Belver, C.; Fernandez-Garcia, M.; Martinez-Arias, A. Selective CO oxidation in excess H_2 over copper-ceria catalysts: Identification of active entities/species. *J. Am. Chem. Soc*., **2007**, 129, 12064-12065.

2. Wu, S. H.; Li, B. Q.; Huang, W. P.; Zhang, S. M.; Shi, J.; Zheng, X. C. Comparative studies of gold catalysts prepared via solvated metal atom impregnation and conventional impregnation: characterization and low-temperature CO oxidation. *React. Kinet. Catal. Lett*. **2003**, 78, 49-58.

3. Daté, M.; Haruta, M. Moisture effect on CO oxidation over Au/TiO_2 catalyst. *J. Catal*. **2001**, 201, 221-224.

4. Lee, S. J.; Gavriilidis, A. Supported Au catalysts for low-temperature CO oxidation prepared by impregnation. *J. Catal*. **2002**, 206, 305-313.

5. Holmgren, A.; Azamoush, F.; Fridell, E. Influence of pre-treatment on the low-temperature activity of Pt/ceria. *Appl. Catal. B-Environ*. **1999**, 22, 49-61.

6. Semon, P. A. Pt-doped and SnO_2-templated TiO_2: properties and reactivity towards CO. *Solid State Ionics*. **1997**, 101, 673-676.

7. Luo, M. F.; Hou, Z. Y.; Yuan, X. X.; Zheng, X. M. Characterization study of CeO_2 supported Pd catalyst for low-temperature carbon monoxide oxidation. *Catal. Lett*. **1998**, 50, 205-209.

8. Sedmak, G.; Hocevar, S.; Levec, J. Kinetics of selective CO oxidation in excess of H_2 over the nanostructured $Cu_{0.1}Ce_{0.9}O_{2-y}$ catalyst. *J. Catal*. **2003**, 213, 135-150.

9. Wang, Y.; Zhu, A.; Zhang, Y.; Au, C. T.; Yang, X.; Shi, C. Catalytic reduction of NO by CO over NiO/CeO_2 catalyst in stoichiometric NO/CO and $NO/CO/O_2$ reaction. *Appl. Catal. B-Environ.* **2008**, 81, 141-149.

10. Aguila,G.; Gracia, F.; Araya, P. CuO and CeO_2 catalysts supported on Al_2O_3, ZrO_2 and SiO_2 in the oxidation of CO at low temperature. *Appl. Catal. A-Gen*. **2008**, 343, 16-24.

11. Mo, L.; Kawi, S. An in situ self-assembled core-shell precursor route to prepare ultrasmall copper nanoparticles on silica catalysts. *J. Mater. Chem. A* **2014**, 2, 7837-7844.

12. Zou, H.; Chen, S.; Liu, Z.; Lin, W. Selective CO oxidation over $CuO-CeO_2$ catalysts doped with transition metal oxides. *Powder Technol.*, **2011**, 207, 238-244.

13. Djega-Mariadassou, G.; Boudart, M. Classical kinetics of catalytic reactions. *J. Catal*. **2003**, 216. 89-97.

14. Sedmak, G.; Hocevar, S.; Levec, J. Kinetics of selective CO oxidation in excess of H_2 over the nanostructured $Cu_{0.1}Ce_{0.9}O_{2-y}$ catalyst. *J. Catal*. **2003**, 213, 135-150.

15. Liu, W.; Flytzani-Stephanopoulos, M. Total oxidation of carbon monoxide and methane over transition metal fluorite oxide composite catalysts: Catalyst composition and activity. *J. Catal.* **1995**, 153, 304−316.

16. Lu, J. Q.; Sun, C. X.; Li, N.; Jia, A. P.; Luo, M. F. Kinetic study of CO oxidation over CuO/MO_2 (M = Si, Ti and Ce). *Appl. Surf. Sci.*, **2013**, 287, 124-134.

17. Li, N.; Chen, Q. Y.; Luo, L. F.; Huang, W. X.; Luo, M. F.; Hu, G. S.; Lu, J. Q. Kinetic study and the effect of particle size on low temperature CO oxidation over Pt/TiO_2 catalysts. *Appl. Catal. B: Environ*., **2013**, 142-143, 523-532.

18. Xu, D.; Cheng, F.; Lu, Q.; Dai, P. Microwave enhanced catalytic degradation of methyl orange in aqueous solution over CuO/CeO_2 catalyst in the absence and presence of H_2O_2. *Ind. Eng. Chem. Res.*, **2014**, 53, 2625–2632.

19. Yang, F.; Wei, J.; Liu, W.; Guo, J.; Yang, Y. Copper doped ceria nanospheres: surface defects promoted catalytic activity and a versatile approach. *J. Mater. Chem. A*, **2014**, 2, 5662-5667.

20. Hossain, S. T.; Almesned, Y.; Zhang, K.; Zell, E. T.; Bernard, D. T.; Balaz, S.; Wang, R. Support structure effect on CO oxidation: A comparative study on SiO_2 nanospheres and CeO_2 nanorods supported CuO_x catalysts. *Appl. Surf. Sci.,* **2018**, 428, 598-608.

21. Ipaskis, D.; Heracleous, E.; Silvester, L.; Bukur, D. B.; Lemonidou, A. A. Reduction and oxidation kinetic modeling of NiO based oxygen transfer. Chem. Eng. J., **2017**, 308, 840-852.

22. Khawam, A.; Flanagan, D. R. Solid state kinetic models: basic and mathematical fundamentals. J. Phys. Chem. B, **2006**, 110, 17315-17328.

Chapter 8: Summary

This dissertation presented the information of CeO_2 nanorods and SiO_2 nanospheres supported CuO catalysts including their synthesis, structural characterization, and catalytic characterization. Reaction mechanism was also discussed in order to design catalysts with enhanced performance in future.

Chapter 3 described how synthesis of catalyst can have an effect on the catalytic activity of CeO_2 nanorods supported CuO catalysts. A series of CuO/CeO_2 catalysts were successfully prepared by using three different CuO impregnation methods. It illustrated that CuO/CeO_2 synthesized by using thermal decomposition method consumed the highest amount of H_2 at low temperatures (142 and 165 ^oC) and converted 100% CO into CO_2 at low temperature (220 ^oC) in comparison to other two catalysts and this happened due to the presence of strongly interacted dispersed CuO particles or Cu-Ce-O solid solution, resulting an increase in oxygen mobility in CeO_2 lattice.

Chapter 4 presented the effect of Cu amount on the catalytic activity of Cu-O-Ce solid solutions and CuO/CeO_2 nanorods catalysts. It concluded that the amount of Cu incorporation into CeO_2 lattice depends on the preparation methods of the catalysts and CeO_2 structure (shape and surface defects etc.). The different distribution and interactions of copper species with CeO_2 in these samples led to varied hydrogen consumption behaviors (temperature and amount). The TPR-TPO thermal cycling treatments suggested an increase of oxygen vacancy concentration and improved low temperature reducibility over the 10 wt% Cu impregnated in Cu-O-Ce samples after each cycle, which was further supported by the CO oxidation analysis.

Chapter 5 and chapter 6 discussed a comparison between reducible CeO_2 and non-reducible SiO_2 support for the application of CO oxidation and the effect of CeO_2-SiO_2 co-support on the catalytic activity. The CuO/CeO_2 nanorods exhibited a great enhancement in catalytic efficiency than the CuO/SiO_2 nanospheres. Incorporation of Cu ions in CeO_2 lattice promoted the lower reduction temperature as well as increasing the catalytic efficiency by increasing oxygen mobility via redox reaction at the catalyst-support interface. Increasing the oxidation temperature (from 400 to 600 ^oC) of CuO/CeO_2 decreased the catalytic activity by decreasing the amount of incorporation of Cu in CeO_2 lattice. Conversely, increasing oxidation temperature of CuO/SiO_2 increased the presence of threefold SiO_3 rings, and incorporation of Cu into these rings increased the catalytic efficiency. Mixing of these two oxide supports in 1:1 ratio and impregnation of 10 wt% CuO on CeO_2-SiO_2 composite eventually increased the catalytic efficiency because the presence of SiO_2 reduced the agglomeration of CeO_2 nanorods leading to an increase of oxygen availability by increasing CuO dispersion on both CeO_2 nanorods and the interface of SiO_2-CeO_2.

Chapter 7 illustrated solid state kinetic study of CuO/CeO_2 by increasing the cycle number of reduction and oxidation reactions in isothermal process. Both reactions followed Avrami-Erofeev or nucleation model. Reduction reactions proceeded via 1.5^{th} order nucleation model in which possible random Cu^0 nucleation and growth occurred. On the other hand, oxidation reactions progressed likely via 3-dimensional growth of Cu^{2+}.

This work suggested that the preparation method of the catalysts could have an effect on the catalytic activity by changing the structure of catalyst and support, varying

dispersion amount of catalyst on the support, varying the interfacial structure, and varying the amount of defects in the support. For CeO_2 supported CuO catalysts, the formation of Cu-O-Ce solid solutions aided in lowering the reduction temperature by increasing the amount of oxygen vacancy in CeO_2 lattice. The oxygen vacancy in CeO_2 could also be increased by increasing the redox reaction cycles. For SiO_2 supported CuO catalysts, incorporation of Cu into SiO_3 rings of SiO_2 helped in lowering the reduction temperature. CeO_2 nanorods supported 10 wt% CuO catalysts, which was synthesized using thermal decomposition method and then oxidized at 400 ^oC, showed the best catalytic activity among all of the prepared catalysts for this project.

Although this dissertation enhances our understanding in CeO_2 and SiO_2 supported catalyst systems, an in-situ characterization of catalysts may give a better understanding in the structure effect of CeO_2 and SiO_2 on the catalytic activity. In the future, we will investigate the structural change in CeO_2 during CO oxidation in an in-situ technique (Raman spectroscopy or TEM). A model catalyst in which shape-controlled CuO impregnated on shape-controlled CeO_2 will be synthesized and characterized to conduct an in-depth analysis of reaction mechanism at CeO_2-CuO interface. The presence of threefold SiO_3 rings in SiO_2 supported catalysts and its effect on the catalytic activity will need more attention in future as this may turn non-active SiO_2 support into an active support like CeO_2.